

CO<sub>2</sub> CAPTURE FROM GASES USING ACTIVATED CARBON

A Thesis Submitted to the College of Graduate and Postdoctoral Studies  
In Partial Fulfillment of the Requirements  
For the Degree of Doctor of Philosophy  
In the Department of Chemical and Biological Engineering  
University of Saskatchewan  
Saskatoon

By

Sepideh Shahkarami

### **Permission to Use**

In presenting this thesis in partial fulfillment of the requirements for a Postgraduate degree from the University of Saskatchewan, I agree that the Libraries of this University may make it freely available for inspection. I further agree that permission for copying of this thesis in any manner, in whole or in part, for scholarly purposes may be granted by Dr. Ajay K. Dalai and Dr. Jafar Soltan who supervised my thesis work or, in their absence, by the Head of the Department or the Dean of the College in which my thesis work was done. It is understood that any copying or publication or use of this thesis or parts thereof for financial gain shall not be allowed without my written permission. It is also understood that due recognition shall be given to me and to the University of Saskatchewan in any scholarly use which may be made of any material in my thesis.

Requests for permission to copy or to make other uses of materials in this thesis/dissertation in whole or part should be addressed to:

Head of the Department of Chemical and Biological Engineering  
57 Campus Drive  
University of Saskatchewan  
Saskatoon, Saskatchewan S7N 5A9 Canada

OR

Dean  
College of Graduate and Postdoctoral Studies  
University of Saskatchewan  
107 Administration Place  
Saskatoon, Saskatchewan S7N 5A2 Canada

## Abstract

Research on the CO<sub>2</sub> adsorption on activated carbon (AC) adsorbents has gained significant interest due to their low cost, low regeneration energy, and eco-friendly characteristics. The current research was focused on the systematic development of AC using different types of biomass, pyrolysis conditions and activation conditions to prepare adsorbent with tailored textural properties for CO<sub>2</sub> separation under simulated flue gas conditions. Impact of MgO impregnation on CO<sub>2</sub> adsorption behavior of AC was also studied and an isothermal mass transfer model was developed to model the CO<sub>2</sub> adsorption process in a binary mixture on porous carbon. The work was divided into four phases. The first phase of the work was focused on the synthesis of activated carbon using steam, CO<sub>2</sub> and potassium hydroxide (KOH) as activating agents and evaluation of the CO<sub>2</sub> adsorption performance under a range of temperature and inlet CO<sub>2</sub> concentrations ( $C_{CO_2}$ ). The KOH treated activated carbon had the best CO<sub>2</sub> adsorption performance of 1.8 mol/kg due to its microporous structure under the optimized experimental conditions of 30 mol% CO<sub>2</sub> and 25°C. All prepared activated carbon samples had a better performance at low temperature (~25°C) and/or high  $C_{CO_2}$  (~30 mol%). In the second phase, the KOH activation conditions in the first phase was used for the activated carbon preparation using three different types of biomass (forest residue, agricultural residue and animal manure) as precursor and two different pyrolysis processes (fast and slow pyrolysis). The main finding in this phase was that activated carbons have different sensitivity to CO<sub>2</sub> separation according to their micro-pore distributions; and total pore volume and surface area are not significant factors for CO<sub>2</sub> adsorption on ACs. Overall, the pinewood saw dust derived ACs showed the best adsorption capacity of 78.1 mg/g (at 15 mol% CO<sub>2</sub> in N<sub>2</sub> and 25°C). In phase 3, the results of impregnating AC with magnesium oxide (MgO) showed that preparation method has a greater impact than metal content on the surface area and porosity of ACs. Moreover, MgO impregnation of AC overcomes the limitation of using not-impregnated AC at moderate temperature and low partial pressure of CO<sub>2</sub>. In the phase 4, an isothermal mass transfer model for CO<sub>2</sub> adsorption in a mixture of CO<sub>2</sub>/N<sub>2</sub> has been developed. The adsorption equilibrium data of CO<sub>2</sub> on KOH activated carbon were determined at 273, 298, 323 and 348 K. The simulation of CO<sub>2</sub> adsorption in a fixed-bed of activated carbon was performed in Python using a bi-Linear Driving Force (bi-LDF) approximation for isothermal mass transfer. The model was used to

reproduce the CO<sub>2</sub> adsorption breakthrough curves for CO<sub>2</sub>/N<sub>2</sub> gas mixture and it can be used for designing a fixed-bed adsorption process to separate CO<sub>2</sub> and N<sub>2</sub> using microporous and mesoporous carbon materials.

## Acknowledgements

I would first like to express my gratitude to my supervisors, Professors A. K. Dalai and J. Soltan for their support, encouragement and collaboration. I also would like to thank the other members of the advisory committee, Professors A. Odeshi, C. Niu, R. Sammynaiken, H. Wang, and S. Shewchuk, for their helpful discussions and suggestions. Finally, I would like to thank Dr. Ondrej Masek from the University of Edinburg for taking time out from his busy schedule to serve as my external examiner.

I'd like to give special thanks to Dr. M. Ghasemi for his professional attitude, skills and persistence in developing the mass transfer model (Python code) of this research work. I must acknowledge the following people for their assistance during my PhD program:

All members of Catalysis and Chemical Reaction Engineering Laboratories, technicians (R. Gerspacher, R. Blondin, R. Prokopishyn and H. Eunike), and secretaries (J. Horosko, K. Bader and M. Paul) of the Department of Chemical and Biological Engineering at the University of Saskatchewan, S. Shokatian from the Department of Chemistry, and Drs. Y. Hu, D. Wang and Ronny Sutarto from the Canadian Light Source. In particular, I am grateful to Dr. Ramin Azargohar for exchanges of knowledge, skills and gaudiness during my graduate program.

I would also like to thank my family for the support they provided me throughout my entire life and in particular, I must acknowledge my husband (Amir) and my sister (Setareh) without whose support and encouragement, I would not have finished this thesis.

I also recognize that this research would not have been possible without the financial assistance of NSERC, the College of Graduate Studies and Research and the Department of Chemical and Biological Engineering at the University of Saskatchewan (Graduate Teaching Assistantships, Graduate Teaching Fellowship, Graduate Research Fellowship and Education Equity Scholarship).

## Table of Contents

<b>Permission to Use</b> .....	i
<b>Abstract</b> .....	ii
<b>Acknowledgements</b> .....	iv
<b>Table of Contents</b> .....	v
<b>List of Tables</b> .....	ix
<b>List of Figures</b> .....	x
<b>Nomenclature</b> .....	xiii
<b>Abbreviations</b> .....	xv
<b>Chapter 1 Introduction and Thesis Outline</b> .....	1
1.1 Introduction .....	1
1.2 Objective: .....	4
1.3 Thesis outline .....	6
<b>Chapter 2 Literature Review</b> .....	8
2.1 Carbon dioxide chemistry .....	8
2.2 Post combustion carbon capture.....	9
2.3 CO <sub>2</sub> adsorption .....	11
2.3.1 Adsorption dynamics, breakthrough curves and selectivity .....	11
2.4 Adsorption isotherms .....	16
2.5 BET surface area and pores size distributions .....	18
2.6 Activated carbon .....	22
2.6.1 Pyrolysis, biochar and activation .....	24
2.6.2 Surface chemistry of activated carbon .....	28
2.6.3 Adsorption on activated carbons.....	29
<b>2.7 Mass transfer model</b> .....	32
2.7.1 Internal mass transfer .....	35
2.7.2 Bi-linear driving force model.....	36
2.8 Error analysis of experimental results .....	41
2.9 Summary .....	42
<b>Chapter 3 Study of the Impact of Activating Agents on Activated Carbons for CO<sub>2</sub> Adsorption</b> .....	42

Contribution of the Ph.D. candidate.....	43
Contribution of this chapter to the overall study.....	43
<b>Abstract</b> .....	43
3.1 Introduction .....	44
3.2 Materials and methods .....	45
3.2.1 Biochar .....	45
3.2.2 Physically activated carbon.....	45
3.2.3 Chemically activated carbon.....	46
3.2.4 Characterization .....	46
3.2.5 Breakthrough CO <sub>2</sub> adsorption measurements.....	47
3.3 Results and discussion.....	50
3.3.1 Characterization of adsorbents.....	50
3.3.2 Adsorption of CO <sub>2</sub> .....	56
3.3.3 Cyclic CO <sub>2</sub> adsorption .....	62
3.4 Conclusions .....	63
<b>Chapter 4 Evaluation of the Effects of Precursors and Pyrolysis Process on Adoption Capacity and Selectivity of Activated Carbons for CO<sub>2</sub> Capture</b> .....	64
Contribution of the Ph.D. candidate.....	64
Contribution of this chapter to the overall study.....	65
<b>Abstract</b> .....	65
4.1 Introduction .....	66
4.2 Material and method.....	67
4.2.1 Biomass.....	67
4.2.2 Fast pyrolysis .....	67
4.2.3 Slow pyrolysis.....	67
4.2.4 KOH activated carbon.....	68
4.2.5 Characterization .....	68
Elemental analysis, ash content, BET surface area, pore size distribution and total pore volume .....	68
Particle size analysis .....	68
Scanning Electron Microscope (SEM).....	69
C 1s Near Edge X-Ray Absorption Fine Structure Spectroscopy (NEXAFS).....	69

4.2.6	Breakthrough CO <sub>2</sub> adsorption measurements .....	69
4.3	Results and discussions .....	70
4.3.1	Characterization of adsorbents.....	70
4.3.2	Adsorption of CO <sub>2</sub> .....	82
4.4	Conclusions .....	86
<b>Chapter 5 Enhanced CO<sub>2</sub> Adsorption Using MgO-Impregnated Activated Carbon: Impact of Preparation Techniques .....</b>		<b>87</b>
	Contribution of the Ph.D. candidate.....	87
	Contribution of this chapter to the overall study.....	87
	<b>Abstract .....</b>	<b>88</b>
5.1	Introduction .....	89
5.2	Materials and methods .....	90
5.2.1	Excess solution impregnation of biochar.....	91
5.2.2	Excess solution impregnation of activated carbon .....	91
5.2.3	Incipient wetness impregnation of activated Carbon .....	92
5.2.4	Characterization.....	92
5.2.5	CO <sub>2</sub> adsorption measurements.....	92
5.3	Results and discussion.....	93
5.3.1	Material characterization .....	93
5.3.2	CO <sub>2</sub> adsorption on impregnated activated carbon .....	101
5.4	Conclusions .....	104
<b>Chapter 6 Equilibrium and Modeling of Isothermal Fixed-Bed CO<sub>2</sub> Adsorption .....</b>		<b>105</b>
	Contribution of the Ph.D. candidate.....	105
	Contribution of this chapter to the overall study.....	105
	<b>Abstract .....</b>	<b>105</b>
6.1	Introduction .....	106
6.2	Material and methods .....	107
6.2.1	Activated carbon.....	107
6.2.2	Adsorption isotherm .....	108
6.3	Mathematical model and solution method .....	108
6.3.1	Model description.....	109
6.3.2	Numerical solution .....	113

6.4	Results and discussions .....	114
6.4.1	Activated carbon properties and adsorption isotherms.....	114
6.4.2	Fixed-bed CO <sub>2</sub> /N <sub>2</sub> mixture adsorption: experimental and modeling.....	117
6.4.3	Controlling mass transfer step .....	120
6.5	Conclusions .....	120
<b>Chapter 7 Conclusions and Recommendations for Future Work.....</b>		<b>122</b>
7.1	Conclusions .....	122
7.2	Recommendations for future work.....	123
<b>References .....</b>		<b>124</b>
<b>Appendix A : Steam, CO<sub>2</sub> and KOH activation set-up for production of activated carbons</b> .....		<b>137</b>
<b>Appendix B : Fixed reactor specifications and calibration curves for CO<sub>2</sub> adsorption</b> <b>experiment in chapter 3 .....</b>		<b>142</b>
<b>Appendix C : The ANOVA results of CO<sub>2</sub> activated carbon.....</b>		<b>145</b>
<b>Appendix D : Willow ring characteristic, GC calibration data, fixed-bed reactor</b> <b>specifications and related calibrations for CO<sub>2</sub> adsorption experiment in chapter 4 .....</b>		<b>146</b>
<b>Appendix E : Calibration data and calculations used in Chapter 5.....</b>		<b>150</b>
<b>Appendix F : Calibration data and calculations used in Chapter 6.....</b>		<b>153</b>
<b>Appendix G : Permission to reuse the published papers, submitted manuscript and Figures</b> .....		<b>158</b>

## List of Tables

Table 2-1: Physical properties of CO <sub>2</sub> .....	8
Table 2-2: Properties of flue gas streams from coal-fired power plants .....	9
Table 2-3: IUPAC classification of pore sizes .....	11
Table 2-4: Summary on different feedstocks, pyrolysis methods, activating agents and their applications.....	26
Table 2-5: CO <sub>2</sub> adsorption capacity of activated carbons .....	30
Table 2-6: Regression coefficients of viscosity calculation for CO <sub>2</sub> and N <sub>2</sub> .....	34
Table 3-1: Physical and chemical properties of CO <sub>2</sub> , steam and KOH activated carbons.....	50
Table 3-2: Relative content of functional groups on CO <sub>2</sub> , steam and KOH activated carbons based on C1s XPS spectra deconvolution .....	56
Table 3-3: Central composite design for two variables and corresponding adsorption capacity	57
Table 3-4: The ANOVA (Analysis of Variance) results of the response surface models for CO <sub>2</sub> adsorption capacity.....	60
Table 4-1: Elemental analysis and physical properties of produced activated carbons .....	74
Table 4-2: CO <sub>2</sub> adsorption capacities and selectivities of the produced activated carbons from the breakthrough measurements with CO <sub>2</sub> /N <sub>2</sub> and CO <sub>2</sub> /N <sub>2</sub> /O <sub>2</sub> mixtures at 25°C .....	83
Table 5-1: Physical characteristics of adsorbents .....	94
Table 5-2: CO <sub>2</sub> adsorption capacities and breakthrough time at 25° C .....	103
Table 6-1: Experimental parameters used in the simulation .....	109
Table 6-2: Boundary and initial conditions.....	113
Table 6-3: Fitting parameters of adsorption equilibrium and kinetic parameters for adsorption on activated carbon.....	115
Table 6-4: Experimental conditions and mass transfer parameters used in model .....	120

## List of Figures

Figure 1-1: Schematic representation of post-combustion, pre-combustion and oxyfuel combustion .....	2
Figure 1-2: Schematic of an amine-based CO <sub>2</sub> capture system .....	4
Figure 2-1: Schematic of an amine-based CO <sub>2</sub> capture system .....	10
Figure 2-2: Typical breakthrough curve.....	12
Figure 2-3: Travel of Mass transfer zone through the bed and the corresponding breakthrough curve	13
Figure 2-4: Graphical method to calculate the adsorption capacity.....	15
Figure 2-5: IUPAC adsorption Isotherms <sup>19</sup> .....	17
Figure 2-6: Four types of hysteresis loop by IUPAC.....	18
Figure 2-7: Temperature swing adsorption .....	32
Figure 2-8: Diffusion mechanism in bi-porous material at low concentration .....	36
Figure 3-1: Schematic of adsorption set-up .....	48
Figure 3-2: N <sub>2</sub> adsorption–desorption isotherms of CO <sub>2</sub> , steam and KOH activated carbons.	51
Figure 3-3: Incremental micropore volume of (a) steam, (b) CO <sub>2</sub> and (c) KOH activated carbons .....	52
Figure 3-4: Incremental mesopore volume of (a) steam and (b) CO <sub>2</sub> activated carbons .....	54
Figure 3-5: Proportion of ultra micropores, supermicropores and mesopores in KOH, CO <sub>2</sub> and steam activated carbons.....	54
Figure 3-6: C1s XPS spectra of the activated carbons prepared using (a) steam, (b) CO <sub>2</sub> and (c) KOH	56
Figure 3-7: Breakthrough curves of steam, CO <sub>2</sub> and KOH activated carbons (ACs) performed at 65°C in 10 mol.% CO <sub>2</sub> in He, and at 25°C in 30 mol.% CO <sub>2</sub> in He .....	58
Figure 3-8: Breakthrough curves for CO <sub>2</sub> adsorption using KOH activated carbon performed in 20 mol. % CO <sub>2</sub> in He at 16, 45 and 73.3°C.....	59
Figure 3-9: Breakthrough curves for CO <sub>2</sub> adsorption using KOH activated carbon performed at 45°C and 5.6 in 20 and 34 mol.% CO <sub>2</sub> in He.....	59
Figure 3-10: Response surface plot of CO <sub>2</sub> adsorption capacity of (a) KOH activated carbon and (b) steam activated carbons .....	62

Figure 3-11: Cyclic CO <sub>2</sub> adsorption performed at 25 °C using steam, CO <sub>2</sub> and KOH activated carbons in 30 mol.% CO <sub>2</sub> in He .....	63
Figure 4-1: Schematic diagram of the adsorption set-up .....	70
Figure 4-2: Yield of saw dust, flax straw, poultry litter, wheat straw and willow ring based activated carbons .....	71
Figure 4-3: Particle size distribution of (a) slow pyrolysis based and (b) fast pyrolysis based activated carbons .....	72
Figure 4-4: SEM images of a) willow ring-slow pyrolysis, b) poultry litter- slow pyrolysis, c) flax straw-slow pyrolysis, d) wheat straw- slow pyrolysis, e) saw dust- slow pyrolysis, f) willow ring-fast pyrolysis, g) poultry litter- fast pyrolysis, h) flax straw- fast pyrolysis, i) wheat straw- fast pyrolysis, j) saw dust- fast pyrolysis activated carbon (12K magnification) and k) SD-FP activated carbon (150K magnification).....	73
Figure 4-5: Incremental mesopore and macropore volume of (a) WR-SP, (b) WS-SP, (c) PL-SP, (d) FS-SP, (e) SD-SP, (f) WR-FP, (g) WS-FP, (h) PL-FP, (i) FS-FP and (j) SD-FP .....	77
Figure 4-6: Incremental micropore volume of (a) WR-SP, (b) WS-SP, (c) PL-SP, (d) FS-SP, (e) SD-SP, (f) WR-FP, (g) WS-FP, (h) PL-FP, (i) FS-FP and (j) SD-FP .....	79
Figure 4-7: C 1s NEXAFS spectra of (a) slow pyrolysis based ACs and (b) fast pyrolysis based ACs	81
Figure 4-8: Breakthrough curves of ACs in a) slow pyrolysis samples in N <sub>2</sub> /CO <sub>2</sub> feed stream b) fast pyrolysis samples in N <sub>2</sub> /CO <sub>2</sub> feed stream, c) slow pyrolysis samples in N <sub>2</sub> /CO <sub>2</sub> /O <sub>2</sub> feed stream and d) fast pyrolysis samples in N <sub>2</sub> /CO <sub>2</sub> /O <sub>2</sub> feed stream .....	82
Figure 4-9: The cyclic CO <sub>2</sub> adsorption performance of (a) slow pyrolysis activated carbons and (b) fast pyrolysis activated carbons in CO <sub>2</sub> /N <sub>2</sub> .....	85
Figure 5-1: N <sub>2</sub> adsorption-desorption isotherms at 77 K.....	94
Figure 5-2: Pore size distributions of (a) 10MgO-B, (b) 10MgO-B-R, (c) 10MgO-AC, (d) 10MgO-AC-R and (e) 10MgO-AC-DRY determined from the N <sub>2</sub> and CO <sub>2</sub> adsorption isotherms at 77 K and 273 K using a NLDFT analysis.....	98
Figure 5-3: Pore size distributions of (a) 3MgO-B, (b) 3MgO-B-R, (c) 3MgO-AC, (d) 3MgO-AC-R and (e) 3MgO-AC-DRY determined from the N <sub>2</sub> and CO <sub>2</sub> adsorption isotherms at 77 K and 273 K using a NLDFT analysis .....	99
Figure 5-4: TG-DTG profiles of 10MgO-AC heated from 30 to 700°C in N <sub>2</sub> flow .....	99

Figure 5-5: Powder X-ray diffraction (XRD) patterns of 10 wt. % MgO loaded activated carbon samples .....	100
Figure 5-6: TPD Profile of 10 wt. % MgO loaded activated carbon (10MgO-AC) .....	100
Figure 5-7: Breakthrough curves of 15% CO <sub>2</sub> in N <sub>2</sub> at 25°C on (a) 3 wt. % and (b) 10 wt. % MgO impregnated activated carbons.....	101
Figure 5-8: CO <sub>2</sub> adsorption on non-treated activated carbon and 10MgO-B-R at 25 and 100 °C	103
Figure 5-9: Cyclic CO <sub>2</sub> adsorption of 15% CO <sub>2</sub> in N <sub>2</sub> at 25°C on 10MgO-B-R .....	104
Figure 6-1: Schematic of mass transfer in a fixed bed reactor showing the mechanism of gas transfer to adsorption sites.....	110
Figure 6-2: N <sub>2</sub> and CO <sub>2</sub> adsorption isotherms of activated carbon at 77 K and 273 K (a), and pore size distribution of activated carbon (b).....	115
Figure 6-3: N <sub>2</sub> (a) and CO <sub>2</sub> (b) adsorption equilibrium data of activated carbon .....	116
Figure 6-4: Comparison of experimentally measured breakthrough curves of CO <sub>2</sub> adsorption on KOH activated carbon using 5, 15 and 25 mol% CO <sub>2</sub> in inlet feed with model predictions. ♦, y <sub>CO<sub>2</sub></sub> =5 mol%; ▲, y <sub>CO<sub>2</sub></sub> =15 mol%; ×, y <sub>CO<sub>2</sub></sub> =25 mol%; solid lines represent the model predictions. ....	118
Figure 6-5: Comparison of experimentally measured breakthrough curves of CO <sub>2</sub> adsorption on KOH activated carbon at 25, 45, 65 and 85 °C with model predictions. ♦, T=25°C; ▲, T=45°C; ×, T=65°C; +, T=85°C; solid lines represent the model predictions. ....	119
Figure 6-6: Comparison of experimentally measured breakthrough curves of CO <sub>2</sub> adsorption on KOH activated carbon using feed flowrate of 30, 50 and 70 ml/min with model predictions. ×, Q= 70ml/min; ▲, Q= 50ml/min; ♦, Q= 30ml/min; solid lines represent the model predictions. ....	119

## Nomenclature

$b_{0i}$  = temperature - independent constant of Langmuir isotherm of component i,  $\text{kPa}^{-1}$

$b_{ij}$  = constant of Langmuir isotherm of component i,  $\text{kPa}^{-1}$

$c_i$  = concentration of component i in bulk gas phase,  $\text{mol/m}^3$

$c_{pi}$  = concentration of component i in macropores,  $\text{mol/m}^3$

$\overline{c_{pi}}$  = average concentration of component i in macropores,  $\text{mol/m}^3$

$C$  = total concentration of bulk gas phase,  $\text{mol/m}^3$

$C_{\text{CO}_2}$  =  $\text{CO}_2$  content

$d_p$  = particle diameter, m

$D_{\text{ax},i}$  = axial dispersion of component i,  $\text{m}^2/\text{s}$

$D_{ci}$  = crystal diffusivity of component i,  $\text{m}^2/\text{s}$

$D_{ci0}$  = temperature - independent pre - exponential constant of component i,  $\text{m}^2/\text{s}$

$D_{ci}^\infty$  = temperature dependant diffusivity constant of component i,  $\text{m}^2/\text{s}$

$D_{i,j}^\infty$  = binary molecular diffusion coefficient at a reference temperature and pressure,  $\text{m}^2/\text{s}$

$D_{i,j}$  = binary molecular diffusion coefficient,  $\text{m}^2/\text{s}$

$D_{K,i}$  = Knudsen diffusivity of component i,  $\text{m}^2/\text{s}$

$D_{m,i}$  = molecular diffusivity of component i,  $\text{m}^2/\text{s}$

$D_{pi}$  = effective macropore diffusivity of component i,  $\text{m}^2/\text{s}$

$E_{a,i}$  = diffusion activation energy of component i, J/mol

$H$  = Henry's law constant

$\Delta H_i$  = adsorption heat of component i, J/mol

$k_{fi}$  = particle - to - fluid mass transfer coefficient

$n$  : the number of independent process variables

$n_c$  : the number of center points or replicates

$q_{ci}^*$  = equilibrium adsorbed concentration of component i, mol/kg

$q_{si}$  = saturation capacity of component i, mol/g

$\overline{q_{ci}}$  = average adsorbed concentration of component i per unit of particle volume, mol/kg

$\overline{q_{pi}}$  = average adsorbed concentration of component i per unit of adsorbent bed volume, mol/kg

$r_c$  = radius of crystal, m

$r_p$  = pore radius, m

$R$  = universal gas constant, J/Kmol

$R$  = universal gas constant, J/Kmol

$R_p$  = Particle radius, m

$t$  = time, s

$T$  = temperature, K

$t_b$  = breakthrough time, °C

$u$  = gas velocity, m/s

$V_{p,b}$  = pore volume determined from  $CO_2$  and  $N_2$  adsorption data at 298 K and 77 K,  $m^3/kg$

$V_c$  = volume of packed - bed,  $m^3$

$W$  = weight of powder, kg

$X, Y,$  and  $Z$  = regression coefficients for chemical compound

$y_i$  = mole fraction of component  $i$

### **Greek Symbols**

$\epsilon_b$  = bed porosity

$\epsilon_p$  = particle porosity

$\epsilon_t$  = total porosity

$\eta_f$  = viscosity of gas mixture, kg/m.s(Pa.s)

$\eta_i$  = viscosity of component  $i$ , kg/m.s(Pa.s)

$\lambda_p$  = Equivalent spherical diameter of the particle

$\rho_f$  = density of gas stream,  $kg/m^3$

$\rho_i$  = density of component  $i$ ,  $kg/m^3$

$\rho_s$  = absolute or skeletal density,  $kg/m^3$

$\rho_p$  = particle density

$\tau_k$  = Knudsen tortuosity factor

$\tau$  = tortuosity factor

$\phi_{i,j}$  = Wilke's parameter

## Abbreviations

3MgO-AC: 3 wt. % MgO loaded activated carbon

3MgO-AC-R: 3 wt. % MgO loaded activated carbon-rinsed

3MgO-AC-DRY: 3 wt. % MgO incipient impregnated activated carbon

3MgO-B: 3 wt. % MgO loaded biochar

3MgO-B-R: 3 wt. % MgO loaded biochar-rinsed

10MgO-AC: 10 wt. % MgO loaded activated carbon

10MgO-AC-R: 10 wt. % MgO loaded activated carbon-rinsed

10MgO-AC-DRY: 10 wt. % MgO incipient impregnated activated carbon

10MgO-B: 10 wt. % MgO loaded biochar

10MgO-B-R: 10 wt. % MgO loaded biochar-rinsed

AC: activated carbons

ANOVA: Analysis of Variance

BET: Brunauer, Emmett, and Teller

Bi-LDF: Bi-linear Driving Force

CCD: Central Composite Design

df: degree of freedom

DFT: density Functional Theory

FP: fast pyrolysis

FS: flax straw

FTIR: Fourier Transform Infra-Red,

FWHM: full width at half maximum

GAI: Generalized Adsorption Isotherm

GC: Gas Chromatograph

H<sub>3</sub>PO<sub>4</sub>: phosphoric acid

He: helium

IPCC: The Intergovernmental Panel on Climate Change

IUPAC: International Union of Pure and Applied Chemistry

KOH: potassium hydroxide

LDF: Linear Driving Force

MFC: Mass Flow Controller

MgCl<sub>2</sub>: Magnesium chloride  
Mg (NO<sub>3</sub>)<sub>2</sub>·6H<sub>2</sub>O: Magnesium nitrate hexahydrate  
MgO: magnesium oxide  
MTZ: Mass Transfer Zone  
NaOH: sodium hydroxide  
NEXAFS: Near Edge X-ray Absorption Fine Structure  
NLDFT: Non-Local Density Functional Theory  
PL: poultry litter  
PSD: Particle Size Distribution  
REIXS: The Resonant Elastic and Inelastic X-ray Scattering  
SD: saw dust  
SEM: Scanning Electron Microscope  
SGM: spherical grating monochromator  
SP: slow pyrolysis  
TCD: Thermal Conductivity Detector  
TGA: ThermoGravimetric Analyzer  
TPD: Temperature-Programmed Desorption  
TSA: Temperature Swing Adsorption  
WR: willow ring  
WS: wheat straw  
XPS: X-Ray Photoelectron Spectroscopy  
XRD: X-Ray Diffraction

## Chapter 1 Introduction and Thesis Outline

### 1.1 Introduction

Global warming has become one of the most important environmental problems in 21<sup>th</sup> century<sup>1</sup> and the rise in CO<sub>2</sub> emissions is considered as the main cause for the global warming. The highest raise in average temperature was observed in the 30-year period of 1983 to 2012 of the last 1400 years in the northern hemisphere<sup>2</sup> which results in 0.85 °C global surface temperature increase in the period of 1880-2012<sup>2</sup>. After Kyoto protocol came into force in 2005 more attention is devoted to this matter. However, signatories of the Kyoto protocol didn't meet their commitments to decrease emissions and the CO<sub>2</sub> content level in atmosphere is recorded to be 400.40 ppm in November 2015<sup>3</sup>. The mitigation scenarios include “energy efficiency optimization, zero and low carbon energy supplies including nuclear power, fossil fuel energies with carbon dioxide capture and storage units, renewable energy sources, enhancement of biological sinks, and reduction of non- CO<sub>2</sub> greenhouse gas emissions”<sup>4</sup>. In the absence of mitigation policies, if CO<sub>2</sub> emission increases with the same rate, it is estimated that CO<sub>2</sub> concentrations in the atmosphere could increase to 600–1550 ppm in 2030<sup>5</sup>. It corresponds to 4.1°C – 4.8°C above pre-industrial average global temperature by the end of the 21<sup>th</sup> century. Carbon capture from major CO<sub>2</sub> emitting industries like coal-fired power plants and fossil-fuel based plants is one of the immediate options to address this issue. In the 11<sup>th</sup> session of the Conference of the Parties serving as the meeting of the Parties to the Kyoto Protocol (CMP 11)<sup>6</sup> that took place from 30 November to 11 December 2015 in Paris, the members agreed to limit average global temperature over the 21<sup>st</sup> century to below 2°C above the pre-industrial levels<sup>6</sup>. However, in most of discussed scenarios, fossil fuel is the main source of energy at least until 2050. So, carbon capture and sequestration could be a main option to address this problem and facilitate stabilizing the atmospheric CO<sub>2</sub> concentrations.

Depending on the fuel type, CO<sub>2</sub> partial pressure and gas stream pressure, three types of carbon capture techniques can be used: post-combustion, pre-combustion and oxyfuel combustion. The schematic of these processes are shown in Figure 1-1<sup>5</sup>. Pre-combustion capture processes convert fuel into a mixture of hydrogen and CO<sub>2</sub>. The separated hydrogen can be burnt with zero-emission of CO<sub>2</sub>. Post-combustion processes separate CO<sub>2</sub> from combustion flue gas stream. In

oxyfuel capture processes, pure oxygen is used for fuel combustion. The exhaust gases of this process are water vapor and CO<sub>2</sub>.

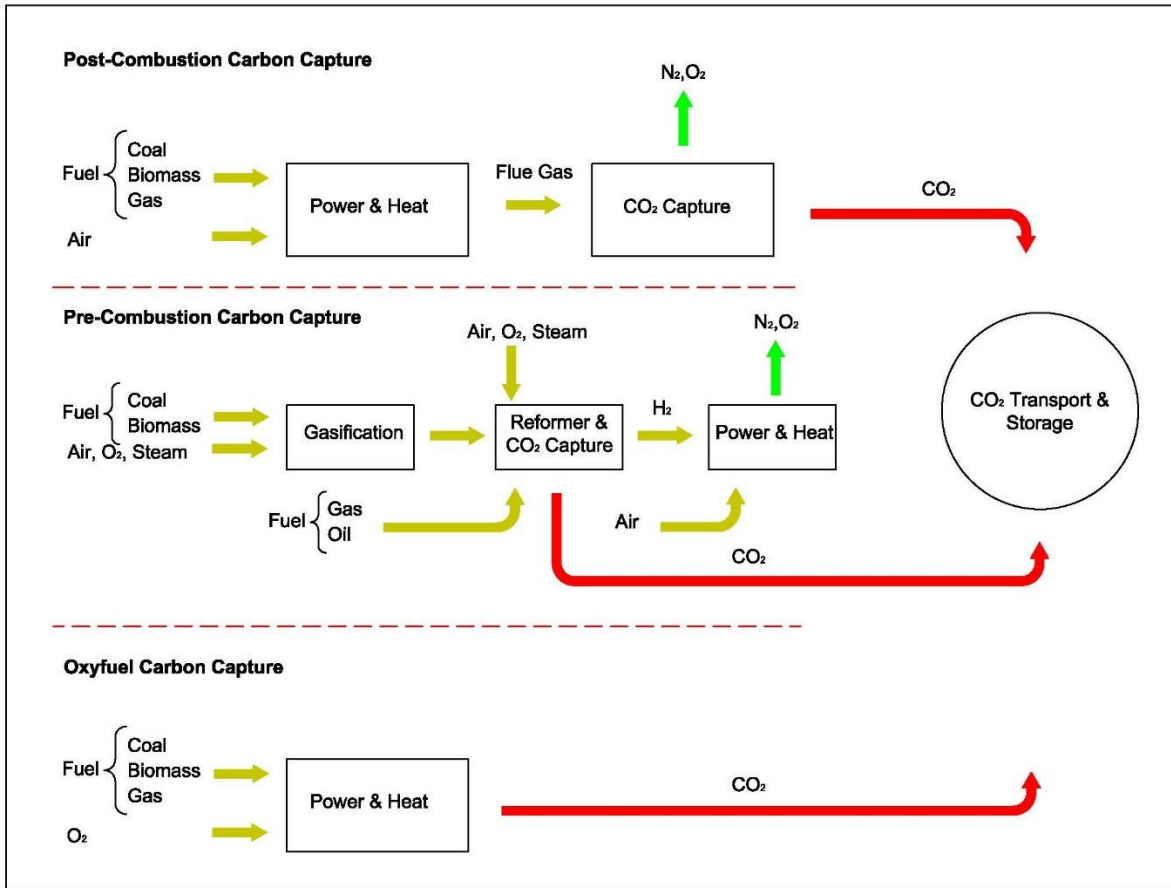


Figure 1-1: Schematic representation of post-combustion, pre-combustion and oxyfuel combustion

Post combustion carbon capture is the preferred technique to reduce CO<sub>2</sub> emission from the existing power plants<sup>5</sup>. All the commercially available processes are similar in concept. Figure 1-2 shows the schematic of this process<sup>4</sup>. The low concentration of CO<sub>2</sub> means that a huge amount of gas should be treated at a high capital cost. The energy penalty associated with the stripping of CO<sub>2</sub> and regeneration of solvent is one of the main technology challenges that must be overcome for the amine absorption based technology in power plants. Two other concerns with amine

solvents are corrosion problem, in the presence of oxygen, and high solvent degradation rates<sup>5,7-9</sup>.

Due to this operation problems involved in amine absorption process, alternative methods are considered. One of these alternatives is CO<sub>2</sub> adsorption on solid surfaces. Due to the large volume to flue gas, capital cost of post-combustion process is large. So, using expensive sorbent materials or material with high disposal expenses can escalate cost related to the process and make it economically unfeasible<sup>4</sup>. Based on IPCC report<sup>10</sup>, a selective adsorbent with high CO<sub>2</sub> uptake might make the design of a full-scale adsorption unit feasible<sup>11</sup>. The ideal adsorbent for CO<sub>2</sub> separation should have some important characteristics such as: high CO<sub>2</sub> adsorption capacity, appropriate selectivity over N<sub>2</sub> and CH<sub>4</sub> and high stability in repetitive cyclic adsorption/desorption process<sup>5</sup>. This thesis focuses on development of low-cost and effective adsorbents for CO<sub>2</sub> capture from coal-fired power plants.

Based on the literature review discussion in chapter 2 the following knowledge gaps were identified:

- Study of impacts of precursor, pyrolysis conditions and activating agents on porosity, surface chemistry of activated carbon were missing from literature.
- The adsorption of CO<sub>2</sub>, in competition with N<sub>2</sub> and other flue gas components were mostly discussed in terms of surface area and surface chemistry. Contribution of parameters such as total pore volume, micro pore volume and ultra micropore on CO<sub>2</sub> adsorption of activated carbon is not clearly understood
- Most of results in the literature are reported based on equilibrium adsorption of CO<sub>2</sub> using pure CO<sub>2</sub> or mixed with an inert gas. Measurement of CO<sub>2</sub> adsorption on activated carbon at low partial pressure of CO<sub>2</sub> (5-15 mol. %) and moderate temperature is very limited.
- Research work on performance study of activated under simulated flue gas conditions require attention. study of the solid adsorbents using simulated post combustion flue gas and different bed configuration can enhance adsorption/desorption performance for CO<sub>2</sub> separation

- Several amine-impregnated solid sorbents were developed using various amine groups to enhance CO<sub>2</sub> adsorption. However, the potential application of impregnation of activated carbon with metal oxides to improve CO<sub>2</sub> adsorption performance at low and moderate temperature in comparison with other surface treatment didn't discussed in the literature.
- Mathematical modeling of the fixed-bed adsorption of carbon dioxide using different mass transfer mechanisms have been discussed in the literature. However, limited work is reported on adsorption kinetics of CO<sub>2</sub>/N<sub>2</sub> adsorption on activated carbons for post combustion conditions.

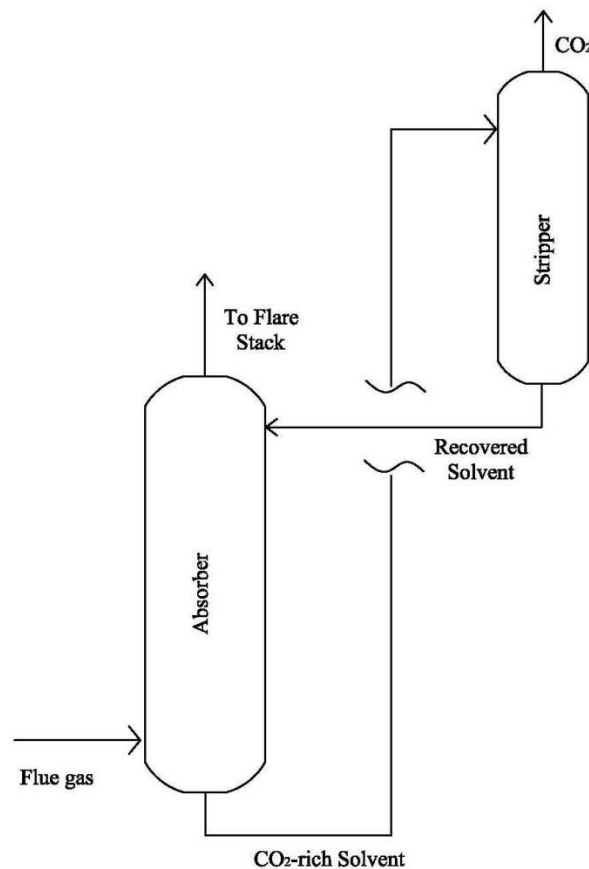


Figure 1-2: Schematic of an amine-based CO<sub>2</sub> capture system

## 1.2 Objective:

The abundance of biomass precursors in Saskatchewan, their important role in the Canadian economy, and the increasing demand and market for environmental applications of biochar and

activated carbon are the motivation for this research project. The underlying principle behind my research was to carbonize the waste biomass in Saskatchewan, convert it to activated carbons as a value added product and use this activated carbon for separation of carbon dioxide from coal-fired power plants. Since the impact of precursors, carbonization method, activating agents and conditions, metal impregnation on physical and chemical properties and CO<sub>2</sub> adsorption behavior of activated carbon are not clear, the following objectives and sub-objectives were set in this work:

- Preparation of activated carbon using three different activating agents:
  - Synthesis of activated carbons from a low cost source in Canada using different activating agents: physical activation (steam and CO<sub>2</sub>) and chemical activation (KOH) and their characterizations.
  - Characterization of the produced activated carbons.
  - Evaluation of the impact of activating agents on CO<sub>2</sub> adsorption performance of the produced activated carbons using various flue gas mixture (10-30 mol. % of CO<sub>2</sub> in He) at 25-65 °C and atmospheric pressure.
- Preparation of activated carbon from different Canadian waste biomasses under different carbonization conditions:
  - Preparation of activated carbons from different sources of biomass and different carbonization techniques: the forest residues (willow ring and saw dust), the agricultural residues (wheat straw and flax Straw) and the animal manure (poultry litter)
  - Characterization of the produced activated carbons.
  - Evaluation of the impact of precursors and pyrolysis methods on CO<sub>2</sub> adsorption capacity, selectivity and stability of produced activated carbons under the flue gas mixture of 15 mol. % of CO<sub>2</sub>, 5 mol. % of O<sub>2</sub> and 80% of N<sub>2</sub> at 25 °C and atmospheric pressure.
- Preparation of metal impregnated activated carbons using different impregnation technique and metal content:

- Preparation of metal impregnated mesoporous activated carbon using: excess solution impregnation of activated carbon, incipient wetness impregnation of activated carbon and excess solution impregnation of biochar.
- Evaluation of impacts of washing step and metal content on porosity and surface chemistry of activated carbon.
- Evaluation of performance of metal impregnated carbons for CO<sub>2</sub> adsorption at 25 and 100 °C in a gas mixture of 15wt. % CO<sub>2</sub> in N<sub>2</sub>.
- Development of a reliable isothermal mass transfer model to simulate CO<sub>2</sub> adsorption
  - Fit a full set of equilibrium data with Langmuir adsorption model.
  - Development of an isothermal mass transfer model to express the performance of the fixed-bed adsorption column for CO<sub>2</sub> adsorption in a binary mixture of CO<sub>2</sub>/N<sub>2</sub> in the range of post-combustion operation conditions.
  - Validation of the model with experimental data.

### 1.3 Thesis outline

Chapter 2 of this thesis is devoted to a comprehensive literature review of post combustion CO<sub>2</sub> capture, CO<sub>2</sub> adsorption, adsorption isotherms, surface area and porosity, synthesis of activated carbons and their properties for CO<sub>2</sub> separation and mass transfer parameters and models for gas adsorption on activated carbons.

To study the effects of activating agents on physical and chemical properties of the activated carbons, activated carbons are prepared from biochar (by product of fast pyrolysis of Whitewood) using three different activating agents of steam, CO<sub>2</sub> and potassium hydroxide using a fixed- bed reactor. In chapter 3, the details of activation methods and conditions, textural properties and surface chemistry of the activated carbons, and CO<sub>2</sub> adsorption capacity and stability of these adsorbents in a binary mixture of CO<sub>2</sub>/ He at atmospheric pressure, temperature range of 25-65 °C and inlet CO<sub>2</sub> concentrations range of 10-30 mol. % are discussed.

It is known that the heteroatoms, derived from precursors, become a part of chemical structure during the carbonization. Biochars derived from different sources and carbonization techniques have different physical and chemical properties<sup>12</sup>. Therefore, preparation of activated carbons

from different precursors or carbonization conditions affects adsorption characteristics of these adsorbents. In chapter 4, the effects of precursors and pyrolysis methods on textural properties and surface functional groups of activated carbons are evaluated. Activated carbons are produced from different waste biomasses including agricultural waste (wheat straw and flax straw), forest residue (saw dust and willow ring) and animal manure (poultry litter). The precursors are carbonized through the fast and slow pyrolysis processes and then activated with potassium hydroxide. The adsorption capacity, selectivity and stability of the produced activated carbon is measured under a flue gas condition of 15 mol% of CO<sub>2</sub>, 5 mol% of O<sub>2</sub> and 80% of N<sub>2</sub> at 25 °C and atmospheric pressure.

More importantly, surface properties of activated carbons can be modified by metal oxide impregnation<sup>13,14</sup>. Magnesium oxide (MgO) is available in natural minerals and can be produced at low cost<sup>15,16</sup>. Selective CO<sub>2</sub> chemisorption on MgO at moderate temperature levels is reported in the literature, indicating that it needs a lower regeneration energy compared to other metal oxides<sup>15</sup>. In chapter 5, the effects of impregnation methods and metal content (3 and 10 wt. %) on adsorption capacity and stability of activated carbons are evaluated. Steam activated carbons are impregnated with MgO using two methods of incipient wetness and excess solution impregnation process. CO<sub>2</sub> Adsorption properties of these adsorbents are compared to single-step prepared activated carbons. In this method, biochar is impregnated with MgO followed by steam activation and the products are compared in terms of porosity, surface chemistry and CO<sub>2</sub> adsorption capacity from a feed mixture of 15% CO<sub>2</sub> in N<sub>2</sub> in a fixed-bed reactor.

A kinetic study is the last step in developing a low-cost adsorbent with tailored adsorptive properties for CO<sub>2</sub>. Chapter 6 includes an isothermal bi-LDF model for adsorption in a fixed-bed reactor to confirm the experimental results in this thesis. The details of mass transfer effects on activated carbons and adsorption process are examined.

Chapter 7 summarizes all the findings of Chapters 3-6 and provides some recommendations for possible future works.

## Chapter 2 Literature Review

This chapter provides a review of the post combustion CO<sub>2</sub> capture, breakthrough CO<sub>2</sub> adsorption, adsorption isotherms, surface area and porosity measurements, proper adsorbents for this process, synthesis of activated carbon, its porous structure and surface chemistry, and mass balance in packed-bed reactor and related mass transfer parameters for gas adsorption.

### 2.1 Carbon dioxide chemistry

Carbon dioxide (CO<sub>2</sub>) is a non-polar, colorless and odorless gas composed of a carbon atom double bonded to two oxygen atoms. CO<sub>2</sub> has sixteen bonding electrons in its valence shell. The C=O bonds are equivalent and are short (1.16 Å), and the molecular diameter is 3.30 Å<sup>17</sup>. Although both carbon-oxygen bonds are polar, the CO<sub>2</sub> molecule doesn't have a permanent electrical dipole due to its centrosymmetric structure. Since two equal dipoles are located nearby, their total dipole moment is zero. Therefore, "only two vibrational bands are detected in the IR spectrum<sup>18</sup> : antisymmetric stretching mode at 2350 cm<sup>-1</sup> and a degenerate pair of bending modes at 667 cm<sup>-1</sup>"<sup>18</sup>. However, CO<sub>2</sub> molecule has a strong quadrupole (-13.71E-40 Coulomb/m<sup>2</sup>) as their positive charges overlap<sup>19</sup>. This quadrupole interacts with the carbon lattice, allowing the gas molecule to enter the pores. Other flue gas component such as nitrogen, hydrogen, oxygen and methane have much smaller quadrupole moments which facilitate CO<sub>2</sub> interaction with walls inside activated carbon pores in competition with other component<sup>20</sup>. Physical properties of CO<sub>2</sub> is provided in Table 2-1<sup>21,22</sup>:

Table 2-1: Physical properties of CO<sub>2</sub>

Molecular weight (g/mol)	44.01
Critical temperature (°C)	31.1
Critical pressure (bar)	73.9 bar
Boiling point @1.013 bar (°C)	- 78.5
Specific volume @ STP	0.506 m <sup>3</sup> kg <sup>-1</sup>
Gas density @ STP	1.976 kg m <sup>-3</sup>
Viscosity @ STP	13.72 μN.s m <sup>-2</sup>
PH of saturated CO <sub>2</sub> solutions	3.7

## 2.2 Post combustion carbon capture

CO<sub>2</sub> removal from a flue gas stream is referred to as post-combustion CO<sub>2</sub> capture. Post-combustion CO<sub>2</sub> capture is followed by compression, transportation and storage of CO<sub>2</sub><sup>23</sup>.

Around 25% of world energy supplies are provided by coal as the world's most abundant fossil fuel source<sup>24</sup>. On the other hand, more than two third of coal-fired power plants are less than 10 years old<sup>25</sup> which makes post combustion carbon capture a vital unit to avoid more CO<sub>2</sub> emission to the atmosphere. A typical flue gas properties of a coal-fired power plant is shown in Table 2-2<sup>19,26,27</sup>.

Table 2-2: Properties of flue gas streams from coal-fired power plants

Species	Concentration	Kinetic Diameter	Dipole moment	Quadrupole moment	Polarizability
	(vol. %)	(nm)	Debye	10 <sup>-40</sup> Coulomb·m <sup>2</sup>	(10 <sup>-24</sup> cm <sup>3</sup> )
CO <sub>2</sub>	15-16%	0.330	0	-13.71, -10.00	2.64,2.91,3.02
O <sub>2</sub>	3-4%	0.346	0	-1.33	1.57, 1.77
H <sub>2</sub> O	5-7	0.280	1.85	-6.67	1.45,1.48
N <sub>2</sub>	Balance	0.364	0	-4.91	0.78, 1.74
SO <sub>2</sub>	800 ppm	0.360	1.63	-14.6	3.72,3.89,4.28
NO	150 ppm	0.317	0.16	-6.00	1.7
NO <sub>2</sub>		0.340	0.316	unknown	3.02
N <sub>2</sub> O		0.03170	0.16.0.54	-12.02, 10.00	3.03, 3.32
HCL	100 ppm	0.346	1.11,3.57	13.28	2.63,2.94
CO	20 ppm	0.0376	0.11, 0.37	-8.33, -6.92	1.95,2.19
Ar	~1%	.340	0	0	1.64,1.83
CH <sub>4</sub>	10 ppm	0.380	0	0	2.6
Flue Gas Process Conditions					
Temperature	25-180	°C			

Pressure	1	atm			
----------	---	-----	--	--	--

The commercially available units offer variations of the similar process concept. Figure 2-1 shows the schematic of this process<sup>4</sup>. The amine solvent binds with the CO<sub>2</sub>. The CO<sub>2</sub> enriched solvent is then sent to a stripper column. In the stripper column, solvent is regenerated and recycled to the absorber reactor. Separated pure CO<sub>2</sub> is then cooled-down and transported for compression and sequestration. The energy penalty of the CO<sub>2</sub> stripping and regeneration of the solvent, corrosion and high solvent degradation rates<sup>5,7-9</sup> are the main technology challenges that must be overcome for the amine absorbent based technology in power plants. Emerging technologies using selective membranes and solid adsorbents instead of liquid solvents are under development.

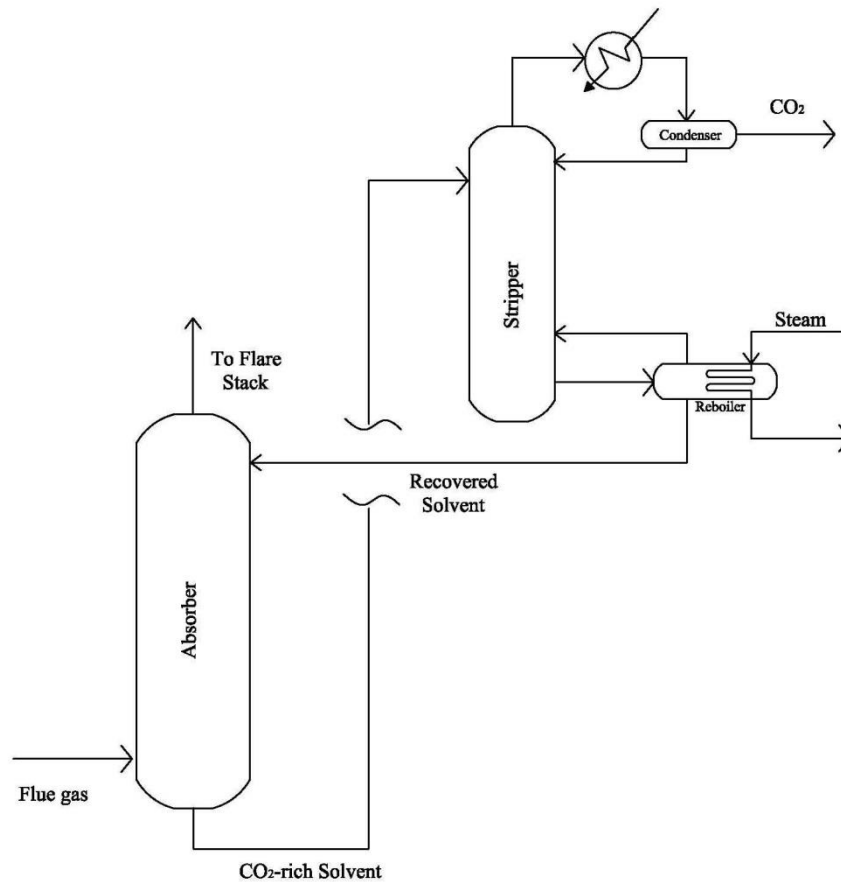


Figure 2-1: Schematic of an amine-based CO<sub>2</sub> capture system

## 2.3 CO<sub>2</sub> adsorption

In an adsorption process, a gas mixture contacts a solid surface which can physically or chemically adsorb a component and remove it from the gas mixture. Adsorption is effective in dilute gas mixture<sup>19</sup>. Adsorbate is the component in the gas mixture before adsorption. It is referred to adsorbate when it adheres to the solid surface or adsorbent<sup>19</sup>. Depending on the nature of the surface forces; there are two different types of adsorption: physical adsorption and chemisorption. In physical adsorption, the Van der Waals forces are dominant while in chemisorption, a chemical bond is formed which is much stronger than Van der Waals forces.

Gas separation in a gas mixture is resulted from one or some of the following: 1) molecular size and/or shape of gas component, 2) the different diffusion rates, 3) the thermodynamic effect (based on the pore wall- gas interactions), and 4) the quantum effect and different diffusion rates in the narrow micropores<sup>28</sup>. With nonpolar adsorbents like activated carbon, the Van der Waals forces are dominant, and the size and polarizability of adsorbate, and pore size distribution of adsorbent are the main factors while surface chemistry of the adsorbent is less dominant<sup>29</sup>. As mentioned above, a large specific surface area is preferable and pore size distribution affects the accessibility or selectivity of the adsorbate to the adsorbent. The pore size classification is assigned by the International Union of Pure and Applied Chemistry (IUPAC)<sup>19,30</sup> and is shown in Table 2-3.

Table 2-3: IUPAC classification of pore sizes

Type	Pore size (nm)
Ultramicro-pores	<0.7
Supermicro-pore	0.7-2
Micro-pore	<2
Meso-pore	2-50
Macro-pore	>50

### 2.3.1 Adsorption dynamics, breakthrough curves and selectivity

A fixed-bed is used on a continuous basis till saturation and then it is disposed of or regenerated for multiple usages. The performance of fixed-beds is evaluated using a breakthrough curve. A

breakthrough curve expresses the increase in the ratio of outlet concentration to the inlet concentration ( $C_{out}/C_{in}$ ) versus time<sup>19</sup>. At a constant inlet gas concentration, the S – shaped breakthrough curve shows the increase in gas content at outlet from zero to one<sup>19</sup>. Figure 2-2 shows the schematic of an adsorption breakthrough curve. The three zones are shown within the bed: (1) the saturated zone nearest the inlet which is in equilibrium with the CO<sub>2</sub> feed concentration, (2) adsorption zone with S-shape curve, and (3) a fresh zone in which no adsorption takes place<sup>19</sup>.

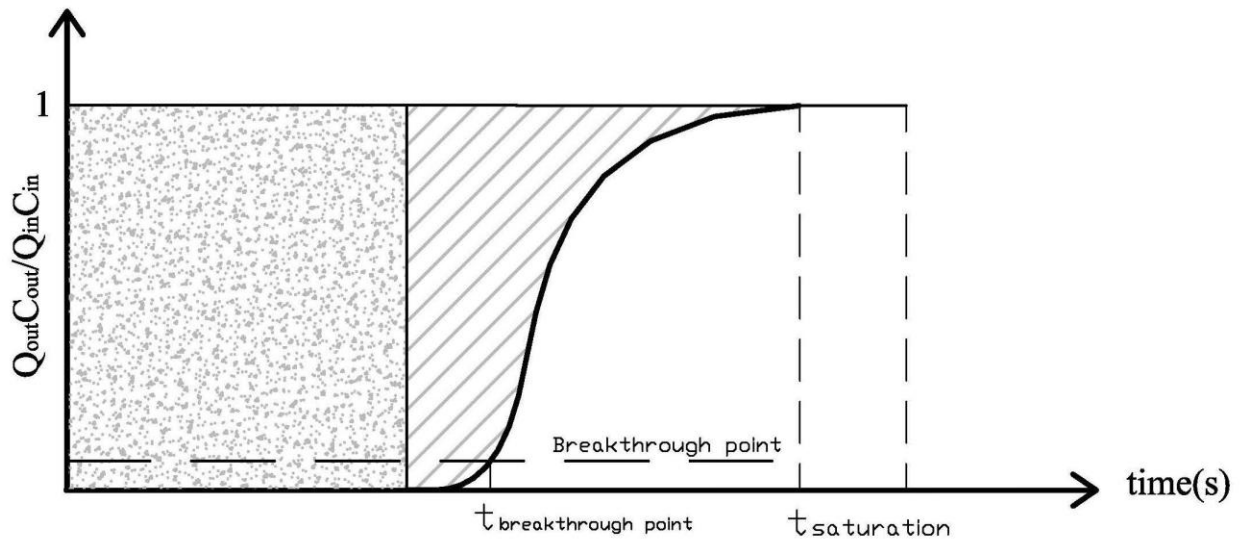


Figure 2-2: Typical breakthrough curve

The breakthrough point is the point in the breakthrough curve at which the outlet concentration reaches a predetermined value. This point depends on the effluent composition. For CO<sub>2</sub> separation, the breakthrough point is usually below 5% of the inlet concentration. The breakthrough time and the slope of the curve are important characteristics of the fixed-bed separation. The fixed-bed adsorption occurs layer by layer over a portion of the bed called mass transfer zone (MTZ) during the operation time. Mass transfer zone starts moving along the bed, from the inlet to the outlet point. Within the MTZ, the degree of saturation with adsorbate decreases from 100% to zero. When this zone is saturated, the MTZ will travel through the bed and a fresh section of bed is in front of the leading edge of the MTZ. When a greater portion of the bed is saturated, the breakthrough point occurs (Figure 2-3). An optimal sorbent has a narrow mass-transfer zone which makes the most efficient use of the sorbent. In fact, a vertical

breakthrough curve and zero mass-transfer resistance and minimal axial dispersion represent an ideal adsorption process.

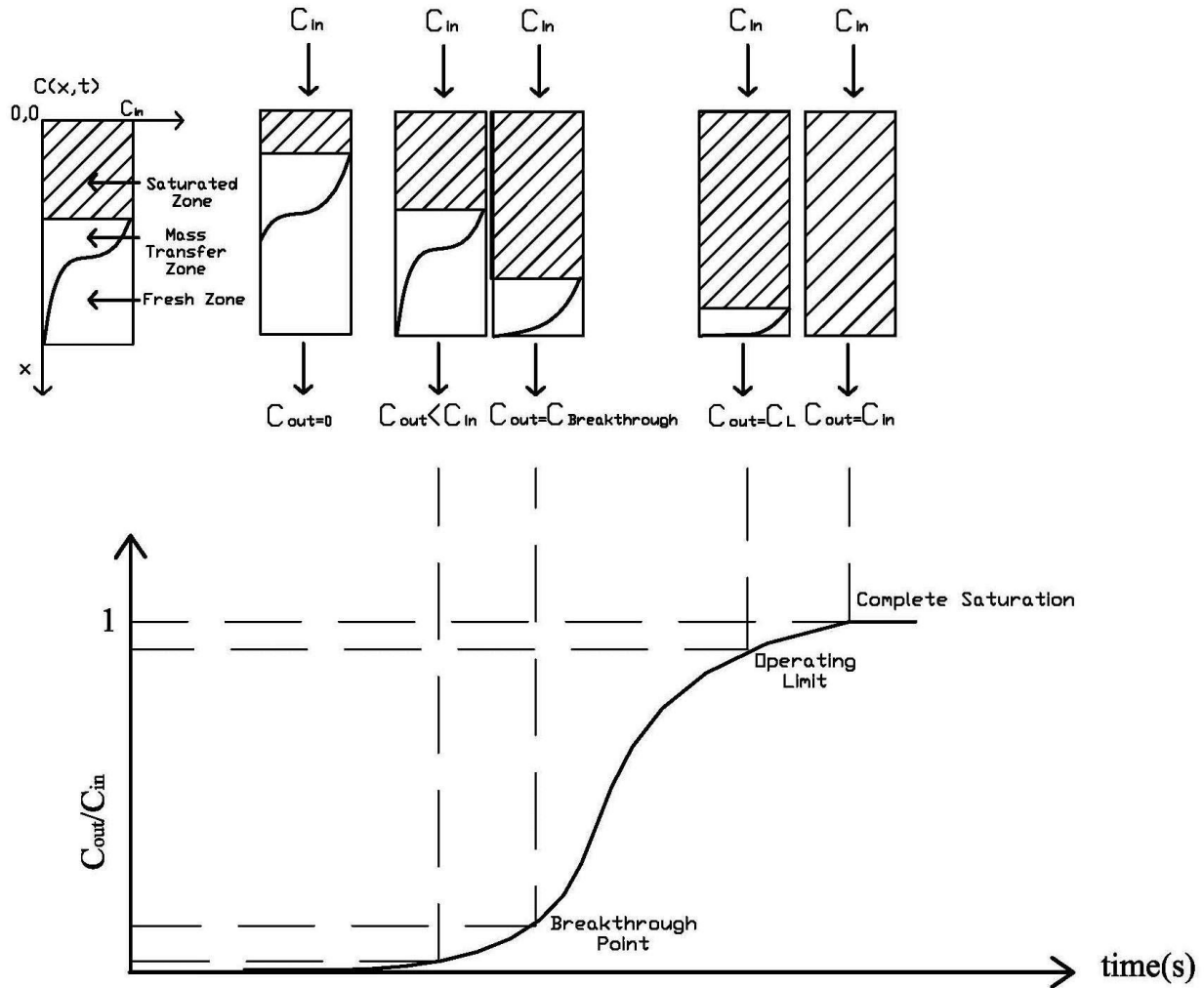


Figure 2-3: Travel of Mass transfer zone through the bed and the corresponding breakthrough curve

The amount of gas adsorbed on adsorbents ( $S$ , mol/g) at a certain time ( $t$ , s) at a constant temperature and inlet gas concentration can be determined by applying Eqs. 2-1 to 2-4<sup>31,32</sup>:

$$S = \frac{M_{\text{adsorbate}}}{m_{\text{Adsorbent}}} \left[ \int_0^{t_s} (Q_{\text{in}} C_{\text{in}} - Q_{\text{out}} C_{\text{out}}) dt - \frac{C_{\text{in}} P \epsilon_T V_c}{ZRT} \right] \quad (2-1)$$

$$\varepsilon_T = \varepsilon_b + (1 - \varepsilon_b)\varepsilon_p \quad (2-2)$$

$$\varepsilon_b = 1 - \frac{W/V_c}{\rho_p} \quad (2-3)$$

$$\varepsilon_p = 1 - \frac{\rho_p}{\rho_s} \quad (2-4)$$

where

$C_{in}$ : adsorbate concentration in inlet flow gas, mol. %

$C_{out}$ : adsorbate concentration in outlet flow gas, mol. %

$M_{adsorbate}$ : molecular weight of adsorbate

P: pressure, Pa

$Q_{in}$ : inlet flow rate, mole/s

$Q_{out}$ : outlet flow rate, mole/s

R: Universal gas constant, J/mole.K

T: temperature, K

$t_s$ : saturation time, s

$V_C$ : volume of the packed bed,  $cm^3$

W: weight of the sample, g

$\varepsilon_b$ : bed porosity

$\varepsilon_p$ : particle porosity

$\varepsilon_T$ : total bed porosity

$\rho_p$  : particle mercury density ,g/cm<sup>3</sup>

$\rho_s$  : solid density ,g/cm<sup>3</sup>

In Eq. 2-1, the integral term (part a) represent the total mass of CO<sub>2</sub> adsorbed on the adsorbent ( $g_{adsorbate}$ ) and is calculated by a graphical method (Figure 2-4) using Eqs. 2-5 and 2-6<sup>32,33</sup>.

$$m = \frac{A_{adsorption}}{A_{total}} \times m_{total} \quad (2-5)$$

$$S_{CO_2} = \frac{m}{m_{adsorbent}} \quad (2-6)$$

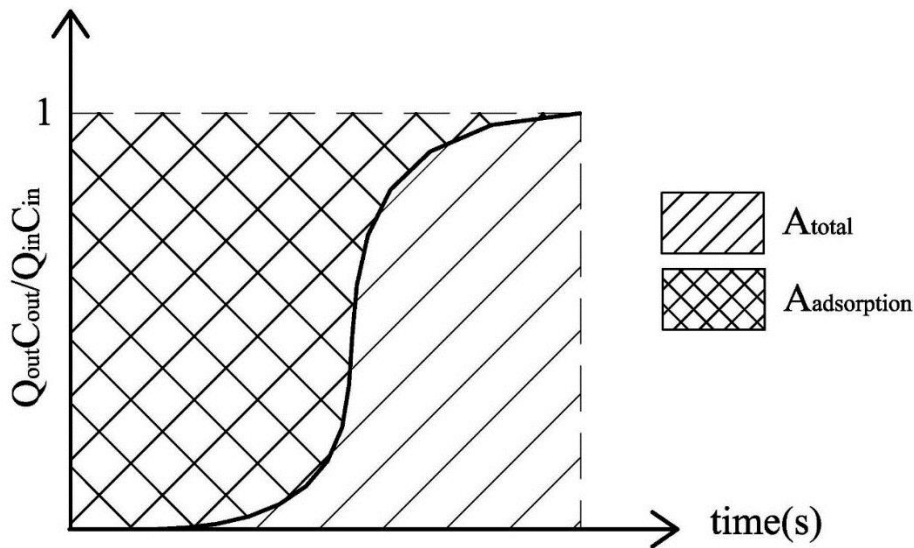


Figure 2-4: Graphical method to calculate the adsorption capacity

where,

$A_{total}$ : total area at saturation time,

$A_{adsorption}$ : area above the curve at time t

m: mass adsorbed at time t, g

$m_{\text{adsorbent}}$ : mass of adsorbent bed, g

$m_{\text{total}}$ : total mass of CO<sub>2</sub> passing through adsorbent at time t, g

S: capacity of adsorbent bed,  $g_{\text{adsorbed}}/g_{\text{adsorbent}}$

A simple method to determine adsorbent selectivity was proposed by Rege and Yang<sup>34</sup> based on the equilibrium adsorption capacities. Selectivity of component i over component j in a gas mixture is calculated as follows( Eq. 2-7):<sup>34</sup>

$$S(i/j) = \frac{x_i/x_j}{y_i/y_j} \quad (2 - 7)$$

where  $x_i$  and  $x_j$  are the mole fractions of the components of i and j on the adsorbent, and  $y_i$  and  $y_j$  are the corresponding mole fractions of the components of i and j in the gas mixture.

## 2.4 Adsorption isotherms

The static adsorption capacity and selectivity of an adsorbent for a single component is usually evaluated using adsorption isotherms, a curve relating the equilibrium concentration of adsorbed phase on the surface as a function of partial pressure of adsorbate in the gas mixture. The six different types of adsorption isotherms are shown in Figure 2-5. Shape of an adsorption isotherm depends on the pore size (mesopore or micropore) and the interaction of the adsorbate with the pore wall. The specific surface area, mean pore size and particle size distribution are calculated using adsorption isotherms<sup>19</sup>. Type I or the Langmuir isotherm represents the microporous adsorbents with a single layer or a few molecular layers. Non-porous materials exhibit Type II or Type III (unfavorable) with strong or weak fluid-wall attractive forces, respectively. Types IV and V represent the strong and weak fluid-wall interaction, respectively, in mesoporous structure where capillary condensation occurs. Both Types IV and V types have a hysteresis loops.

Hysteresis loops occur in the multilayer adsorption and associated with capillary condensation. IUPAC classification of hysteresis loops are shown in Figure 2-6<sup>35,36</sup>. Type H<sub>1</sub> is a fairly narrow loop with very steep and nearly parallel adsorption and desorption branches. Type H<sub>1</sub> loop that represents adsorbents with a narrow distribution of uniform pores has parallel adsorption/desorption branches. Type H<sub>2</sub> loop occurs in the porous materials with pores of different sizes

and shapes. Type H<sub>3</sub> loop usually occurs in the aggregates of porous particles with slit-shaped pores. Hysteresis loop of Type H<sub>4</sub> also occurs by slit-shaped pores but porous materials with dominant microporous structure<sup>35,36</sup>. Type VI occurs in step-wise adsorption process for some materials with relatively strong fluid-wall forces<sup>19</sup>.

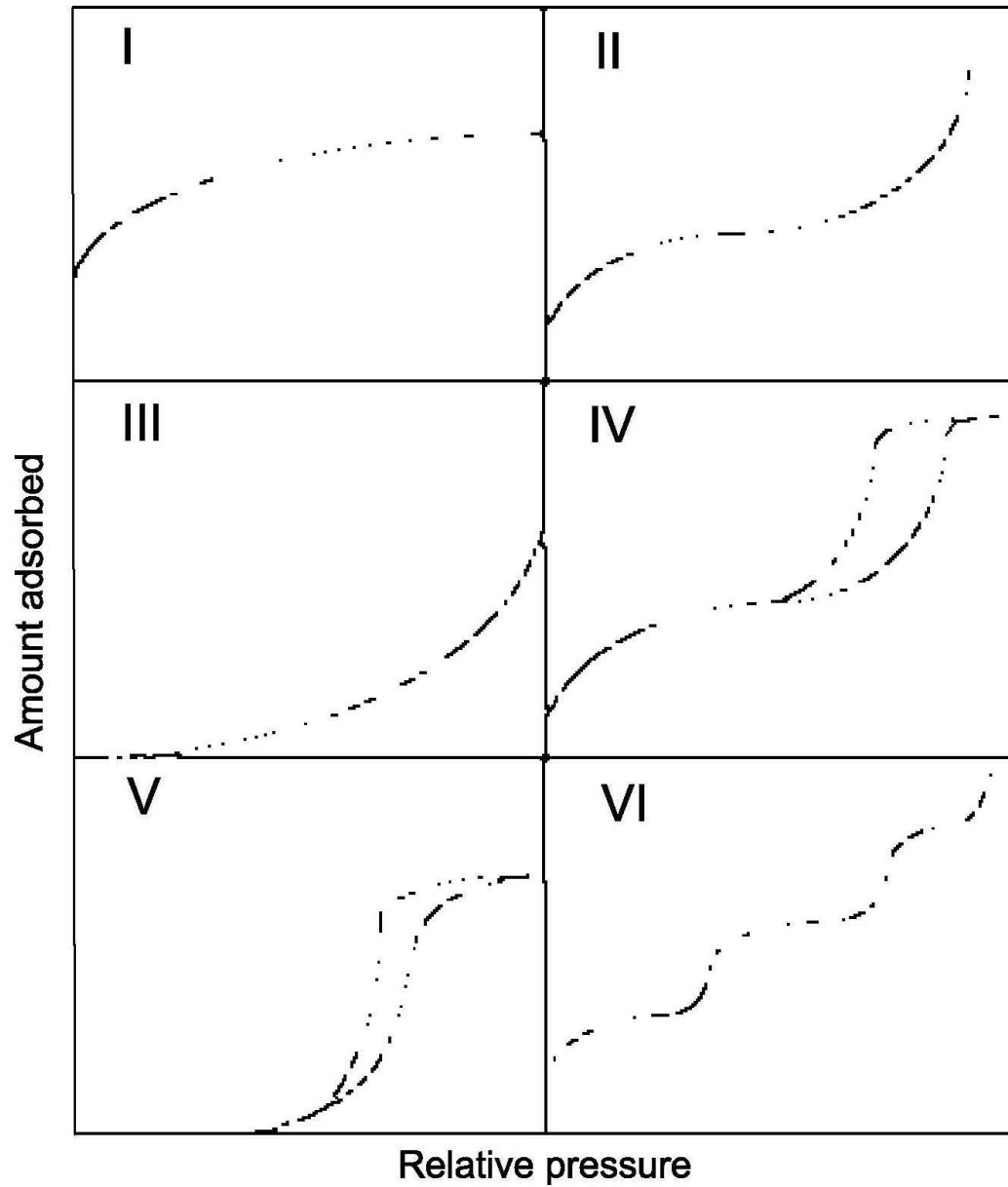


Figure 2-5: IUPAC adsorption Isotherms<sup>19</sup>

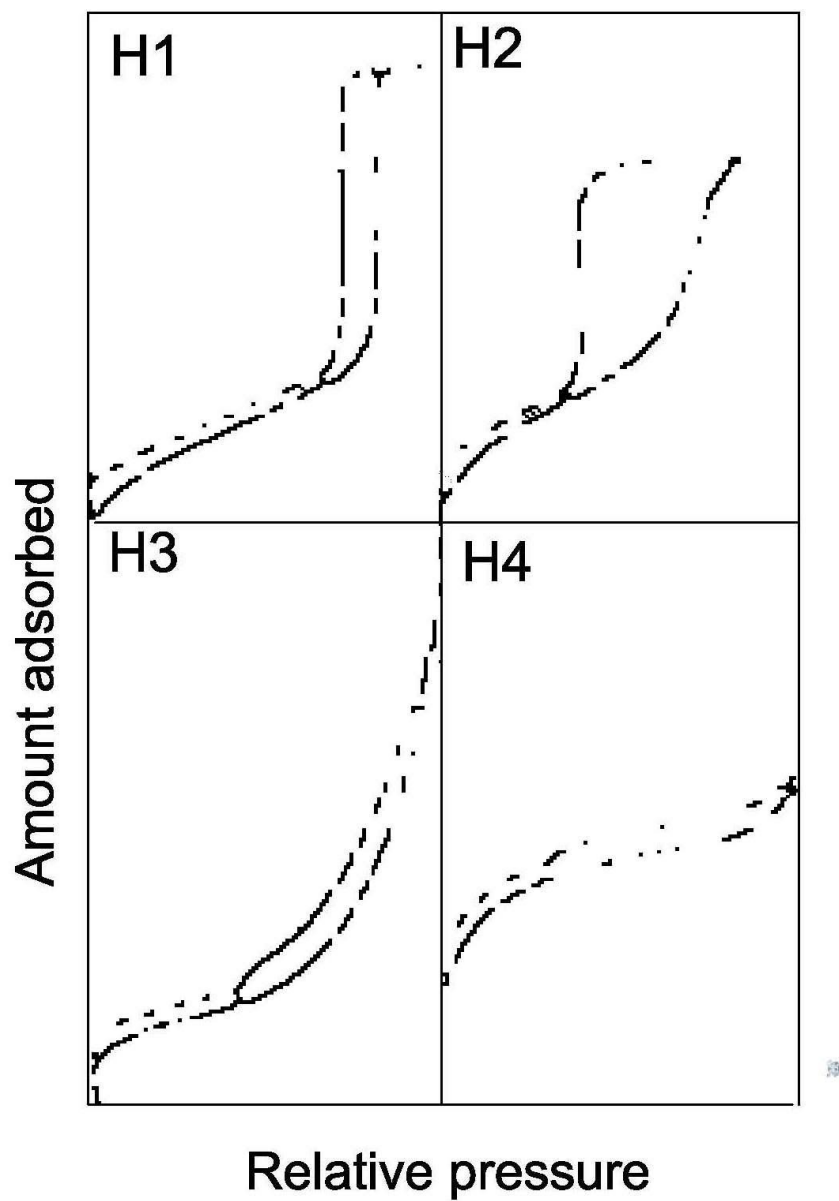


Figure 2-6: Four types of hysteresis loop by IUPAC

### 2.5 BET surface area and pores size distributions

Nitrogen adsorption at 77K is the standard method for mesopore size analysis. The specific surface area of an adsorbent is determined by  $N_2$  adsorption on solid adsorbent. The Brunauer-

Emmett-Teller (BET) analysis<sup>37</sup> is the extended Langmuir adsorption isotherm to multilayer adsorption with the following assumptions:

- 1- a Langmuir isotherm applies to each layer and no transmigration occurs between layers
- 2- All sites on the surface are equivalent
- 3- Multiple nitrogen molecules can be adsorbed to each site
- 4- No interaction between adsorbed molecules exists
- 5- Except for the first layer, nitrogen is in the liquid phase.

The BET equation is shown in Eq. 2-8<sup>37</sup>:

$$\frac{1}{W((P_0/P) - 1)} = \frac{1}{W_m C} + \frac{C - 1}{W_m C} \left( \frac{P}{P_0} \right) \quad (2-8)$$

where

W: weight of gas adsorbed (g)

P/P<sub>0</sub>: relative pressure

W<sub>m</sub>: weight of adsorbate as monolayer (g)

C: BET constant

Plot of 1/ [W (P<sub>0</sub>/P) -1] vs. P/P<sub>0</sub> yield a linear graph. Using the intercept and slope of this line, the values of W<sub>m</sub> and C can be derived.

Total surface area (S<sub>t</sub>) and the specific surface area (S<sub>BET</sub>) are derived as follows (Eq. 2-9 and 2-10):

$$S_t = \frac{W_m N_A}{M} \quad (2-9)$$

$$S_{BET} = \frac{S_t}{W} \quad (2-10)$$

where

N: Avogadro's number ( $6.023 \times 10^{23}$ )

M: molecular weight of adsorbate

A: adsorbate cross sectional area

The linearity of this plot is limited to a small part of the Type II isotherm ( $P/P_0 < 0.1$ )<sup>38</sup> and at least three data points in this relative pressure range is required.

### **Total pore volume and pore size distribution**

Total pore volume is calculated based on the amount of liquid adsorbed at a relative pressure located after the condensation step<sup>39</sup> (usually  $P/P_0 = 0.95$ ) using Eq. 2-11:

$$V_{\text{liq}} = \frac{PV_{\text{ads}}V_m}{RT} \quad (2-11)$$

where

$V_{\text{ads}}$ : volume of adsorbed  $N_2$

$V_{\text{liq}}$ : volume of liquid  $N_2$  in pores

$V_m$ : molar volume of liquid adsorbate

P: ambient pressure

T: ambient temperature

Various methods are established to determine the pore size distribution on porous solids. In 1981, Seaton et al.<sup>40</sup> for the first time suggested using the density functional theory for the pore size distribution of porous carbons from nitrogen adsorption isotherms. In a similar work<sup>41</sup>, the porous carbon network was simulated as a continuous size distribution of individual slit-shaped graphitic pores. Considerable progress was made toward our understanding of liquid behavior and its phase changes constrained by the presence of walls, capillaries, and slits in 1980s and this

model is further customized and developed for a full range of porous materials and soon was accepted as a standard method to determine the pore size distribution and analysis of micropores by gas adsorption<sup>42,43</sup>.

Density functional theory uses the gas-gas and gas-solid interactions to calculate the pore size distribution based on the statistical mechanical model calculations. In this method, a series of isotherms are theoretically developed for the individual pores. The theoretical isotherms that fit the experimental data are selected and the pore size distribution is calculated based on the individual pores.

The relation between theoretical isotherms and the experimental isotherm on a porous solid can be interpreted in terms of a Generalized Adsorption Isotherm (GAI) equation (Eq. 2-12):

$$N(P/P_0) = \int_{W_{\min}}^{W_{\max}} N(P/P_0, W) f(W) dW \quad (2-12)$$

where

$N(P/P_0)$ : experimental adsorption data

$W$ : pore width

$N(P/P_0, W)$ : isotherm on a single pore of width  $W$

$f(W)$ : pore size distribution function

Typically, grand thermodynamic potential is function of local fluid density, local chemical potential and external potential<sup>44</sup> (Eq. 2-13).

$$\Omega[\rho(\mathbf{r})] = \underbrace{F[\rho(\mathbf{r})]}_{\text{(fluid-fluid interaction)}} + \int d\mathbf{r} \rho(\mathbf{r}) \left[ \underbrace{\phi(\mathbf{r})}_{\text{(solid-fluid interaction)}} - \mu \right] \quad (2-13)$$

where

$F[\rho(\mathbf{r})]$ : the free energy functional,

$\varphi(r)$ : the external potential,

$\mu$ : Chemical potential

$\rho$ : local density

The fluid density in the pore is not constant and “it is subjected to adsorption forces in the vicinity of the pore walls”<sup>36</sup>. “The density distribution can be characterized in terms of a density profile,  $\rho(r)$ , expressed as a function of distance,  $r$ , from the wall across the pore”<sup>36</sup>. In NLDFT approach, the equilibrium local density profile of the adsorbate for all locations in the pore at a given temperature, chemical potential and volume is calculated by minimization of the grand thermodynamic potential<sup>42</sup>. Once the equilibrium distribution of the fluid local density at a range of the chemical potential is calculated and its averaged fluid local density determined, the theoretical adsorption isotherm can be developed.

Characterization of mesoporous materials is typically determined using  $N_2$  adsorption at 77 K. However, the pore size and volume analysis of the microporous materials with  $N_2$  is not accurate. The saturation pressure of  $N_2$  at 77 k is 760 Torr. The pore filling in ultra-micro pores requires a very low relative pressure (e.g.  $10^{-8}$ ) which results in a limited diffusion and very slow adsorption equilibrium which challenges the sensitivity of the  $N_2$  adsorption to determine the pore size distribution of the microporous materials. To overcome the slow diffusion rate and determine the pore volume in ultra-micropores,  $CO_2$  adsorption at 273 K is recommended<sup>19</sup>.  $CO_2$  has a higher diffusion rate and accelerated adsorption equilibrium.  $CO_2$  has a saturation pressure of 26,400 Torr at 273 K and  $CO_2$  adsorption starts at relative pressure of about  $10^{-4}$  which can diffuse into the narrowest micropores up to 1.5 nm<sup>39</sup>. The combination of  $CO_2$  adsorption analysis results combined with the  $N_2$  adsorption analysis is used for the full range characterization.

## 2.6 Activated carbon

One of the oldest and the most accepted industrial adsorbents are activated carbons with large surface areas per weight. Activated carbon is produced by combustion, partial combustion, or thermal decomposition of carbonaceous materials<sup>45</sup>. The structure of activated carbon is a

combination of an amorphous structure and a graphite-like microcrystalline structure that forms a series of slit-shaped channels. The micro-crystallite layers of activated carbon are randomly oriented and less ordered and the interlayer spacing of activated carbon (0.34-0.35 nm) is larger than that of graphite, 0.335 nm. This microcrystalline, known as turbostratic, is built up during the carbonization process and impacted by carbonization conditions<sup>46</sup>.

This random orientation in micro-crystallite layers is formed by the presence of heteroatoms such as oxygen, nitrogen and hydrogen, and by the defects in the carbon structure<sup>47</sup>. The heteroatoms are bonded to carbon at the edges and corners of the aromatic sheets, or attached to carbon atoms at defect sites<sup>47</sup>. Porosity of activated carbon depends on the nature of precursors, carbonization process and activating agent and conditions. Carbonization burns off most of the non-carbon species and produces char with non-porous structure and high content of carbon. Activation of char with an oxidation agent like steam, CO<sub>2</sub> or potassium hydroxide (KOH) results in development of internal surface area of char and removal of carbon atoms by reaction with oxidation agent at high temperature which forms an extended porous structure<sup>47</sup>. Porosity is a function of the activating agent, conditions (temperature, flow rate and mass ratio of carbon to oxygen) and carbon burn-off<sup>45,48</sup>.

The economic viability of the activated carbon as an adsorbent relies on its capacity, selectivity and stability in multi cycles adsorption process. The adsorption capacity mostly depends on porosity but selectivity is also a function of surface chemistry of the activated carbon. Carbon-oxygen functional groups are known to have the most impact on activated carbon characteristics such as the wettability, acidity, and selectivity. Precursors, such as biomass, are usually rich in oxygen and the nature of the precursors is an important factor in formation of oxygen-carbon surface groups. The heteroatoms are also introduced during the carbonization and activation process<sup>46</sup>. Oxygen functional groups on carbon surface are classified into three groups, acidic, basic and neutral groups. The impregnation of activated carbons with metal oxides can improve the adsorption characteristic and surface chemistry of activated carbon for gas adsorption<sup>47</sup>.

### 2.6.1 Pyrolysis, biochar and activation

Pyrolysis is the thermal degradation process that is used for a variety of feedstock, from agricultural and forestry biomass to animal manure, to convert them to value-added products<sup>49</sup>. Chars (carbon-rich solids), gases (CO, CO<sub>2</sub>, and CH<sub>4</sub>, with smaller amounts of hydrogen, ethane, and ethylene) and tars (bio-oils) are the main products of this process<sup>49,50</sup>. Pyrolysis processes are classified into two main groups, fast and slow pyrolysis. The main characteristic of fast pyrolysis processes are as follows: high heating rates of the feedstock, pyrolysis temperature ranging from 400 to 550 °C, short vapor residence time (0.5 to 10 s), and low particle size of biomass

Slow pyrolysis processes are known by the following characteristics: low heating rate of the feedstock, long solid residence time (30 min to several hours) and the pyrolysis temperature varies with the feedstock.

The yields of the pyrolysis products (bio-char, bio-oil and non-condensable gaseous products) and its characteristics depend on the nature of the biomass and the process conditions. Pyrolysis temperature, heating rate, gas flow rate and residence time are the most important factors in pyrolysis process, respectively<sup>51</sup>.

#### **Biochar**

Biochar is the nonvolatile solid residue from the carbonization of biomass in absence of oxygen. Biochar has a high carbon content and low surface area which is usually used for soil treatment<sup>50</sup>. The production yield and characteristics of biochar depend on the production methods, and parameters like heating rate, temperature, residence time and moisture content of precursor can impact the final product. Usually slower heating rate, longer residence time and higher pressure result in larger yields of biochar. In addition to its agricultural application, as a soil amendment, biochar can be used as a precursor to produce activated carbon<sup>49</sup>. Biochar can be produce from all biological resources including manures, marine and lignocellulosic biomass. Chemical properties of the produced biochar depend on the precursor and pyrolysis conditions and can exhibit a wide range of porosity, composition and chemistry<sup>52</sup>.

## Char activation

Activated carbons are usually prepared from biochar using different activation methods such as steam activation, CO<sub>2</sub> activation, KOH activation and phosphoric acid (H<sub>3</sub>PO<sub>4</sub>) activation<sup>53</sup>. The methods of activation can be divided into two types, physical activation or chemical activation depending on whether a gaseous or solid activating agent is used for activation. Different types of biochar are reported in the literature as a precursor for activated carbon production<sup>49,54,55</sup>. A summary of precursors, pyrolysis methods, activating agents and application of produced activated carbon is provided in Table 2-4.

## Physical activation

Oxidation agents such as steam, CO<sub>2</sub> or mixture of both are used at mild temperature at 700-950 °C for physical activation of char. In this process, steam and CO<sub>2</sub> remove carbon atoms via formation of CO+H<sub>2</sub> or CO<sup>56</sup>.

Steam is the most common activating agent. In this process, steam penetrates to the internal structure of the char and reacts with carbon that results in pore opening. With the further widening of pores, carbon pore walls collapse and results in formation of mesopores in steam activated carbon<sup>57,58</sup> (Eq. 2-14 to 2-16).



Reactions **2-15** and **2-16** are exothermic, and reaction **2-14** is endothermic. This endothermic nature of the reactions facilitates the control of water-gas reaction.

In CO<sub>2</sub> activation, CO<sub>2</sub> is used as oxidizing agent to penetrate into the char; and selectively eliminates carbon atom, creates porosity and releases carbon monoxide (Eq. 2-17):



Table 2-4: Summary of different feedstocks, pyrolysis methods, activating agents and their applications

Precursor	Pyrolysis method	Activating agent	Application	Surface Area (m <sup>2</sup> /g)	Pore volume (cm <sup>3</sup> /g)	Ref.
<ul style="list-style-type: none"> <li>• grass cuttings</li> <li>• horse manure</li> <li>• beer waste</li> <li>• bio-sludge</li> </ul>	hydrothermally carbonization	CO <sub>2</sub>	CO <sub>2</sub> adsorption	841 749 622 489	0.379 0.816 0.317 0.387	54
pine nut shell	slow pyrolysis	KOH	CO <sub>2</sub> adsorption	NA	NA	55
Kernel shell	slow pyrolysis	KOH	N/A	17 -217	0.016-0.12	59
Teak saw dust	vacuum slow pyrolysis	steam	N/A	439-1150	NA	60
rubberwood saw dust	slow pyrolysis	steam	N/A	279-1095	NA	61
<ul style="list-style-type: none"> <li>• Broiler litter</li> <li>• Soybean straw</li> <li>• 0.96Guayule shrub</li> <li>• Guayule bagasse</li> </ul>	fast pyrolysis	Steam	Metal ion adsorption(Cu <sup>2+</sup> ,Cd <sup>2+</sup> ,Ni <sup>2+</sup> ,andZn <sup>2+</sup> )	<ul style="list-style-type: none"> <li>• 136</li> <li>• 204</li> <li>• 293</li> <li>• 249</li> <li>• 455</li> <li>• 716</li> <li>• 535</li> </ul>	<ul style="list-style-type: none"> <li>• 0.052</li> <li>• 0.077</li> <li>• 0.112</li> <li>• 0.113</li> <li>• 0.174</li> <li>• 0.318</li> <li>• 0.213</li> <li>• 0.344</li> </ul>	62

<ul style="list-style-type: none"> <li>• Corn stover</li> <li>• Corn cob</li> <li>• Switchgrass</li> <li>• Alfalfa stems</li> </ul>				• 793		
peanut hulls	unknown	steam ZnCl <sub>2</sub> KOH H <sub>3</sub> PO <sub>4</sub>	N/A	97-253	0.053-0.223	63
pistachio-nut shells	slow pyrolysis	steam	N/A	639-1015	NA	64
corn cobs	slow pyrolysis	steam H <sub>3</sub> PO <sub>4</sub>		607-960	0.296-0.629	65

### Chemical activation

Chemical activation with hydroxides such as KOH and sodium hydroxide (NaOH) gives rise to surface area and pore volume and is used to produce activated carbon with a highly developed porosity of micropores and some small mesopores<sup>57</sup>. KOH activation was first proposed in 1978 by Wennerberg and O'Grady<sup>66</sup>. KOH melts down at 360 °C. Chemical activation is usually carried out by mixing char with chemical activating agent followed by the carbonization under inert gas at 400–900 °C. Then sample is washed with acid and water to remove the remaining impregnating agent and salts and open the pores<sup>57</sup>. The reduction of KOH to potassium as shown in Eq. 2-18<sup>66,67</sup> results in the development of porous structure in KOH chemical activation:



The free metallic potassium (K) penetrates between lattices of the carbon. Formation of intercalated potassium resulted in the stretching of the lattice. With increasing temperature, the intercalated potassium is then removed from the graphitic structure resulting in extended micro

porosity<sup>57,66</sup>. The main products of reaction below 700 °C are hydrogen, water, carbon monoxide, carbon dioxide, potassium oxide and carbonate (Eq. 2-19 to 2-22)<sup>66</sup>:



Although the activation starts with these reactions (Eq. 2-19 to 2-22), it further proceeds with the following reactions to form the metallic potassium at temperatures above 700 °C (Eq. 2-23 and 2-24)<sup>66</sup>:



The pore size distribution of the produced activated carbon depends on the nature of the biochar, activating agent, mass ratio of KOH to carbon, temperature, resident time and flow rate. Because the solid-hydroxide reactivity of the solid is a key factor in this process, the nature of the precursors are very important<sup>67</sup>. Mass ratio of KOH to carbon and temperature are the controlling factors to maximize the ratio of ultra micropores to micropores in this reactions<sup>57,66</sup>. The activation conditions for KOH activation in this work is adopted from a previous work using a similar experimental setup<sup>57</sup>.

### 2.6.2 Surface chemistry of activated carbon

The microcrystalline structure in activated carbon is formed randomly and it has defects and/or partial burned graphitic layers in the crystallite, a variation in arrangement of electron clouds developed in carbon structure. The creation of unpaired electrons and incomplete saturated valance<sup>47</sup> due to formation of these electron clouds affect the adsorption properties of the activated carbon. Besides, heteroatoms are important parameters to form the chemical structure

of activated carbon. They bond to carbon atom at the edge and/or corner of the aromatic sheets/ defect points to form surface functional groups. Carbon-oxygen functional groups are undoubtedly the main functional groups due to their abundant quantities that significantly impact polarity, acidity, wettability and catalytic reactivity of activated carbons<sup>68</sup>. Carboxyls, lactones, phenols, quinones and hydro-quinones are the main oxygen functional groups in carbon structure. Carboxyls, lactones, phenols are known as weakly acidic groups of Brönsted-type acid base reactions. The acidic surface functional groups are not thermally stable and decompose with heat treatment in inert gas in temperature range of 320-750°C.

Although the structure of the basic functional groups is not completely understood, pyrone, chromene, and quinone are categorized as basic functional groups. “In ammonia/amine treatment, nitrogen can replace the oxygen in ether-type functional groups and increases the basic characteristic of the surface”<sup>47,57</sup>.

### 2.6.3 Adsorption on activated carbons

Regardless of preparation techniques and activation conditions, activated carbons usually exhibit lower adsorption capacities as compared to zeolites or molecular sieves under low partial pressure of CO<sub>2</sub><sup>69-71</sup>. However, activated carbon adsorbents are fully regenerated at 100-150 °C while zeolite usually cannot gain their initial adsorption capacity. Activated carbons are low cost and thermally stable adsorbents that are less affected by the presence of moisture in the gas mixture<sup>72,73</sup>. On the other hand, CO<sub>2</sub> uptake decrease with temperature due to the exothermic nature of CO<sub>2</sub> adsorption<sup>74-76</sup>. A summary of CO<sub>2</sub> adsorption conditions and capacity of activated carbon and other solid adsorbent materials in the literature are provided in Table 2-5<sup>77</sup>.

Amine /ammonia treatment of activated carbon is the most common technique to improve CO<sub>2</sub> adsorption performance of activated carbon. Activated carbon treated with ammonia gas at temperatures >200 °C showed a larger CO<sub>2</sub> adsorption capacity as compared to the un-treated activated carbons<sup>78</sup>; this was attributed to the introduction of nitrogen- containing functional groups onto the carbon surface. Zhang et al.<sup>79</sup> found that the impregnation of activated carbon with poly ethyleneimine (PEI) could enhance the CO<sub>2</sub> adsorption capacity of activated carbons up to 2.13 mmol g<sup>-1</sup> at 75 °C. Similar results are reported in the literature<sup>16,58,79</sup>. However, the

amine impregnation causes a significant decrease of the surface areas and pore volume due to the pore filling / blockage on carbon surface.

Table 2-5: CO<sub>2</sub> adsorption capacity of activated carbons

Adsorbent	Adsorption temperature(K)	CO <sub>2</sub> Pressure (Bar)	CO <sub>2</sub> adsorption capacity (mmol/g)	Ref
Activated carbon	298	1	2.07	80
Activated carbon	298	0.1	1.1	74
	328	0.1	1.1	
	298	1	3.2	
	328	1	1.6	
Activated carbon	298	0.2	0.75	75
	373	0.2	0.1	
Activated carbon	288	1	2.45	71
AC Norit RB1	294.2	0.1	2.456	81
	294.2	0.8	6.027	
	311.2	0.1	1.759	
	329.6	0.1	1.263	
	348.3 K	0.1	0.911	
Activated carbon (RB)	303	1	1.39	76
Activated carbon (MSC V)	303	1	1.82	
Activated carbon (BPL)	303	1	1.93	
Activated carbon (horse manure)	273	0.1	1.36	54
Activated carbon (grass cuttings)	273	0.1	1.45	
Activated carbon (beer waste)	273	0.1	1.31	
Activated carbon (biosludge)	273	0.1	0.84	
Activated carbon (beer waste)	273	0.1	0.8	
Zeolite 13X	293	0.15	2.63	77

Zeolite 13X	295	1	4.61
Zeolite 13X	298	1	4.66
Molecular sieve 13X	298	1	2.8-3.6
Molecular sieve 4A	298	1	2.3-3.1
Silicalite	303	0.15	0.45
K <sub>2</sub> CO <sub>3</sub>	373	0.35	2.1
Na <sub>2</sub> CO <sub>3</sub>	333-343	0.1-0.4	0.5-3.2

### Adsorption cycles

In addition to adsorption capacity and selectivity, the long-term stability and regenerability of the adsorbents are important characteristic. Three main regeneration methods are temperature swing adsorption (TSA), pressure swing adsorption (PSA) and vacuum swing adsorption (VSA). The CO<sub>2</sub> adsorption on activated carbon is principally “attributable to physical force, which makes the regeneration process of CO<sub>2</sub> at a relatively low temperature feasible in TSA”<sup>82</sup>.

Figure 2-8 shows the schematic of TSA in which a gas steam of component *i* at partial pressure of  $p_1$  flows through the packed-bed at  $T_1$  to reach equilibrium ( $q_1$ ). For bed regeneration, the bed temperature is increased to  $T_2$  and desorption process is continued to reach the second equilibrium at  $q_2$  ( $q_2 < q_1$ ). In a dual-bed system, the adsorption and desorption time must be equal. Therefore, the full regeneration to the initial capacity is not always possible.

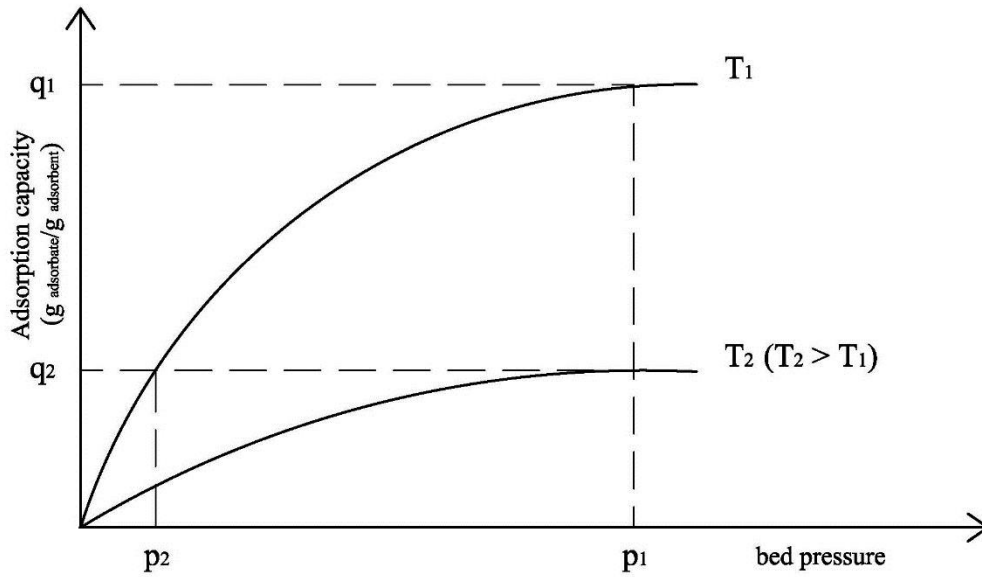


Figure 2-7: Temperature swing adsorption

## 2.7 Mass transfer model

The mechanism of CO<sub>2</sub> transport from a gas mixture to the active sites on the adsorbent surface and physical adsorption includes three main stages through the packed-bed: External bulk mass transfer through the film surrounding the particles, diffusion through the pores and adsorption. They are explained in details below:

### Bulk mass transfer

Moisture in the flue gas and air results in the formation of the fluid film around the particles or pellets through which molecular diffusion of CO<sub>2</sub> occurs. This step is represented by the mass transfer coefficient of the film, according to the linear law of Fick (Eq. 2-25)<sup>19</sup>:

$$N_{f,i} = k_{f,i}(C_{i,b} - C_{i,s}) \quad (2-25)$$

where  $N_{f,i}$  is the mass flux,  $k_{f,i}$  is the mass transfer coefficient,  $C_{b,i}$  is the bulk concentration of component  $i$  and  $C_{i,s}$  is the component  $i$  concentration at the surface of the particle.

Several studies reported heat and mass transfer coefficient data in packed beds<sup>83-86</sup>. For a Reynolds number 3-10000, Wakao and Funazkri<sup>84</sup> collected data of evaporation of water, evaporation of organic solvent, sublimation of naphthalene and dissolution of solid in a packed bed. The developed correlation for packed bed is described as (Eq. 2-26 to 2-29):

$$Sh_i = 2 + 1.1Re^{0.6}Sc_i^{1/3} \quad (2 - 26)$$

In this correlation:

$$Sh_i = \frac{k_{f,i}d_p}{D_{m,i}} \quad (2 - 27)$$

$$Sc_i = \frac{\eta_f}{\rho_f D_{m,i}} \quad (2 - 28)$$

$$Re = \frac{\rho_f u d_p}{\varepsilon_b \eta_f} \quad (2 - 29)$$

where  $d_p$  is the particle diameter,  $D_{m,i}$  is the molecular diffusion coefficient,  $\eta_f$  is the fluid viscosity,  $\rho_f$  is the fluid density,  $k_{f,i}$  is the mass transfer coefficient,  $u$  is the superficial velocity and  $\varepsilon_b$  is the bed porosity. In this equation, density of the gas mixture is defined as (Eq. 2-30 and 2-31):

$$\rho_f = \sum_i y_i \rho_i \quad (2 - 30)$$

$$\rho_i = \frac{M_i P}{RT} \quad (2 - 31)$$

Viscosity of binary mixture at low pressures is determined by the method of Wilke (Eq. 2-32 to Eq. 2-35)<sup>87</sup>:

$$\eta_f = \frac{\sum_{i=1}^n y_i \eta_i}{\sum_{\substack{j=1 \\ j \neq i}}^n y_j \phi_{ij}} \quad (2 - 32)$$

$$\varphi_{ij} = \frac{1}{\sqrt{8\left(1 + \frac{M_i}{M_j}\right)^{1/2}}} \left[ 1 + \left(\frac{\eta_i}{\eta_j}\right)^{1/2} \left(\frac{M_j}{M_i}\right)^{1/4} \right]^2 \quad (2-33)$$

$$\varphi_{ji} = \frac{\eta_j}{\eta_i} \frac{M_i}{M_j} \varphi_{ij} \quad (2-34)$$

$$\eta_i = X_i + Y_i T + Z_i T^2 \quad (2-35)$$

where  $y_i$  is the mole fraction of component  $i$ ,  $M_i$  and  $M_j$  are the molecular weight of component  $i$  and  $j$ , respectively,  $T$  is the temperature (K),  $X$ ,  $Y$ , and  $Z$  are regression coefficients for chemical compound and  $\eta_i$  is the viscosity of component  $i$ .  $X$ ,  $Y$  and  $Z$  for  $\text{CO}_2$  and  $\text{N}_2$  are shown in Table 2-6:

Table 2-6: Regression coefficients of viscosity calculation for  $\text{CO}_2$  and  $\text{N}_2$

	$\text{CO}_2$	$\text{N}_2$
X	11.811	42.606
Y	4.98E-01	4.75E-01
Z	-1.09E-04	-9.88E-05

Bed porosity is approximated “by the ratio between the total volume of void space between the particles and the volume of the bed”<sup>88</sup> as follows (Eq. 2-36):

$$\varepsilon_b = \frac{V_b - \sum V_p}{V_b} = 1 - \frac{\rho_b}{\rho_p} = 1 - \frac{W/V_b}{\rho_p} \quad (2-36)$$

where  $W$  is weight of the bed,  $V_b$  is volume of the bed and  $\rho_p$  is the particle density or apparent density which is defined as the ratio of weight of the bed to the volume measured including the pore volume as well as the void spaces of the particle. Particle density is approximated based on

the skeletal density (true density) and pore volume determined by N<sub>2</sub> and CO<sub>2</sub> adsorption data (pore size distribution) as follows (Eq. 2-37)<sup>88</sup>:

$$V_{p,b} = \frac{1}{\rho_p} - \frac{1}{\rho_s} \quad (2-37)$$

Skeletal density in this equation is defined as a ratio of the mass of solid to the solid volume measured excluding the pores and the void spaces.

### 2.7.1 Internal mass transfer

From the surface on the particles, the gas molecules diffuse into the micro/meso/macro pore networks and then adsorb on the internal surface of the particles. To understand the mass transfer mechanism and find the resistance step a mass transfer model is required to recognize which resistance dominates. Various kinetic models have been developed in the past. Linear driving force (LDF)<sup>89</sup> model with an effective diffusion coefficient is believed to be the earliest adsorption model pertaining the adsorption rate based on the adsorption capacity (Eq. 2-38)<sup>90</sup>.

$$\frac{\partial q}{\partial t} = k_{LDF}(q^* - \bar{q}) = \frac{15D_{pi}}{R_p^2}(q^* - \bar{q}) \quad (2-38)$$

where  $K_{LDF}$  is the mass transfer coefficient,  $q^*$  is equilibrium concentration at the surface of the particle (mol of adsorbate/mass of particle),  $\bar{q}$  is the mean solid concentration over the particle volume (mol of adsorbate/mass of particle),  $D_{pi}$  is the particle diffusion coefficient (m<sup>2</sup>/min) and  $R_p$  is the particle radius (m). This model for bi-porous adsorbents, where both macro-pore and micropores are important, is not accurate. In the later models<sup>91,92</sup> for bi-porous structures, the adsorption rate was described by both mass transfer resistance in micropores and macro-pores. These models are also restricted by adsorbate concentration. At high concentration where the impact of viscous flow and surface diffusion are significant, these models fail. Surface diffusion is also becomes important in adsorbents with large surface area. To model adsorption rate in a range of operating conditions, all these mass transfer mechanisms must be considered. For CO<sub>2</sub> adsorption, the CO<sub>2</sub> concentration is usually below 20 mol% and the impact of viscose flow is negligible.

### 2.7.2 Bi-linear driving force model

In this work, the Bi-linear Driving Force (Bi-LDF) model proposed by Grande and Rodrigues<sup>93</sup> is used which includes a combination of molecular diffusion and Knudsen and surface diffusion. Bulk and Knudsen diffusion occur together while surface diffusion occurs in parallel to these two mechanisms (Figure 2-9). This model describes all three mass transfer mechanism<sup>94</sup>.

Bulk mass transfer is due to the molecule-molecule collisions and in large pore and/or at high concentration becomes more important.

Knudsen diffusion is due to the molecule-pore wall collisions and “when the mean free path of the gas molecule is larger than the pore diameter becomes important”<sup>19</sup>.

Surface diffusion is due to the diffusion of the adsorbed molecule along the surface of pore wall and it becomes important at high concentration or high surface area. In ultra micropores, “the diffusing molecules never escape the potential field of the adsorbing surface and the transport involves the adsorbed molecules “hopping” across the adsorption sites”<sup>95</sup>.

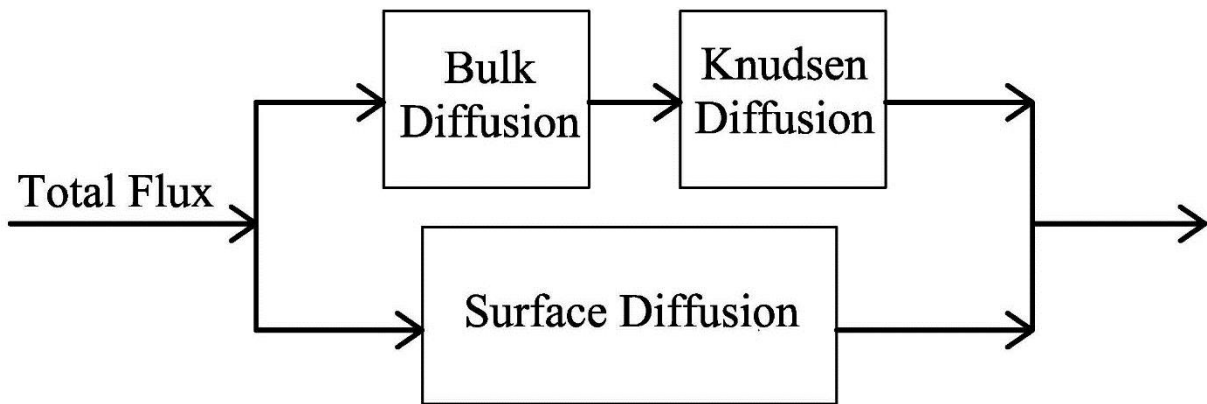


Figure 2-8: Diffusion mechanism in bi-porous material at low concentration

In Bi-LDF model, an effective LDF coefficient is proposed to combine the molecular and Knudsen diffusion rate (Eq. 2-39 to Eq. 2-41).

$$\frac{\partial c_{pi}}{\partial t} = k_{pi}(c_i - \bar{c}_{pi}) \quad (2-39)$$

$$k_{pi} = \frac{15\varepsilon_p D_{pi}}{R_p^2} \frac{Bi_i}{Bi_i + 1} \quad (2-40)$$

$$Bi_i = \frac{R_p k_{f,i}}{5\varepsilon_p D_{pi}} \quad (2-41)$$

In Eq. 2-41, the ratio of internal macropore to the external film resistance is determined by  $Bi_i$ , the Biot number, and  $D_{pi}$  represents the effective macropore diffusivity corrected for the tortuosity of component  $i$ <sup>96</sup>.  $D_{pi}$  is calculated as follows (Eq. 2-42)<sup>87,97</sup>:

$$\frac{1}{D_{pi}} = \frac{1}{D_{K,i}} + \frac{1}{D_{m,i}} \quad (2-42)$$

In this equation  $D_{K,i}$  is the Knudsen diffusivity and  $D_{m,i}$  is the macropore diffusivity. Knudsen diffusivity is calculated as follows (Eq. 2-43)<sup>97</sup>:

$$D_{K,i} = \frac{d_p \varepsilon_p}{3\tau_K} \sqrt{\frac{8RT}{\pi M_i}} \quad (2-43)$$

where  $\tau_k$  is the tortuosity factor<sup>98,99</sup> as follows (Eq. 2-44):

$$\tau_k = \frac{\varepsilon_p}{0.4\varepsilon_p - 0.0328} \quad (2-44)$$

The macropore diffusivity in a binary mixture is calculated as follows (Eq. 2-45 to 2-47)<sup>98,99</sup>:

$$D_{m,i} = \frac{(1 - y_i)}{\sum_{\substack{j=1 \\ j \neq i}} \frac{y_j}{D_{i,j}}} \quad (2-45)$$

$$D_{i,j} = \frac{\varepsilon_p D_{i,j}^0}{\tau} \left( \frac{P_0}{P} \right) \left( \frac{T}{T_0} \right)^{1.75} \quad (2-46)$$

$$\tau = 1 + 0.5(1 - \varepsilon_p) \quad (2-47)$$

“For the micropores, the Darken equation, one of the earliest models to describe surface diffusion, is used to describe the concentration dependence of micropore diffusivity”<sup>96,100</sup>(Eq. 2-48).

$$\frac{\partial q_{ci}}{\partial t} = \frac{15D_{ci}}{r_c^2} (1 - \varepsilon_p) \rho_p (q_{ci}^* - \bar{q}_{ci}) \quad (2-48)$$

In this equation, “ $D_{ci}$  is the crystal diffusivity,  $r_c$  is the crystal radius,  $q_{ci}^*$  is the adsorbed phase concentration in equilibrium with concentration of component  $i$  over the particle and  $\bar{q}_{ci}$  is the averaged adsorbed phase concentration”<sup>101</sup>.

Adsorption on heterogeneous adsorbents can be well described by a Langmuir model (Eq. 2-49)

$$q_{ci}^* = \frac{q_{si} b_i p_i}{1 + b_i p_i} \quad (2-49)$$

where  $q_{si}$  is the saturation capacity of adsorbate  $i$ , and  $b_i$  is the temperature-dependent isotherm constants as follows (Eq. 2-50):

$$b_i(T) = b_i(T_0) \exp\left(\frac{-\Delta H_{ads,i}}{R} \left(\frac{1}{T} - \frac{1}{T_0}\right)\right) \quad (2-50)$$

The crystal diffusivity at any loading is a function of surface diffusion at zero loading multiplied by the thermodynamic correction factor of  $\frac{\partial \ln p_i}{\partial \ln q_{ci}}$  (Eq. 2-51)<sup>46,96</sup>.

$$D_{ci} = D_{ci}^{\infty} \left. \frac{d \ln(p_i)}{d \ln(q_{ci})} \right|_T \quad (2-51)$$

“Crystal diffusivity of the adsorbed molecule in micropores can be explained as an activated process”<sup>101,102</sup>(Eq. 2-52):

$$D_{ci}^{\infty} = D_{ci0} \exp\left(\frac{-E_{ai}}{RT}\right) \quad (2-52)$$

The exponential term in this equation “expresses the probability of a molecule to have sufficient kinetic energy to surmount the energy barrier”<sup>102</sup>; where,  $D_{ci0}$  is the limiting diffusivity at high temperature and  $E_{a,i}$  is the activation energy. For a Langmuir isotherm, the thermodynamic factor of  $\frac{\partial \ln p_i}{\partial \ln q_{ci}}$  is calculated as (Eq. 2-53)<sup>96,103</sup>:

$$\left. \frac{d \ln(p_i)}{d \ln(q_{ci})} \right|_T = \frac{1}{1-\theta} = \frac{1}{1-q_{ci}^*/q_{si}} \quad (2-53)$$

An overall adsorption in a particle can be described as (Eq. 2-54):

$$\rho_p \bar{q}_{pi} = \varepsilon_p c_{pi} + (1-\varepsilon_p) \rho_s \bar{q}_{ci} \quad (2-54)$$

where  $\rho_s$  is the skeletal density,  $\rho_p$  is the apparent density,  $\varepsilon_p$  is the particle porosity,  $c_{pi}$  is the concentration of component  $i$  in the macropores,  $q_{pi}$  is the averaged adsorbate concentration of component  $i$  per unit adsorbent particle mass<sup>96</sup> (mol/g) and  $q_{ci}$  is the averaged adsorbate concentration of component  $i$  per unit crystal mass<sup>96</sup> (mol/g). Therefore, combining the Eq. 2-48 and 2-54 results in an overall adsorption using the bi-LDF rate equation( Eq. 2-55)<sup>101</sup>:

$$\rho_p \frac{\partial \bar{q}_{pi}}{\partial t} = k_{pi}(c_i - \bar{c}_{pi}) + \frac{15D_{ci}}{r_c^2} (1-\varepsilon_p) \rho_s (q_{ci}^* - \bar{q}_{ci}) \quad (2-55)$$

If the radial gradients in pressure and concentration of the gases in the solid and the gas are negligible, the overall mass balance for the packed-bed can be written as (Eq. 2-56):

$$\varepsilon_t \frac{\partial c_i}{\partial t} + (1-\varepsilon_b) \rho_s \frac{\partial \bar{q}_{pi}}{\partial t} = -\varepsilon_b \frac{\partial u c_i}{\partial z} + \varepsilon_b \frac{\partial}{\partial z} \left( D_{ax} \frac{\partial c_i}{\partial z} \right) \quad (2-56)$$

Combining Eq. 2-55 and 2-56 results in (Eq. 2-57):

$$\varepsilon_t \frac{\partial c_i}{\partial t} + (1-\varepsilon_b) \left[ k_{pi}(c_i - \bar{c}_{pi}) + \frac{15D_{ci}}{r_c^2} (1-\varepsilon_p) \rho_s (q_{ci}^* - \bar{q}_{ci}) \right] = -\varepsilon_b u \frac{\partial c_i}{\partial z} + \varepsilon_b \frac{\partial}{\partial z} \left( D_{ax,i} \frac{\partial c_i}{\partial z} \right) \quad (2-57)$$

“where  $D_{ax}$  is the axial dispersion coefficient,  $u$  is the superficial velocity in bed,  $z$  is the axial distance variable,  $t$  is the time,  $\varepsilon_b$  is the bed porosity”<sup>19</sup> and  $\varepsilon_t$  is the total porosity of the packed bed. In this equation, the following terms exist:

Diffusion term  $\varepsilon_b \frac{\partial}{\partial z} \left( D_{ax} \frac{\partial c_i}{\partial z} \right)$ :

Since axial mixing reduces the separation efficiency and it is not an undesirable term, minimizing this term is one of the main concerns to enhance the separation factor<sup>19</sup>. Molecular diffusion and turbulent mixing are known as the main driving forces of axial dispersion in a packed bed<sup>19</sup>. Gas velocity determines that either molecular diffusion or turbulent mixing is dominant. The axial Peclet number for flow around the particle describes axial dispersion in the gas flow (Eq. 2-58):

$$\frac{1}{Pe} = \frac{D_{ax}}{ud_p} \quad (2-58)$$

where  $u$  is the gas superficial velocity and  $d_p$  is the particle diameter. Wakao and Funazkri<sup>84</sup> developed the following equation for  $Re > 5$  (Eq. 2-59):

$$\frac{\varepsilon_b D_{ax}}{D_{m,i}} = 20 + 0.5(Sc)(Re) \quad (2-59)$$

This equation is valid for evaporation, sublimation, dissolution or a diffusion controlled chemical reaction in non-porous surfaces. Although this equation does not exactly fit the adsorption process in porous beds, it can be used with some error to estimate the axial dispersion for gas adsorption in porous beds<sup>96,101,104</sup>.

Convection term  $\frac{\partial uc_i}{\partial z}$ : This term represents the advection or bulk mass transfer of substances in the  $z$  direction due to motion of a gas over the surface.

Accumulation term  $\frac{\partial c_i}{\partial t}$  : This term accounts for the changes in mass/ concentration of component i per unit of time.

Adsorption term  $\frac{\partial \bar{q}_{pi}}{\partial t}$  : This term shows mass transfer from the gas phase to the solid phase as explained above.

## 2.8 Error analysis of experimental results

Since most of the results in this thesis are experimental basis and there is always a margin of doubt in any measurement, error in experiment for experimental analysis have been calculated and average results are reported<sup>105</sup>.

$$\text{Standard Deviation} = \sqrt{\frac{1}{M(N-1)} \sum_{j=1}^M \sum_{i=1}^N (x_{ij} - \bar{x}_j)^2} \quad (2-60)$$

$$\bar{x}_j = \frac{1}{N} \sum_{i=1}^N x_{ij} \quad (2-61)$$

Degree of freedom =  $M(N-1)$

where

M: Number of series of analyses

N: number of measurements in each series of analyses

$X_{ij}$ : the observed values of the sample

$\bar{x}_j$  : the mean value of these observation

## 2.9 Summary

The ideal adsorbent for CO<sub>2</sub> separation should have some important characteristics such as high cyclic CO<sub>2</sub> adsorption capacity, appropriate selectivity over N<sub>2</sub> and O<sub>2</sub> and high stability in repetitive cyclic adsorption/desorption process. Due to huge volume of flue gas, capital cost of post-combustion process is large. So, using expensive sorbent materials or materials with high disposal expenses can escalate cost related to the process and make it economically unfeasible. This research focused on development of low-cost and effective adsorbents for CO<sub>2</sub> capture from coal-fired power plants.

## **Chapter 3 Study of the Impact of Activating Agents on Activated Carbons for CO<sub>2</sub> Adsorption**

A similar version of this chapter has been published in the Journal of Environmental Sciences.

- *Shahkarami, S.; Azargohar, R.; Dalai, A. K.; Soltan, J. Breakthrough CO<sub>2</sub> Adsorption in Bio-Based Activated Carbons. J. Environ. Sci. 2015, 34, 68-76.*

In addition, some parts of this chapter were presented at the following conferences and symposiums:

- Enhanced CO<sub>2</sub> Adsorption on Activated Carbon, 66<sup>th</sup> Canadian Chemical Engineering Conference, Quebec City, QC, October 16-19, 2016.
- Selective CO<sub>2</sub> Adsorption on Activated Carbons, 24<sup>th</sup> Canadian Symposium on Catalysis Ottawa, ON, Canada, May 8-11, 2016.
- CO<sub>2</sub> Capture on Bio-based Activated Carbons, Biorefinery I- Chemicals and Materials from thermo Chemical Biomass, Chania, Greece, September 27-October 2, 2015.
- Development of Activated Carbon Adsorbents for CO<sub>2</sub> Capture, 64<sup>rd</sup> Canadian Chemical Engineering Conference, Niagara Falls, ON, Canada, October 19-22 2014.

- Study the Performance of Bio-based Activated Carbons for CO<sub>2</sub> Capture, 63<sup>rd</sup> Canadian Chemical Engineering Conference, Fredericton, NB, Canada, October 20-23, 2013.

#### Contribution of the Ph.D. candidate

The bench-scale adsorption set-up was designed and installed by Sepideh Shahkarami. A LabVIEW program for accurate data recording was designed and linked to the adsorption set-up by Sepideh Shahkarami. The activation conditions were selected by Sepideh Shahkarami with assistance from Dr. Ramin Azargohar. The experimental design (in Design-Expert® software V9) were planned and experiments were conducted by Sepideh Shahkarami. All the sample characterizations were performed and the related data were analyzed by Sepideh Shahkarami. The data analyses and interpretations were conducted by Sepideh Shahkarami. All of the written text was prepared by Sepideh Shahkarami and all the experiments were discussed with Drs. A.K. Dalai and J. Soltan.

#### Contribution of this chapter to the overall study

In order to develop an optimized activated carbon adsorbent with high CO<sub>2</sub> uptake, it was necessary to study the impact of activating agent on CO<sub>2</sub> adsorption performance of activated carbons. In this part of research, the main focus was on the impacts of activating agents on the porosity and surface chemistry of activated carbon as well as CO<sub>2</sub> adsorption performance of the produced activated carbons under different adsorption conditions.

#### **Abstract**

In this work, the effects of different methods of activation on CO<sub>2</sub> adsorption performance of activated carbon were studied. Activated carbons were prepared from biochar, obtained from fast pyrolysis of white wood, using three different activation methods of steam activation, CO<sub>2</sub> activation and KOH activation. CO<sub>2</sub> adsorption behavior of the produced activated carbons were studied in a fixed-bed reactor set-up at atmospheric pressure, temperature range of 25-65°C and inlet CO<sub>2</sub> concentrations range of 10-30 mol.% in He to determine the effects of the surface area, porosity and surface chemistry on adsorption capacity of the samples. Characterization of the micropore and mesopore texture was carried out using N<sub>2</sub> and CO<sub>2</sub> adsorption at 77 and 273 K,

respectively. Central composite design was used to evaluate the combined effects of temperature and concentration of CO<sub>2</sub> on the adsorption behavior of the adsorbents. The KOH activated carbon with total micropore volume of 0.62 cm<sup>3</sup>/g and surface area of 1400 m<sup>2</sup>/g had the highest CO<sub>2</sub> adsorption capacity of 1.8 mol/kg due to its microporous structure and high surface area under the optimized experimental conditions of 30 mol.% CO<sub>2</sub> and 25°C. The performance of the adsorbents in multi-cyclic adsorption process was also assessed and the adsorption capacity of KOH and CO<sub>2</sub> activated carbons remained remarkably stable after 50 cycles with low temperature (160°C) regeneration.

### 3.1 Introduction

Activated carbons are known to have large adsorption capacity for CO<sub>2</sub> and they can be produced from low cost and abundant precursors such as bio-char<sup>31</sup>. It has been shown that surface area and pore size distribution of activated carbon affect CO<sub>2</sub> capture performance of activated carbon<sup>106</sup>. Moreover, starting precursors have a significant effect on CO<sub>2</sub> adsorption behavior of activated carbons<sup>47,55</sup>. However, a comparison of different methods of activation of biochar on its CO<sub>2</sub> adsorption performance has not been reported before. This work focused on the effect of different activation methods on porosity, surface area and adsorption capacity of the activated carbons to explain CO<sub>2</sub> adsorption behavior in activated carbons. Steam, CO<sub>2</sub> and KOH were used as activating agents for activation of biochar obtained from fast pyrolysis of whitewood.

The main challenge of post combustion carbon capture processes is operation at low concentration of CO<sub>2</sub><sup>82</sup>. In this work, the CO<sub>2</sub> adsorption performance of the adsorbents was investigated at atmospheric pressure, temperatures range of 25-65 °C and CO<sub>2</sub> concentrations ( $C_{CO_2}$ ) range of 10-30 mol. % and the influence of activation method, porous structure, surface area and surface chemistry on performance of the adsorbents were studied. Adsorption capacity was analyzed using breakthrough curve in an isothermal fixed-bed reactor and the bed adsorption capacity was studied as a function of both breakthrough time and the S-shape of the breakthrough curve under the designed operating conditions. Central composite design (CCD) method was applied for experimental design to find optimized process conditions and second-order models were developed to predict the adsorption capacity of adsorbents as functions of temperature and

concentration of CO<sub>2</sub> in inlet stream. These models showed the significance of variables and the interactions among them on the CO<sub>2</sub> adsorption process.

## 3.2 Materials and methods

### 3.2.1 Biochar

The biochar used in this study was a by-product of fast pyrolysis of whitewood provided by Dynamotive Energy Systems Corporation (BC, Canada). According to the manufacturer, the operating conditions for this process were 500°C, atmospheric pressure and residence time less than 1 sec. The biochar yield of this process was 10-15 wt. %. The as-received biochar was sieved, and particle size range of 178-710 µm was collected for activation processes.

### 3.2.2 Physically activated carbon

Physically activated carbon was prepared using carbon dioxide and steam as activating agents. Before activation, sieved biochar was dried in air for 12 h at 110 °C. The process conditions of the steam and CO<sub>2</sub> activated carbon were chosen to obtain similar BET surface area and total pore volume in both products. The detailed information for activation set-up was described in Appendix A<sup>107</sup>. The activation yield was calculated using the mass ratio of produced activated carbon to biochar.

#### Steam Activation

In each batch, 20 g of biochar was loaded into the reactor and heated to 700°C with the heating rate of 3°C/min while flowing nitrogen carrier gas at the flow rate of 140 standard mL/min. Steam was injected into the reactor with the steam-to-carbon mass ratio of 1.06 for 1.4 h. After the injection, the reactor was cooled down to room temperature under nitrogen flow. The yield of product was 55 wt. % in steam activation process.

#### CO<sub>2</sub> Activation

In each run, 15 g of biochar was placed in the fixed-bed reactor under an argon flow rate of 100 standard mL/min. The temperature of the reactor was increased to 890 °C with the heating rate of 3°C/min. Then, the gas was switched to CO<sub>2</sub> with the flow rate of 130 standard mL/min. After 100

min, the reactor was cooled down to room temperature under argon gas flow. The yield of product was 52 wt. % in CO<sub>2</sub> activation process.

The Schematic of experimental set-up, procedure and calibration are provided in Appendix A.

### 3.2.3 Chemically activated carbon

The physical activation set-up was also used for chemical activation of biochar. KOH was used as the activating agent. Biochar was impregnated with KOH in 100 mL of distilled water with carbon-to-KOH mass ratio of 0.81 on dry basis. After 4 h at the room temperature, the prepared mixture was dried in oven at 110°C for 12 h. 20 g of the dried sample was placed in the reactor under a nitrogen flow of 240 standard mL/min and was heated to 300°C with the heating rate of 3°C/min, and was held for 1 h at 300°C<sup>108</sup>. Then, the temperature of the reactor was increased to 775°C with the heating rate of 3°C/min and held at this temperature for 2 h before cooling down to room temperature. In the next step, the sample was washed with hot water, followed by 0.1 M HCl, and finally by distilled water to remove the soluble salts and the potassium compounds<sup>109,110</sup>. Then the sample was dried in oven overnight at 110°C in air. The product yield of chemical activation was 33 wt. %. The details of activation process, experimental set-up and calibrations are provided in Appendix A.

### 3.2.4 Characterization

#### **Elemental analysis and ash content**

The mass fractions of carbon, hydrogen, nitrogen and sulfur in the samples were determined from elemental analysis performed on a Vario EL III elemental analyzer (Vario EL III, Elementar, Germany). Oxygen content of samples was determined by difference. The ash contents of biochar and activated carbons were measured according to ASTM D2866 - 11.

#### **BET surface area, pore volume and pore size distribution**

The nitrogen adsorption isotherms of activated carbon samples at 77 K and BET (Brunauer-Emmett-Teller) surface area and total pore volume of the samples were determined using ASAP 2020 system (ASAP 2020, Micromeritics Instruments Inc., USA). The samples were degassed at

300°C to a vacuum of 550  $\mu\text{m Hg}$  prior to the analysis. The micropore size distribution was determined using the non-local Density Functional Theory (NLDFT)<sup>42,111</sup> applying  $\text{N}_2$  and  $\text{CO}_2$  adsorption on slit-pore carbon<sup>112</sup> at 77 K and 273 K, respectively. Nitrogen at 77 K has a saturation pressure of 760 Torr and  $\text{N}_2$  adsorption starts at relative pressure ( $P/P_0$ ) between  $10^{-7}$  and  $10^{-5}$  whereas  $\text{CO}_2$  has a saturation pressure of 26,400 Torr and  $\text{CO}_2$  adsorption starts at relative pressure of about  $10^{-4}$ . Since diffusion rates of  $\text{N}_2$  and consequently attaining equilibrium in ultramicropores with diameter between 0.5 and 1 nm is very slow and requires very low relative pressure and high uptake of  $\text{N}_2$ ,  $\text{CO}_2$  adsorption at 273K was used to overcome diffusion limitations<sup>19</sup>. The  $\text{CO}_2$  analysis results were combined with the  $\text{N}_2$  adsorption analysis for the full range characterization. IUPAC (International Union of Pure and Applied Chemistry) classification was considered for pore size distribution<sup>30</sup>. Ultramicropores have pore width less than 0.7 nm, super-micropores show pore width between 0.7 and 2 nm, and mesopores have pore width between 2 and 50 nm.

### **X-ray photoelectron spectroscopy (XPS)**

Surface chemistry of the activated carbon samples was studied and oxygenated functional groups on the surface were quantified using X-ray photoelectron spectroscopy. This was equipped with an omicron monochromatized Al  $K\alpha$  source ( $h\nu = 1486.7$  eV) and SPHERA EA125 hemispherical electron energy analyzer in the Surface Science Facility at the Resonant Elastic and Inelastic X-ray Scattering (REIXS) beamline 10ID-2 of the Canadian Light Source (The Surface Science Facility, Canadian Light Source, Canada). The survey scan spectra were collected in the 0-1200 eV binding energy range in 0.5 eV steps with pass energy of 50 eV. High resolution scanning of the C1s region was also conducted in 0.1 eV steps with pass energy of 25 eV. An accelerating voltage of 15 kV and an emission current of 20 mA were used for the analysis. The operating pressure was less than  $2 \times 10^{-10}$  mbar. Peak deconvolutions of high-resolution C1s spectra were conducted using the Casa XPS software (version 2.3.16 PR 1.6).

#### **3.2.5 Breakthrough $\text{CO}_2$ adsorption measurements**

$\text{CO}_2$  adsorption was performed in an isothermal fixed-bed tubular reactor. A K-type thermocouple was placed inside the reactor and the reactor temperature was controlled using a heating tape and

a temperature controller (2416, Eurotherm, USA). The reactor was loaded with 5 g of activated carbon and pre-heated at 160°C for 2 h under helium (He) flow before the adsorption experiments. After cooling down the reactor to the desired operating temperature, the feed gas was switched from He to He/CO<sub>2</sub> gas mixture. The total feed flow rate was maintained constant at 50 standard mL/min in all experiments. The feed flow rates were controlled with mass flow controllers (5850E A/B, Brooks Instrument, USA). For continuous monitoring, the outlet gas flow rate was recorded and the dynamic CO<sub>2</sub> adsorption capacity was measured using a micro-gas chromatograph analyzer (CP-4900, Varian, USA) equipped with a thermal conductivity detector (TCD). The standard gas composition () and calibration curves are provided in Appendix B. The adsorption process was continued up to the saturation point where the outlet concentration of CO<sub>2</sub> reached the inlet concentration of CO<sub>2</sub>. The schematic diagram of the set-up schematic is shown in **Fig. 3-1** and the details of the set-up and calculation methods are described in section 2.3.1 and Appendix B.

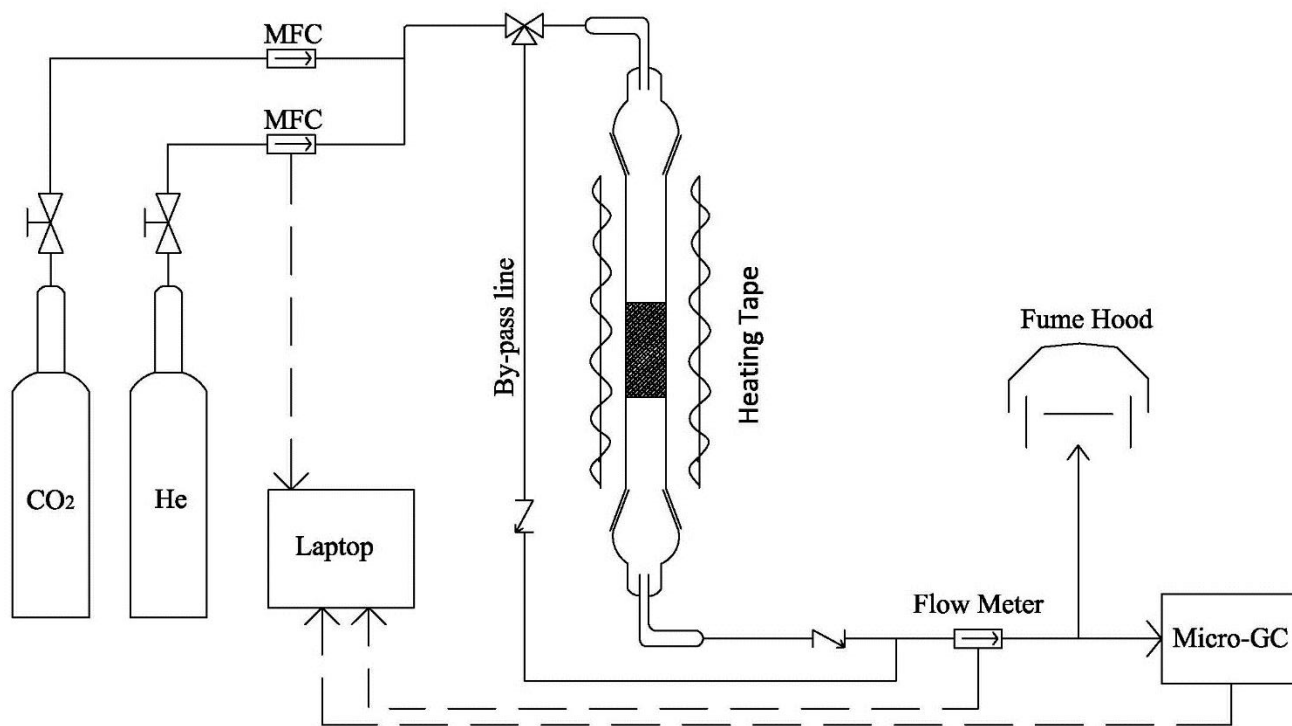


Figure 3-1: Schematic of adsorption set-up

The CO<sub>2</sub> adsorption process was studied using central composite design to optimize the process conditions and determine the interaction effect of parameters. For the experimental design, C<sub>CO<sub>2</sub></sub> and temperature (*T*) were selected as experimental variables and they were studied at two levels of 10-30 mol.% and 25-65 °C, respectively. For a 2 level study, the total number of experiments is given as  $2^n + 2n + n_c$  where *n* is the number of independent process variables and *n<sub>c</sub>* is the number of center points or replicates used to estimate the residual error<sup>31,107</sup>. Each center point adds one degree of freedom (df) from which the experimental error is estimated. Therefore, 14 experiments including 8 factorial and axial points as well as 6 replications at the center point were conducted for the adsorption process using each type of the activated carbons (ACs) (Table 3-3). The model helps to assess the responses in the variables space and to find the best region to reach the optimum response. The second-order model is used to estimate the response (Eq. 3-1):

$$y = \beta_0 + \beta_1x_1 + \beta_2x_2 + \beta_{11}x_1^2 + \beta_{22}x_2^2 + \beta_{12}x_1x_2 + \varepsilon \quad (3-1)$$

where *y* is the predicted response,  $\beta_0$  is the constant,  $\beta_1$  and  $\beta_2$  are the linear coefficients,  $\beta_{11}$  and  $\beta_{22}$  are the quadratic coefficients,  $\beta_{12}$  is the interaction coefficients, *x<sub>1</sub>* and *x<sub>2</sub>* are the coded values of the parameters and  $\varepsilon$  is the residual error<sup>113</sup>. The model predicts the behavior of the response as a function of the variables and their interaction. The fitness of the model is evaluated using Analysis of Variance (ANOVA) and squared-R<sup>113</sup>. The response factors in this study are the CO<sub>2</sub> adsorption capacity and the breakthrough time (*t<sub>b</sub>*). Adsorption capacities are expressed in milligrams of CO<sub>2</sub> adsorbed per gram of adsorbent and *t<sub>b</sub>* is defined as the time that the ratio of outlet C<sub>CO<sub>2</sub></sub> to the inlet C<sub>CO<sub>2</sub></sub> reaches 0.05. Multi-cycle adsorption/desorption performance of the adsorbents was studied to examine their durability using a temperature swing adsorption (TSA) cyclic process. For desorption, when the adsorbent was saturated, gas flow was switched to He flow and temperature was raised to 160°C and maintained at this temperature for 2 h. The adsorbents were subjected to 50 consecutive adsorption–desorption cycles and their performance was compared.

### 3.3 Results and discussion

#### 3.3.1 Characterization of adsorbents

The elemental analysis, ash content, BET surface area and total pore volume of the adsorbents are summarized in Table 3-1. Elemental analysis results show that KOH activation followed by acid treatment results in an increase in the hydrogen, nitrogen and oxygen content and decrease in the carbon content of the activated carbon product. Activation conditions are selected to keep the surface area of CO<sub>2</sub> activated carbon and steam activated carbon in a close range in order to study the effects of activating agent and pore volume on the adsorption behavior of the samples.

Table 3-1: Physical and chemical properties of CO<sub>2</sub>, steam and KOH activated carbons

Sample	Activation yield (%)	Elemental analysis* (wt.%)					Ash content (%)	S <sub>BET</sub> (m <sup>2</sup> /g)	total pore volume (cm <sup>3</sup> /g)
		C	H	N	S	O			
Steam AC	59	92.57	1.81	0.23	0.00	5.39	3.62	840	0.55
CO <sub>2</sub> AC	55	92.05	2.00	0.58	0.00	5.37	4.97	820	0.45
KOH AC	35	85.98	4.29	1.21	0.01	8.51	2.02	1400	0.62

*\*Elemental analysis was on a dry ash-free basis, and oxygen content was determined by difference*

Figure 3-2 shows the N<sub>2</sub> adsorption isotherms of the activated carbon. The narrow hysteresis loops in isotherms of steam and CO<sub>2</sub> activated carbons indicated that both physically activated carbons were mesoporous.

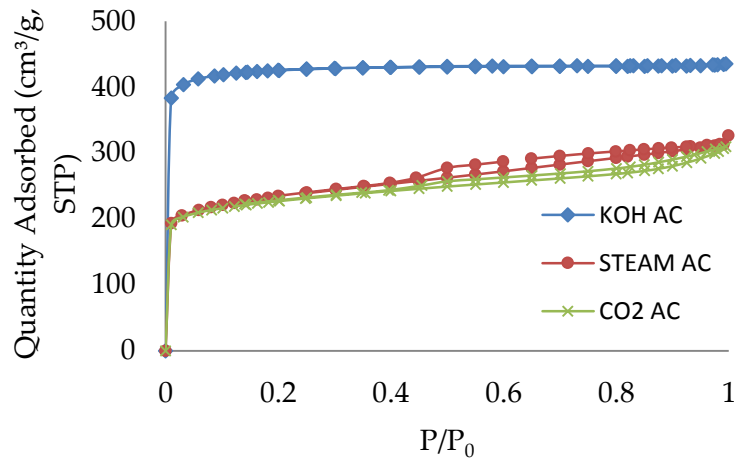


Figure 3-2: N<sub>2</sub> adsorption–desorption isotherms of CO<sub>2</sub>, steam and KOH activated carbons

The micropore and mesopore size distributions of adsorbents are presented in Figure 3-3 and Figure 3-4. The ultra-micro pores, super-micropores and meso-pores ratio of samples are also shown in Figure 3-5. BET surface area of KOH activated carbon was larger than that of the physically activated carbon due to its large micropore volume. The contribution of meso-pores in chemically activated carbon porous structure was negligible. The micropore volume of steam and CO<sub>2</sub> activated carbon were quite close while the total pore volume of the steam activated carbon was more than that of CO<sub>2</sub> activated carbon. KOH activated carbon had the highest ultra-micropores and super-micropores volume.

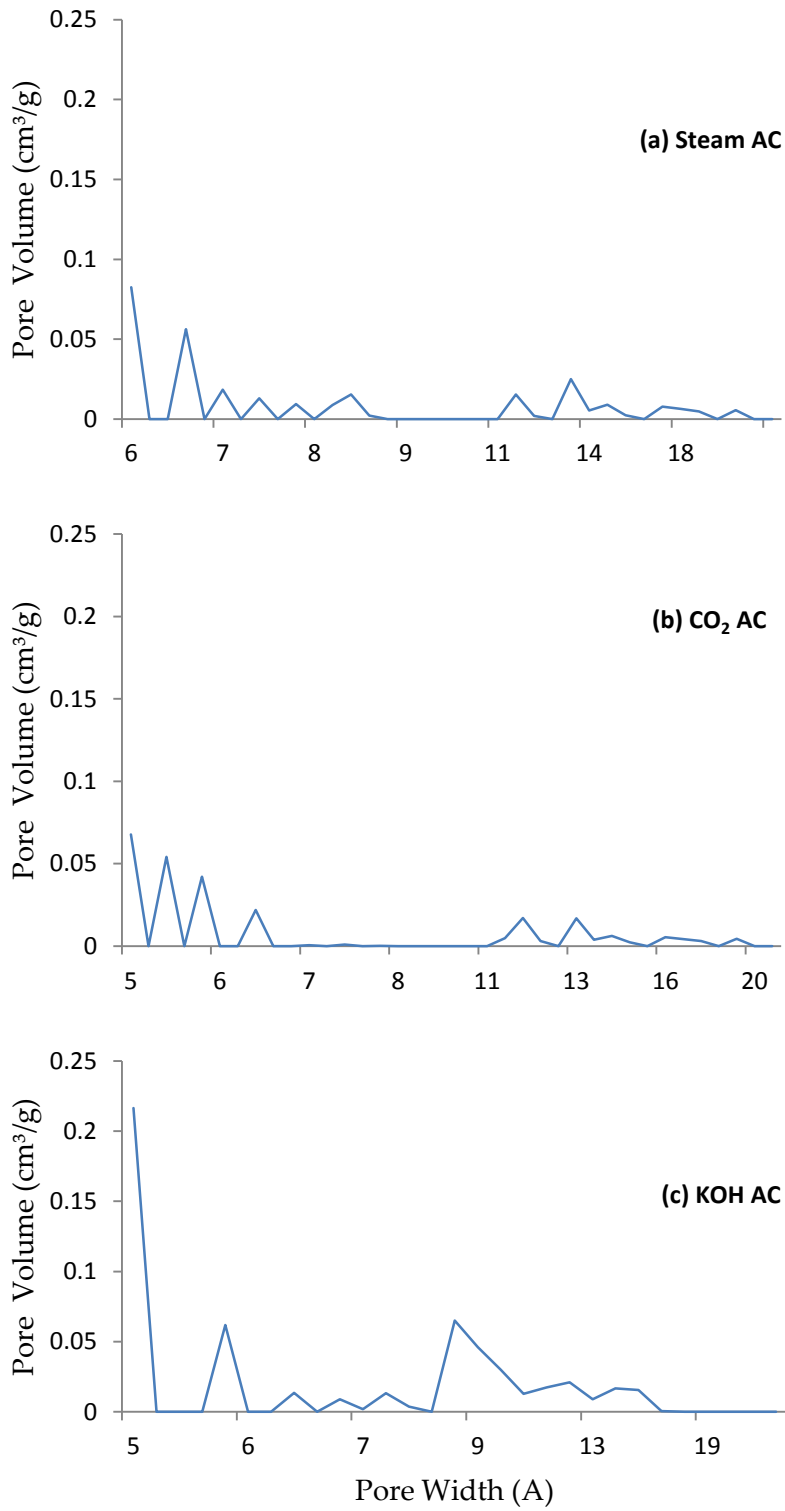
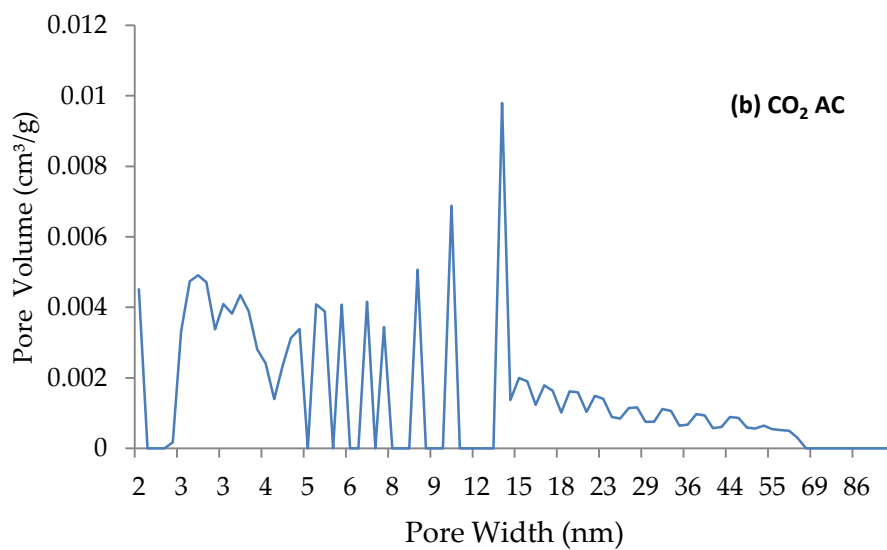
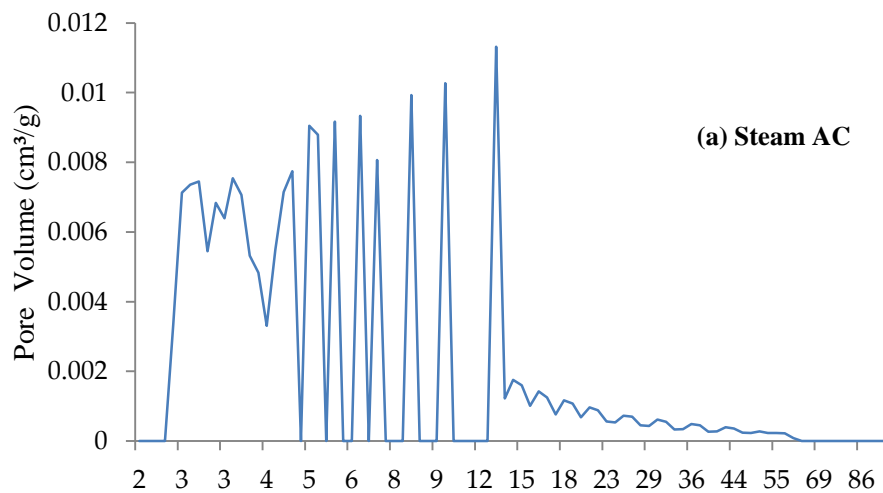


Figure 3-3: Incremental micropore volume of (a) steam, (b) CO<sub>2</sub> and (c) KOH activated carbons



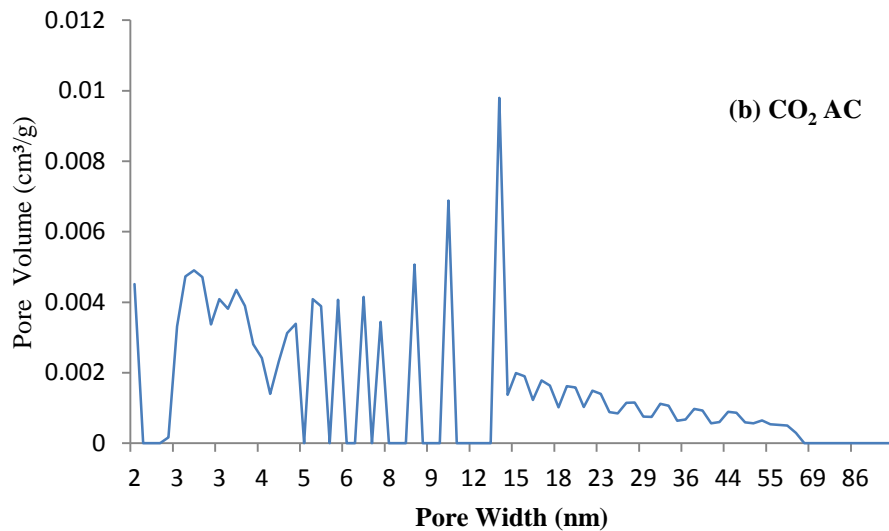


Figure 3-4: Incremental mesopore volume of (a) steam and (b) CO<sub>2</sub> activated carbons

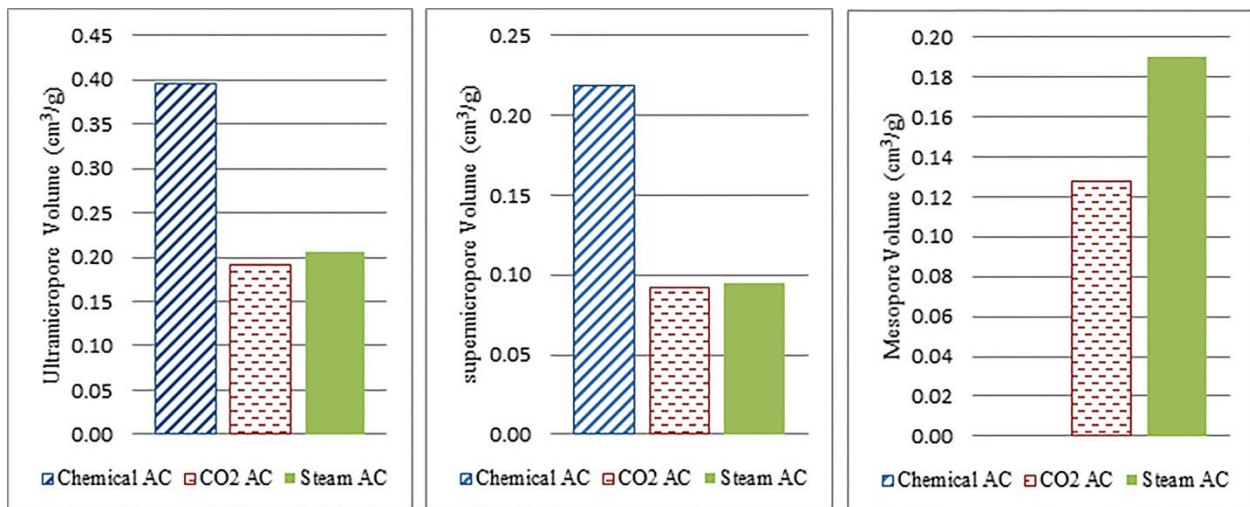
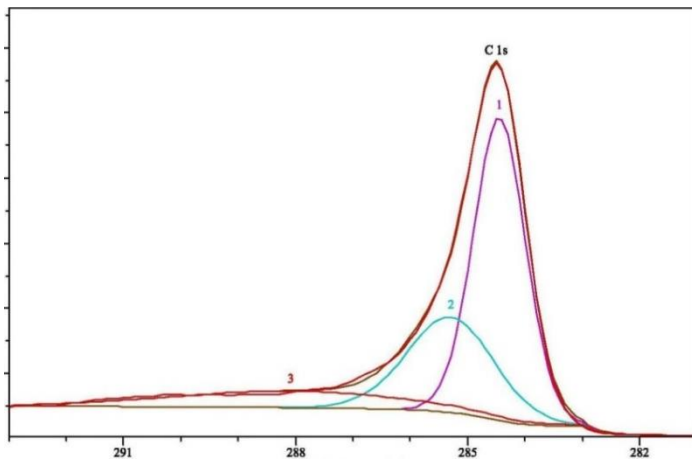


Figure 3-5: Proportion of ultra micropores, supermicropores and mesopores in KOH, CO<sub>2</sub> and steam activated carbons

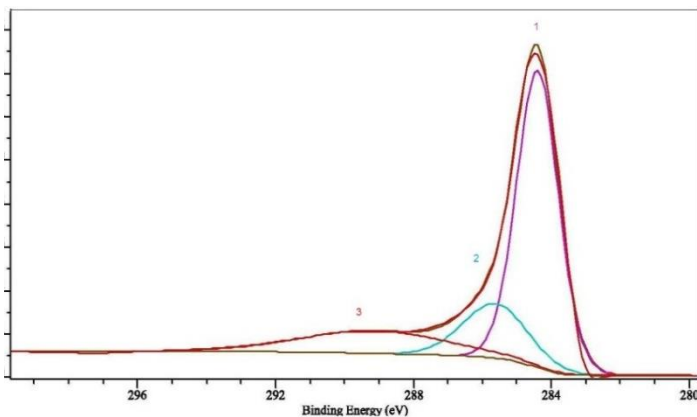
The XPS spectra and deconvolution of C1s spectra are shown in Figure 3-6, and the relative content of each functional group<sup>114–117</sup> are presented in Table 3-2. The surface acidity was a result of oxygen functional groups such as phenolic, carboxyl, lactone, and aldehyde groups. Four peaks were detected in deconvolution of the C1s spectra of activated carbons: peak 1 (284.5 eV), –C=C–, graphitized carbon; peak 2 (286.1 eV), –C–OH, .C–O–C≡, C–O–R; peak 3 (288.7 eV), –C=O; and

peak 4 (289.3 eV), -COOH. Nitrogen peak was not detected on the spectra of the samples. A comparison of the C1s spectra of the different samples showed the contributions of different oxygen groups in physically and chemically activated carbons. Table 3-2 shows that the identified surface functional groups on steam and CO<sub>2</sub> activated carbons are similar while chemically activated carbon has a lower content of graphitic carbon and different oxygen groups on the surface. These results suggest that KOH activation process would introduce more oxygen atoms to the surface of the activated carbon. Peak 3 which represents ketone and aldehyde groups on the surface<sup>47</sup> was only identified in KOH activated carbon spectrum while contribution of carboxylic groups at 289.3 eV was smaller in this sample.

#### Steam AC



#### CO<sub>2</sub> AC



## KOH AC

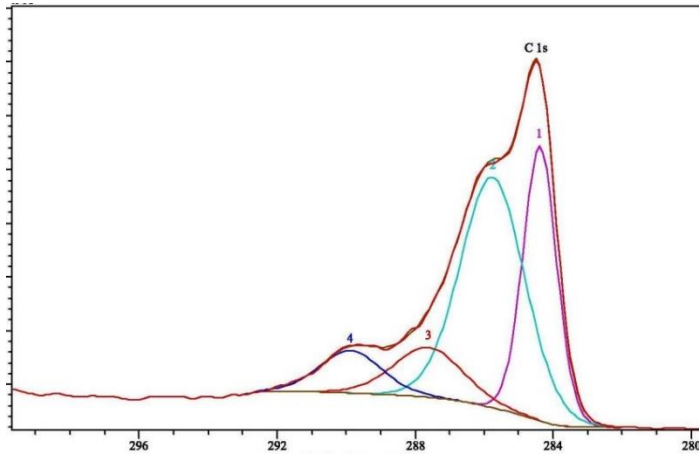


Figure 3-6: C1s XPS spectra of the activated carbons prepared using (a) steam, (b) CO<sub>2</sub> and (c) KOH

Table 3-2: Relative content of functional groups on CO<sub>2</sub>, steam and KOH activated carbons based on C1s XPS spectra deconvolution

Samples	C1s (%)				
	O/C	peak 1	peak 2	peak 3	peak 4
CO <sub>2</sub> AC	0.15	65.9	17.3	-	16.9
Steam AC	0.17	56.11	29.58	-	14.31
KOH AC	0.21	30.41	49.56	11.16	8.87

### 3.3.2 Adsorption of CO<sub>2</sub>

The results of breakthrough adsorption measurements of KOH, CO<sub>2</sub> and steam activated carbons are summarized in Table 3-3. Gas adsorption begins from the bed inlet and most of the mass transfer occurs in this region. After saturation of the inlet region, the mass-transfer zone (MTZ) moves down through the bed gradually. At the  $t_b$ , the adsorbent between the inlet and the MTZ is fully saturated with CO<sub>2</sub>. As the breakthrough continues the  $C_{CO_2}$  in the outlet increases gradually to the inlet concentration. At this point, no more adsorption can take place in the bed.

As can be seen in Table 3-3, in general, chemically activated carbon presents higher adsorption capacity than the physically activated carbon at high CO<sub>2</sub> concentration. This can be related to the

higher surface area and higher micropore volume specially ultra-micropore volume of the chemically activated carbon<sup>30</sup>. Although according to the literature<sup>117</sup>, the interaction of CO<sub>2</sub>-oxygen functional groups have negative impact on the CO<sub>2</sub> adsorption on the activated carbon, KOH activated carbon with higher content of oxygen groups results in a better performance which probably accounts for the larger impact of porosity of CO<sub>2</sub> adsorption behavior. CO<sub>2</sub> activated carbon and steam activated carbon present similar adsorption behavior, indicating that activating agent is not a significant parameter in CO<sub>2</sub> adsorption on physically activated carbons. Both temperature and  $C_{CO_2}$  affect the shape and breakthrough time of the adsorbent. As is expected, adsorption capacity of all samples decreases with increasing temperature because of the exothermic nature of CO<sub>2</sub> adsorption<sup>31</sup> while an increase in  $C_{CO_2}$  increases CO<sub>2</sub> adsorption capacity dramatically. The highest and lowest adsorption capacities are achieved at 30%  $C_{CO_2}$ , 25°C and 10%  $C_{CO_2}$ , 65°C, respectively.

Table 3-3: Central composite design for two variables and corresponding adsorption capacity

Runs	Parameters		Adsorption capacity (mgCO <sub>2</sub> /g <sub>adsorbent</sub> )		
	Temperature (°C)	$C_{CO_2}$ (mol.%)	KOH AC	CO <sub>2</sub> AC	Steam AC
1	45.0	20	36	36	36
2	25.0	10	27	28	26
3	45.0	20	37	35	35
4	65.0	30	40	29	36
5	45.0	20	37	36	35
6	65.0	10	14	12	15
7	25.0	30	78	63	59
8	73.3	20	25	26	26
9	45.0	34.2	60	55	53
10	45.0	20	37	37	36
11	45.0	20	37	36	35
12	45.0	5.9	13	14	12
13	45.0	20	37	37	34
14	16.7	20	74.0	54	49

Figure 3-7 shows the effects of these process conditions on the breakthrough curve and  $t_b$  for all three types of adsorbents at these conditions. At 30%  $C_{CO_2}$ , 25°C, breakthrough curves of steam and  $CO_2$  ACs coincide and chemical activated carbon presents longer breakthrough time and higher capacity but wider breakthrough curve. The wider curve can result from the mass transfer resistance or axial dispersion<sup>19,31</sup> due to smaller particle size of KOH activated carbon. Results of the experiments also show that at  $t > 65^\circ C$  chemical activated carbon, and consequently larger pore volume and surface area, have no real advantage over physically activated carbon. The slope of breakthrough curves and  $t_b$  also vary with temperature and  $C_{CO_2}$ .

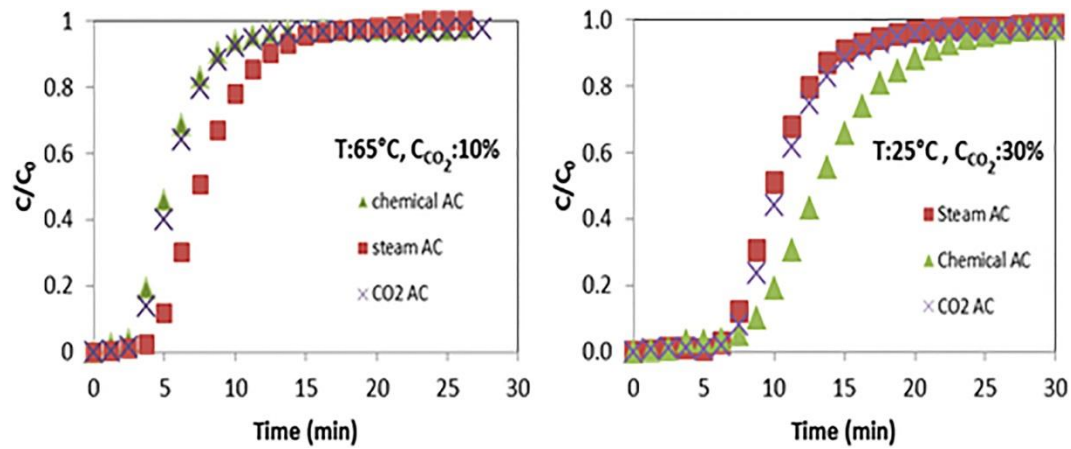


Figure 3-7: Breakthrough curves of steam,  $CO_2$  and KOH activated carbons (ACs) performed at 65°C in 10 mol.%  $CO_2$  in He, and at 25°C in 30 mol.%  $CO_2$  in He

At a constant  $CO_2$  concentration, the higher the temperature is, the narrower the mass transfer zone and the shorter  $t_b$  (Figure 3-8).

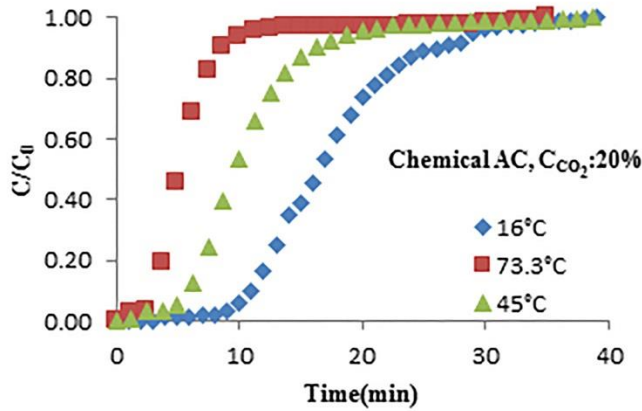


Figure 3-8: Breakthrough curves for CO<sub>2</sub> adsorption using KOH activated carbon performed in 20 mol. % CO<sub>2</sub> in He at 16, 45 and 73.3°C

On the other hand, an increase in  $C_{CO_2}$  at a constant temperature also increases the slope of the breakthrough curve, but it is less significant and it does not affect  $t_b$  (Figure 3-9).

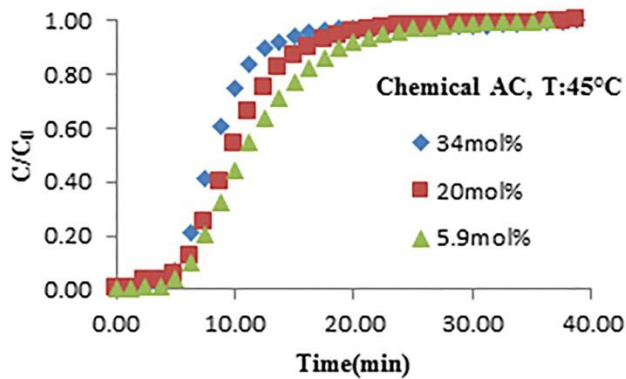


Figure 3-9: Breakthrough curves for CO<sub>2</sub> adsorption using KOH activated carbon performed at 45°C and 5.6 in 20 and 34 mol.% CO<sub>2</sub> in He

Design Expert software version 8.0.7.1 was used to analyze the results. The CO<sub>2</sub> adsorption results are analyzed to develop a regression model, in order to evaluate the effect of process conditions and their interactions, and to predict the adsorption behavior of adsorbent under different conditions. For the steam and chemical activated carbons, the experimental results are fitted with the quadratic models which proved the best for the lack of fit and model statistics tests. The

provisional models are tested for  $P$ -value, lack of fit and  $R^2$ , and the final models are obtained after the elimination of the insignificant parameters and interactions. Table 3-4 presents ANOVA of  $\text{CO}_2$  adsorption models on chemical and steam activated carbons after elimination of the insignificant terms. For  $\text{CO}_2$  activated carbon, there is a significant lack of fit indicating that the provisional model is inadequate.

The ANOVA results for  $\text{CO}_2$  adsorption capacity of  $\text{CO}_2$  activated carbon are provided in Appendix C (Table C-1). For chemical activated carbon, interaction between two factors is insignificant ( $p$ -value  $> 0.05$ ) and is omitted. The final model of  $\text{CO}_2$  adsorption on chemical activated carbon as a function of temperature and  $C_{\text{CO}_2}$  is as follows (Eq. 3-2):

$$\log_{10}(\text{CO}_2 \text{ adsorption capacity}) = 1.3085 - 0.0133 T + 0.0512 C_{\text{CO}_2} + 0.0001 T^2 - 0.001 C_{\text{CO}_2}^2 \quad (3-2)$$

Eq. 3-2 shows that adsorption capacity depends directly on  $C_{\text{CO}_2}$  and the square of temperature and inversely on temperature and the square of  $C_{\text{CO}_2}$ . It also shows that  $C_{\text{CO}_2}$  has the most significant effect followed by temperature and the square of  $C_{\text{CO}_2}$ . The high value of  $R^2$  (0.994) confirms that most of the data variation is fitted with this model. Figure 3-10a shows the response surface plot of  $\text{CO}_2$  adsorption capacity in chemically activated carbon. For the steam activated carbon interaction of independent factors is significant (Eq. 3-3):

$$\text{CO}_2 \text{ Adsorption Capacity} = +10.6943 - 0.3167 T + 2.6947 C_{\text{CO}_2} - 0.0150 T C_{\text{CO}_2} + 0.0022 T^2 - 0.0157 C_{\text{CO}_2}^2 \quad (3-3)$$

Table 3-4: The ANOVA (Analysis of Variance) results of the response surface models for  $\text{CO}_2$  adsorption capacity

	KOH AC				Steam AC			
	Sum of square	Mean square	df	$p$ -value	Sum of square	Mean square	df	$p$ -value
Model	0.67	0.17	4	<0.0001	2167.13	433.43	5	<0.0001
$T$	0.21	0.21	1	<0.0001	557.91	557.91	1	<0.0001
$C_{\text{CO}_2}$	0.42	0.42	1	<0.0001	1547.45	1547.45	1	<0.0001

$TC_{CO_2}$	-	-	-	-	36	36	1	0.0002
$T^2$	3.922E-003	3.922E-003	1	0.0236	5.79	5.79	1	0.0221
$C_{CO_2}^2$	0.037	0.037	1	<0.0001	18.26	18.26	1	0.0013
Residual	4.037E-003	5.047E-004	8		4.73	0.68	7	
Lack of fit	3.411E-003	8.527E-004	4	0.0648	2.64	0.88	3	0.3065
Pure error	6.265E-004	1.566E-004	4		2.09	0.52	4	
Total	0.68		13		2172.19		13	
$R^2$	0.9940				0.9978			
Adjusted $R^2$	0.9910				0.9963			
Predicted $R^2$	0.9629				0.9888			

As can be observed in Eq. 3-3, adsorption capacity of steam activated carbon increases as  $C_{CO_2}$  and the square of temperature increase and as temperature and the square of  $C_{CO_2}$  decrease but interaction of temperature and  $C_{CO_2}$  also affect the adsorption inversely. Figure 3-10b shows the three-dimensional surface response plot for  $CO_2$  adsorption capacity of steam activated carbon as well as the effect of temperature and  $C_{CO_2}$  on  $CO_2$  adsorption capacity.

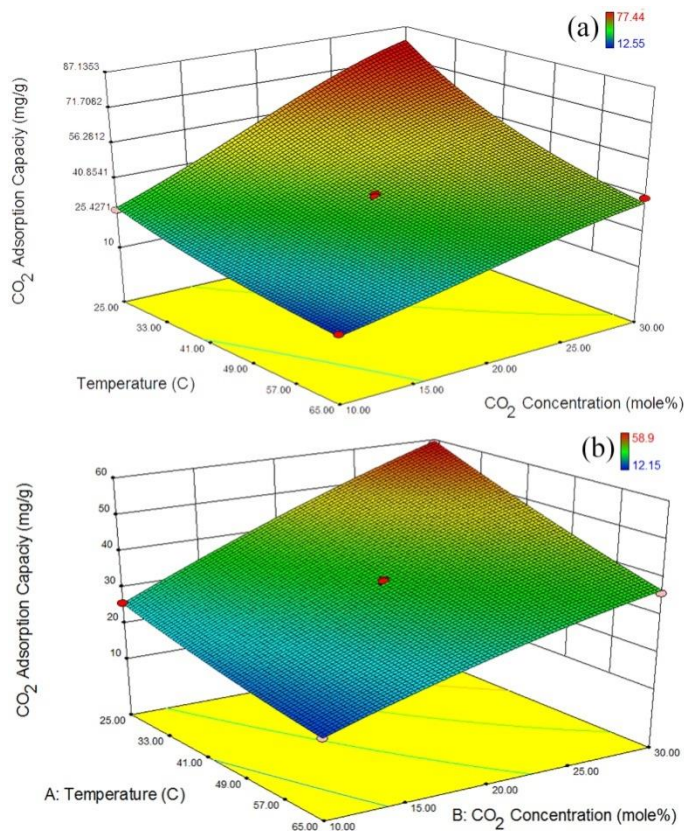


Figure 3-10: Response surface plot of CO<sub>2</sub> adsorption capacity of (a) KOH activated carbon and (b) steam activated carbons

### 3.3.3 Cyclic CO<sub>2</sub> adsorption

The CO<sub>2</sub> adsorption performance of KOH activated carbon, CO<sub>2</sub> activated carbon and steam activated carbon in 50 cycles is presented in Figure 3-11. The adsorption index (%) in this figure is the ratio of the adsorption capacity of the regenerated adsorbent and the fresh adsorbent<sup>118</sup>. As can be seen in Figure 3-11, chemical and CO<sub>2</sub> activated carbons can be fully regenerated and used in 50 cycles but adsorption capacity of the steam activated carbon starts decreasing after about 20 cycles, suggesting that steam activated carbon is not a favorable adsorbent for multi-cyclic CO<sub>2</sub> adsorption.

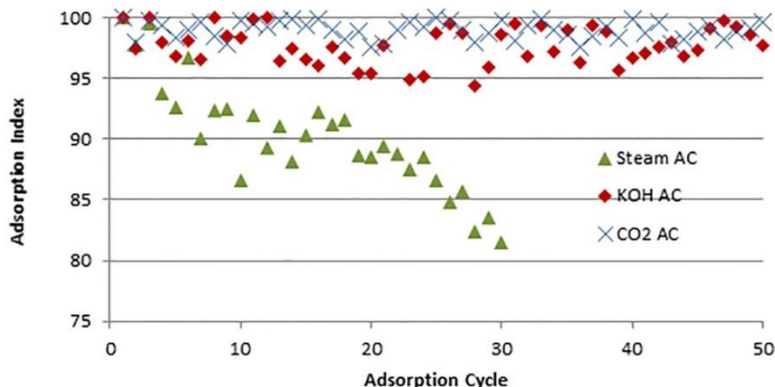


Figure 3-11: Cyclic CO<sub>2</sub> adsorption performed at 25 °C using steam, CO<sub>2</sub> and KOH activated carbons in 30 mol.% CO<sub>2</sub> in He

### 3.4 Conclusions

The CO<sub>2</sub> adsorption performances of KOH, CO<sub>2</sub> and steam activated carbons are tested under different temperatures and CO<sub>2</sub> concentrations. Adsorption results demonstrate that, in this range of parameters, the adsorption behavior of activated carbon can be mainly influenced by porosity of the adsorbent. Steam activated carbon and CO<sub>2</sub> activated carbon with the close range of surface area, the total porosity, micro porosity and similar surface chemistry present the same adsorption behavior, indicating the fact that activating agent is not a significant factor on performance of activated carbon for CO<sub>2</sub> capture under these operating conditions. Overall, KOH activated carbon with higher surface area and porosity can be considered as the best option for CO<sub>2</sub> capture at atmospheric pressure and low temperature of CO<sub>2</sub>. It has been shown that the KOH activated carbon does not offer any advantages at higher temperature. The optimum adsorption capacity was achieved at 30% C<sub>CO<sub>2</sub></sub>, 25°C. Moreover, all adsorbents were tested for durability and both CO<sub>2</sub> and KOH activated carbons remain active in a temperature swing process for at least 50 cycles and KOH activated carbon adsorbs more CO<sub>2</sub> under the same conditions. In this range of parameters, C<sub>CO<sub>2</sub></sub> is also found to be the most significant factor in the adsorption process.

## **Chapter 4 Evaluation of the Effects of Precursors and Pyrolysis Process on Adoption Capacity and Selectivity of Activated Carbons for CO<sub>2</sub> Capture**

A similar version of this chapter has been published in the journal of Energy & Fuels

- *Shahkarami, S.; Dalai, A. K.; Soltan, J.; Hu, Y.; Wang, D. Selective CO<sub>2</sub> Capture by Activated Carbons: Evaluation of the Effects of Precursors and Pyrolysis Process. Energy & Fuels 2015, 29, 7433-7440.*

In addition, some parts of this chapter were presented at the following conferences and symposiums:

- Enhanced CO<sub>2</sub> Adsorption on Activated Carbon, 66<sup>th</sup> Canadian Chemical Engineering Conference, Quebec city, QC, October 16-19, 2016
- Selective CO<sub>2</sub> Adsorption on Activated Carbons, 24<sup>th</sup> Canadian Symposium on Catalysis Ottawa, ON, Canada, May 8-11 2016.
- CO<sub>2</sub> Capture on Bio-based Activated Carbons, Biorefinery I- Chemicals and Materials from thermo Chemical Biomass, Chania, Greece, September 27-October 2, 2015.
- Selective CO<sub>2</sub> Capture on Activated Carbon, 3<sup>rd</sup> Post Combustion Capture Conference and SaskPower Symposium, Regina, Canada, 8-11 September 2015
- Development of Activated Carbon Adsorbents for CO<sub>2</sub> Capture, 64<sup>rd</sup> Canadian Chemical Engineering Conference, Niagara Falls, ON, Canada, October 19-22, 2014.

Contribution of the Ph.D. candidate

In consultation with supervisors, the bench-scale adsorption set-up redesigned, installed and calibrated by Sepideh Shahkarami. All the slow pyrolysis-derived biochar samples and all the activated carbon samples were prepared by Sepideh Shahkarami. All the experiments were planned and conducted by Sepideh Shahkarami. With exception of the NEXAFS measurements, all the sample characterizations were performed and the related data were analyzed by Sepideh Shahkarami. NEXAFS measurements were carried out by Dr. Dongniu Wang at the Canadian Light Source (Saskatoon, Canada). The data analyses and interpretations were conducted by

Sepideh Shahkarami. All of the written text was prepared by Sepideh Shahkarami and all the experiments were discussed with Drs. Y. Hu, A.K. Dalai and J. Soltan.

Contribution of this chapter to the overall study

In Chapter 4, the importance of the biomass and pyrolysis techniques was discussed. The nature of the precursors and carbonization methods are also important factors in porosity and formation of the surface functional groups on the surface of the produced activated carbons. To develop an activated carbon adsorbent with tailored properties, the effects of the precursor and carbonization techniques on CO<sub>2</sub> adsorption capacity and selectivity of activated carbons were studied. In this chapter, the impacts of the selected biomass (precursors) and pyrolysis conditions (fast and slow pyrolysis) on the textural properties and surface chemistry of the prepared activated carbon samples are discussed and the performances of the samples in CO<sub>2</sub>/N<sub>2</sub> and CO<sub>2</sub>/O<sub>2</sub>/N<sub>2</sub> feed stream is evaluated.

### **Abstract**

Activated carbons were produced from different Canadian waste biomasses including agricultural waste (wheat straw and flax straw), forest residue (saw dust and willow ring) and animal manure (poultry litter). The precursors were carbonized through the fast and slow pyrolysis processes and then activated with potassium hydroxide. A fixed-bed reactor was used for temperature swing adsorption of CO<sub>2</sub> in a gas mixture of N<sub>2</sub>, O<sub>2</sub> and CO<sub>2</sub> to study the cyclic CO<sub>2</sub> adsorption capacity and selectivity of the produced activated carbons. The breakthrough adsorption capacity of the produced activated carbon was measured under a flue gas condition of 15 mol% of CO<sub>2</sub>, 5 mol% of O<sub>2</sub> and 80% of N<sub>2</sub> at 25 °C and atmospheric pressure. Slow pyrolysis based activated carbon has lower surface area and total pore volume but higher adsorption capacity in the presence of N<sub>2</sub>. Saw dust based activated carbon synthesized using slow pyrolysis process creates the highest ultramicropores volume of 0.36 cm<sup>3</sup>/g; and the highest adsorption capacity in N<sub>2</sub> (78.1 mg/g) but low selectivity (2.8) over O<sub>2</sub> because of the oxygen functional groups on the surface. Ultra micropores and surface chemistry of adsorbents are far more important than particle size, total pore volume and internal surface area of the adsorbents. All the samples fully recovered their initial adsorption capacity in each cycle ( for up to

ten cycles). This work also demonstrated that adsorption capacity and selectivity of activated carbon can be controlled and optimized through choice of starting material and carbonization conditions.

#### 4.1 Introduction

Activated carbon (AC) is one of the oldest and well known adsorbents that present a large surface area and high degree of porosity and it has been used for different pollutant removals. However, this material has proven to show a significant decrease in its CO<sub>2</sub> adsorption capacity at low partial pressure of CO<sub>2</sub> in flue gas and in the presence of other components. The flue gas of a coal-fired power plant usually contains 14%-15% of CO<sub>2</sub> which is balanced with N<sub>2</sub>, O<sub>2</sub> and other minor components such as CO, SO<sub>2</sub>, SO<sub>3</sub> and NO<sub>x</sub><sup>26,119</sup>. In this work, the CO<sub>2</sub> capture capacity, the breakthrough time and selectivity of the adsorbents for CO<sub>2</sub> separation in a CO<sub>2</sub>/O<sub>2</sub>/N<sub>2</sub> gas mixture of constant composition (15/5/80 mol %) was studied and compared using a fixed-bed reactor at 25 °C and 1 atmosphere.

The activated carbon preparation involves two steps of carbonization and activation<sup>68</sup>. Carbonization is a high temperature process under inert atmosphere, which leads to elimination of most non-carbon elements. The product of carbonization, char, is then activated with an activating agent, mostly steam, CO<sub>2</sub>, KOH or H<sub>3</sub>PO<sub>4</sub><sup>120</sup> to develop a porous structure with large internal surface area. The heteroatoms in the produced activated carbon structure are resulted from the precursors or are associated with carbon atom during the process of carbonization and activation. The comparison of biochars derived from different sources<sup>12</sup> indicated that the precursors and the combustion techniques affect the chemistry of the produced biochar. Therefore, the preparation of activated carbons from different starting materials, carbonization conditions, activating agents and activating conditions can affect both physical and chemical characteristics of the final product which affect adsorption behavior of these adsorbents<sup>54,121</sup>. However, the simultaneous effect of carbonization techniques and precursors on CO<sub>2</sub> adsorption behavior of activated carbon in simulated flue gas conditions has not been reported yet. The main purpose of this research was to study the effect of nature of precursors and carbonization process on physical and chemical properties of activated carbon and influence of these factors on CO<sub>2</sub> adsorption capacity, selectivity and stability of the produced activated carbon in multi-cycle

adsorption process. In the present work, three types of abundant feedstocks were used: forest residue, agricultural residue and animal manure. The selected precursors were carbonized using both fast and slow pyrolysis processes and were converted to KOH activated carbon. The physical and chemical properties of the produced activated carbon were determined by measuring BET surface area, total and micro pore volume, particle size distribution, elemental analysis, scanning electron microscope (SEM) analysis and near edge X-ray absorption fine structure spectroscopy (NEXAFS).

## 4.2 Material and method

### 4.2.1 Biomass

Three different types of waste biomass (collected in Saskatchewan, Canada) were used as precursors in this study. Pinewood saw dust (SD) and willow ring (WR) as the forest residues, wheat straw (WS) and flax straw (FS) as the agricultural residues and poultry litter (PL) as the animal manure were carbonized through fast and slow pyrolysis process. The physical and chemical properties of the flax straw, wheat straw, saw dust and poultry litter are presented elsewhere<sup>122</sup>. The ash content, moisture content, volatile material and fixed carbon of willow ring is provided in the Appendix D.

### 4.2.2 Fast pyrolysis

Fast pyrolysis of the precursors was carried out at the Saskatchewan Research Council (Saskatoon, Canada) in a mobile pyrolysis unit made by ABRI Tech Inc. (QC, Canada) at 475°C under atmospheric condition. Steel beads were used as heat carrier without any fluidizing gas. The residence time of vapor and produced char are 1 s and 15 min, respectively. The separation of char from steel beads was based on density difference. Details of the experimental set-up and properties of the produced chars are presented elsewhere<sup>122</sup>.

### 4.2.3 Slow pyrolysis

Slow pyrolysis of the biomass was performed in a one inch diameter fixed-bed Inconel tubular reactor under N<sub>2</sub> flow of 100 standard milliliter per minute (SmL/min) at 500 °C. The bed heating was provided using a vertical furnace and a temperature controller (Eurotherm 2416). In

each batch, 10 g of biomass was loaded in the reactor and heated to 500 °C with a heating rate of 7 °C/min. N<sub>2</sub> flow rate was controlled by a mass-flow controller (Brooks Instrument 5850S/B) at 100 ml/min. Temperature calibration of furnace is provided in Appendix D.

#### 4.2.4 KOH activated carbon

10 g of produced biochar was impregnated with KOH as described in section 3.2.3 (chemical activated carbon). The produced activated carbons are denoted as follows: SD= saw dust, PL=poultry litter, WR=willow ring, WS=wheat straw, FS= flax straw, SP= slow pyrolysis and FP=fast pyrolysis. For example, activated carbon prepared from fast pyrolysis of saw dust is denoted as SD-FP AC. Figure 4-2 shows the yields of activation process. The yield of activation process is defined as the mass ratio of activated carbon to the biochar on a scale of 100<sup>59</sup>.

#### 4.2.5 Characterization

Elemental analysis, ash content, BET surface area, pore size distribution and total pore volume

The elemental, ash content, BET surface area, total pore volume and pore size distribution of the activated carbons were determined as described in section 3.2.4.

Particle size analysis

Particle size distribution (PSD) of the samples was determined using a laser diffraction particle size distribution analyzer (Malvern instruments Ltd., Malvern, UK). laser diffraction depends on the relationship between particle size, the angle and intensity of scattered beam. In this machine, intensity of light scattered at different angles are measured as a laser beam passes through the sample. Intensity of the scattered beam is inversely related to the particle size. Mie Scattering Theory is used to convert scattered light intensity and scattering angle into particle size information.

## Scanning Electron Microscope (SEM)

The morphology and pore structure of produced activated carbons are examined by means of a field emission scanning electron microscope (SU8010, Hitachi, Japan). Scanning is performed at magnification range of 1500 to 150,000.

## C 1s Near Edge X-Ray Absorption Fine Structure Spectroscopy (NEXAFS)

NEXAFS is a powerful and element-specific technique which can give a better understanding of the chemical characteristics of activated carbon. Total electron yield (TEY) method was used as the detection method to collect the sample drain current ( $I$ ) and normalize it by recording the beam current from a gold mesh ( $I_0$ ). The powder sample was grounded and mounted on a carbon free indium foil. The High Resolution Spherical Grating Monochromator (SGM) beamline was configured for a resolving power of ca. 7500 at the C K edge (exit slit gap 50  $\mu\text{m}$ ) and the photon energy was scanned from 270 to 310 eV<sup>123</sup>. C K-edge (1s) NEXAFS spectra were obtained on the SGM beamline 11ID-1 at the Canadian Light Source (Saskatoon, Canada). The details of sample measurements are described elsewhere<sup>124</sup>.

### 4.2.6 Breakthrough CO<sub>2</sub> adsorption measurements

All the experimental breakthrough curves were obtained by passing the gas mixture through the one-inch fixed-bed Inconel tubular reactor. Chemical analysis was conducted using a dual channel micro-gas chromatograph (490 micro-GC, Agilent Technologies Inc., USA) equipped with a micro-thermal conductivity detector ( $\mu\text{TCD}$ ). The inlet flow rates, outlet flow rates and CO<sub>2</sub>/N<sub>2</sub>/O<sub>2</sub> mole fractions are measured using mass flow controllers, flow meter and micro-GC, respectively, for breakthrough adsorption. All the breakthrough experiments were repeated twice, and the average values were reported. Argon and helium are used as carrier gases in the dual channel micro-gas, respectively. Channel one column separates and measures nitrogen and oxygen while channel two column separates and analyzes carbon dioxide. The TCD is calibrated using mixtures of known composition. The GC calibration data is provided in Appendix D. schematics of experimental set-up is shown in Figure 4-1 and related calibration data are provided in Appendix D. The adsorption measurements involve two steps of measuring the CO<sub>2</sub> adsorption capacity in a N<sub>2</sub>/CO<sub>2</sub> (85/15 mol %) feed stream and then measuring the CO<sub>2</sub>

adsorption capacity and selectivity of CO<sub>2</sub> in N<sub>2</sub>/CO<sub>2</sub>/O<sub>2</sub> feed stream (80/15/5 mol %). The reactor is loaded with 1.5 g of activated carbon and pre-heated at 160 °C for 2 h under N<sub>2</sub> before the adsorption experiments. After cooling down to 25 °C, the feed gas is passed through the reactor. The total feed flow rate in both steps is held constant at 50 SmL/min. The adsorption process is continued until saturation where the outlet concentration of CO<sub>2</sub> reaches the inlet concentration of CO<sub>2</sub>. Adsorption capacity and selectivity were calculated as described in section 2.3.1.

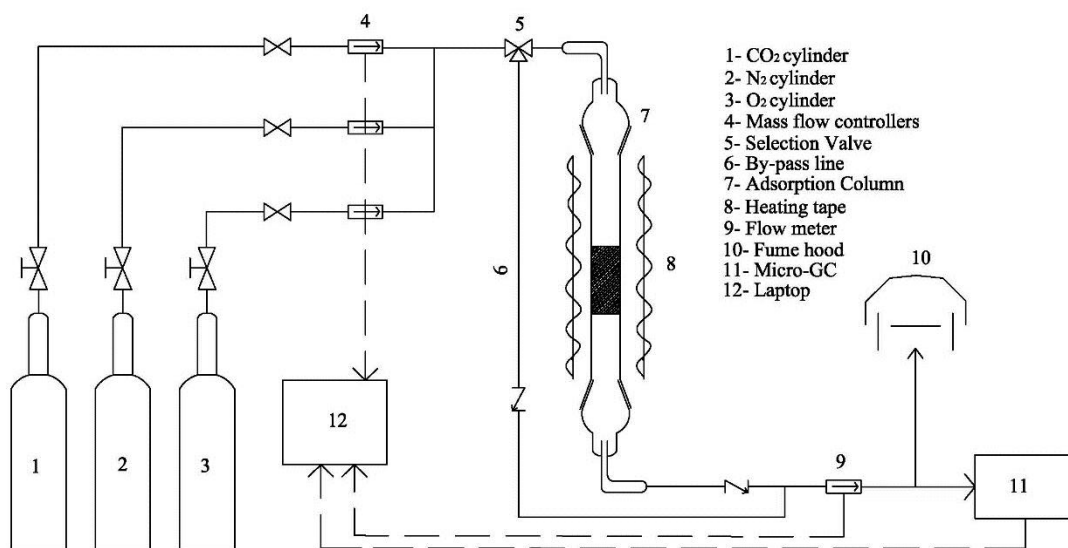


Figure 4-1: Schematic diagram of the adsorption set-up

Multi-cycles adsorption/desorption are studied for the adsorbents to examine their durability using a temperature swing adsorption (TSA) cyclic process. For desorption, when the adsorbent is saturated, gas flow is switched from feed gas to N<sub>2</sub> flow and temperature is raised to 160 °C for 2 h. The adsorbents are subjected to 10 continuous adsorption–desorption cycles and their performance are compared.

### 4.3 Results and discussions

#### 4.3.1 Characterization of adsorbents

Figure 4-2 illustrates the effects of carbonization techniques on the yield of the produced activated carbon for each of the precursors. It is evident that slow pyrolysis generally results in

higher activation yields. The higher pyrolysis and activation yields of the slow pyrolysis products can be attributed to the secondary coking and re-polymerization reactions due to the longer vapor–solid residence time and low heating rate in the slow pyrolysis process<sup>125</sup>. The yields of poultry litter based AC obtained through both fast and slow pyrolysis process were found to be significantly lower than others.

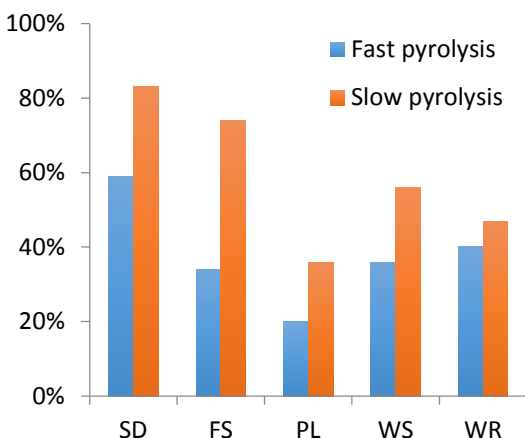


Figure 4-2: Yield of saw dust, flax straw, poultry litter, wheat straw and willow ring based activated carbons

The particle size distributions of the produced activated carbons from the precursors in both slow and fast pyrolysis are shown in Figure 4-3. Samples derived from saw dust comprise smaller particles than samples derived from other precursors. As it can be observed in Figure 4-3, the FP based ACs are generally finer. In FP based ACs, SD-FP AC is the finest produced sample followed by FS-FP AC; and WR-FP AC is the largest produced sample. In SP based ACs, SD-SP AC has the finest particle size distribution followed by WR-SP AC and FS-SP AC, and PL-SP AC has the largest particle size.

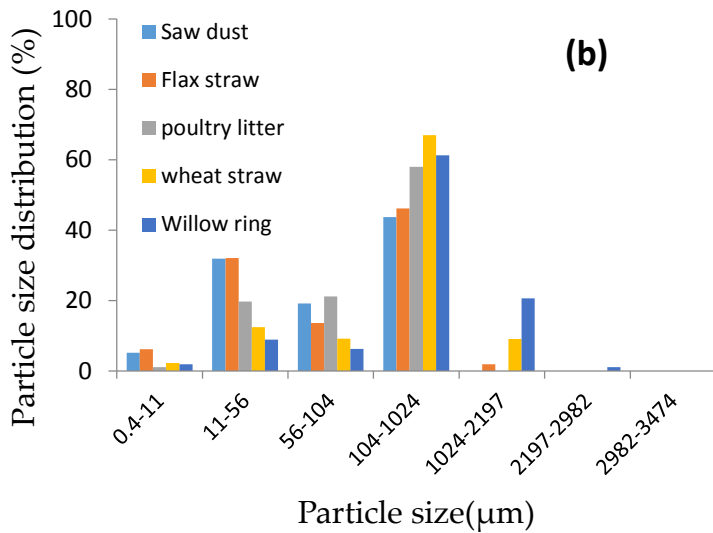
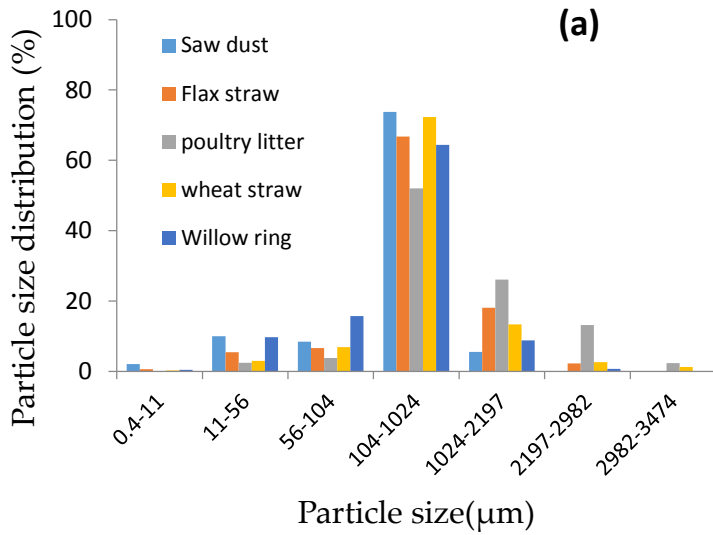


Figure 4-3: Particle size distribution of (a) slow pyrolysis based and (b) fast pyrolysis based activated carbons

The SEM images of the biochar and activated carbon are shown in Figure 4-4. As it can be observed in Figure 4-4, there are significant differences in the surface morphology of the produced activated carbon samples. PL-FP AC has a uniform and highly porous honey-comb structure. FS-FP and WS-FP ACs also exhibit a well pronounced array of honey-comb structures, indicating higher possibility of gas trap. Although the honey-comb structure cannot be seen at 12k resolution in SD-FP AC, a fully developed array of honey-comb structures is

observed at 150k (Figure 4-4k). The SEM images of SP based ACs had an irregular and porous surface. It demonstrates that there are small cavities and attached fine particles on the SP activated carbon surface.

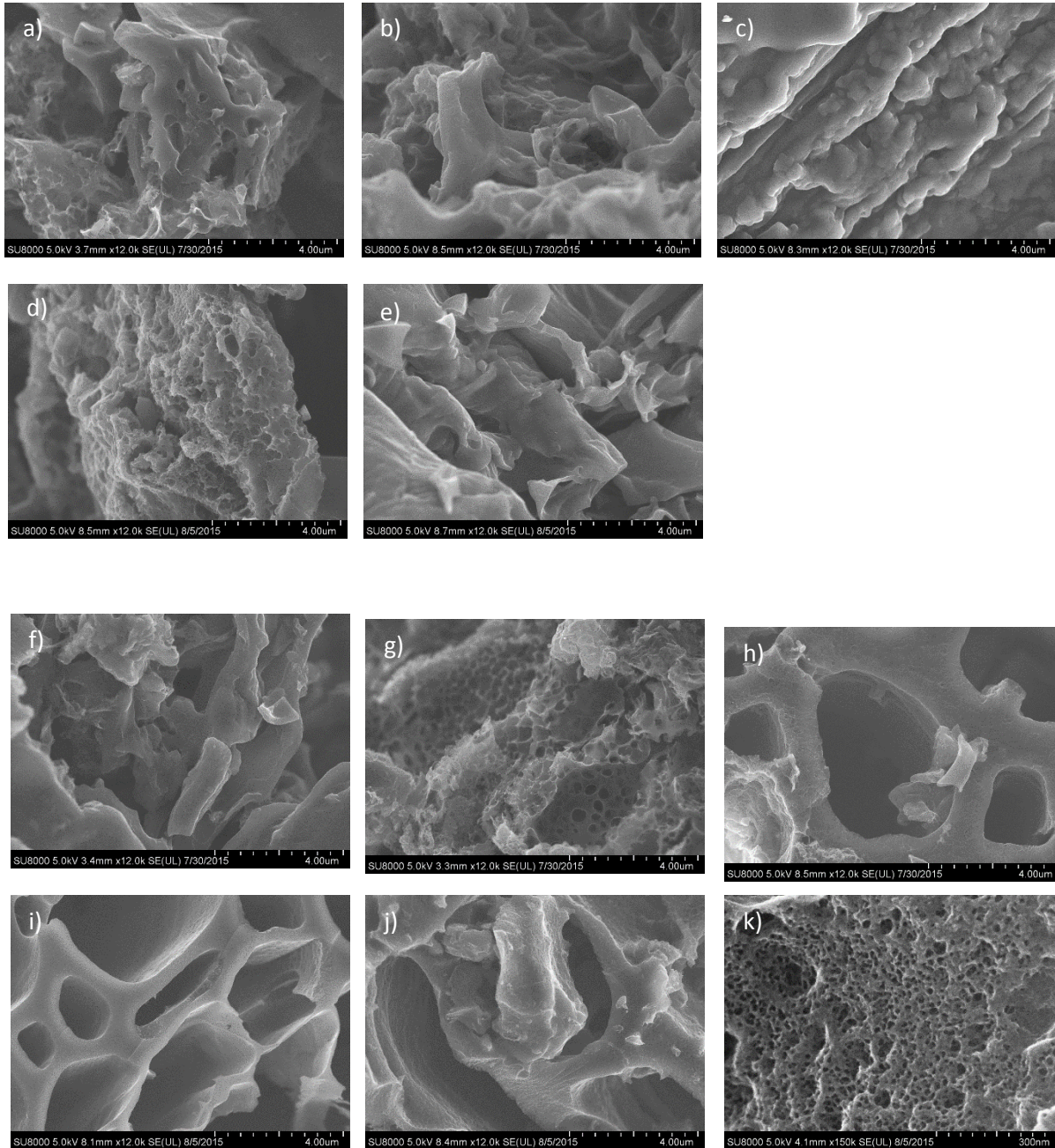


Figure 4-4: SEM images of a) willow ring-slow pyrolysis, b) poultry litter- slow pyrolysis, c) flax straw-slow pyrolysis, d) wheat straw- slow pyrolysis, e) saw dust- slow pyrolysis, f) willow ring-fast pyrolysis, g) poultry litter- fast pyrolysis, h) flax straw- fast pyrolysis, i) wheat straw- fast pyrolysis, j) saw dust- fast pyrolysis activated carbon (12K magnification) and k) SD-FP activated carbon (150K magnification)

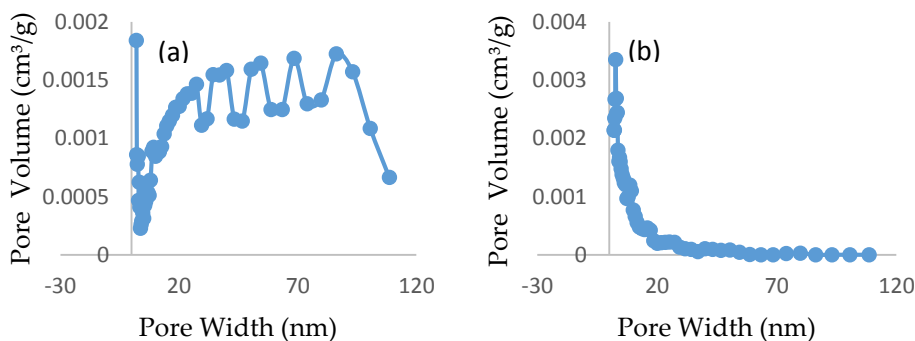
The characteristics of activated carbon samples are presented in Table 4-1. The reported elemental analysis is on dry ash-free basis. Ash in the activated carbons is the inorganic residuals of the precursors. Ash contents of the PL-FP and PL-SP ACs are 1.12% and 0.54%, respectively, which are much lower than those of biochar samples<sup>122</sup>. The small amount of ash content and low activation yield of PL based AC suggest that most of the ash content is eliminated through the acid treatment process<sup>110</sup> which results in production of fine powders with high carbon content and extended surface area.

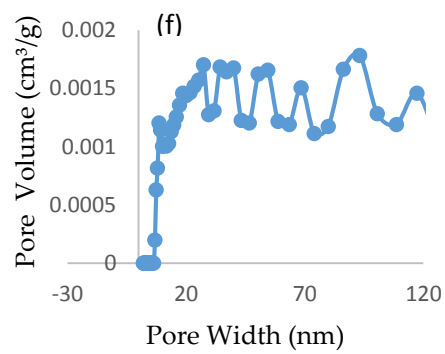
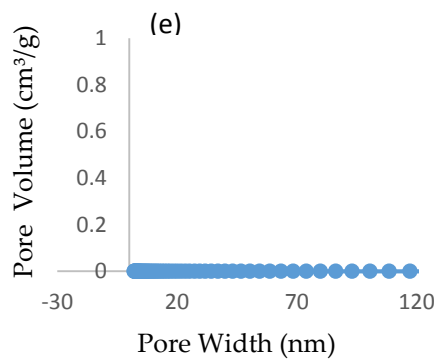
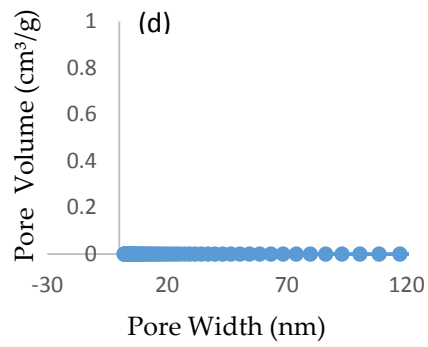
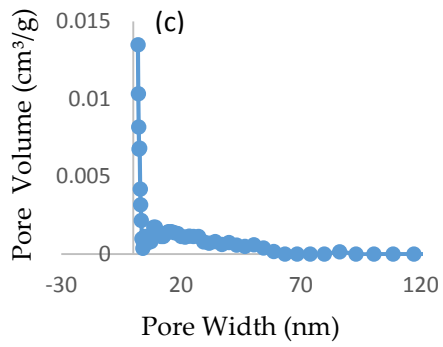
Table 4-1: Elemental analysis and physical properties of produced activated carbons

	Fast Pyrolysis					Slow Pyrolysis				
	SD-FP	FS-FP	PL-FP	WS-FP	WR-FP	SD-SP	FS-SP	PL-SP	WS-SP	WR-SP
N, wt%	0.43	1.43	0.90	0.58	0.48	0.20	0.44	0.58	0.30	0.44
C, wt%	89.58	85.54	86.46	84.13	86.21	88.13	85.37	90.52	82.59	84.89
S, wt%	0.02	0.03	0.13	0.04	0.10	0.03	0.15	0.04	0.04	0.02
H, wt%	2.33	2.63	2.61	2.55	2.25	2.74	3.61	2.25	3.16	2.69
O, wt% (by difference)	7.64	10.37	9.90	12.70	10.96	8.91	10.42	6.61	13.90	11.96
Ash content, wt%	0.79	1.21	1.12	2.37	2.52	0.72	0.84	0.54	4.86	2.49
BET, m <sup>2</sup> /g	1501	1660	2889	1462	1602	1268	1281	1879	1212	1563
Ultra Micropore volume, cm <sup>3</sup> /g	0.224	0.151	0.101	0.149	0.192	0.360	0.252	0.063	0.243	0.313
Micropore volume, cm <sup>3</sup> /g	0.527	0.577	1.017	0.476	0.589	0.430	0.453	0.616	0.406	0.574
Mesopore volume cm <sup>3</sup> /g	0.044	0.038	0.162	0.044	0.038	0.000	0.000	0.046	0.042	0.034

Macropore	0.009	0.00	0.035	0.091	0.014	0.00	0.00	0.03	0.00	0.01
volume cm <sup>3</sup> /g		1				0	0	2	0	7
Total pore		0.83				0.43	0.45	0.69	0.44	0.62
volume, cm <sup>3</sup> /g	0.580	7	1.214	0.612	0.641	0	3	4	8	5

Elemental analysis results show that fast pyrolysis followed by KOH activation, compared to slow pyrolysis process, results in an increase in nitrogen content and decrease in hydrogen content of the produced activated carbons. The types of the precursor and pyrolysis conditions also influence surface areas and porosity characteristics of the produced activated carbons. The pore size distributions of the produced activated carbon are provided in Figures 4-5 and 4-6. The activated carbons produced through fast pyrolysis have larger surface area, total pore volume and total micropore volume while the contribution of ultra-micropores is lower in these samples. Moreover, the contribution of mesopores in FP based AC is more significant. In both cases, PL based AC shows the largest surface area, largest total pore volume and smallest ultra-micropores volume.





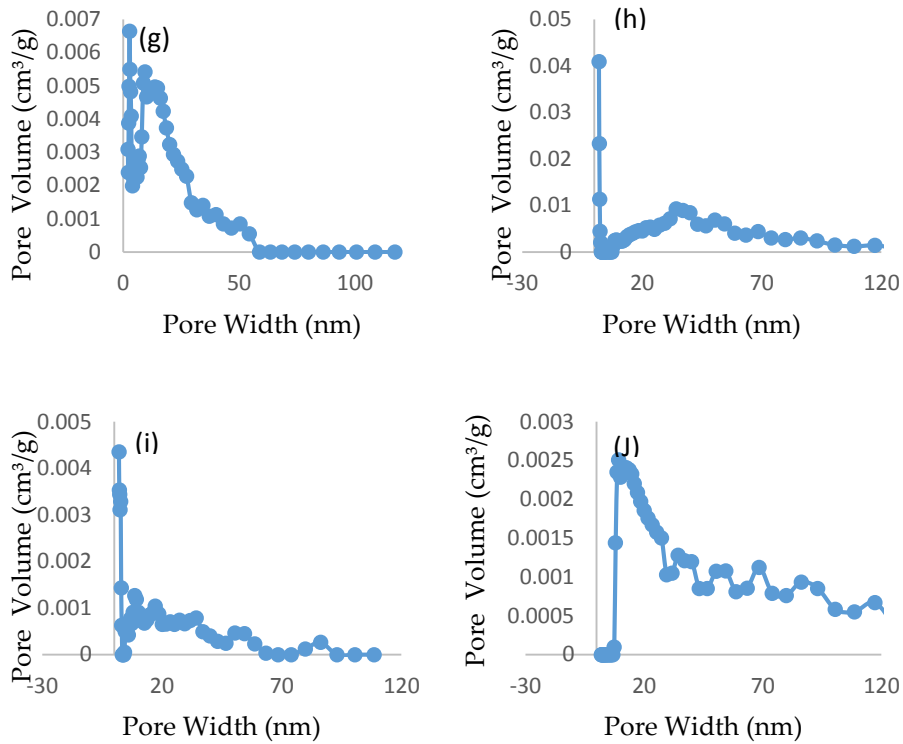
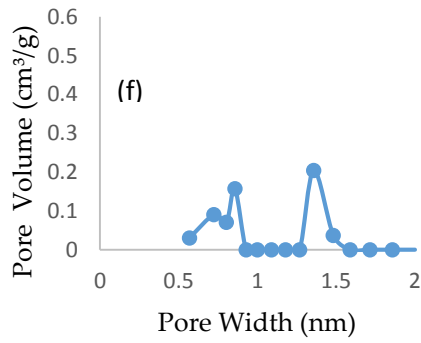
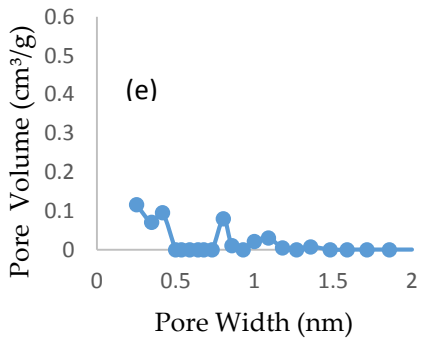
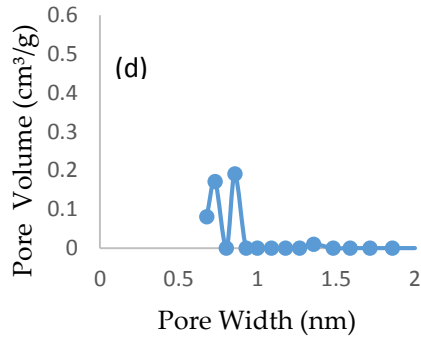
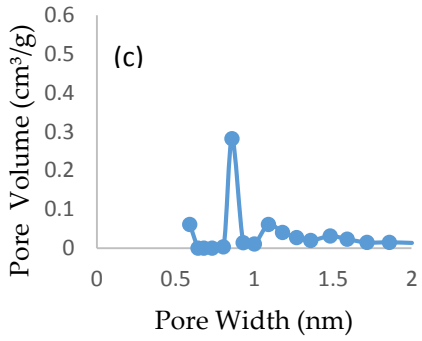
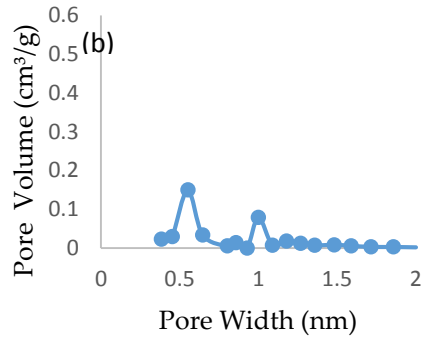
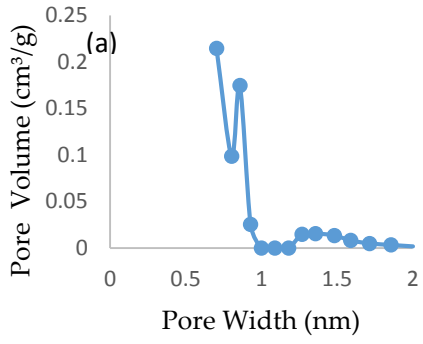


Figure 4-5: Incremental mesopore and macropore volume of (a) WR-SP, (b) WS-SP, (c) PL-SP, (d) FS-SP, (e) SD-SP, (f) WR-FP, (g) WS-FP, (h) PL-FP, (i) FS-FP and (j) SD-FP



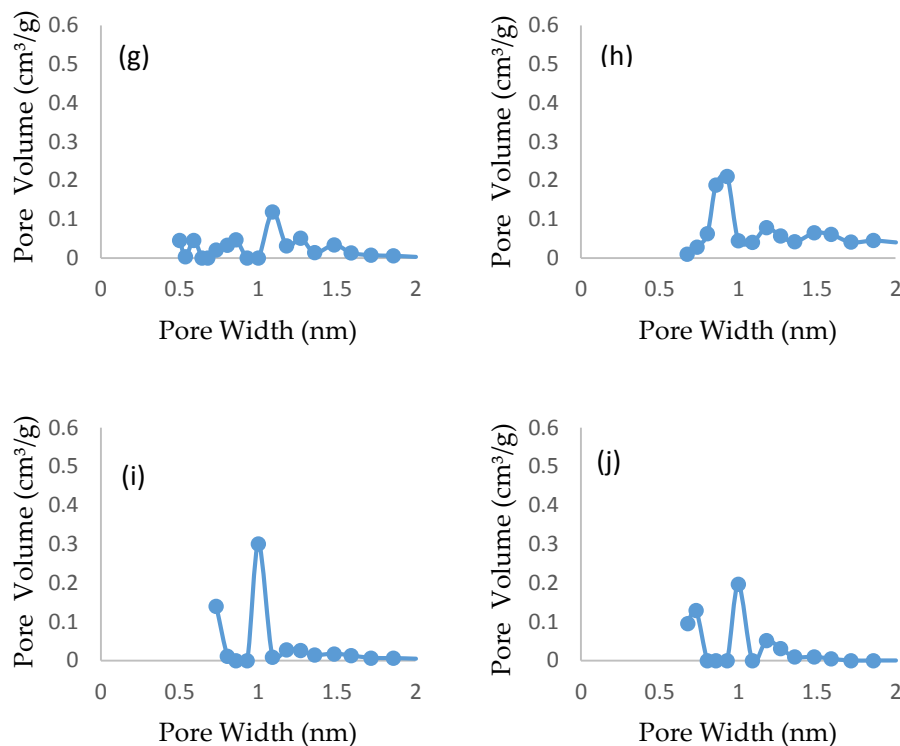


Figure 4-6: Incremental micropore volume of (a) WR-SP, (b) WS-SP, (c) PL-SP, (d) FS-SP, (e) SD-SP, (f) WR-FP, (g) WS-FP, (h) PL-FP, (i) FS-FP and (j) SD-FP

The C K-edge NEXAFS spectra of SP based ACs are compared in Figure 4-7(a). Three region are common in the C K-edge spectra appearing at 285 eV (C=C), 288 (C/O) and 292 eV ( $\delta^*$ ). In all the samples, two  $C1s \rightarrow \pi^*$  transitions near 285.4 eV and 288.4 eV are dominant. However, the aromaticity is the main feature of the spectra exhibiting as an asymmetric peak transition near 285.4 eV in all the spectra of the SP based ACs with the exception of SD-SP AC. This peak is correlated with  $C1s - \pi^*$  transition of aromatic (C-R) or double-bonded alkyl carbon (C=C)<sup>123,126</sup>. The symmetry and broad of this peak suggest multiple resonance<sup>123</sup> in this region. The small shoulder near 284.5 eV is attributed to the  $C1s - \pi^*$  transition of unsaturated C=C<sup>127,128</sup> which is more notable in FS-SP and WR-SP ACs. In SD-SP AC, the intensity of 285.2 eV peak is remarkably smaller followed by a broad shoulder at 287.2 eV and a sharp peak at 288.4 eV (Figure 4-7 (a)). The  $C1s \rightarrow \pi_{C=O}^*$  transition at 288.4 eV represents unsaturated carboxylic carbon<sup>123,129,130</sup>. This distinct peak at 288.4 eV also indicates that SD-SP AC has considerably

more C = O  $\pi^*$  bonds in its structure compared to other SP based ACs. The broad shoulder centered at 287.2 eV reveals overlapping bonds in this region that present different functional groups on the surface. This transition corresponds to C-O bond and the aromatic carbons with oxygen substitute including phenolic, ether or a ketone groups<sup>123,129,131,132</sup>. In addition, the spectrum of PL-SP AC exhibits a shoulder at 285.8 eV. The shoulder near 284.3 eV is inconspicuous. However, an additional shoulder appeared as a peak at 285.74 eV. Since the change in the polarization of electron cloud in a chemical bond leads to energy shifts in the transition<sup>123</sup>, this shoulder can be correlated to the bonding of a substituent to the benzene ring results<sup>133,134</sup>. The intensity of the transition at 288.4 eV is also much weaker in PL-SP AC reflecting the lower carboxyl content in this sample. Finally, the spectra of FS-SP, WR-SP and WS-SP ACs are very similar. However, the peak intensities at 285.42eV and 288.4eV in FS-SP spectrum are considerably smaller due to the fewer C = C  $\pi^*$  and C = O  $\pi^*$  bonds in FS-SP AC, respectively<sup>126</sup>. The spectra of WS-SP AC revealed a peak centered at 287.1 eV reflecting a small portion of phenolic, ether or ketone groups in its structure. The peak near 289.5 eV is also observed in all the spectra reflecting the transition O-substituted alkyl carbon groups such as alcohol groups or carbonyl groups<sup>123,129,130</sup>. The SD-SP and PL-SP ACs present unique characteristics in their spectra suggesting differences in the functional groups distributions and surface properties. SD-SP AC exhibits a small portion of aromatic C1s  $\rightarrow \pi_{C=C}^*$  and the largest proportion of C1s  $\rightarrow \pi_{C=O}^*$  transition in its spectra which is similar to that of marine sediments<sup>123</sup> while soot, grass char and wood char<sup>123</sup> exhibit a higher proportion of C = C  $\pi^*$  in their spectra. On the other hand, PL-SP AC spectra reveal a pronounced peak of C1s  $\rightarrow \pi_{C=C}^*$  transition and the carboxylic peak is significantly smaller.

The C K-edge NEXAFS spectra of FP based ACs are shown in Figure 4-7(b). In FP samples, two transitions near 285.4 eV and 288.4 eV are common to all of the FP spectra with the exception of SD-FP AC. The shoulder of unsaturated C near 284.2eV is more distinct in the FP based ACs. SD-FP AC shows a significantly different spectrum from the other fast pyrolysis products, exhibiting a broad and intense peak at 284.4 eV followed by a notable shoulder centered at 285.1 eV. The difference in the aromatic C peak position in the SD-FP AC is attributed to significant presence of unsaturated C in SD-FP AC. Besides, the peak of oxygenated

groups centered at 288.4 eV show a lower intensity as compared to SD-SP AC suggesting smaller amounts of C=O in its structure. The shoulder near 287 eV representing the overlapping bonds in 286-287.9 eV is observed in all the FP samples. However, this shoulder is more distinct in SP-FP and WS-FP ACs. The features of FS-FP and WR-FP AC spectra in particular are similar to PL-FP AC spectrum.

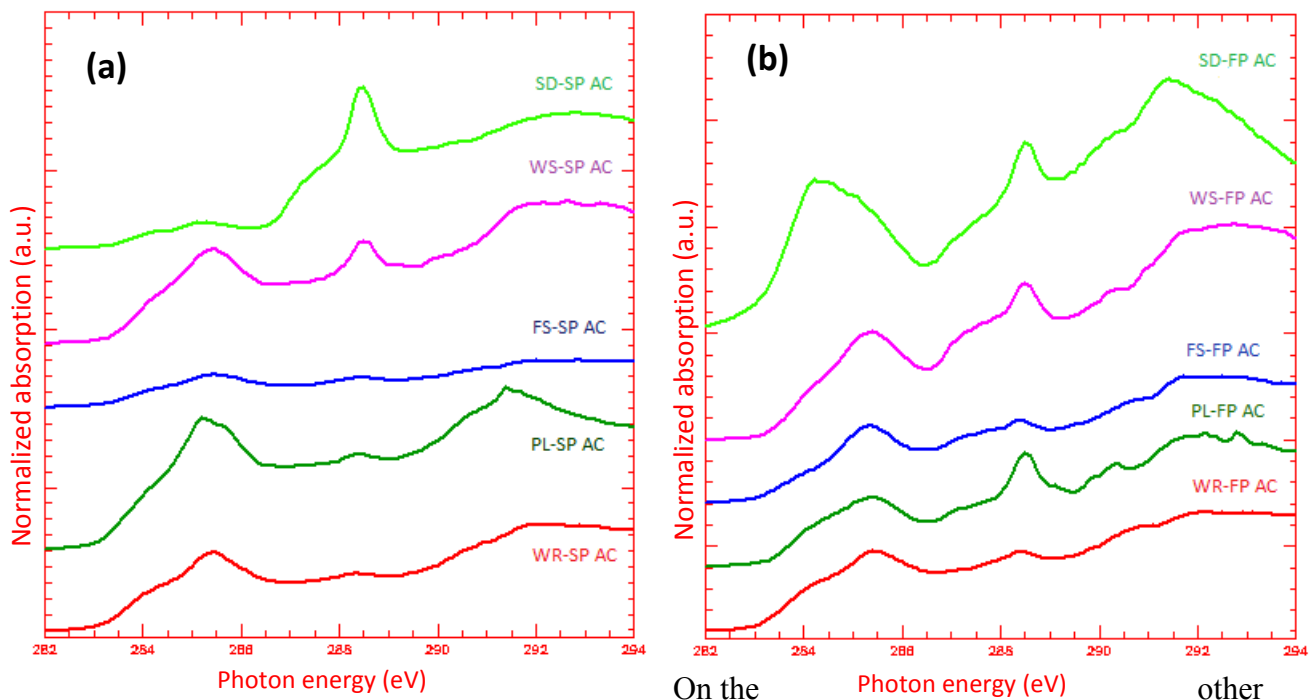


Figure 4-7: C 1s NEXAFS spectra of (a) slow pyrolysis based ACs and (b) fast pyrolysis based ACs

hand, WR-SP and WR-FP ACs reflect the same features in their spectra indicating they have similar surface properties. PL-FP AC exhibits a broad asymmetric peak at 285.3 eV with a shoulder at a lower 284.35 eV. The sharp peak at 288.5 eV reflects a much larger contribution of carboxylic group as compared to PL-SP AC. Although a distinct trend is not observed in these samples, it is obvious that there are significant variations in the degree of oxidation and functional groups in fast and slow pyrolysis. The dominant functional group for a fast pyrolysis product is carboxylic while slow pyrolysis process mostly leads to a highly aromatic structure.

### 4.3.2 Adsorption of CO<sub>2</sub>

The breakthrough curves of CO<sub>2</sub> adsorption and the average results of cyclic breakthrough adsorption measurements in CO<sub>2</sub>/N<sub>2</sub> and CO<sub>2</sub>/O<sub>2</sub>/N<sub>2</sub> gas mixtures are shown in Figure 4-8 and Table 4-2, respectively.

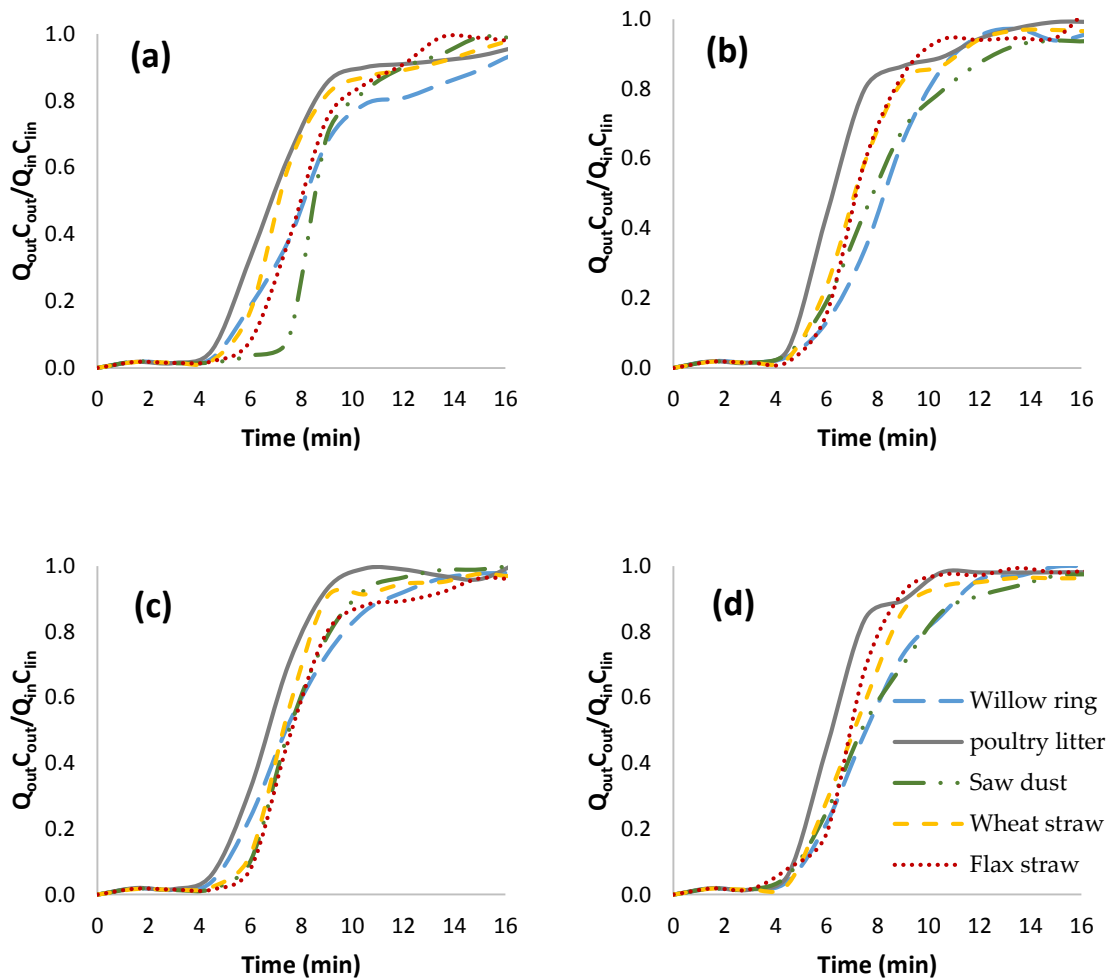


Figure 4-8: Breakthrough curves of ACs in a) slow pyrolysis samples in N<sub>2</sub>/CO<sub>2</sub> feed stream b) fast pyrolysis samples in N<sub>2</sub>/CO<sub>2</sub> feed stream, c) slow pyrolysis samples in N<sub>2</sub>/CO<sub>2</sub>/O<sub>2</sub> feed stream and d) fast pyrolysis samples in N<sub>2</sub>/CO<sub>2</sub>/O<sub>2</sub> feed stream

The experiments include ten consecutive cycles where the adsorbent reached saturation and then was regenerated during the TSA process. All samples adsorbed CO<sub>2</sub> reversibly and regained

more than 90% of their initial adsorption capacity by regeneration. The cyclic CO<sub>2</sub> adsorption performance of the produced activated carbon is presented in Figure 4-9.

The largest breakthrough time and adsorption capacity are found to be 7.5 min and 78.1 mg/g of SD-SP AC, respectively; and the lowest breakthrough time and adsorption capacity are for PL-FP AC (4.5 min, 55.5 mg/g) in the CO<sub>2</sub>/N<sub>2</sub> gas mixture.

Table 4-2: CO<sub>2</sub> adsorption capacities and selectivities of the produced activated carbons from the breakthrough measurements with CO<sub>2</sub>/N<sub>2</sub> and CO<sub>2</sub>/N<sub>2</sub>/O<sub>2</sub> mixtures at 25°C

	Fast Pyrolysis					Slow Pyrolysis				
	<b>SD-FP</b>	<b>FS-FP</b>	<b>PL-FP</b>	<b>WS-FP</b>	<b>WR-FP</b>	<b>SD-SP</b>	<b>FS-SP</b>	<b>PL-SP</b>	<b>WS-SP</b>	<b>WR-SP</b>
Adsorption Capacity in N <sub>2</sub> , mg/g	73.6	66.0	55.5	64.3	70.3	78.1	72.2	61.7	70.8	75.1
Standard Deviation	0.28	0.04	0.85	0.42	0.11	0.42	0.42	0.91	0.28	0.07
Adsorption Capacity in N <sub>2</sub> & O <sub>2</sub> , mg/g	69.5	60.2	54.8	62.7	67.2	65.9	66.5	60.9	70.5	70.1
Standard Deviation.	0.83	0.42	0.63	0.77	0.42	0.28	0.14	0.83	0.98	0.28
Selectivity over O <sub>2</sub>	3.9	2.6	2.1	2.7	2.7	2.8	2.9	2.8	3.5	3.2
Selectivity over N <sub>2</sub>	28.1	22.3	17.4	22.1	25.8	29.3	27.9	22.0	26.0	28.6

This steep curve results in maximizing adsorbent capacity at the breakpoint. As shown in Table 4-2, in spite of their smaller surface area and smaller pore volume, SP based ACs have larger adsorption capacity than the FP based ACs in CO<sub>2</sub>/N<sub>2</sub> feed mainly due to their higher ultra-micropore volume reflecting that the ultra-micropores is a selective factor for CO<sub>2</sub> adsorption in CO<sub>2</sub>/N<sub>2</sub> mixture. Similar results have also been reported before<sup>30,135-137</sup> suggesting that the overlap of potential fields of opposite pore walls enhances the interaction of CO<sub>2</sub> molecules and pore walls in the pore width <1nm<sup>30,138</sup>. These results indicate the important role of ultra-micropores in CO<sub>2</sub> adsorption as compared to surface area and total pore volume. In addition, Liu et al.<sup>20</sup> showed that CO<sub>2</sub> is selectively adsorbed on the adsorbents with oxygen functional groups on their surfaces due to the strong quadrupole moment of CO<sub>2</sub> compared to that of N<sub>2</sub>. In both cases, in CO<sub>2</sub>/N<sub>2</sub> feed stream, SD based ACs present the highest adsorption capacity and selectivity followed by WR-SP AC while PL based ACs exhibit the lowest adsorption capacity. This substantiates the important effect of nature of the precursors on adsorption behavior of activated carbon. When multicomponent adsorbates are contained in the feed, breakthrough behavior becomes more complicated<sup>139</sup>. To study the effects of presence of oxygen in feed stream on adsorption behavior of the samples, the CO<sub>2</sub>/N<sub>2</sub>/O<sub>2</sub> breakthrough curves are compared to CO<sub>2</sub>/N<sub>2</sub> results. Because N<sub>2</sub>, CO<sub>2</sub>, and O<sub>2</sub> have kinetic diameters of 3.64, 3.30, and 3.46 °A<sup>19</sup>, respectively, separation of O<sub>2</sub> and CO<sub>2</sub> is more difficult. Both are nonpolar and have similar kinetic diameters, therefore the adsorbent cannot differentiate CO<sub>2</sub>, and O<sub>2</sub>. In all cases, a reduction of the t<sub>b</sub> and adsorption capacity is observed in the presence of oxygen in feed which suggests that O<sub>2</sub> is a stronger adsorbate<sup>45</sup> than CO<sub>2</sub> to adsorb on activated carbon. This could be caused by the differences in the molecular weight of O<sub>2</sub> and CO<sub>2</sub> which facilitates the O<sub>2</sub> diffusion in the bulk gas. For SP based ACs, the most and least selective CO<sub>2</sub> adsorptions occur on WS-SP and SD-SP AC, respectively. While for FP based ACs, SD-FP and PL-FP are the most and least selective adsorbent which can be attributed to the oxygen functional groups on the surface of adsorbents. SD-SP AC with highest content of oxygen functional groups appeared to be the least selective for CO<sub>2</sub> while SD-FP with a small content of C=O bonds in its structure and a much larger contribution of C=C is highly selective for CO<sub>2</sub> over N<sub>2</sub>. The impact of surface chemistry is obvious by observing the trend of selectivity in Table 4-2 which confirms that although the presence of ultra micropores is the dominant factor for CO<sub>2</sub> adsorption on activated carbon, the oxygen functional groups on the surface can also significantly affect the adsorption

selectivity. The results also show that pyrolysis conditions affect the breakthrough curve of the adsorbents. A comparison between the SD-FP AC and SD-SP AC in Figure 7 shows a sharper breakthrough curve due to the higher mass transfer rate of the SD-SP AC in CO<sub>2</sub>/N<sub>2</sub> mixture. Since molecular diffusivity in a multicomponent mixture is a function of mole fraction of species and molecular weight, the presence of oxygen results in a wider breakthrough curve in CO<sub>2</sub>/O<sub>2</sub>/N<sub>2</sub> mixture<sup>140</sup>.

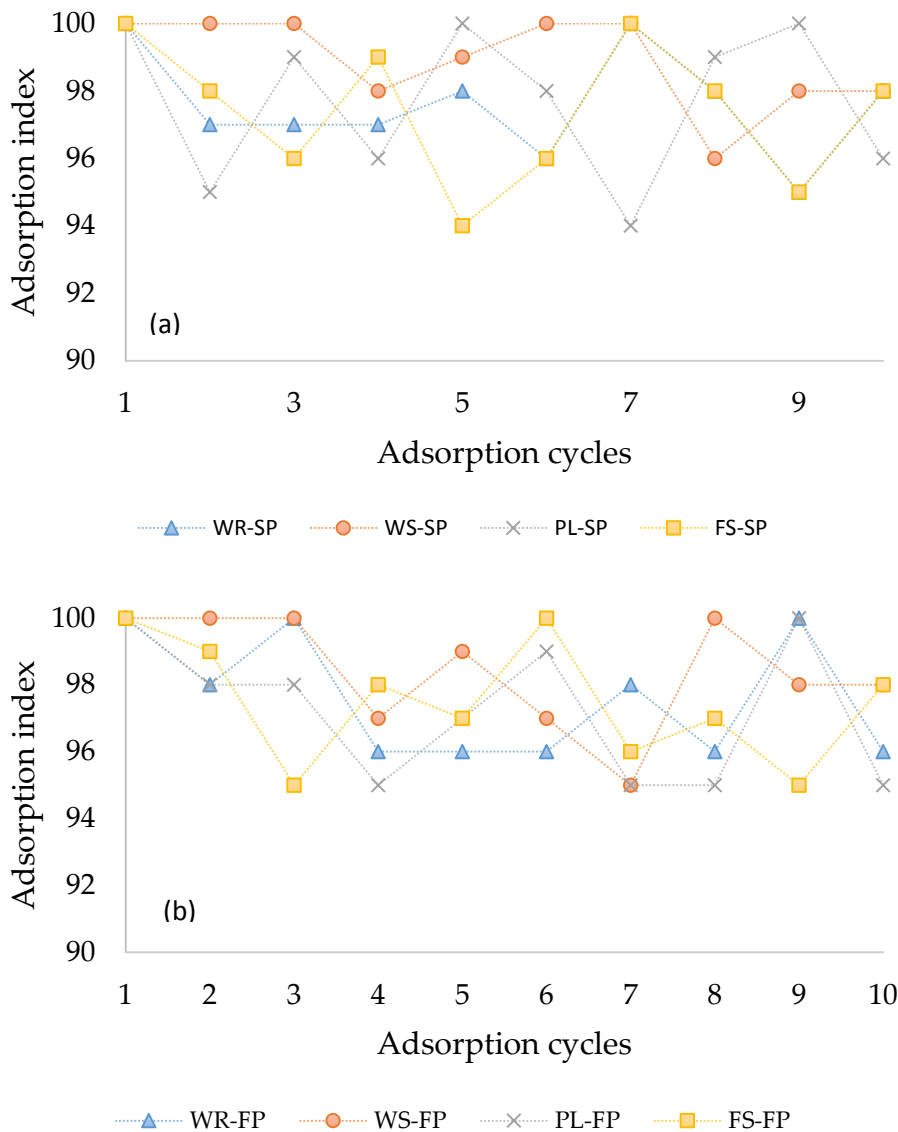


Figure 4-9: The cyclic CO<sub>2</sub> adsorption performance of (a) slow pyrolysis activated carbons and (b) fast pyrolysis activated carbons in CO<sub>2</sub>/N<sub>2</sub>

#### 4.4 Conclusions

The major differences in surface chemistry, porous structure and morphology of activated carbons derived from the fast and slow pyrolysis of different source of biomass are identified. Overall for the same precursor, the fast pyrolysis process leads to larger surface area and total pore volume, smaller particle size and ultra-pore volume, and a larger contribution of phenolic/ketone and carboxylic groups. A slow pyrolysis process leads to formation of extensive aromatic regions with smaller contribution of C=O on the surface. The influence of nature of the precursor, pyrolysis conditions and presence of oxygen are studied in a fixed-bed reactor at 25 °C and atmospheric pressure for N<sub>2</sub>/CO<sub>2</sub>/O<sub>2</sub> feed stream. The presence of ultra micropores is found to be the most important parameter in absence of O<sub>2</sub> in feed stream while the selective adsorption of CO<sub>2</sub> over O<sub>2</sub> and N<sub>2</sub> takes place because of the surface chemistry of the activated carbon. Although there is no trend in the C K-edge spectra of fast and slow pyrolysis products, the selectivity of adsorbents for CO<sub>2</sub> over O<sub>2</sub> can be explained by the presence of C-O and C=O functional groups on the surface. SD-SP AC results in a longer t<sub>b</sub> of 7.5 min, and higher adsorption capacity of 78.1 mg/g, but less selectivity, 2.8, in the presence of O<sub>2</sub>. For the SD-SP AC, the CO<sub>2</sub> uptake is improved by 20% in absence on N<sub>2</sub>. Besides, all adsorbents are regenerated to more than 94% of their initial adsorption capacity in ten cycles.

## **Chapter 5 Enhanced CO<sub>2</sub> Adsorption Using MgO-Impregnated Activated Carbon: Impact of Preparation Techniques**

A similar version of this chapter has been published in the Journal of Industrial & Engineering Chemistry Research.

- *Shahkarami, S.; Dalai, A. K.; Soltan, J. Enhanced CO<sub>2</sub> Adsorption Using MgO-Impregnated Activated Carbon: Impact of Preparation Techniques. Ind. Eng. Chem. Res. 2016, vol. 55, pp. 5955-5964.*

In addition, some parts of this chapter were presented at the following conferences and symposiums:

- Selective CO<sub>2</sub> Adsorption on Activated Carbons, 24<sup>th</sup> Canadian Symposium on Catalysis Ottawa, ON, Canada, May 8-11, 2016.
- Surface modification of activated carbon for CO<sub>2</sub> capture, 65<sup>th</sup> Canadian Chemical Engineering Conference, Calgary, Canada, October 2015

Contribution of the Ph.D. candidate

In consultation with supervisors, the experiments were designed and conducted by Sepideh Shahkarami. All the samples were prepared and impregnated by Sepideh Shahkarami. All characterizations were performed and the related data were analyzed by Sepideh Shahkarami. The data analyses and interpretations were conducted by Sepideh Shahkarami. All of the written text was prepared by Sepideh Shahkarami and all the experiments were discussed with Drs. A.K. Dalai and J. Soltan.

Contribution of this chapter to the overall study

In the Chapters 3 and 4, it was shown that the CO<sub>2</sub> adsorption capacity and selectivity of the activated carbon can be optimized by a number of parameters including activating agent,

carbonization conditions and the nature of precursors. However, CO<sub>2</sub> adsorption capacity of activated carbon is limited by adsorption conditions. CO<sub>2</sub> adsorption capacity decreases with increasing temperature and decreasing the CO<sub>2</sub> content in gas mixture. The main objective of the research presented in this chapter is to present the effects of metal impregnation of the activated carbon on CO<sub>2</sub> adsorption performance of this adsorbent for CO<sub>2</sub> separation at low and moderate temperature conditions.

### **Abstract**

The development of a facile and sustainable approach to produce magnesium oxide (MgO) activated carbons impregnated through a single-step activation of biochar is reported. In a single-step activation process, biochar is impregnated with 3 and 10 wt. % of magnesium salt solutions followed by steam activation. In a two-step method, activated carbon, the product of steam activation of biochar, is impregnated with magnesium salt using the incipient wetness and excess solution impregnation process and calcined. The impacts of activation method, impregnation method, and metal content are evaluated, and the product qualities are compared in terms of porosity and surface chemistry. The sorbents are then used for CO<sub>2</sub> capture in low partial pressure of CO<sub>2</sub> at 25 and 100 °C from a feed containing 15% CO<sub>2</sub> in N<sub>2</sub> in a fixed-bed reactor. The incipient wetness of activated carbons results in the highest CO<sub>2</sub> uptake (49 mg/g) at 25 °C, while single-step impregnation of biochar with rinsing step yields the largest surface area (760 m<sup>2</sup>/g) and the second highest CO<sub>2</sub> uptake (47 mg/g). The increase in Mg content from 3 to 10 wt % results in the smaller surface area and higher CO<sub>2</sub> uptake suggesting that the metal content has a greater impact than porosity and surface area. Rinsing the Mg impregnated activated carbon with water results in the larger surface area and higher CO<sub>2</sub> uptake in all samples. Moreover, the CO<sub>2</sub> adsorption runs at 100 °C shows a 65% increase using MgO impregnated activated carbon as compared to steam activated carbon indicating that MgO impregnation of activated carbon can overcome the limitation of using nontreated activated carbon at moderate operating temperature of 100 °C and low partial pressure of CO<sub>2</sub> of 15 mol %.

## 5.1 Introduction

Although the CO<sub>2</sub> adsorption capacity of activated carbon decreases with temperature and at low partial pressure of CO<sub>2</sub>, the surface properties and adsorption behavior of activated carbons can be enhanced by amine treatment or metal impregnation of activated carbon. Increase in CO<sub>2</sub> adsorption capacity and high selectivity have been reported by modifications of the surface chemistry of the porous materials by incorporating basic sites of metal oxides that can interact with acidic CO<sub>2</sub>. Impregnation of activated carbon with basic metal oxides can improve the surface chemistry and adsorption capacity of activated carbons for post-combustion carbon capture<sup>13,14,141,142</sup>. MgO is available in natural minerals and can be produced in large quantities at low cost<sup>15</sup>. Chemisorption of CO<sub>2</sub> at temperatures below 200°C on MgO is highly selective and needs a lower regeneration energy as compared to other metal oxides<sup>15,16,143</sup>. The interaction between the adsorbed CO<sub>2</sub> and the basic sites is weaker than that in the case of other alkali metal oxide which explains the lower working temperature of this adsorbent for CO<sub>2</sub> separation<sup>15,144</sup>. The CO<sub>2</sub> adsorption sites on MgO are associated with low coordinated O<sup>2-</sup> ions<sup>15,145</sup> and the basicity of the O<sup>2-</sup> mainly depends on its coordination. CO<sub>2</sub> interacts with basic O<sup>2-</sup> to form a monolayer of CO<sub>3</sub><sup>2-</sup><sup>145</sup>. The small surface area MgO particles results in the formation of a termination layer of carbonate on the surface which limits the further reaction of the magnesium oxide with CO<sub>2</sub><sup>146</sup>. Because the CO<sub>2</sub> uptake of MgO is rather small and to enhance the adsorption performance of MgO, mesoporous MgO is proposed for CO<sub>2</sub> adsorption applications<sup>15,144,146</sup>. The facile mass transport in mesoporous MgO with large surface area (~120–136 m<sup>2</sup> g<sup>-1</sup>) results in an enhanced CO<sub>2</sub> uptake as compared to the MgO nanoparticles which is mostly attributed to its large surface area<sup>146</sup>. Bhagiyalakshmi et al.<sup>144</sup> reported 8 wt. % CO<sub>2</sub> uptakes on mesoporous MgO (250 m<sup>2</sup> g<sup>-1</sup>) as compared to 1-2wt. % CO<sub>2</sub> uptake on nonporous MgO at 25°C. Compared to mesoporous MgO, the mesoporous carbon stabilized MgO nanoparticles produced from the fast pyrolysis of MgCl<sub>2</sub> loaded biomass exhibit a much higher adsorption capacity (240 mg/g at 80 °C), selectivity (112 and 11 over N<sub>2</sub> and O<sub>2</sub>, respectively) and stability for CO<sub>2</sub> separation<sup>143</sup>. In the pyrolysis process, MgO acts as an in situ template to form the porous structure<sup>143</sup> and increase in surface area from 14 to 306 m<sup>2</sup> g<sup>-1</sup> was reported. With regard to the impact of porosity and coordination of O<sup>2-</sup> in mass transport and basic properties of MgO based materials, a practical method to produce MgO impregnated

activated carbon with mesoporous structure and high surface area can be an alternative for CO<sub>2</sub> separation at moderate temperature.

Metal impregnation of activated carbon is usually performed using either incipient wetness or excess solution impregnation followed by a calcination<sup>142,147</sup>. Merging the activation and calcination processes into one step can be an efficient and practical alternative to produce metal impregnated activated carbon<sup>142</sup>. In this method, biochar is impregnated using excess salt solution and then activated with steam at the desired conditions. In addition, metal content and rinsing of the samples can impact the adsorption behavior and CO<sub>2</sub> uptake of the impregnated activated carbons<sup>14</sup>.

In this work, in a single-step process, biochar was impregnated with MgO followed by steam activation. In a two-step process, biochar was activated by steam followed by MgO impregnation and calcined. The impacts of preparation methods, metal content and rinsing step on physical and chemical properties and CO<sub>2</sub> uptake of the activated carbons in a binary mixture of CO<sub>2</sub>/N<sub>2</sub> is evaluated.

## 5.2 Materials and methods

Biochar, the feedstock, was produced by the fast pyrolysis of whitewood( same as the bichoar used in Chapter 3) and provided by Dynamotive Energy Systems Corporation (BC, Canada). The particle size range of 178–710 µm was collected for activation processes. Activated carbon used in this study was produced through steam activation of whitewood biochar as described in section 3.2.2 and Appendix A. For activation of biochar, appropriate amount of biochar was loaded in a fixed bed reactor and heated to 700 °C with the heating rate of 3°C/min under nitrogen at the flow rate of 140 standard mL/min (STP). Then, steam was injected into the reactor with the steam-to-carbon mass ratio of 1.06 for 1.4 h. The reactor was then cooled down to room temperature under nitrogen flow<sup>1</sup>. MgO impregnated activated carbons are produced through single-step process of steam activation of MgO impregnated biochar and two-step process of production of steam activated carbon from biochar followed by MgO impregnation of steam activated carbon and calcination. In all cases, the ratio of Mg weight to the

impregnated activated carbon is calculated and considered as metal loading. Magnesium nitrate hexahydrate ( $\text{Mg}(\text{NO}_3)_2 \cdot 6\text{H}_2\text{O}$ ) was obtained from Aldrich (Milwaukee, USA).

### 5.2.1 Excess solution impregnation of biochar

Prior to the impregnation, biochar was dried at 100 °C overnight. Then, the biochar was treated with magnesium nitrate of an appropriate concentration in 100 ml water for 15 h. After that, the sample was dried at 100°C for 15 h in an oven. The procedure was followed by the steam activation process. In order to evaluate the impact of rinsing step on the CO<sub>2</sub> adsorption of impregnated activated carbons, the samples were prepared with and without rinsing after steam activation. The impregnated activated carbons were rinsed with distilled water and then the samples were dried at 100°C for 15 h in an oven. The produced samples are denoted as 3MgO-B: 3 wt. % MgO loaded biochar, 3MgO-B-R: 3 wt. % MgO loaded biochar-rinsed, 10MgO-B:10 wt. % MgO loaded biochar and 10MgO-B-R:10 wt. % MgO loaded biochar- rinsed. The details of impregnation conditions, activation yield and weight loss after rinsing are described in Table E1 of Appendix E.

### 5.2.2 Excess solution impregnation of activated carbon

Activated carbons, prepared through the steam activation of biochar, were impregnated in 100 ml water with metal nitrate of an appropriate concentration (3 and 10 wt. %) for 15 h. The mixtures of activated carbon and solutions of metal nitrate were then dried in the oven for 15 h. The procedure was followed by calcination at 325 °C for 4 h. The impregnated activated carbons were then rinsed and dried at 100 °C for 15 h in an oven. The produced samples were denoted as 3MgO-AC: 3 wt. % MgO loaded activated carbon, 3MgO-AC-R: 3 wt. % MgO loaded activated carbon-rinsed, 10MgO-AC:10 wt. % MgO loaded activated carbon and 10MgO-AC-R:10 wt. % MgO loaded activated carbon-rinsed. The details of the impregnation conditions, activation yield and weight loss after rinsing and calcination conditions are described in Table E2 of Appendix E.

### 5.2.3 Incipient wetness impregnation of activated Carbon

Prior to the impregnation, the total pore volume of the sample was estimated by BET measurements. Metal nitrate with an appropriate concentration was dissolved in the water, and the solution was added to the activated carbon drop by drop. The mixture is kept at room temperature for 15 h. Then the sample was dried at 100 °C for 15 h in an oven. The procedure was followed by calcination at 325 °C for 4h. The produced samples are denoted as 3MgO-AC-DRY: 3 wt % MgO incipient impregnated activated carbon and 10MgO-AC-DRY: 10 wt. % MgO incipient impregnated activated carbon

### 5.2.4 Characterization

The BET surface area, total pore volume and pore size distribution of the activated carbons were determined as described in section 3.2.4. The thermal stability of the activated carbons was determined by Thermogravimetric Analyzer (Q500, TA Instruments, USA) in the temperature range of 30-700 °C at a heating rate of 5°C/min under nitrogen flow. Powder X-ray diffraction (XRD) data were collected with a D8 Advance (Bruker, USA) with a rotating copper anode (Cu K- $\alpha$ ) and an INEL CPS-120 detector, operating in the 2  $\theta$  range of 10- 90° with a scan rate of 2°. The temperature-programmed desorption (TPD) of carbon dioxide was carried out using an Autosorb IQ (Quantachrome, USA). The sample was placed in the reactor and heated in helium flow of 50 ml/min at 150°C for 30 min to remove the physically adsorbed CO<sub>2</sub>. The sample was then cooled down to 50 °C, and the TPD profile was recorded by increasing the temperature from 50 to 700 °C at a heating rate of 10°C /min under 50 mL/min of He.

### 5.2.5 CO<sub>2</sub> adsorption measurements

The CO<sub>2</sub> adsorption properties of the prepared samples were evaluated by passing the CO<sub>2</sub>/N<sub>2</sub> gas mixture through the one-inch fixed-bed Inconel tubular reactor using a dual channel Micro-Gas Chromatograph (490 micro-GC, Agilent Technologies Inc., USA) equipped with a micro-thermal conductivity detector ( $\mu$ TCD) as described in **section 4.2.6** . Adsorption capacity and selectivity were calculated as described in section 2.3.1. The reactor was loaded with 5 g of activated carbon and pre-heated at 160 °C for 2 h under N<sub>2</sub> flow of 50ml/min before the adsorption experiments. After cooling down to desired temperature, the CO<sub>2</sub>/N<sub>2</sub> feed stream

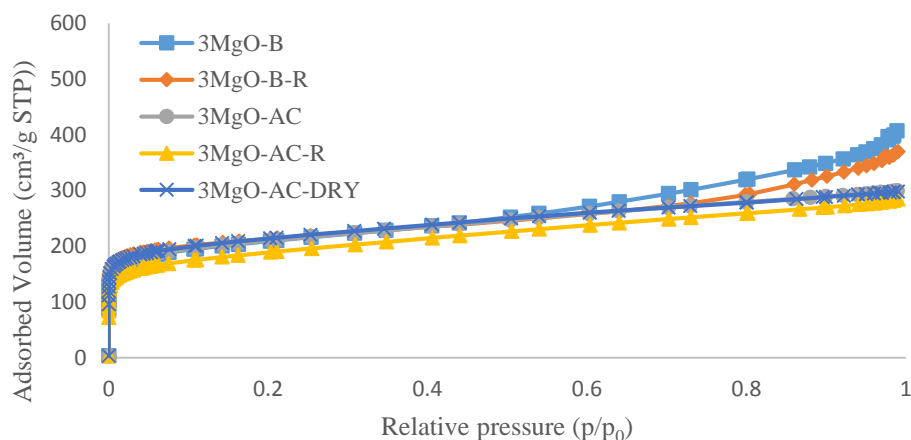
(15/85 mol. %) was passed through the reactor at 50 SmL/min. The adsorption process was continued, and the inlet flow rates, outlet flow rates, and CO<sub>2</sub>/N<sub>2</sub> mole fractions were recorded until saturation. All the experiments were repeated twice, and average results are reported.

### 5.3 Results and discussion

#### 5.3.1 Material characterization

In our preliminary experiments, activated carbon impregnated with 3, 10, 20 and 30 wt. % magnesium are prepared by incipient wetness impregnation method and their physical properties and their performances are evaluated at 25 and 100 °C. The surface area and pore volume of prepared adsorbent showed a significant decrease at  $\geq 20$  wt. % content and more. The CO<sub>2</sub> uptake in all cases increased with increase in metal loading but the increase in breakthrough time and CO<sub>2</sub> uptake were not remarkable at  $\geq 20$  wt. % content. Therefore, we limited the magnesium concentration to 3 and 10 wt. % in this work.

Figure 5-1 and Table 5-1 show the nitrogen adsorption-desorption isotherms at 77K and textural properties of all samples, respectively. The nitrogen sorption isotherms of all samples show the type IV patterns of mesoporous materials with hysteresis loops of Type H4, indicating the presences of slit-shaped pores mainly in micropore size distribution range<sup>36</sup>.



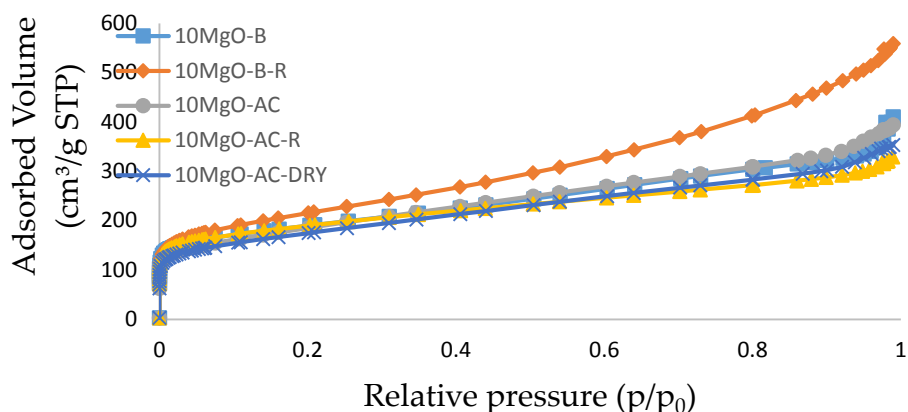


Figure 5-1: N<sub>2</sub> adsorption-desorption isotherms at 77 K

Although, the nitrogen sorption isotherm do not show the considerable difference, and pore volumes remain in the same range, with the exception of 10MgO-B-R, the pore size distributions of samples show some variation (Figures 5-2 and 5-3).

Table 5-1: Physical characteristics of adsorbents

	3MgO-B	3MgO-B-R	3MgO-AC	3MgO-AC-R	3MgO-AC-Dry
BET surface area (m <sup>2</sup> /g)	741	760	667	743	760
Total pore volume (cm <sup>3</sup> /g)	0.421	0.560	0.348	0.403	0.399
Ultra-micro-pore volume, cm <sup>3</sup> /g	0.162	0.175	0.128	0.188	0.089
Micro-pore volume, cm <sup>3</sup> /g	0.221	0.222	0.191	0.197	0.232
Meso-pore volume cm <sup>3</sup> /g	0.197	0.321	0.157	0.201	0.165
Macro-pore volume cm <sup>3</sup> /g	0.002	0.017	0.000	0.005	0.003
	10MgO-B	10MgO-B-R	10MgO-AC	10MgO-AC-R	10MgO-AC-Dry
BET surface area (m <sup>2</sup> /g)	676	760	651	671	615
Total pore volume (cm <sup>3</sup> /g)	0.547	0.801	0.337	0.449	0.496
Ultra-micro-pore volume, cm <sup>3</sup> /g	0.143	0.123	0.122	0.106	0.123
Micro-pore volume, cm <sup>3</sup> /g	0.170	0.164	0.173	0.139	0.147

Meso-pore volume cm <sup>3</sup> /g	0.293	0.589	0.161	0.309	0.331
Macro-pore volume cm <sup>3</sup> /g	0.083	0.049	0.002	0.001	0.017

As shown in Table 5-1, 3MgO-B-R and 10MgO-B-R have the largest surface area and pore volume. The increase of pore volume of MgO-B-R compared to steam activated carbon (0.556 cm<sup>3</sup>/g) implies that impregnation of biochar may have catalyzed some steam activation process. This increase in of the pore volume is also confirmed by the DFT pore size distribution curves shown in Figures 5-2 and 5-3. These results indicate that, regardless of metal content, the excess solution impregnation of biochar leads to larger surface area and pore volume. This means that the main impact of the preparation is to alter the pore size distribution without a significant change in surface area. The rinsing step also increases the pore volume and surface area. The lower surface area and pore volume of unrinsed sample can be attributed to the deposition of magnesium oxides on the walls and/or blocking the smaller pores of the activated carbons<sup>148</sup>. Despite the different impacts of the preparation method, 10 wt. % metal content results in larger mesopore volume and total pore volume of the samples while micropore pore volume decreases. The standard deviation of measured surface area in all not-rinsed samples is less than  $\pm 4$  and in 3 and 10 wt. % MgO impregnated samples with rinsing step were  $\pm 13$  and  $\pm 17$ , respectively.

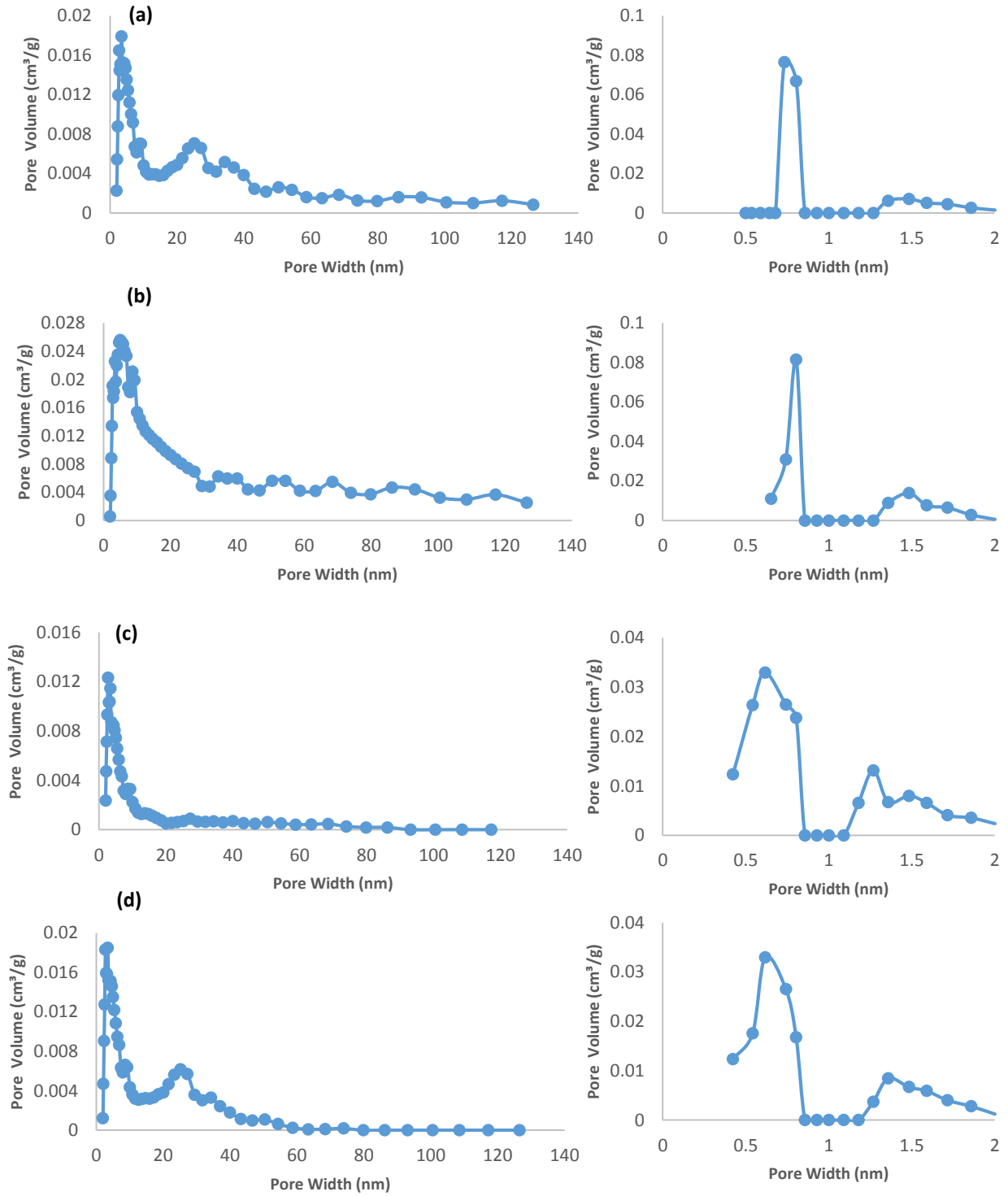
The TG/DTG profiles of thermal decomposition of the precursors are provided in Figure 5-4. A peak at 180 °C followed by a broad shoulder at 210 °C is associated with the loss of physically absorbed water on the activated carbon surface. A sharp peak at 325°C and a distinct mass loss of the sample indicate the thermal decomposition of precursors and formation of MgO on activated carbon surface<sup>149</sup>.

The XRD patterns of the 10 wt. % impregnated samples are shown in Figure 5-5. The XRD patterns of samples show five diffraction peak at  $2\theta$  of 37.1, 43.1, 62.5, 74.7 and 78.6 which indicate (111), (200), (220), (311), and (222) lattice plans of MgO, respectively<sup>143</sup>. As it can be observed in Figure 5-5, the preparation method impacts intensities of the reflections and FWHM (full width at half maximum) values in the XRD pattern. The wide FWHM of MgO-AC and MgO-AC-DRY indicate that the average crystallite size of MgO on these samples is smaller than MgO-B. The increase in intensity and narrow FWHM values of the diffraction peak in MgO-B implies that MgO crystallite size on carbon samples increases in single-step

impregnation of activated carbon. The average MgO crystallite size is calculated using the Scherrer equation(Eq. 5-1)<sup>150</sup>.

$$t = \frac{K * \lambda}{B * \cos\theta_B} \quad (5-1)$$

where t is the average crystal size, K is the constant (dependent on crystallite shape),  $\lambda$  is the X-ray wavelength,  $\beta$  is the FWHM of the reflection peak, and  $\theta_B$  is the Bragg angle. The average MgO crystallite size of 10MgO-B, 10MgO-AC and 10MgO-AC-DRY are 16.7, 1.8 and 2.6 nm.



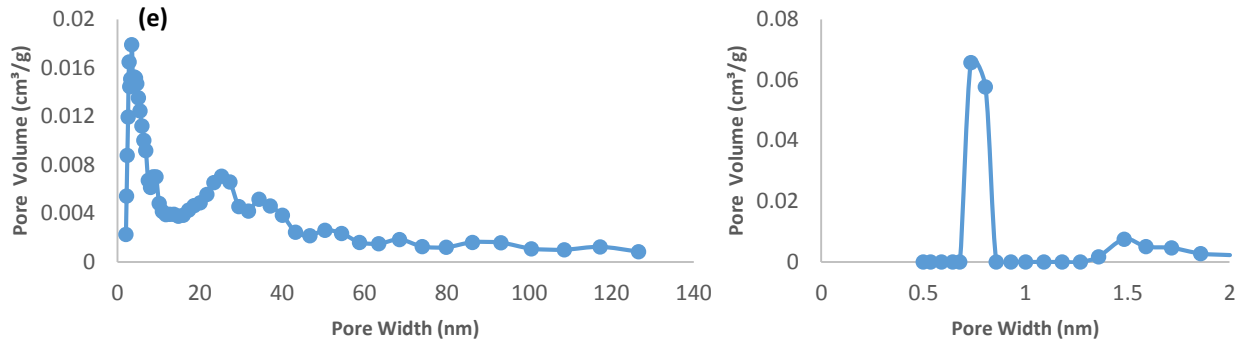
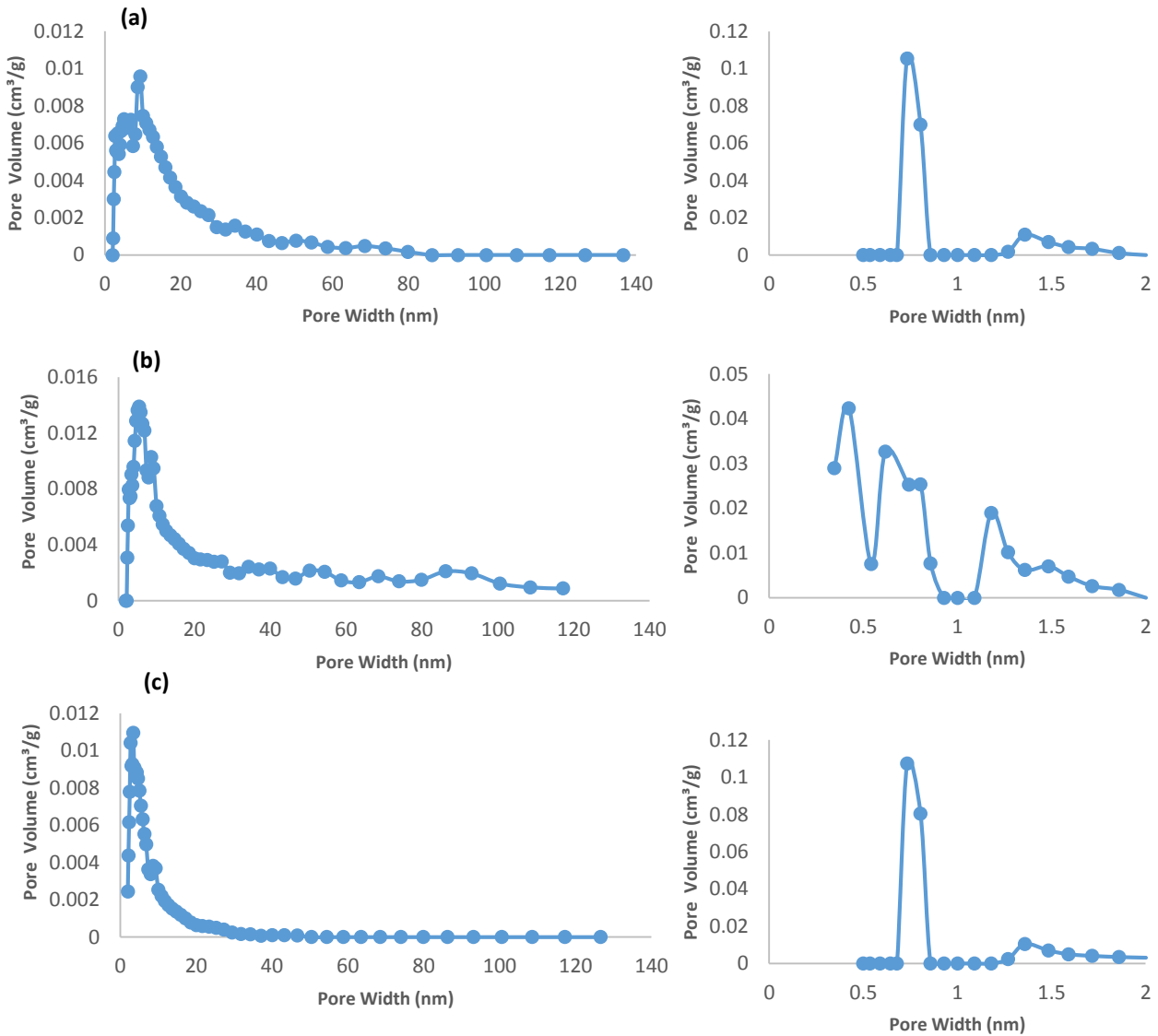


Figure 5-2: Pore size distributions of (a) 10MgO-B, (b) 10MgO-B-R, (c) 10MgO-AC, (d) 10MgO-AC-R and (e) 10MgO-AC-DRY determined from the N<sub>2</sub> and CO<sub>2</sub> adsorption isotherms at 77 K and 273 K using a NLDFT analysis



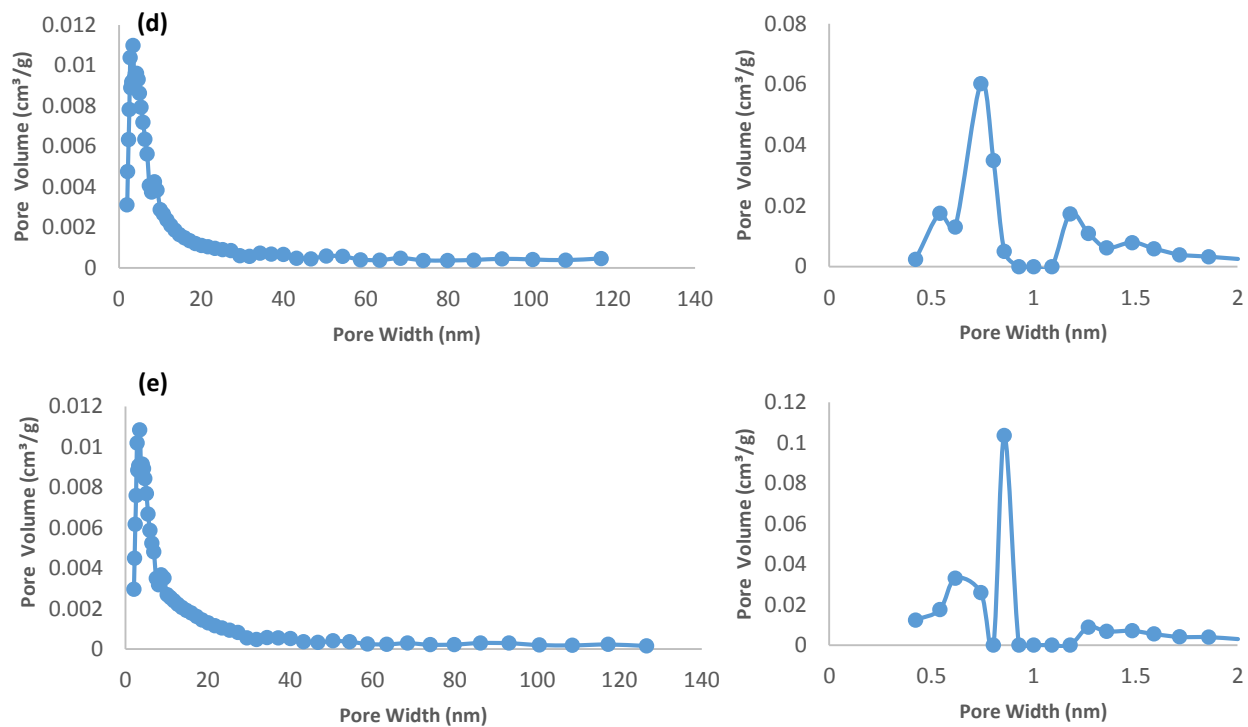


Figure 5-3: Pore size distributions of (a) 3MgO-B, (b) 3MgO-B-R, (c) 3MgO-AC, (d) 3MgO-AC-R and (e) 3MgO-AC-DRY determined from the N<sub>2</sub> and CO<sub>2</sub> adsorption isotherms at 77 K and 273 K using a NLDFIT analysis

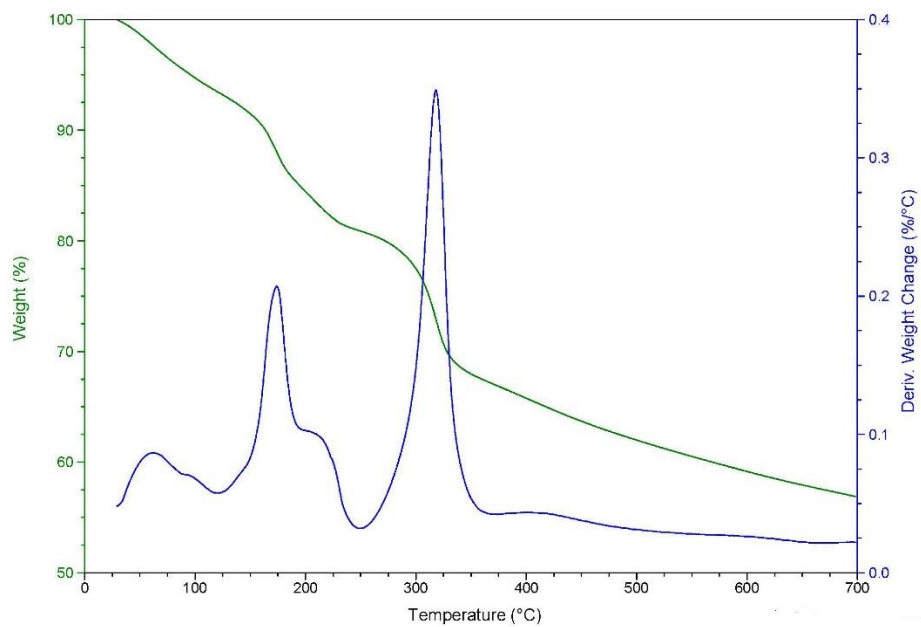


Figure 5-4: TG-DTG profiles of 10MgO-AC heated from 30 to 700°C in N<sub>2</sub> flow

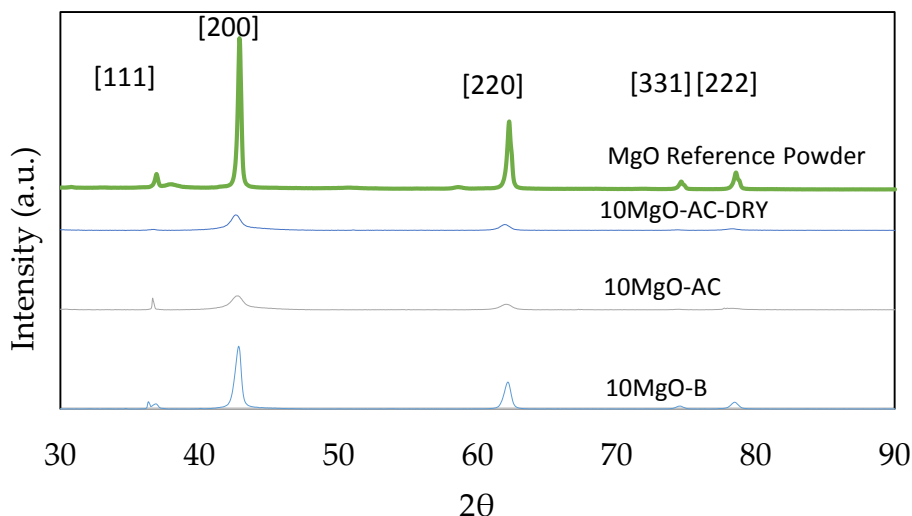


Figure 5-5: Powder X-ray diffraction (XRD) patterns of 10 wt. % MgO loaded activated carbon samples

Figure 5-6 demonstrates the TPD curve for CO<sub>2</sub> adsorbed 10MgO-AC-DRY. The sample is heated at 150°C prior to the measurement, so the initial weight loss due to the physisorbed CO<sub>2</sub> cannot be seen in the curve. The broad weight loss from 520 to 600°C is due to the chemisorbed CO<sub>2</sub> indicating that the complete regeneration occurs only by heating at 600°C.

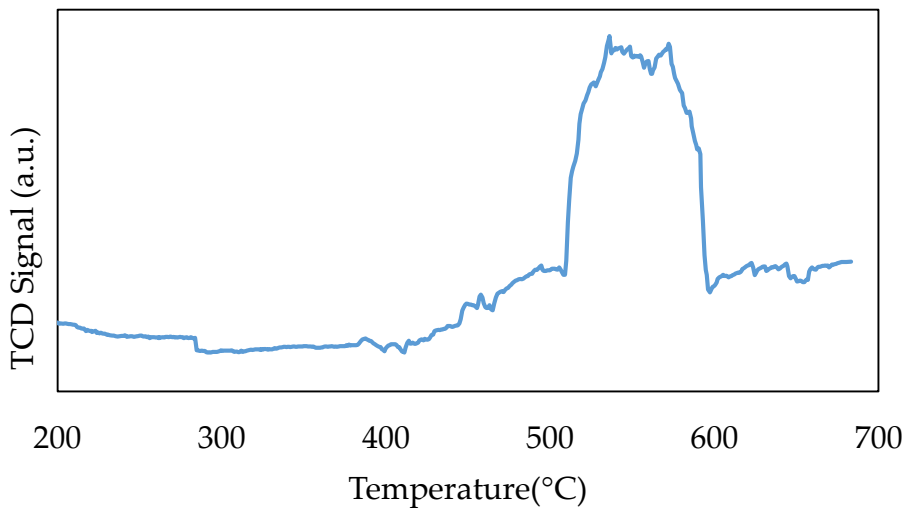


Figure 5-6: TPD Profile of 10 wt. % MgO loaded activated carbon (10MgO-AC)

### 5.3.2 CO<sub>2</sub> adsorption on impregnated activated carbon

The adsorption curves of 3 and 10 wt. % loaded activated carbons and CO<sub>2</sub> adsorption capacity and breakthrough time in CO<sub>2</sub>/N<sub>2</sub> feed steam at 25 °C are shown in Figure 5-7 and Table 5-2, respectively. With the exception of 10MgO-B, increase in metal oxide content enhanced the breakthrough time and CO<sub>2</sub> adsorption capacity, regardless of preparation method, and this is believed to be because of an increase in chemisorption of CO<sub>2</sub> on activated carbon. Rinsing step increases surface area, pore volume and CO<sub>2</sub> uptake of samples in both biochar and activated carbon samples. Impregnation of biochar with rinsing step results in the largest surface area and total pore volume and a significant increase in CO<sub>2</sub> uptake and breakthrough time.

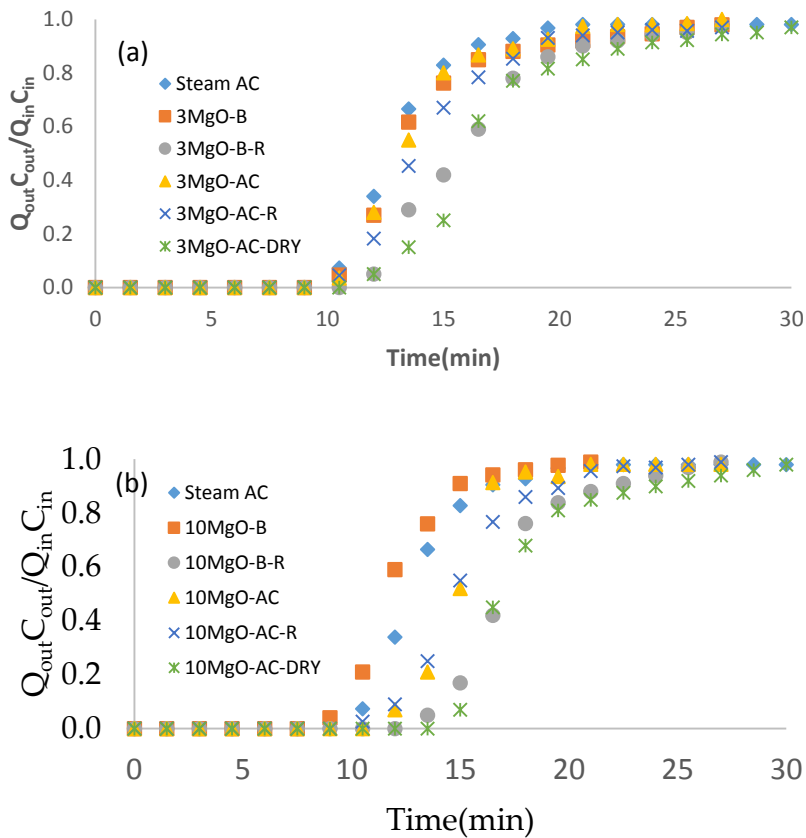


Figure 5-7: Breakthrough curves of 15% CO<sub>2</sub> in N<sub>2</sub> at 25°C on (a) 3 wt. % and (b) 10 wt. % MgO impregnated activated carbons

Although the similar increase is observed in impregnation of activated carbon (MgO-AC-R), the increase is more significant in 10 MgO-B-R. Regardless of their higher surface area, 3 wt. % loading of MgO on biochar and activated carbon does not have a considerable impact on the breakthrough curve and adsorption capacity except for 3MgO-B-R and 3MgO-AC-DRY indicating that metal content is more influential than surface area for CO<sub>2</sub> adsorption. The results also indicate that CO<sub>2</sub> uptake of 10MgO-AC-DRY increased by 40% as compared to that for untreated activated carbon. MgO-B-R activated carbon with well-dispersed metal particles and higher surface area than untreated activated carbon, exhibits a notable increase in both breakthrough time and CO<sub>2</sub> uptake. These results suggest that combination of impregnation and activation step into a single-step process can be an alternative technique to produce metal impregnated activated carbon for CO<sub>2</sub> adsorption.

Our initial evaluation suggests that impregnation of biochar through single-step process is an effective technique for production of CO<sub>2</sub> sorbents; hence, 10MgO-B-R was chosen for further investigation. As it is shown in Figure 5-8, CO<sub>2</sub> physisorption on activated carbon decreases with temperature due to exothermic nature of this process. The adsorption of CO<sub>2</sub> at 100 °C in the CO<sub>2</sub>/N<sub>2</sub> feed stream is conducted in the same experimental set-up. CO<sub>2</sub> adsorption breakthrough curves of untreated activated carbon and 10MgO-B-R at 25 and 100 °C are shown in Figure 5-8. The CO<sub>2</sub> uptake at 100 °C exhibits a significant increase from 15.7 to 25.8 mg/g after treatment indicating that metal impregnation has a potential for moderate temperature post-combustion carbon capture at the lower content of CO<sub>2</sub>.

For a practical application of an adsorbent, stability and regenerability are also important. Figure 5-9 shows the regenerability of 10MgO-B-R in five cycles. The adsorption index (%) is the ratio of CO<sub>2</sub> uptake of regenerated adsorbent to the virgin one<sup>118</sup>. In the multicycle study, the adsorbent is fully regenerated at 600°C keeping more than 93% of the initial adsorption capacity.

Table 5-2: CO<sub>2</sub> adsorption capacities and breakthrough time at 25° C

	AC	3MgO-B	3MgO-B-R	3MgO-AC	3MgO-AC-R	3MgO-AC-DRY
CO <sub>2</sub> adsorption						
capacity (mg <sub>adsorbed</sub> /g adsorbent)	35	38	44	38	40	46
Breakthrough time (s)	602	637	720	635	641	720
Standard deviation	±0.3	±0.4	±0.5	±0.9	±0.8	±0.8

	AC	10MgO-B	10MgO-B-R	10MgO-AC	10MgO-AC-R	10MgO-AC-DRY
CO <sub>2</sub> Adsorption						
capacity (mg <sub>adsorbed</sub> /g adsorbent)	35	34	47	40	42	49
Breakthrough time (s)	602	563	811	694	664	874
Standard deviation	±0.3	±0.8	±0.6	±0.8	±1.0	±0.5

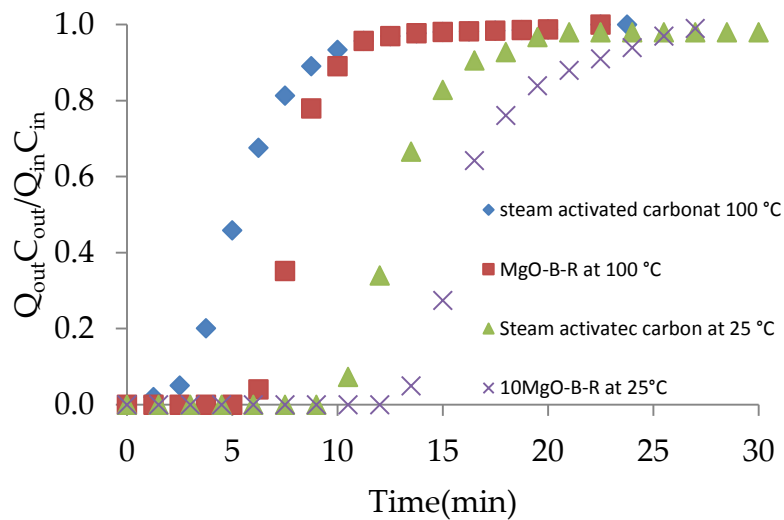


Figure 5-8: CO<sub>2</sub> adsorption on non-treated activated carbon and 10MgO-B-R at 25 and 100 °C

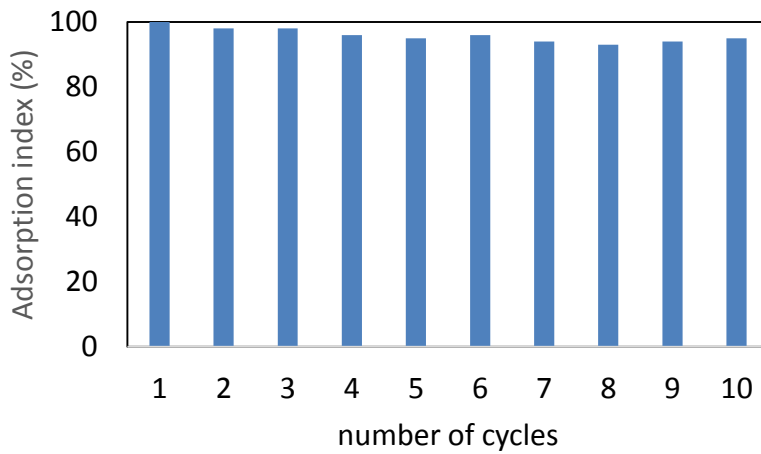


Figure 5-9: Cyclic CO<sub>2</sub> adsorption of 15% CO<sub>2</sub> in N<sub>2</sub> at 25°C on 10MgO-B-R

#### 5.4 Conclusions

MgO impregnated activated carbons are produced using different preparation techniques and compared to not-treated activated carbon in terms of pore size distribution, surface area, CO<sub>2</sub> uptake and breakthrough time at 25 and 100°C and for adsorption under a binary mixture of CO<sub>2</sub>/N<sub>2</sub>. Preparation method has the greatest impact on the surface area, porosity and dispersion of metal in activated carbons. Surface area and pore size distribution are impacted by both metal content and preparation method. Largest surface area of 760 m<sup>2</sup>/g is developed using the excess solution impregnation of biochar with rinsing step. 10 wt. % MgO loaded activated carbon produced through incipient wetness with a surface area of 615 m<sup>2</sup>/g has the highest CO<sub>2</sub> adsorption capacity (49 mg/g) suggesting that preparation method and metal content are more important than surface area and porosity of the samples. Rinsing step before calcination can positively impact the impregnation of MgO on activated carbon for CO<sub>2</sub> adsorption.

## Chapter 6 Equilibrium and Modeling of Isothermal Fixed-Bed CO<sub>2</sub> Adsorption

A similar version of this chapter has been submitted to the International Journal of Greenhouse Gases Control:

- *Shahkarami, S.; Ghasemi, M.; Dalai, A. K.; Soltan, J.; CO<sub>2</sub> Adsorption on Activated Carbon: Equilibrium, and Kinetics of Fixed-Bed Isothermal Adsorption, international journal of greenhouse gas control, under communication.*

In addition, some parts of this chapter were presented at the following conference:

- Enhanced CO<sub>2</sub> Adsorption on Activated Carbon, 66<sup>th</sup> Canadian Chemical Engineering Conference, Quebec City, QC, October 16-19, 2016.

Contribution of the Ph.D. candidate

In consultation with supervisors, all the activated carbon samples were prepared by Sepideh Shahkarami. All the experiments were planned and conducted by Sepideh Shahkarami. The samples characterizations were performed and the related data were analyzed by Sepideh Shahkarami. Mass transfer model and all the related equations and calculation were selected by Sepideh Shahkarami. The adsorption isotherms were derived and fitted by Sepideh Shahkarami with assistance of Amir Abolhassani. The data analyses and interpretations were conducted by Sepideh Shahkarami. The program code in Python was written by Dr. Mehdi Ghasemi. All of the written text was prepared by Sepideh Shahkarami and all the experiments were discussed with Drs. A.K. Dalai and J. Soltan.

Contribution of this chapter to the overall study

This chapter contains the development of an isothermal mass transfer model for CO<sub>2</sub> adsorption in a binary mixture under post-combustion capture conditions. Additionally, the experimental results were compared to model prediction to validate the model.

**Abstract**

The equilibria and kinetics of CO<sub>2</sub> adsorption on microporous activated carbon have been studied using a fixed-bed adsorption set-up. Adsorption equilibria of pure component were measured at 0, 25, 50 and 75 °C on activated carbon bed and the data were fitted with the Langmuir model. The breakthrough curves were obtained using CO<sub>2</sub> balanced in N<sub>2</sub> at feed concentrations of 5%, 15% and 25 mol.%; temperatures of 25, 45, 65 and 85 °C and feed flowrates of 30, 50 and 70 ml/min. Results indicated that temperature has the greatest impact on breakthrough time and adsorption capacity. Decrease in feed flowrate increases adsorption capacity and breakthrough time while the adsorption capacity was independent of the initial CO<sub>2</sub> content.

A mathematical model based on the bilinear driving force (bi-LDF) model was developed to calculate the overall mass transfer coefficient. The model describes mass transfer due to bulk, Knudsen and intracrystalline diffusion. The total porosity of the bed was calculated by taking the particle porosity and bed porosity into account. The reproducibility of adsorption breakthrough curves of the model was validated with experimental data. In all cases, the predicted breakthrough curves were in agreement with the experimental data. It was shown that for CO<sub>2</sub> adsorption on microporous activated carbon, the controlling mass transfer step is micropore mass transfer resistance.

## 6.1 Introduction

To design a CO<sub>2</sub> adsorption process, development of a mass transfer model to describe the transport of CO<sub>2</sub> from a gas mixture to the adsorption sites of the activated carbon and adsorption model of the bed is essential. Using independently acquired equilibrium data, the model can be used to predict the breakthrough curves and adsorption behavior of the bed without extensive experimental data. In most of numerical studies on CO<sub>2</sub> adsorption, linear driving force (LDF) model is to approximate the adsorption rate<sup>151–154</sup>. The bilinear driving force (bi-LDF) model, proposed by Azevedo and Rodrigues,<sup>155</sup> provides a close approximation of the mass balances in macro-pores and in micro-pores. In this model, both macro-pores and the micro-pores diffusion are represented by LDF model.

The objective of this work is to accurately measure the kinetic data and diffusion parameters, and to develop an isothermal mass transfer model for CO<sub>2</sub> adsorption on a fixed-bed of microporous KOH activated carbon bed in a binary mixture of CO<sub>2</sub>/N<sub>2</sub> feed stream. The flow pattern is described as an axially dispersed plug flow model and the adsorption rate is represented by a Bi-LDF model that treats the macro pore and micropore resistances independently<sup>96</sup>. The bed porosity, particle size, density, mass transfer coefficients, Langmuir constants are calculated independently.

## 6.2 Material and methods

### 6.2.1 Activated carbon

The KOH activated carbon was prepared from biochar (by-product of fast pyrolysis of whitewood). “The as-received biochar was sieved, and particle size range of 150-355 μm was collected for activation process. Biochar was impregnated with KOH in 100 ml of water with biochar to KOH mass ratio of 0.81 on a dry basis. After 15 h mixing at the room temperature, the mixture was dried in an oven at 110 °C for 15 h. The dried sample was then loaded in the tubular reactor under a nitrogen flow of 240 SmL/min and heated to 300 °C and held for 1 h at 300 °C<sup>108</sup>. The temperature of the reactor was then increased to 775 °C with a heating rate of 3 °C/min and held at this temperature for 2 h before cooling down to room temperature. The sample was then washed with hot water, followed by 0.1M HCl, and finally distilled water to remove the soluble salts and the potassium compounds<sup>91,109,110</sup>. The sample was then dried in an oven overnight at 110 °C. Finally, the prepared activated carbon was sieved, and particle size range of 150-355 μm was collected for activation processes<sup>1</sup>. The N<sub>2</sub> and CO<sub>2</sub> adsorption isotherms were measured at 77 and 273 K, respectively, using ASAP 2020 (Micromeritics Instruments Inc.) and the micropore size distribution and particle pore volume( $V_{p,b}$ ) was determined using the non-local Density Function Theory (NLDFT)<sup>42</sup>. The specific surface area was determined using BET (Brunauer, Emmett, and Teller) method. Skeletaldensity ( $\rho_s$ ) was measured using helium pycnometer (Quantachrome instrument, USA). Other physical properties of produced activated carbon are described in Chapter 2 (Eq. 2-36 and 2-37).

## 6.2.2 Adsorption isotherm

The equilibrium data of CO<sub>2</sub> and N<sub>2</sub> adsorption on the collected activated carbon samples were measured in the adsorption experimental set-up with a packed column at 0, 25 and 50 and 75 °C. The adsorption capacity of CO<sub>2</sub> in a fixed-bed reactor was calculated using CO<sub>2</sub> diluted with argon. Before the adsorption measurements, the bed was pre-heated at 150 °C for 15 h. The total flow rate was maintained constant at 50 ml/min and the bed temperature was controlled using a K-type thermocouple and temperature controller (2416, Eurotherm, USA). The details of the adsorption set-up and the related calculation are reported before<sup>1,53</sup>. Physical properties of the fixed-bed are given in Table 6-1. The calculated experimental data are then fitted to Langmuir isotherm (Eq. 6-1).

$$q_{ci}^* = \frac{q_{si} b_i p_i}{1 + b_i p_i} \quad (6-1)$$

where  $q_{si}$  is the saturation capacities (temperature-independent),  $b_i$  is the isotherm parameter for gas  $i$ , and  $p_i$  is the partial pressure of component  $i$ . In this equation, the isotherm parameter is calculated using Arrhenius-type temperature dependence (Eq. 6-2):

$$b_i(T) = b_i(T_0) \exp\left(\frac{-\Delta H_{adsi}}{R} \left(\frac{1}{T} - \frac{1}{T_0}\right)\right) \quad (6-2)$$

The isotherm parameters are calculated from the independent fits of the single component data to the Langmuir isotherm.

## 6.3 Mathematical model and solution method

The adsorption models are used to study the gas transfer from gas mixture to a solid sorbent and predict the change in concentration profiles along the bed due to any changes in process conditions. A mass balance on an isothermal fixed-bed (Figure 6-1) was used to explain the mass-transfer process through a bed. The mechanism of CO<sub>2</sub> transfer for gas–solid adsorption includes diffusion through the film surrounding adsorbent particle and then diffusion into the macropores and micropores to the adsorption sites of adsorbent.

Table 6-1: Experimental parameters used in the simulation

Specific surface area	1461	m <sup>2</sup> /g
Pore volume	5.8E-04	m <sup>3</sup>
Bed length	0.030	m
Bed diameter	0.022	m
Total flowrate	50	ml/min
Skeletal density( $\rho_s$ )	2111	kg/m <sup>3</sup>
particle density( $\rho_p$ )	952	kg/m <sup>3</sup>
bulk density ( $\rho_b$ )	435	kg/m <sup>3</sup>
bed porosity( $\epsilon_b$ )	0.543	
particle porosity( $\epsilon_p$ )	0.549	
total porosity( $\epsilon_t$ )	0.794	
Mean particle radius( $R_p$ )	1.1E-04	m
mean pore radius( $r_p$ )	6.54E-09	m

### 6.3.1 Model description

An isothermal bi-LDF was developed to study the CO<sub>2</sub> adsorption from a CO<sub>2</sub>/N<sub>2</sub> gas mixture using a fixed-bed of KOH activated carbon. Bi-LDF model includes both macropore (molecular and Knudsen diffusions) and micropore resistances in a linear model. The following assumptions are considered in this model:

- The adsorption process is isothermal.
- An axially dispersed plug flow model describes the flow pattern in the fixed bed.
- The Bi- LDF model is used to calculate the adsorption rate.
- The radial gradient of pressure, velocity and concentration of the gases in the solid and the gas are negligible.
- The adsorption behaviors are described by the Langmuir isotherm model.

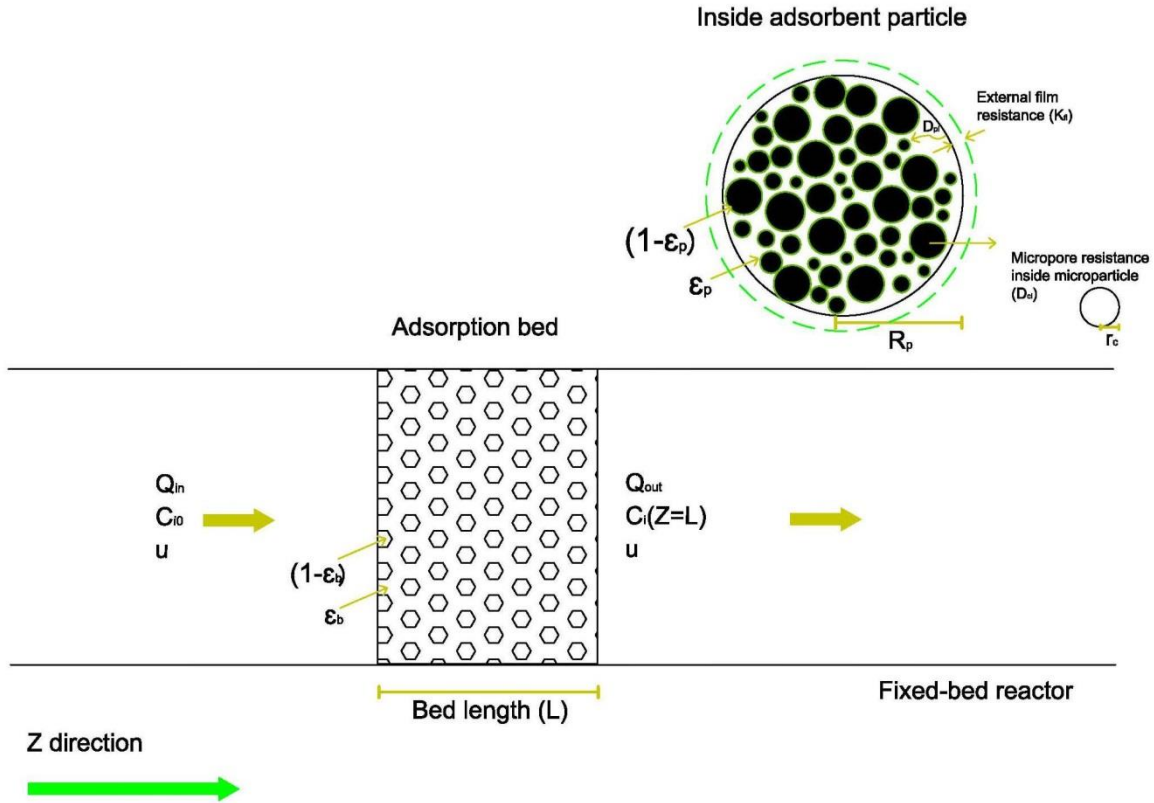


Figure 6-1: Schematic of mass transfer in a fixed bed reactor showing the mechanism of gas transfer to adsorption sites

The overall mass balance for the component  $i$  ( $i=CO_2, N_2$ ) in the  $z$  direction (Figure 6-1) is given as Eq. 6-3<sup>156</sup>:

$$\varepsilon_t \frac{\partial c_i}{\partial t} + (1 - \varepsilon_b) \rho_p \frac{\partial \bar{q}_{pi}}{\partial t} = -\varepsilon_b u \frac{\partial c_i}{\partial z} + \varepsilon_b \frac{\partial}{\partial z} \left( D_{ax} \frac{\partial c_i}{\partial z} \right) \quad (6-3)$$

In equation 6-3, the average adsorbed concentration of  $i$  ( $\bar{q}_{pi}$ ) per unit of adsorbent particle mass is equal to concentration in gas phase of component  $i$  ( $c_{pi}$ ) trapped in the macropores and average adsorbed concentration of component  $i$  ( $\bar{q}_{ci}$ ) per unit of particle volume<sup>96</sup>(Eq. 6-4):

$$\rho_p \bar{q}_{pi} = \varepsilon_p c_{pi} + (1 - \varepsilon_p) \rho_s \bar{q}_{ci} \quad (6-4)$$

Combining the macropore and micropore resistances into a bi-LDF model results in an overall adsorption using the bi-LDF rate equation (Eq. 6- 5) <sup>101</sup>:

$$\rho_p \frac{\partial \bar{q}_{pi}}{\partial t} = k_{pi} (c_i - \bar{c}_{pi}) + \frac{15D_{ci}}{r_c^2} (1 - \varepsilon_p) \rho_s (q_{ci}^* - \bar{q}_{ci}) \quad (6-5)$$

Combining Equations 6-3 and 6-5 results in the mass balance of component i using bi-LDF model (Eq. 6-6):

$$\begin{aligned} \varepsilon_t \frac{\partial c_i}{\partial t} + (1 - \varepsilon_b) \left[ k_{pi} (c_i - \bar{c}_{pi}) + \frac{15D_{ci}}{r_c^2} (1 - \varepsilon_p) \rho_s (q_{ci}^* - \bar{q}_{ci}) \right] = -\varepsilon_b u \frac{\partial c_i}{\partial z} + \\ \varepsilon_b \frac{\partial}{\partial z} \left( D_{ax,i} \frac{\partial c_i}{\partial z} \right) \end{aligned} \quad (6-6)$$

where  $k_{pi}$  is the effective LDF constant that represents the effects of external fluid film, molecular and Knudsen diffusion resistances in the macropores (Eq. 6-7 and 6-8):

$$k_{pi} = \frac{15\varepsilon_p D_{pi}}{R_p^2} \frac{Bi_i}{Bi_i + 1} \quad (6-7)$$

$$Bi_i = \frac{R_p k_{f,i}}{5\varepsilon_p D_{pi}} \quad (6-8)$$

“ $Bi$  is the Biot number representing the ratio of internal macropore to the external film resistance; and  $D_{pi}$  is the effective macropore diffusivity corrected for the tortuosity of component  $i$ ”<sup>96</sup>.  $D_{pi}$  is calculated as follows<sup>87,97</sup>(Eq. 6- 9):

$$\frac{1}{D_{pi}} = \frac{1}{D_{K,i}} + \frac{1}{D_{m,i}} \quad (6-9)$$

In Equation 6-9,  $D_{K,i}$  is the Knudsen diffusivity and  $D_{m,i}$  is the macropore diffusivity. Knudsen and macropore diffusivity are calculated as described in Chapter 2 (Eq. 2-43 to 2-47)

The crystal diffusivity ( $D_{ci}$ ) at any loading is a function of surface diffusion at zero loading multiplied by the thermodynamic correction factor of  $\frac{\partial \ln p_i}{\partial \ln q_{ci}}$  <sup>46,96</sup> as follows (Eq. 6-10):

$$D_{ci} = D_{ci}^{\infty} \left. \frac{d \ln(p_i)}{d \ln(q_{ci})} \right|_T \quad (6-10)$$

Crystal diffusivity of the adsorbed molecules in the micropores may be explained as an activated process <sup>101,102</sup> (Eq. 6-11):

$$D_{ci}^{\infty} = D_{ci0} \exp\left(\frac{-E_{ai}}{RT}\right) \quad (6-11)$$

The exponential term in this equation “expresses the probability of a molecule to having sufficient kinetic energy to surmount the energy barrier”<sup>102</sup>.  $D_{ci0}$  is the “limiting diffusivity at high temperature and  $E_{a,i}$  is the activation energy”<sup>104</sup>.

The average of adsorbed amount ( $\bar{q}_{ci}$ ) in Equation 6 is described as<sup>154,157</sup> (Eq. 6-12 and 6-13):

$$\bar{q}_{ci}(t) = \frac{3}{r_c^3} \int_0^{r_c} r^2 q_{ci}(r, t) dr \quad (6-12)$$

$$\frac{\partial q_{ci}(r, t)}{\partial t} = \frac{1}{r^2} \frac{\partial}{\partial r} \left[ D_{c0i} r^2 \frac{\partial q_{ci}}{\partial r} \right] \quad (6-13)$$

In Equation 6-6, the axial dispersion in a packed bed was calculated using a correlation developed by Wakao and Funazkri <sup>84</sup> (Eq. 6-14):

$$\frac{\epsilon_b D_{ax}}{D_{m,i}} = 20 + 0.5(Sc)(Re) \quad (6-14)$$

The equations that describe bed, particle and total porosity, gas density, gas viscosity, Reynolds number, Schmidt number, Sherwood number and external fluid film mass transfer

coefficient are detailed in Chapter 2 ( section 2-7). The boundary and initial conditions are shown in Table 6-2.

Table 6-2: Boundary and initial conditions

---

Boundary conditions
$-D_{ax,i} \frac{\partial c_i}{\partial z} \Big _{z=0} = u_0 (c_{i0} - c_i _{z=0})$
$\frac{\partial c(z=L)}{\partial z} = 0$
$q_{ci}(r_C, t) = q_{ci}^* = H_i \bar{c}_{pi}$
$\frac{\partial q_{ci}}{\partial r} \Big _{(0,t)} = 0$
$\frac{\partial P}{\partial t} = 0$
Initial conditions
$q_{ci}(z, t = 0) = 0$
$c_{pi}(r, 0) = 0$
$q_{ci}(r, t = 0) = 0$
$c = \sum c_i = P / RT_0$

---

### 6.3.2 Numerical solution

A Linux machine running Ubuntu 16.04 with 8 processors: Intel Core i7-2600 CPU @ 3.40GHz and 16 GB of RAM were used to solve the system of equations.

The solver is written in Python 2.7 implementing a Galerkin type method to approximate solutions of integro-differential equations, symbolically. For this particular set of equations, a family of functions consisting of polynomials and signomial functions were used.

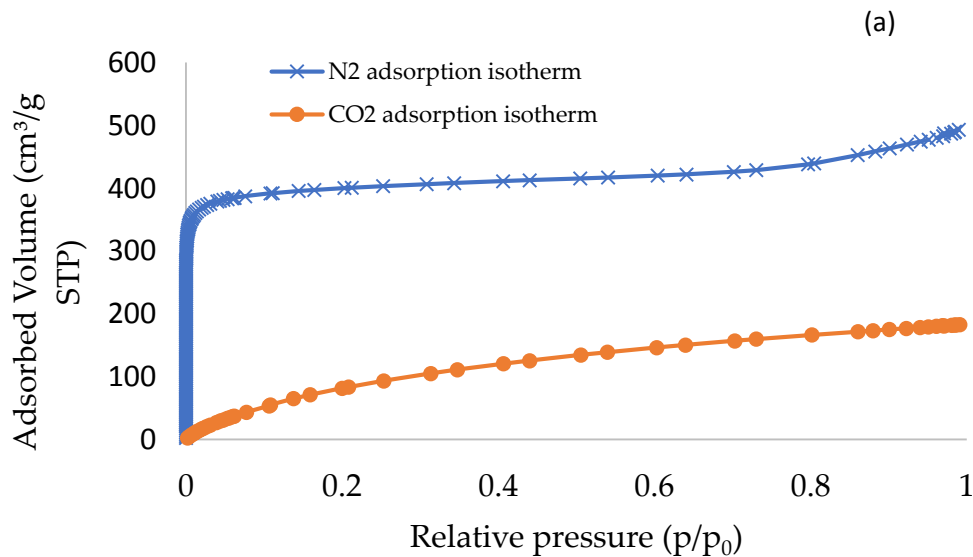
Source code: pyProximation available at <https://github.com/mghasemi/pyProximation>

## 6.4 Results and discussions

### 6.4.1 Activated carbon properties and adsorption isotherms

The characteristic properties of the activated carbon sample and the adsorption bed used in the simulations are provided in Table 6-1. N<sub>2</sub> adsorption-desorption isotherm at 77K, CO<sub>2</sub> adsorption-desorption isotherm at 273K and pore size distribution of the activated carbon are shown in Figure 6-2.

The nitrogen adsorption-desorption isotherm shows the type IV patterns of mesoporous materials. H4 hysteresis loop appeared in N<sub>2</sub> isotherm which is associated with the presences of narrow slit- shaped pores. The N<sub>2</sub> and CO<sub>2</sub> isotherms are similar to those reported previously<sup>158,159</sup>. The pore size distribution results show a larger amount of micropore (0.48 cm<sup>3</sup>/g) resulting in a high BET specific surface area (1461 m<sup>2</sup>/g) and large particle porosity (0.549).



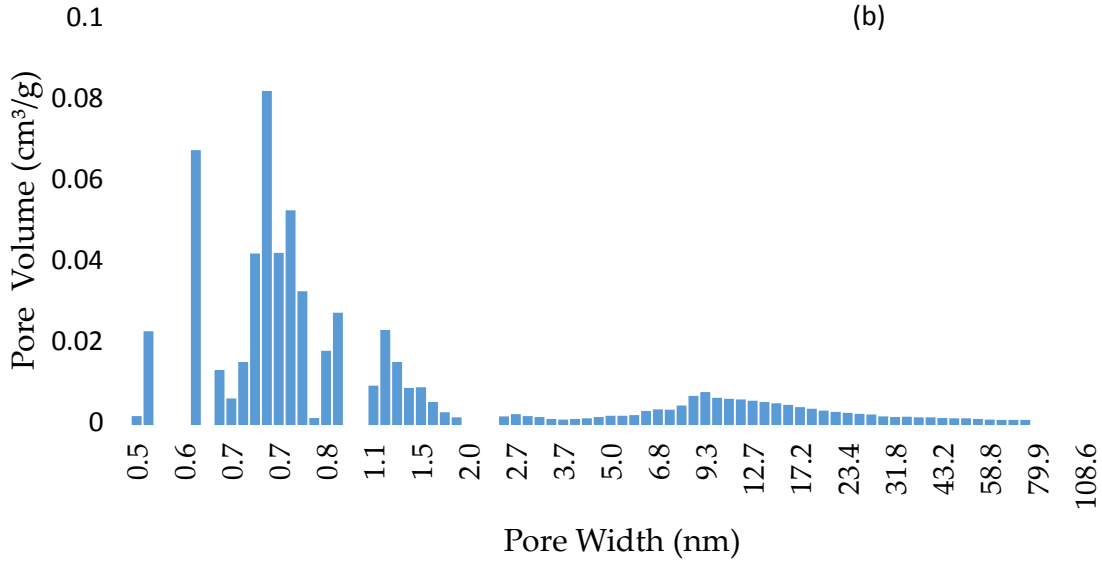


Figure 6-2: N<sub>2</sub> and CO<sub>2</sub> adsorption isotherms of activated carbon at 77 K and 273 K (a), and pore size distribution of activated carbon (b).

Figure 6- 3 shows CO<sub>2</sub> adsorption isotherms at 0, 25, 50 and 75 °C, respectively. The isothermal equilibrium constants ( $b_0$ ), saturation capacity of CO<sub>2</sub> on activated carbon ( $q_s$ ) and heat of adsorption of CO<sub>2</sub> were estimated from independent fits of CO<sub>2</sub> equilibrium data to Langmuir isotherm model. The fitting parameters are shown in Table 6- 3. The N<sub>2</sub> isotherms on activated carbon have a linear shape. The slope of the CO<sub>2</sub> isotherm is higher compared to that of N<sub>2</sub> isotherm which is associated with a better interaction of CO<sub>2</sub> and the activated carbon. Our previous studies also showed differential adsorption of CO<sub>2</sub> over N<sub>2</sub> on activated carbon<sup>53</sup>, which confirms our assumption that competitive adsorption of N<sub>2</sub> is negligible. Due to exothermic nature of adsorption, CO<sub>2</sub> adsorption capacity decreases with increase in temperature<sup>160</sup>.

Table 6-3: Fitting parameters of adsorption equilibrium and kinetic parameters for adsorption on activated carbon.

gas	$q_s$	$b_0$	$-\Delta H$	$D_{ci0}/r_c^2$	$E_{ai}$
	mol/kg	kPa <sup>-1</sup>	KJ/mol	S <sup>-1</sup>	kJ/mol
CO <sub>2</sub>	10.82	7.3E-6	17.44	12.995	18.05

The value of  $D_{ci}/r_c^2$  and  $E_{ai}$  are adopted from literature while others are calculated.

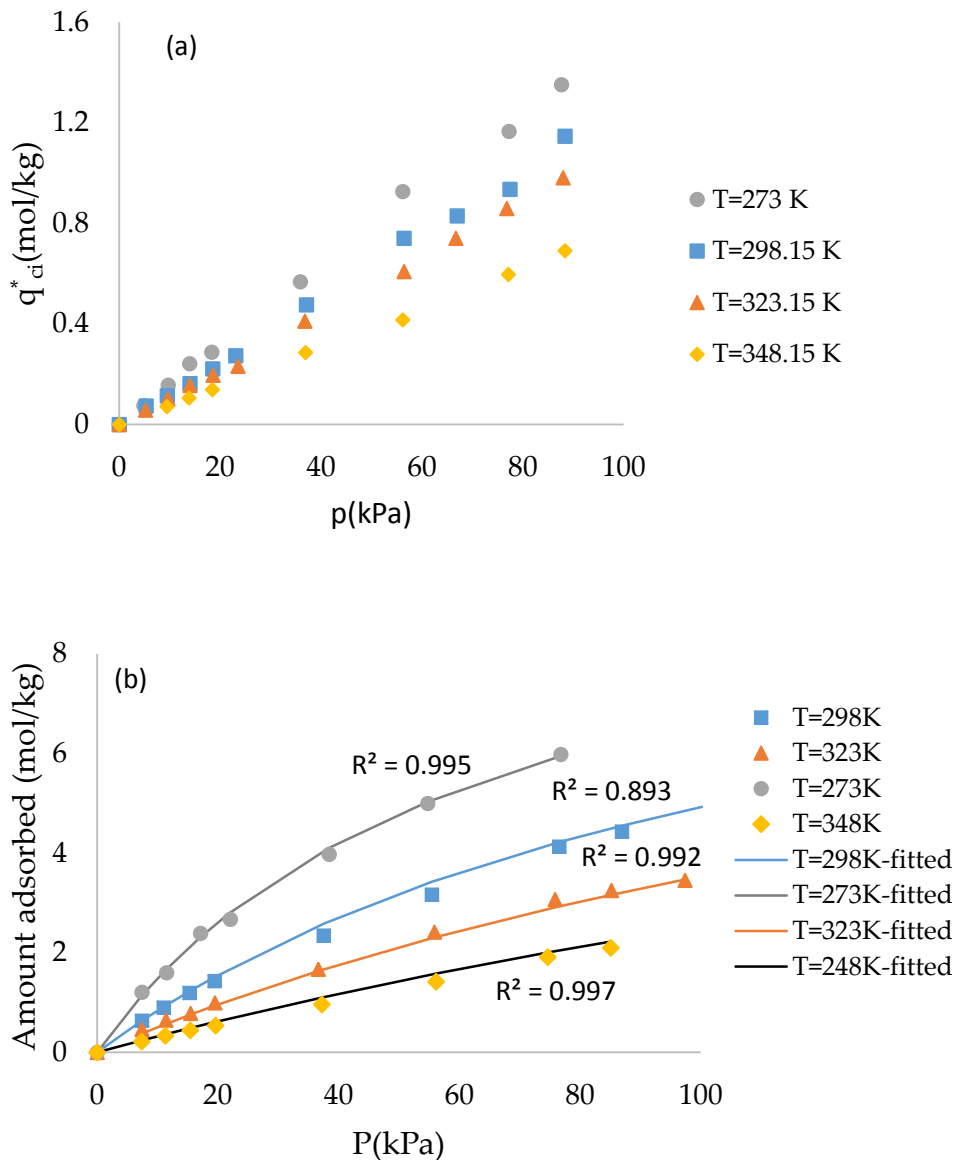


Figure 6-3:  $N_2$  (a) and  $CO_2$  (b) adsorption equilibrium data of activated carbon

#### 6.4.2 Fixed-bed CO<sub>2</sub>/N<sub>2</sub> mixture adsorption: experimental and modeling

A set of breakthrough CO<sub>2</sub> adsorption experiments with feed composition of 5-25 mol% CO<sub>2</sub> in N<sub>2</sub> at temperature range of 25-85 °C and feed flowrate of 30-70 ml/min were performed and simulated using the model described above to verify the mass transfer model and calculate the parameters at different conditions. Figures 6-4 to 6-6 show the comparison of the experimental data and simulation curves obtained for CO<sub>2</sub> adsorption on KOH activated carbon. In this work, the predicted gradient of C<sub>CO<sub>2</sub></sub> at z = L are compared with breakthrough experiments for CO<sub>2</sub> adsorption in a mixture of CO<sub>2</sub>/N<sub>2</sub>. Two important parameters in breakthrough curves are breakthrough point (t<sub>b</sub>) and mass transfer zone (MTZ). Breakthrough point is a point where C<sub>i</sub> (z=L)/C<sub>i0</sub> is 0.05. Most of the mass-transfer occurs in a small region when (z=L)/C<sub>i0</sub> varies between 0.05 to 1 which is called mass transfer zone<sup>19</sup>. The adsorption capacity of activated carbon was measured in 300 cycles and it was regenerated to more 96% of its original capacity. The adsorption capacity is reported as the number of mol of CO<sub>2</sub> adsorbed per kg of adsorbent (mol/kg) and it can be converted to mg/g by multiplying by 44(CO<sub>2</sub> molecular weight).

Figure 6-4 shows the impact of CO<sub>2</sub> content on adsorption of CO<sub>2</sub> onto activated carbon. Increase in the feed concentration results in earlier CO<sub>2</sub> breakthrough point and faster saturation of bed. Higher CO<sub>2</sub> content also results in narrower mass transfer zone and steeper breakthrough curve. Figure 6-5 shows how temperature impacts the adsorption of CO<sub>2</sub> onto activated carbon. Increase in temperature results in earlier breakthrough point and shorter breakthrough time which is associated with exothermic nature of adsorption process. Higher temperature also made the breakthrough curves steeper resulting in decreasing the mass transfer zone. The results indicate that the impact of temperature are more important than CO<sub>2</sub> content and feed flowrate. As it observed in Figure 6-6, the higher feed flowrate results in shorter retention time of the gas in the fixed bed and earlier breakthrough time and faster saturation of bed. Working at a higher feed flow rate results in more CO<sub>2</sub> going through bed which leads to faster saturation of bed. However, the feed flow rate doesn't have a great impact on CO<sub>2</sub> adsorption capacity of activated carbon. These observations are in agreement with those reported before<sup>160,161</sup>.

The breakthrough CO<sub>2</sub> adsorption results in Figures 6-4 to 6-6 illustrate that the binary adsorption of CO<sub>2</sub> in N<sub>2</sub> on KOH activated carbon are well represented by the Langmuir model

with the parameters calculated according to single component adsorption measurements. In the case of different CO<sub>2</sub> initial content (see Figure 6-4), the model presents a closer prediction near breakthrough point to the experimental data as compared to data in Figures 6-5 and 6-6. The reproducibility of the experimental results with simulation confirms the assumptions in this model under this operation conditions. The experimental conditions and mass transfer parameters used in the model are summarized in Table 6-4.

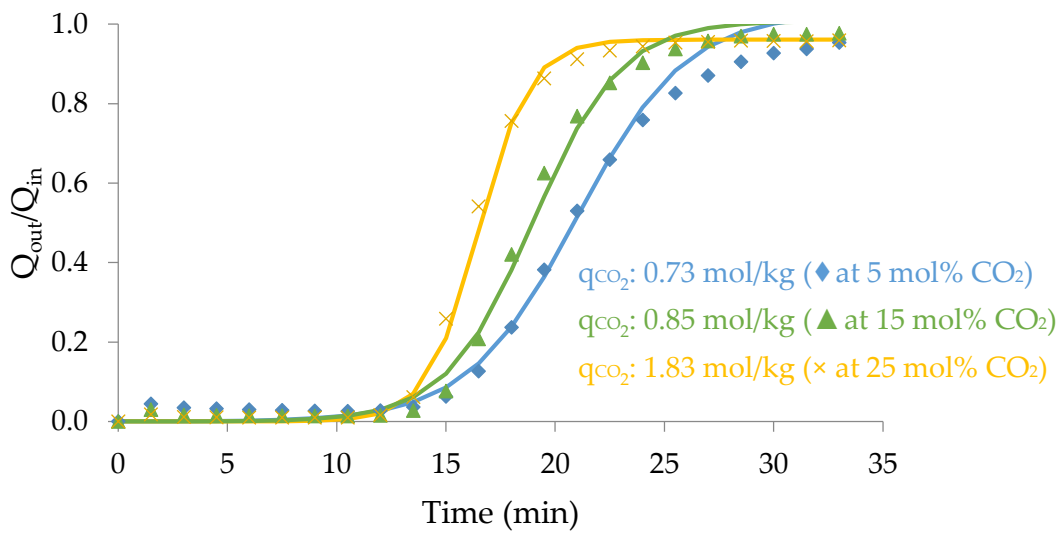


Figure 6-4: Comparison of experimentally measured breakthrough curves of CO<sub>2</sub> adsorption on KOH activated carbon using 5, 15 and 25 mol% CO<sub>2</sub> in inlet feed with model predictions. ◆,  $y_{CO_2}=5$  mol%; ▲,  $y_{CO_2}=15$  mol%; ×,  $y_{CO_2}=25$  mol%; solid lines represent the model predictions.

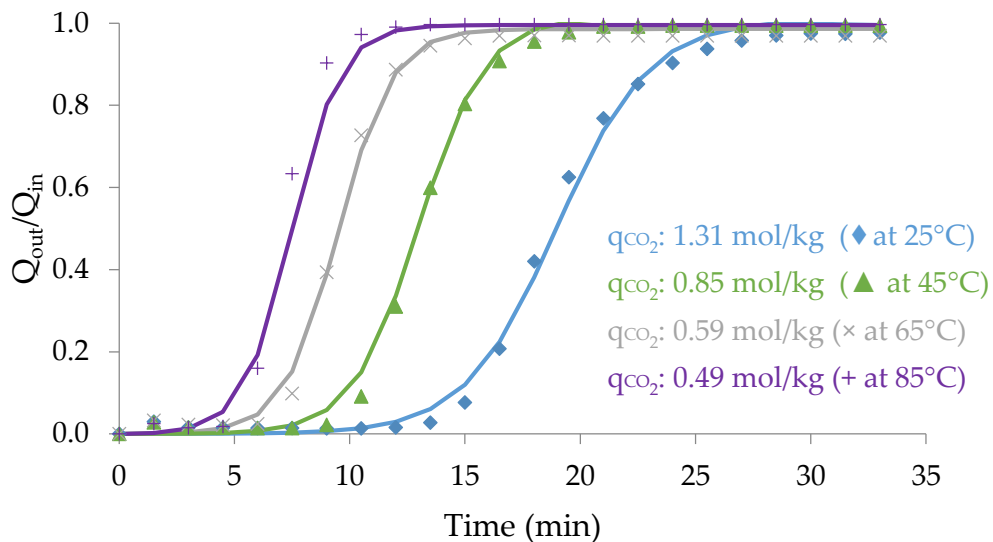


Figure 6-5: Comparison of experimentally measured breakthrough curves of CO<sub>2</sub> adsorption on KOH activated carbon at 25, 45, 65 and 85 °C with model predictions. ♦, T=25°C; ▲, T=45°C; ×, T=65°C; +, T=85°C; solid lines represent the model predictions.

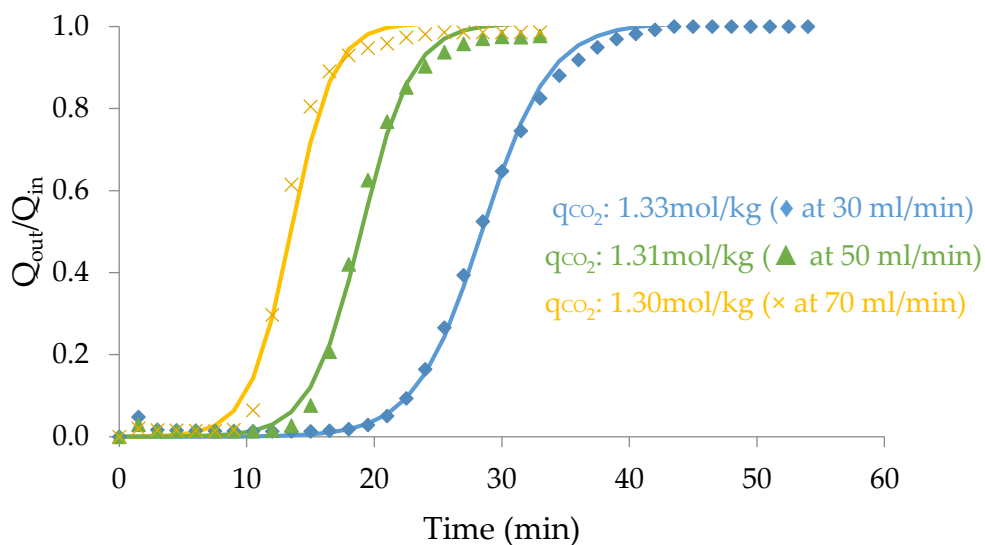


Figure 6-6: Comparison of experimentally measured breakthrough curves of CO<sub>2</sub> adsorption on KOH activated carbon using feed flowrate of 30, 50 and 70 ml/min with model predictions. ×, Q= 70ml/min; ▲, Q= 50ml/min; ♦, Q= 30ml/min; solid lines represent the model predictions.

Table 6-4: Experimental conditions and mass transfer parameters used in model

No.	Temperature	flowrate	mole fraction of CO <sub>2</sub>	D <sub>ax</sub>	D <sub>p</sub>	k <sub>f</sub>
	°C	ml/min	Mol%	cm <sup>2</sup> /s	cm <sup>2</sup> /s	cm/s
1	25	50	15	2.724	2.962×10 <sup>-3</sup>	7.488
2	45	50	15	3.051	3.0693×10 <sup>-3</sup>	8.329
3	65	50	15	3.394	3.173×10 <sup>-3</sup>	9.210
4	85	50	15	3.752	3.273×10 <sup>-3</sup>	10.130

### 6.4.3 Controlling mass transfer step

According to Silva <sup>162</sup>, the controlling mechanism in adsorption process can be disguised using Equations 6-15 and 6-16. If  $\gamma (1 + \alpha) < 0.1$ , then the micropore diffusion is the controlling mechanism in adsorption process; if  $\gamma (1 + \alpha) > 10$ , then the macropore diffusion is the controlling mechanism in adsorption process and if  $0.1 < \gamma (1 + \alpha) < 10$  then both macropore and micropore diffusion are important in the adsorption process,

$$\gamma = \frac{D_c/r_c^2}{D_p/R_p^2} \quad (6-15)$$

$$\alpha = \frac{1 - \varepsilon_p}{\varepsilon_p} H \quad (6-16)$$

According to the calculated parameters in this system,  $\gamma (1 + \alpha) < 0.1$ , which confirms that the micropore resistance is the controlling mass transport mechanism for CO<sub>2</sub> adsorption on KOH activated carbon under the studied adsorption condition. These results confirm that the micropores play a critical role in CO<sub>2</sub> adsorption at post combustion flue gas conditions.

### 6.5 Conclusions

The fixed-bed adsorption of CO<sub>2</sub> from CO<sub>2</sub>/N<sub>2</sub> mixtures on activated carbon was studied. The single-component adsorption equilibrium of CO<sub>2</sub> and N<sub>2</sub> were measured at 0, 25, 50 and 75 °C

and fitted with the Langmuir model. An isothermal bi-LDF model was developed for CO<sub>2</sub> adsorption in a binary mixture of CO<sub>2</sub>/N<sub>2</sub>. The breakthrough curves of the CO<sub>2</sub> adsorption from CO<sub>2</sub>/N<sub>2</sub> mixtures on activated carbon were measured experimentally and compared to theoretical breakthrough curves at different experimental conditions such as feed flow rate, adsorption temperature, and feed concentration. Higher feed flowrate and higher CO<sub>2</sub> content result in earlier breakthrough time, however temperature has the greatest impact on CO<sub>2</sub> adsorption on activated carbon. It was observed that the decrease in temperature results in a longer breakthrough time and wider mass transfer zone. According to the experimental data and simulation results, it was confirmed that the micropore diffusion is the controlling step for CO<sub>2</sub> adsorption on the microporous activated carbon.

## Chapter 7 Conclusions and Recommendations for Future Work

### 7.1 Conclusions

The overall objective of this work was to (1) understand the impact of precursors, pyrolysis conditions and activating agents on physical properties and adsorption performance of activated carbon, (2) understand the effect of process conditions on the adsorption process and optimize these conditions, (3) enhance CO<sub>2</sub> adsorption performance of the activated carbon using metal impregnation, and (4) develop a mass transfer model to simulate and predict CO<sub>2</sub> adsorption for scale-up of this process.

This study examined the effects of three different types of activating agents on physical and chemical properties of the activated carbon. The adsorption performance of the prepared activated carbons was then tested under a temperature range of 25–65°C and inlet CO<sub>2</sub> concentration range of 10–30 mol.% in inert gas. Decrease in temperature and increase in initial CO<sub>2</sub> content resulted in higher CO<sub>2</sub> adsorption. KOH activated carbon with larger surface area and microporous structure had a better performance for CO<sub>2</sub> adsorption. However, at high temperature and/or low concentration of CO<sub>2</sub>, all activated carbon samples show poor CO<sub>2</sub> adsorption capacities. The optimum conditions for better CO<sub>2</sub> are low temperature and high CO<sub>2</sub> content.

Study of the impact of biomass and pyrolysis method revealed that the significant differences in surface chemistry, porous structure and morphology of the activated carbons are resulted from pyrolysis conditions. Overall for the same precursor, the fast pyrolysis process led to larger surface area and total pore volume, smaller particle size and ultra-pore volume, and a larger contribution of phenolic/ketone and carboxylic groups. However, activating agent determined the porosity of the activated carbon and impact of the pyrolysis method and biomass is not as remarkable as that of activating agent.

The CO<sub>2</sub> uptake is closely related to the pore size distribution of activated carbons the gas diffusion in activated carbons is controlled within the micropore resistance<sup>153</sup>. The enlargement of the pore width of microspores resulted in remarkable decrease in CO<sub>2</sub> adsorption capacity. Similar behavior was reported before for AC at different temperature<sup>55,136,153</sup>. This result is a key

point of this thesis and optimization of pyrolysis/activation process to maximize the ration of the ultra-micropore volume to total pore volume for better CO<sub>2</sub> adsorption capacity and selectivity required attention.

To improve CO<sub>2</sub> adsorption at moderate temperature, MgO impregnated activated carbon was prepared using different preparation methods. Preparation method affects the porosity and metal dispersion on activated carbons. Impregnation of activated carbon with magnesium oxide improved the adsorption performance by increasing the breakthrough time. However, increase in breakthrough time is more remarkable at higher temperature. Comparison of the results of CO<sub>2</sub> adsorption on MgO-impregnated activated carbon at 100 °C with not-impregnated activated carbon shows a 65% increase using MgO impregnated activated carbon.

An isothermal bi-LDF model was developed to simulate the CO<sub>2</sub> adsorption experiments. The equilibrium data were fitted to Langmuir isotherm and the developed model was compared to experimental results. It was confirmed that the controlling mass transfer step is micropore mass transfer resistance.

## 7.2 Recommendations for future work

- Impact of presence of moisture and other greenhouse gases such as moisture, methane, carbon monoxide, SO<sub>2</sub> and NO<sub>x</sub> on adsorption capacity and selectivity of activated carbon should be studied.
- Different methods of gas desorption such as vacuum desorption or combination of thermal and vacuum desorption should be tested to optimize the desorption process.
- Feasibility study and life cycle assessments of the fixed-bed adsorption and technical-economical comparison of this technology should be performed with the existing absorption units to evaluate the industrial application of this process.
- A comparison of the promising solid sorbents such as zeolite, MOFs and carbo nanotubes based on technical and economical evaluation should be studied.
- Surface chemistry and micro-structure of saw dust from different sources as a precursor of activated carbon should be evaluated.

## References

- (1) Shahkarami, S.; Azargohar, R.; Dalai, A. K.; Soltan, J. Breakthrough CO<sub>2</sub> Adsorption in Bio-Based Activated Carbons. *J. Environ. Sci.* **2015**, *34*, 68.
- (2) IPCC. *Climate Change 2014 Synthesis Report Summary Chapter for Policymakers*; 2014.
- (3) US Department of Commerce, NOAA, E. S. R. L. ESRL Global Monitoring Division - Global Greenhouse Gas Reference Network <http://www.esrl.noaa.gov/gmd/ccgg/trends/> (accessed Jan 6, 2016).
- (4) *IPCC Special Report on Carbon Dioxide Capture and Storage*; 2005.
- (5) Leung, D. Y. C.; Caramanna, G.; Maroto-Valer, M. M. An Overview of Current Status of Carbon Dioxide Capture and Storage Technologies. *Renew. Sustain. Energy Rev.* **2014**, *39*, 426.
- (6) United Nations. *Adoption of the Paris Agreement*; 2015; Vol. 21930.
- (7) Herzog, H.; Meldon, J.; Hatton, A. *Advanced Post-Combustion CO<sub>2</sub> Capture*; 2009.
- (8) Krutka, H. M.; Sjostrom, S.; Bustard, C. J.; Durham, M.; Baldrey, K. Summary of Post-Combustion CO<sub>2</sub> Capture Technologies for Existing Coal-Fired Power Plants. In *Air & Waste Management Association Annual Conference*; 2007; pp 1–10.
- (9) Olajire, A. a. CO<sub>2</sub> Capture and Separation Technologies for End-of-Pipe Applications - A Review. *Energy*. 2010, pp 2610–2628.
- (10) Metz B., Davidson O., Coninck H., L. M. and M. L. *IPCC Special Report on Carbon Dioxide Capture and Storage*; Cambridge, 2005.
- (11) Su, F.; Lu, C.; Cnen, W.; Bai, H.; Hwang, J. F. Capture of CO<sub>2</sub> from Flue Gas via Multiwalled Carbon Nanotubes. *Sci. Total Environ.* **2009**, *407* (8), 3017.
- (12) Fernandes, M. B.; Skjemstad, J. O.; Johnson, B. B.; Wells, J. D.; Brooks, P. Characterization of Carbonaceous Combustion Residues. I. Morphological, Elemental and Spectroscopic Features. *Chemosphere* **2003**, *51*, 785.
- (13) Jang, D.-I.; Park, S.-J. Influence of Nickel Oxide on Carbon Dioxide Adsorption Behaviors of Activated Carbons. *Fuel* **2012**, *102*, 439.
- (14) Somy, A.; Mehrnia, M. R.; Amrei, H. D.; Ghanizadeh, A.; Safari, M. Adsorption of Carbon Dioxide Using Impregnated Activated Carbon Promoted by Zinc. *Int. J. Greenh. Gas Control* **2009**, *3*, 249.
- (15) Wang, S.; Yan, S.; Ma, X.; Gong, J. Recent Advances in Capture of Carbon Dioxide

- Using Alkali-Metal-Based Oxides. *Energy Environ. Sci.* **2011**, *4*, 3805.
- (16) Wang, Q.; Luo, J.; Zhong, Z.; Borgna, A. CO<sub>2</sub> Capture by Solid Adsorbents and Their Applications: Current Status and New Trends. *Energy Environ. Sci.* **2011**, *4*, 42.
- (17) Greenwood, N. N.; Earnshaw, A. *Chemistry of the Elements*; Elsevier, 2012.
- (18) House, J. E. *Fundamentals of Quantum Chemistry*; Academic Press, 2004.
- (19) Wilcox, J. Adsorption. In *Carbon Capture*; Springer: New York, NY, 2012; pp 115–175.
- (20) Liu, Y.; Wilcox, J. Molecular Simulation Studies of CO<sub>2</sub> Adsorption by Carbon Model Compounds for Carbon Capture and Sequestration Applications. *Environ. Sci. Technol.* **2013**, *47*, 95.
- (21) Freund, P.; Bachu, S.; Gupta, M. Annex I - Properties of CO<sub>2</sub> and Carbon-Based Fuels; 2006.
- (22) carbon dioxide | CO<sub>2</sub> - PubChem  
[https://pubchem.ncbi.nlm.nih.gov/compound/carbon\\_dioxide#section=Top](https://pubchem.ncbi.nlm.nih.gov/compound/carbon_dioxide#section=Top) (accessed Feb 12, 2016).
- (23) Post-Combustion CO<sub>2</sub> Control | netl.doe.gov  
<http://www.netl.doe.gov/research/coal/carbon-capture/post-combustion> (accessed Jan 13, 2016).
- (24) Schock, R. N.; Sims, R. E. H.; Torres-Martínez, J.; Adegbululgbé, A.; Fenhann, J.; Konstantinaviciute, I.; Moomaw, W.; Nimir, H. B.; Schlamadinger, B.; Turner, C.; et al. *Energy Supply*; 2007.
- (25) Matthias Finkenrath, J. S. and D. V. CCS Retrofit-Analysis of the Globally Installed Coal Fired Plant Fleet. *Int. Energy Agency Inf. Pap.* **2012**, *9*.
- (26) Granite, E. J.; Pennline, H. W. Photochemical Removal of Mercury from Flue Gas. *Ind. Eng. Chem. Res.* **2002**, *41* (22), 5470.
- (27) Zevenhoven, R.; Kilpinen, P. Flue Gases and Fuel Gases. In *Control of Pollutants in Flue Gases and Fuel Gases*; 2001; p 2.1-2.12.
- (28) Li, J.-R.; Kuppler, R. J.; Zhou, H.-C. Selective Gas Adsorption and Separation in Metal-Organic Frameworks. *Chem. Soc. Rev.* **2009**, *38* (5), 1477.
- (29) *Adsorption and Diffusion*; Karge, H. G., Weitkamp, J., Eds.; Springer-Verlag Berlin Heidelberg, 2008; Vol. 53.
- (30) Jiménez, V.; Ramírez-Lucas, A.; Díaz, J. A.; Sánchez, P.; Romero, A. CO<sub>2</sub> Capture in

- Different Carbon Materials. *Environ. Sci. Technol.* **2012**, *46* (13), 7407.
- (31) García, S.; Gil, M. V.; Martín, C. F.; Pis, J. J.; Rubiera, F.; Pevida, C. Breakthrough Adsorption Study of a Commercial Activated Carbon for Pre-Combustion CO<sub>2</sub> Capture. *Chem. Eng. J.* **2011**, *171* (2), 549.
- (32) Plaza, M. G.; García, S.; Rubiera, F.; Pis, J. J.; Pevida, C. Post-Combustion CO<sub>2</sub> Capture with a Commercial Activated Carbon: Comparison of Different Regeneration Strategies. *Chem. Eng. J.* **2010**, *163* (1–2), 41.
- (33) Konduru, N.; Lindner, P.; Assaf-anid, N. M. Curbing the Greenhouse Effect by Carbon Dioxide Adsorption with Zeolite 13X. *AIChE J.* **2007**, *53* (12), 3137.
- (34) Yang, R. T. *Adsorbents: Fundamentals and Applications*; John Wiley & Sons, 2003.
- (35) Sing, K. S. W.; Everett, D. H.; Haul, R. a. W.; Moscou, L.; Pierotti, R. a.; Rouquérol, J.; Siemieniewska, T. Reporting Physisorption Data for Gas/Solid Systems. *Pure Appl. Chem.* **1982**, *54* (11), 2201.
- (36) Rouquerol, F.; Rouquerol, J.; Sing, K. Assessment of Mesoporosity. In *Adsorption by Powders and Porous Solids: Principles, Methodology and Applications*; Academic Press: San Diego, 1999; pp 191–217.
- (37) Brunauer, S.; Emmett, P. H.; Teller, E. Adsorption of Gases in Multimolecular Layers. *J. Am. Chem. Soc.* **1938**, *60* (1), 309.
- (38) *Physical Adsorption: Experiment, Theory and Applications*; Fraissard, J., Ed.; Springer Netherlands, 1997.
- (39) Lowell, S.; Shields, J. E.; Thomas, M. A.; Thommes, M. *Characterization of Porous Solids and Powders: Surface Area, Pore Size and Density*; Springer Science & Business Media, 2012.
- (40) Seaton, N. A.; Walton, J. P. R. B.; Quirke, N. A New Analysis Method for the Determination of the Pore Size Distribution of Porous Carbons from Nitrogen Adsorption Measurements. *Carbon N. Y.* **1989**, *27* (6), 853.
- (41) Lastoskie, C.; Gubbins, K. E.; Quirke, N. Pore Size Distribution Analysis of Microporous Carbons: A Density Functional Theory Approach. *J. Phys. Chem.* **1993**, *97* (18), 4786.
- (42) Landers, J.; Gor, G. Y.; Neimark, A. V. Density Functional Theory Methods for Characterization of Porous Materials. *Colloids Surfaces A Physicochem. Eng. Asp.* **2013**, *437*, 3.

- (43) ISO 15901-3:2007 - Pore size distribution and porosity of solid materials by mercury porosimetry and gas adsorption -- Part 3: Analysis of micropores by gas adsorption [http://www.iso.org/iso/iso\\_catalogue/catalogue\\_tc/catalogue\\_detail.htm?csnumber=40364](http://www.iso.org/iso/iso_catalogue/catalogue_tc/catalogue_detail.htm?csnumber=40364) (accessed Jan 15, 2016).
- (44) Blanco, A. A. G.; de Oliveira, J. C. A.; López, R.; Moreno-Piraján, J. C.; Giraldo, L.; Zgrablich, G.; Sapag, K. A Study of the Pore Size Distribution for Activated Carbon Monoliths and Their Relationship with the Storage of Methane and Hydrogen. *Colloids Surfaces A Physicochem. Eng. Asp.* **2010**, *357* (1), 74.
- (45) Marsh, H.; Reinoso, F. R. *Activated Carbon*; Elsevier, 2006.
- (46) Duong, D. Do. *Adsorption Analysis: Equilibria and Kinetics, Volume 1*; 1998; Vol. 2.
- (47) Bansal, R. C.; Goya, M. *Activated Carbon Adsorption*; CRC Press, 2005.
- (48) *Fundamental Issues in Control of Carbon Gasification Reactivity*; L. Lahaye, P. E., Ed.; Springer Science & Business Media, 2012.
- (49) Cruz, D. C.; Berruti, F.; Briens, C. Production of Bio-Coal and Activated Carbon from Biomass. **2012**, *1* (I), 30.
- (50) *Biochar: Production, Characterization, and Applications*; Yong Sik Ok, Sophie M. Uchimiya, Scott X. Chang, N. B., Ed.; CRC Press, 2015.
- (51) Ioannidou, O.; Zabaniotou, A. Agricultural Residues as Precursors for Activated Carbon production—A Review. *Renew. Sustain. Energy Rev.* **2007**, *11* (9), 1966.
- (52) Elzobair, K. BIOCHAR EFFECTS ON SOIL MICROBIAL COMMUNITIES AND RESISTANCE OF ENZYMES TO STRESS, Colorado State University, 2013.
- (53) Shahkarami, S.; Dalai, A. K.; Soltan, J.; Hu, Y.; Wang, D. Selective CO<sub>2</sub> Capture by Activated Carbons: Evaluation of the Effects of Precursors and Pyrolysis Process. *Energy & Fuels* **2015**, *29*, 7433.
- (54) Wenming Hao, Eva Björkman, Malte Lilliestråle, N. H. Activated Carbons Prepared from Hydrothermally Carbonized Waste Biomass Used as Adsorbents for CO<sub>2</sub>. *Appl. Energy* **2013**, *112*, 526.
- (55) Deng, S.; Wei, H.; Chen, T.; Wang, B.; Huang, J.; Yu, G. Superior CO<sub>2</sub> Adsorption on Pine Nut Shell-Derived Activated Carbons and the Effective Micropores at Different Temperatures. *Chem. Eng. J.* **2014**, *253*, 46.
- (56) F. Rodríguez-Reinoso, M. Molina-Sabio, M. T. G. The Use of Steam and CO<sub>2</sub> as

- Activating Agents in the Preparation of Activated Carbons. *Carbon N. Y.* **1995**, 33 (1), 15.
- (57) Azargohar, R. (University of S. Production Of Activated Carbon And Its Catalytic Application For Oxidation Of Hydrogen Sulphide. **2009**.
- (58) Lee, H. C.; Monji, M.; Parsley, D.; Sahimi, M.; Liu, P.; Egolfopoulos, F.; Tsotsis, T. Use of Steam Activation as a Post-Treatment Technique in the Preparation of Carbon Molecular Sieve Membranes. *Ind. Eng. Chem. Res.* **2013**, 52 (3), 1122.
- (59) Abechi, S. E.; Gimba, C. E.; Uzairu, A.; Dallatu, Y. A. Preparation and Characterization of Activated Carbon from Palm Kernel Shell by Chemical Activation. *Res. J. Chem. Sci.* **2013**, 3 (7), 54.
- (60) Ismadji, S.; Sudaryanto, Y.; Hartono, S. B.; Setiawan, L. E. K.; Ayucitra, a. Activated Carbon from Char Obtained from Vacuum Pyrolysis of Teak Sawdust: Pore Structure Development and Characterization. *Bioresour. Technol.* **2005**, 96 (12), 1364.
- (61) Prakash Kumar, B. G.; Shivakamy, K.; Miranda, L. R.; Velan, M. Preparation of Steam Activated Carbon from Rubberwood Sawdust (*Hevea Brasiliensis*) and Its Adsorption Kinetics. *J. Hazard. Mater.* **2006**, 136 (3), 922.
- (62) Lima, I. M.; Boateng, A. a.; Klasson, K. T. Physicochemical and Adsorptive Properties of Fast-Pyrolysis Bio-Chars and Their Steam Activated Counterparts. *J. Chem. Technol. Biotechnol.* **2010**, 85 (May), 1515.
- (63) Girgis, B. S.; Yunis, S. S.; Soliman, A. M. Characteristics of Activated Carbon from Peanut Hulls in Relation to Conditions of Preparation. *Mater. Lett.* **2002**, 57 (1), 164.
- (64) Yang, T.; Lua, A. C. Characteristics of Activated Carbons Prepared from Pistachio-Nut Shells by Potassium Hydroxide Activation. *Microporous Mesoporous Mater.* **2003**, 63 (1–3), 113.
- (65) El-Hendawy, a. N. a; Samra, S. E.; Girgis, B. S. Adsorption Characteristics of Activated Carbons Obtained from Corncobs. *Colloids Surfaces A Physicochem. Eng. Asp.* **2001**, 180 (3), 209.
- (66) Romanos, J.; Beckner, M.; Rash, T.; Firlej, L.; Kuchta, B.; Yu, P.; Suppes, G.; Wexler, C.; Pfeifer, P. Nanospace Engineering of KOH Activated Carbon. *Nanotechnology* **2011**, 23 (1), 15401.
- (67) Lillo-Ródenas, M. A.; Juan-Juan, J.; Cazorla-Amorós, D.; Linares-Solano, A. About Reactions Occurring during Chemical Activation with Hydroxides. *Carbon N. Y.* **2004**, 42

- (7), 1365.
- (68) Bansal, R.; Goyal, M. *Activated Carbon Adsorption*; 2005.
- (69) Zhang, Z.; Zhang, W.; Chen, X.; Xia, Q.; Li, Z. On Zeolite 13X and Activated Carbon with Higher Surface Area. *Sep. Sci. Technol.* **2010**, *45* (5), 710.
- (70) Hauchhum, L.; Mahanta, P. Carbon Dioxide Adsorption on Zeolites and Activated Carbon by Pressure Swing Adsorption in a Fixed Bed. *Int. J. Energy Environ. Eng.* **2014**, *5* (4), 349.
- (71) Chue, K. T.; Kim, J. N.; Yoo, J.; Cho, S. H.; Yang, T. Comparison of Activated Carbon and Zeolite 13X for CO<sub>2</sub> Recovery from Flue Gas by Pressure Swing Adsorption. *Ind. Eng. Chem. Res.* **1995**, *34* (2), 591.
- (72) Himeno, S.; Komatsu, T.; Fujita, S. High-Pressure Adsorption Equilibria of Methane and Carbon Dioxide on Several Activated Carbons. *J. Chem. Eng. Data* **2005**, *50* (2), 369.
- (73) Lal, R. Sequestration of Atmospheric CO<sub>2</sub> in Global Carbon Pools. *Energy Environ. Sci.* **2008**, *1* (1), 86.
- (74) Na, B.-K.; Koo, K.-K.; Eum, H.-M.; Lee, H.; Song, H. K. CO<sub>2</sub> Recovery from Flue Gas by PSA Process Using Activated Carbon. *Korean J. Chem. Eng.* **2001**, *18* (2), 220.
- (75) Do, D. D.; Wang, K. A New Model for the Description of Adsorption Kinetics in Heterogeneous Activated Carbon. *Carbon N. Y.* **1998**, *36* (10), 1539.
- (76) Sircar, S.; Golden, T. C. Isothermal and Isobaric Desorption of Carbon Dioxide by Purge. *Ind. Eng. Chem. Res.* **1995**, *34* (8), 2881.
- (77) Samanta, A.; Zhao, A.; Shimizu, G. K. H.; Sarkar, P.; Gupta, R. Post-Combustion CO<sub>2</sub> Capture Using Solid Sorbents : A Review. *Ind. Eng. Chem. Res.* **2012**, *51* (4), 1438.
- (78) Przepiórski, J.; Skrodzewicz, M.; Morawski, A. W. High Temperature Ammonia Treatment of Activated Carbon for Enhancement of CO<sub>2</sub> Adsorption. *Appl. Surf. Sci.* **2004**, *225* (1–4), 235.
- (79) Zhang, Y.; Maroto-valer, M. M.; Tang, Z. Microporous Activated Carbons Produced From Unburned Carbon in Fly Ash and Their Application for CO<sub>2</sub> Capture. *Div. Fuel Chem., Am. Chem. Soc. Prepr. Symp. Prepr. Symp.* **2004**, *49* (1), 304.
- (80) Kikkinides, E. S.; Yang, R. T. Concentration and Recovery of CO<sub>2</sub> from Flue Gas by Pressure Swing Adsorption. *Ind. Eng. Chem. Res.* **1993**, *32* (11), 2714.
- (81) Vaart, R. van der; Huiskes, C.; Bosch, H.; Reith, T. Single and Mixed Gas Adsorption

- Equilibria of Carbon Dioxide / Methane on Activated Carbon. *Adsorption* **2000**, 6 (4), 311.
- (82) Lu, C.; Bai, H.; Wu, B.; Su, F.; Hwang, J. F. Comparative Study of CO<sub>2</sub> Capture by Carbon Nanotubes, Activated Carbons, and Zeolites. *Energy & Fuels* **2008**, 22 (5), 3050.
- (83) Ranz, W. E.; Marshall, W. R. Evaporation from Drops. Parts I & II. *Chem. Eng. Progr* **1952**, 48 (22), 141.
- (84) Wakao, N.; Funazkri, T. Effect of Fluid Dispersion Coefficients on Particle-to-Fluid Mass Transfer Coefficients in Packed Beds. *Chem. Eng. Sci.* **1978**, 33 (10), 1375.
- (85) Thoenes, D.; Kramers, H. Mass Transfer from Spheres in Various Regular Packings to a Flowing Fluid. *Chem. Eng. Sci.* **1958**, 8 (3–4), 271.
- (86) Petrovic, L. J.; Thodos, G. Mass Transfer in Flow of Gases through Packed Beds. Low Reynolds Number Region. *Ind. Eng. Chem. Fundam.* **1968**, 7 (2), 274.
- (87) Green, D. W.; Perry, R. H. *Perry's Chemical Engineers' Handbook, Eighth Edition*; McGraw-Hill: New York, Chicago, San Francisco, Lisbon, London, Madrid, Mexico City, Milan, New Delhi, San Juan, Seoul, Singapore, Sydney, Toronto, 2008.
- (88) Oka, S.; Anthony, E. J. *Fluidized Bed Combustion*; CRC Press, 2003.
- (89) Lagergren, S. About the Theory of so-Called Adsorption of Soluble Substances. *K. Sven. vetenskapsakademiens Handl.* **1898**, 24 (4), 1.
- (90) Qiu, H.; Lv, L.; Pan, B.; Zhang, Q. Q.; Zhang, W.; Zhang, Q. Q. Critical Review in Adsorption Kinetic Models. *J. Zhejiang Univ. Sci. A* **2009**, 10 (5), 716.
- (91) Ruthven, D. M.; Xu, Z.; Farooq, S. Sorption Kinetics in PSA Systems. *Gas Sep. Purif.* **1993**, 7 (2), 75.
- (92) Haq, N.; Ruthven, D. M. Chromatographic Study of Sorption and Diffusion in 4A Zeolite. *J. Colloid Interface Sci.* **1986**, 112 (1), 154.
- (93) Grande, C. a; Rodrigues, A. E. Adsorption of Binary Mixtures of Propane–Propylene in Carbon Molecular Sieve 4A. *Ind. Eng. Chem. Res.* **2004**, 43 (25), 8057.
- (94) *Nanoporous Materials: Science and Engineering*; Lu, G. Q., Zhao, X. S., Eds.; World Scientific, 2004; Vol. 22.
- (95) Shi, J. Q.; Durucan, S. A Bidisperse Pore Diffusion Model for Methane Displacement Desorption in Coal by CO<sub>2</sub> Injection☆. *Fuel* **2003**, 82 (10), 1219.
- (96) Khalighi, M.; Farooq, S.; Karimi, I. Nonisothermal Pore Diffusion Model for a Kinetically

- Controlled Pressure Swing Adsorption Process. *Ind. Eng. Chem. Res.* **2012**, *51* (32), 10659.
- (97) Butt, J. B. Mass Transfer in Heterogeneous Catalysis, C. N. Satterfield, Massachusetts Institute of Technology Press, Cambridge, Mass.(1970). 267 Pages. *AIChE J.* **1970**, *16* (3), 509.
- (98) Mugge, J. *Adsorption Isotherms from Temperature-Programmed Physiosorption-Equilibrium & Kinetics*; University of Twente, 2000.
- (99) Do, H. D.; Do, D. D. Maxwell-Stefan Analysis of Multicomponent Transient Diffusion in a Capillary and Adsorption of Hydrocarbons in Activated Carbon Particle. *Chem. Eng. Sci.* **1998**, *53* (6), 1239.
- (100) Do, D.; Do, H. Surface Diffusion of Hydrocarbons in Activated Carbon: Comparison between Constant Molar Flow, Differential Permeation and Differential Adsorption Bed Methods. *Adsorption* **2001**, *7*, 189.
- (101) Grande, C. A.; Rodrigues, A. E. Propane/propylene Separation by Pressure Swing Adsorption Using Zeolite 4A. *Ind. Eng. Chem. Res.* **2005**, *44* (23), 8815.
- (102) Lito, P. F.; Santiago, A. S.; Cardoso, S. P.; Figueiredo, B. R.; Silva, C. M. New Expressions for Single and Binary Permeation through Zeolite Membranes for Different Isotherm Models. *J. Memb. Sci.* **2011**, *367* (1–2), 21.
- (103) Krishna, R.; Vlugt, T. J. H.; Smit, B. Influence of Isotherm Inflection on Diffusion in Silicalite. *Chem. Eng. Sci.* **1999**, *54* (12), 1751.
- (104) Shen, C.; Yu, J.; Li, P.; Grande, C.; Rodrigues, A. Capture of CO<sub>2</sub> from Flue Gas by Vacuum Pressure Swing Adsorption Using Activated Carbon Beads. *Adsorption* **2011**, *17* (1), 179.
- (105) Bell, S. A Beginner's Guide to Uncertainty of Measurement. *Meas. Good Pract. Guid.* **1999**, No. 2, 41.
- (106) Heidari, A.; Younesi, H. Evaluation of CO<sub>2</sub> Adsorption with Eucalyptus Wood Based Activated Carbon Modified by Ammonia Solution through Heat Treatment. *Chem. Eng. J.* **2014**, *254*, 503.
- (107) Azargohar, R.; Dalai, a. K. Production of Activated Carbon from Luscar Char: Experimental and Modeling Studies. *Microporous Mesoporous Mater.* **2005**, *85* (3), 219.
- (108) Otowa, T.; Nojima, Y.; Miyazaki, T. Development of KOH Activated High Surface Area

- Carbon and Its Application to Drinking Water Purification. *Carbon N. Y.* **1997**, *35* (9), 1315.
- (109) Lillo-Rodenas, M. A.; Lozano-Castello, D.; Cazorla-Amoros, D.; Linares-Solano, A. Preparation of Activated Carbons from Spanish Anthracite: II. Activation by NaOH. *Carbon N. Y.* **2001**, *39* (5), 751.
- (110) Lozano-Castello', D.; Lillo-Ro'denas, M. A.; Cazorla-Amoro's, D.; Linares-Solano, A. Preparation of Activated Carbons from Spanish Anthracite: I. Activation by KOH. *Carbon N. Y.* **2001**, *39* (5), 741.
- (111) De, M.; Azargohar, R.; Dalai, A. K.; Shewchuk, S. R. Mercury Removal by Bio-Char Based Modified Activated Carbons. *Fuel* **2013**, *103*, 570.
- (112) Carter, E. M.; Katz, L. E.; Speitel, G. E.; Ramirez, D. Gas-Phase Formaldehyde Adsorption Isotherm Studies on Activated Carbon: Correlations of Adsorption Capacity to Surface Functional Group Density. *Environ. Sci. Technol.* **2011**, *45* (15), 6498.
- (113) García, S.; Gil, M. V.; Pis, J. J.; Rubiera, F.; Pevida, C. Cyclic Operation of a Fixed-Bed Pressure and Temperature Swing Process for CO<sub>2</sub> Capture: Experimental and Statistical Analysis. *Int. J. Greenh. Gas Control* **2013**, *12*, 35.
- (114) Zhou, J.-H.; Sui, Z.-J.; Zhu, J.; Li, P.; Chen, D.; Dai, Y.-C.; Yuan, W.-K. Characterization of Surface Oxygen Complexes on Carbon Nanofibers by TPD, XPS and FT-IR. *Carbon N. Y.* **2007**, *45* (4), 785.
- (115) Plaza, M. G.; Pevida, C.; Arias, B.; Fermoso, J.; Casal, M. D.; Martín, C. F.; Rubiera, F.; Pis, J. J. Development of Low-Cost Biomass-Based Adsorbents for Postcombustion CO<sub>2</sub> Capture. *Fuel* **2009**, *88* (12), 2442.
- (116) Shen, W.; Li, Z.; Liu, Y. Surface Chemical Functional Groups Modification of Porous Carbon. *Recent Patents Chem. Eng.* **2008**, *1* (1), 27.
- (117) Shafeeyan, M. S.; Daud, W. M. A. W.; Houshmand, A.; Shamiri, A. A Review on Surface Modification of Activated Carbon for Carbon Dioxide Adsorption. *J. Anal. Appl. Pyrolysis* **2010**, *89* (2), 143.
- (118) Hsu, S.-C.; Lu, C.; Su, F.; Zeng, W.; Chen, W. Thermodynamics and Regeneration Studies of CO<sub>2</sub> Adsorption on Multiwalled Carbon Nanotubes. *Chem. Eng. Sci.* **2010**, *65*, 1354.
- (119) Sjostrom, S.; Krutka, H. Evaluation of Solid Sorbents as a Retrofit Technology for CO<sub>2</sub>

- Capture. *Fuel* **2010**, *89* (6), 1298.
- (120) Liu, Q.; Zheng, T.; Wang, P.; Guo, L. Preparation and Characterization of Activated Carbon from Bamboo by Microwave-Induced Phosphoric Acid Activation. *Ind. Crops Prod.* **2010**, *31*, 233.
- (121) Sevilla, M.; Fuertes, a. B.; Mokaya, R. High Density Hydrogen Storage in Superactivated Carbons from Hydrothermally Carbonized Renewable Organic Materials. *Energy Environ. Sci.* **2011**, *4*, 1400.
- (122) Azargohar, R.; Jacobson, K. L.; Powell, E. E.; Dalai, A. K. Evaluation of Properties of Fast Pyrolysis Products Obtained, from Canadian Waste Biomass. *J. Anal. Appl. Pyrolysis* **2013**, *104*, 330.
- (123) Heymann, K.; Lehmann, J.; Solomon, D.; Schmidt, M. W. I.; Regier, T. C 1s K-Edge near Edge X-Ray Absorption Fine Structure (NEXAFS) Spectroscopy for Characterizing Functional Group Chemistry of Black Carbon. *Org. Geochem.* **2011**, *42* (9), 1055.
- (124) Regier, T.; Krochak, J.; Sham, T. K.; Hu, Y. F.; Thompson, J.; Blyth, R. I. R. Performance and Capabilities of the Canadian Dragon: The SGM Beamline at the Canadian Light Source. *Nucl. Instruments Methods Phys. Res. Sect. A Accel. Spectrometers, Detect. Assoc. Equip.* **2007**, *582*, 93.
- (125) Nanda, S.; Azargohar, R.; Kozinski, J. a.; Dalai, A. K. Characteristic Studies on the Pyrolysis Products from Hydrolyzed Canadian Lignocellulosic Feedstocks. *Bioenergy Res.* **2014**, *7* (1), 174.
- (126) Stöhr, J. *NEXAFS Spectroscopy*; Springer-Verlag Berlin Heidelberg, 1992.
- (127) Urquhart, S. G.; Ade, H. Trends in the Carbonyl Core (C 1S, O 1S)  $\rightarrow$   $\Pi^*c=O$  Transition in the near-Edge X-Ray Absorption Fine Structure Spectra of Organic Molecules. *J. Phys. Chem. B* **2002**, *106* (34), 8531.
- (128) Gillespie, a. W.; Sanei, H.; Diochon, a.; Ellert, B. H.; Regier, T. Z.; Chevrier, D.; Dynes, J. J.; Tarnocai, C.; Gregorich, E. G. Perennially and Annually Frozen Soil Carbon Differ in Their Susceptibility to Decomposition: Analysis of Subarctic Earth Hummocks by Bioassay, XANES and Pyrolysis. *Soil Biol. Biochem.* **2014**, *68*, 106.
- (129) J. Lehmann, D. Solomon, J. Brandes, H. Fleckenstein, C. J. and J. T. Synchrotron-Based near-Edge X-Ray Spectroscopy of Natural Organic Matter in Soils and Sediments. In *Biophysico-Chemical Processes Involving Natural Nonliving Organic Matter in*

- Environmental Systems*; Senesi, N., Xing, B., Huang, P. M., Eds.; John Wiley & Sons, Inc.: Hoboken, NJ, USA, 2009.
- (130) Solomon, D.; Lehmann, J.; Harden, J.; Wang, J.; Kinyangi, J.; Heymann, K.; Karunakaran, C.; Lu, Y.; Wirick, S.; Jacobsen, C. Micro- and Nano-Environments of Carbon Sequestration: Multi-Element STXM–NEXAFS Spectromicroscopy Assessment of Microbial Carbon and Mineral Associations. *Chem. Geol.* **2012**, *329*, 53.
- (131) Hopkins, R. J.; Tivanski, A. V.; Marten, B. D.; Gilles, M. K. Chemical Bonding and Structure of Black Carbon Reference Materials and Individual Carbonaceous Atmospheric Aerosols. *J. Aerosol Sci.* **2007**, *38* (6), 573.
- (132) Lehmann, J.; Liang, B.; Solomon, D.; Lerotic, M.; Luizão, F.; Kinyangi, J.; Schäfer, T.; Wirick, S.; Jacobsen, C. Near-Edge X-Ray Absorption Fine Structure (NEXAFS) Spectroscopy for Mapping Nano-Scale Distribution of Organic Carbon Forms in Soil: Application to Black Carbon Particles. *Global Biogeochem. Cycles* **2005**, *19* (1), n/a.
- (133) Cooney, R. R.; Urquhart, S. G. Chemical Trends in the near-Edge X-Ray Absorption Fine Structure of Monosubstituted and Para-Bisubstituted Benzenes. *J. Phys. Chem. B* **2004**, *108* (306), 18185.
- (134) Nováková, E.; Mitrea, G.; Peth, C.; Thieme, J.; Mann, K.; Salditt, T. Solid Supported Multicomponent Lipid Membranes Studied by X-Ray Spectromicroscopy. *Biointerphases* **2008**, *3*, FB44.
- (135) Sevilla, M.; Fuertes, A. B. Sustainable Porous Carbons with a Superior Performance for CO<sub>2</sub> Capture. *Energy Environ. Sci.* **2011**, *4* (5), 1765.
- (136) Sevilla, M.; Falco, C.; Titirici, M.-M.; Fuertes, A. B. High-Performance CO<sub>2</sub> Sorbents from Algae. *RSC Adv.* **2012**, 12792.
- (137) Presser, V.; McDonough, J.; Yeon, S.-H.; Gogotsi, Y. Effect of Pore Size on Carbon Dioxide Sorption by Carbide Derived Carbon. *Energy Environ. Sci.* **2011**, *4*, 3059.
- (138) Zhang, Z.; Zhou, J.; Xing, W.; Xue, Q.; Yan, Z.; Zhuo, S.; Qiao, S. Z. Critical Role of Small Micropores in High CO<sub>2</sub> Uptake. *Phys. Chem. Chem. Phys.* **2013**, *15* (7), 2523.
- (139) Suzuki, M. *Adsorption Engineering*; Kodansha, 1990; Vol. 14.
- (140) Toth, J. *Adsorption Theory, Modeling, And Analysis*; Marcel Dekker Inc: New York, 2002.
- (141) Lee, C. S.; Ong, Y. L.; Aroua, M. K.; Daud, W. M. a W. Impregnation of Palm Shell-

- Based Activated Carbon with Sterically Hindered Amines for CO<sub>2</sub> Adsorption. *Chem. Eng. J.* **2013**, *219*, 558.
- (142) Dastgheib, S. a.; Ren, J.; Rostam-Abadi, M.; Chang, R. Preparation of Functionalized and Metal-Impregnated Activated Carbon by a Single-Step Activation Method. *Appl. Surf. Sci.* **2014**, *290*, 92.
- (143) Liu, W. J.; Jiang, H.; Tian, K.; Ding, Y. W.; Yu, H. Q. Mesoporous Carbon Stabilized MgO Nanoparticles Synthesized by Pyrolysis of MgCl<sub>2</sub> Preloaded Waste Biomass for Highly Efficient CO<sub>2</sub> Capture. *Environ. Sci. Technol.* **2013**, *47*, 9397.
- (144) Bhagiyalakshmi, M.; Lee, J. Y.; Jang, H. T. Synthesis of Mesoporous Magnesium Oxide: Its Application to CO<sub>2</sub> Chemisorption. *Int. J. Greenh. Gas Control* **2010**, *4* (1), 51.
- (145) Ochs, D.; Braun, B.; Maus-Friedrichs, W.; Kemper, V. CO<sub>2</sub> Chemisorption at Ca and CaO Surfaces: A Study with MIES, UPS(HeI) and XPS. *Surf. Sci.* **1998**, *417* (2–3), 406.
- (146) Bian, S.-W.; Baltrusaitis, J.; Galhotra, P.; Grassian, V. H. A Template-Free, Thermal Decomposition Method to Synthesize Mesoporous MgO with a Nanocrystalline Framework and Its Application in Carbon Dioxide Adsorption. *J. Mater. Chem.* **2010**, *20* (39), 8705.
- (147) Bandosz, T. J. Surface Chemistry of Carbon Materials. In *Carbon Materials for Catalysis*; Serp, P., Figueiredo, J. L., Eds.; Wiley: New Jersey, 2008; pp 45–92.
- (148) Zhao, G.; Shi, J.; Liu, G.; Liu, Y.; Wang, Z.; Zhang, W.; Jia, M. Efficient Porous Carbon-Supported MgO Catalysts for the Transesterification of Dimethyl Carbonate with Diethyl Carbonate. *J. Mol. Catal. A Chem.* **2010**, *327*, 32.
- (149) Ding, Y.; Zhang, G.; Wu, H.; Hai, B.; Wang, L.; Qian, Y. Nanoscale Magnesium Hydroxide and Magnesium Oxide Powders: Control over Size, Shape, and Structure via Hydrothermal Synthesis. *Chem. Mater.* **2001**, *13*, 435.
- (150) Badoga, S.; Dalai, A. K.; Adjaye, J.; Hu, Y. Combined Effects of EDTA and Heteroatoms (Ti, Zr, and Al) on Catalytic Activity of SBA-15 Supported NiMo Catalyst for Hydrotreating of Heavy Gas Oil. *Ind. Eng. Chem. Res.* **2014**, *53* (6), 2137.
- (151) Agarwal, A.; Biegler, L. T.; Zitney, S. E. A Superstructure-Based Optimal Synthesis of PSA Cycles for Post-Combustion CO<sub>2</sub> Capture. *AIChE J.* **2010**, *56* (7), 1813.
- (152) Dantas, T. L. P.; Amorim, S. M.; Luna, F. M. T.; Silva, I. J.; de Azevedo, D. C. S.; Rodrigues, A. E.; Moreira, R. F. P. M. Adsorption of Carbon Dioxide onto Activated

- Carbon and Nitrogen-Enriched Activated Carbon: Surface Changes, Equilibrium, and Modeling of Fixed-Bed Adsorption. *Sep. Sci. Technol.* **2009**, *45* (1), 73.
- (153) Grande, C. a.; Lopes, F. V. S.; Ribeiro, A. M.; Loureiro, J. M.; Rodrigues, A. E. Adsorption of Off-Gases from Steam Methane Reforming (H<sub>2</sub>, CO<sub>2</sub>, CH<sub>4</sub>, CO and N<sub>2</sub>) on Activated Carbon. *Sep. Sci. Technol.* **2008**, *43* (6), 1338.
- (154) Shafeeyan, M. S.; Wan Daud, W. M. A.; Shamiri, A. A Review of Mathematical Modeling of Fixed-Bed Columns for Carbon Dioxide Adsorption. *Chem. Eng. Res. Des.* **2014**, *92* (5), 961.
- (155) Azevedo, D. C. S.; Rodrigues, A. E. Bilinear Driving Force Approximation in the Modeling of a Simulated Moving Bed Using Bidisperse Adsorbents. *Ind. Eng. Chem. Res.* **1999**, *38* (9), 3519.
- (156) Ruthven, D. M. *Principles of Adsorption and Adsorption Processes*; Wiley, 1984.
- (157) Cavenati, S.; Grande, C. a.; Rodrigues, A. E. Upgrade of Methane from Landfill Gas by Pressure Swing Adsorption. *Energy & Fuels* **2005**, *19* (6), 2545.
- (158) Shen, C.; Grande, C. A.; Li, P.; Yu, J.; Rodrigues, A. E. Adsorption Equilibria and Kinetics of CO<sub>2</sub> and N<sub>2</sub> on Activated Carbon Beads. *Chem. Eng. J.* **2010**, *160* (2), 398.
- (159) Vargas, D. P.; Balsamo, M.; Giraldo, L.; Erto, A.; Lancia, A.; Moreno-Piraján, J. C. Equilibrium and Dynamic CO<sub>2</sub> Adsorption on Activated Carbon Honeycomb Monoliths. *Ind. Eng. Chem. Res.* **2015**, acs.iecr.5b03234.
- (160) Mulgundmath, V. P.; Tezel, F. H.; Jones, R. A.; Thibault, J. Fixed Bed Adsorption for the Removal of Carbon Dioxide from Nitrogen: Breakthrough Behaviour and Modelling for Heat and Mass Transfer. *Sep. Purif. Technol.* **2012**, *85*, 17.
- (161) Sabouni, R.; Kazemian, H.; Rohani, S. Mathematical Modeling and Experimental Breakthrough Curves of Carbon Dioxide Adsorption on Metal Organic Framework CPM-5. *Environ. Sci. Technol.* **2013**, *47* (16), 9372.
- (162) Silva, J. C.; Rodrigues, A. E. Analysis of ZLC Technique for Diffusivity Measurements in Bidisperse Porous Adsorbent Pellets. *Gas Sep. Purif.* **1996**, *10* (4), 207.

## Appendix A : Steam, CO<sub>2</sub> and KOH activation set-up for production of activated carbons

### Activation of biochar with steam:

The schematic of steam activation set-up for is shown in Figure A.1. A fixed bed, Inconel reactor (25.4 mm OD, 22 mm ID, length of 870 mm) was used for activation of biochar with steam. A vertical furnace (3210 series, max temperature of 1200 °C, Applied Test System Inc.) was used to keep the reactor at a constant temperature. Temperature calibration of bed was recorded by placing a K-type thermocouple in the middle of the bed and is shown in Figure A.2.

Temperatures of the furnace and boiler were controlled by two temperature controllers (Eurotherm 2416 and Omega CN 7500, respectively). Nitrogen flow was controlled by a mass flow controller (Brooks Instrument, 5850S) and the calibration data is shown in Figure A.3. Water is injected by a metering pump (Genie Kent) to the boiler and steam was generated in a boiler (stainless steel tube embedded in a insulated aluminum block). The calibration data of water injection pump is shown in Figure A.4.

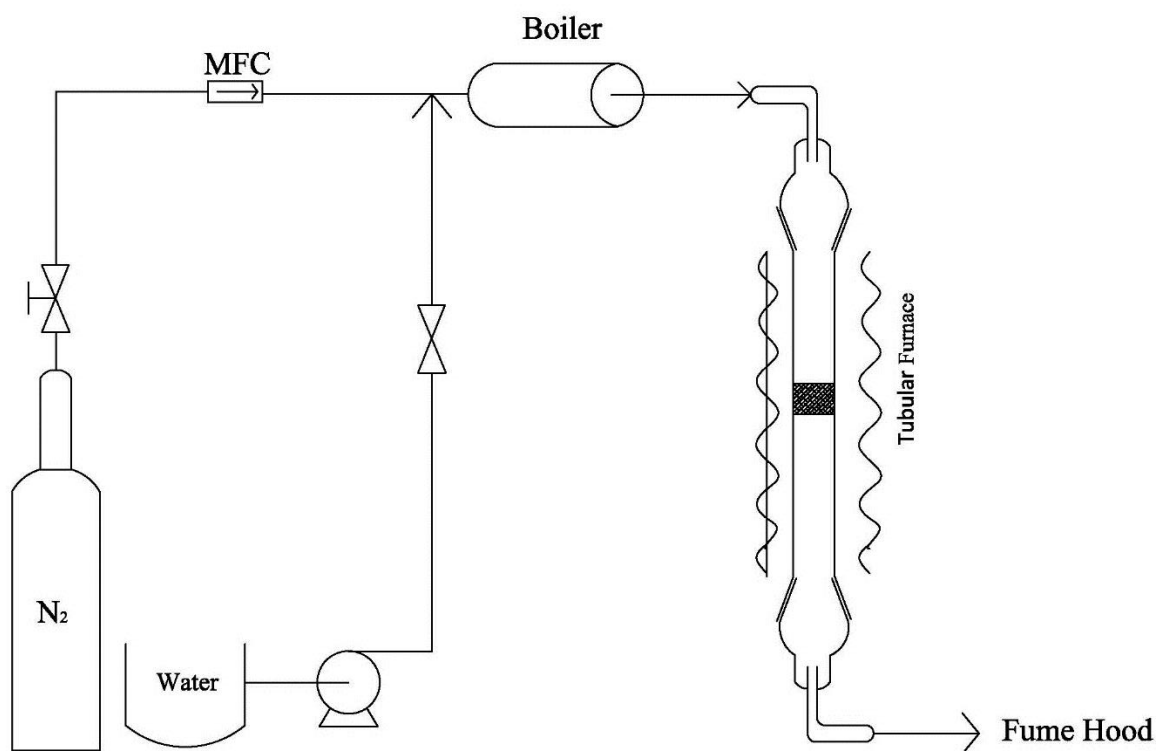


Figure A.1: Schematic of steam activation set-up

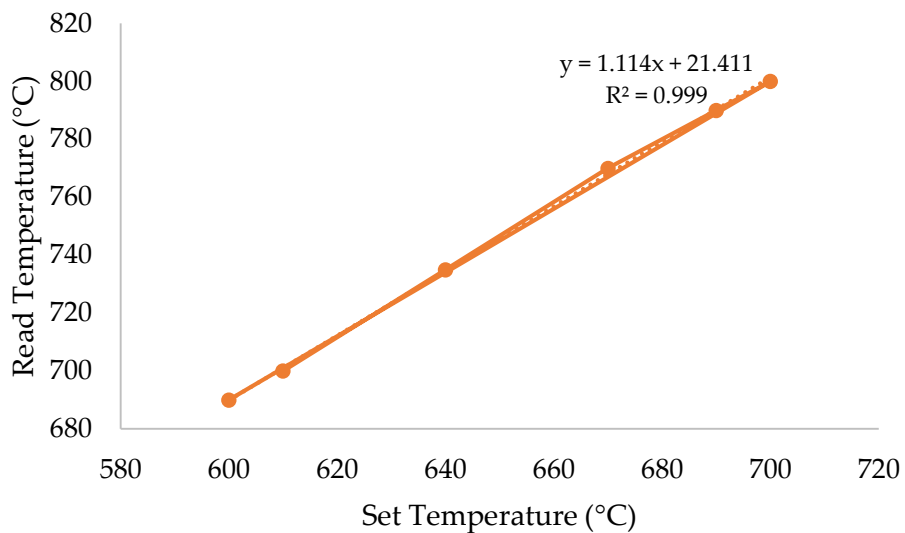


Figure A.2: Temperature calibration data for the furnace installed on the steam activation set-up

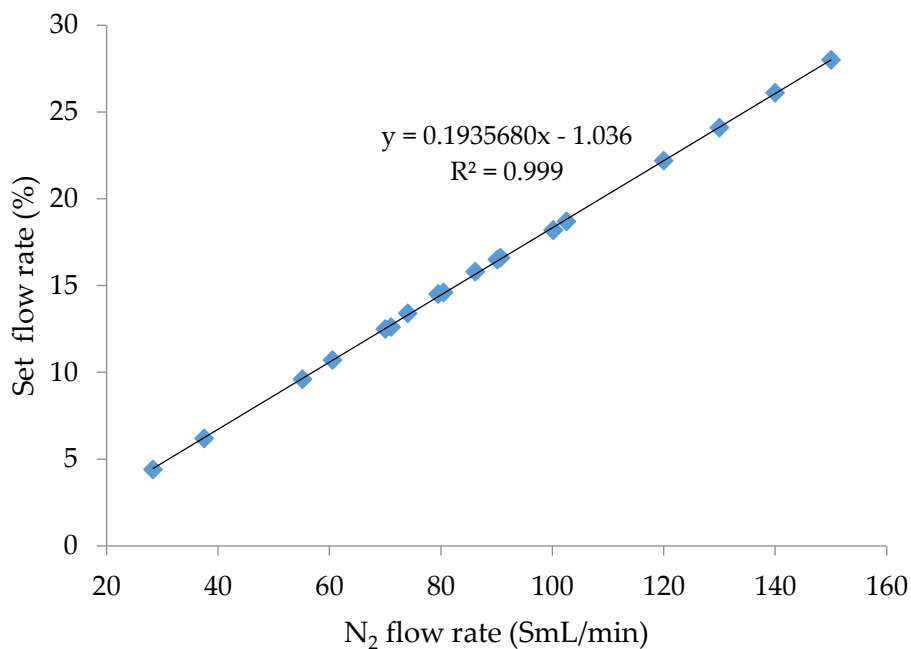


Figure A.3: Calibration data for N<sub>2</sub> mass flow controller used in the steam activation set-up

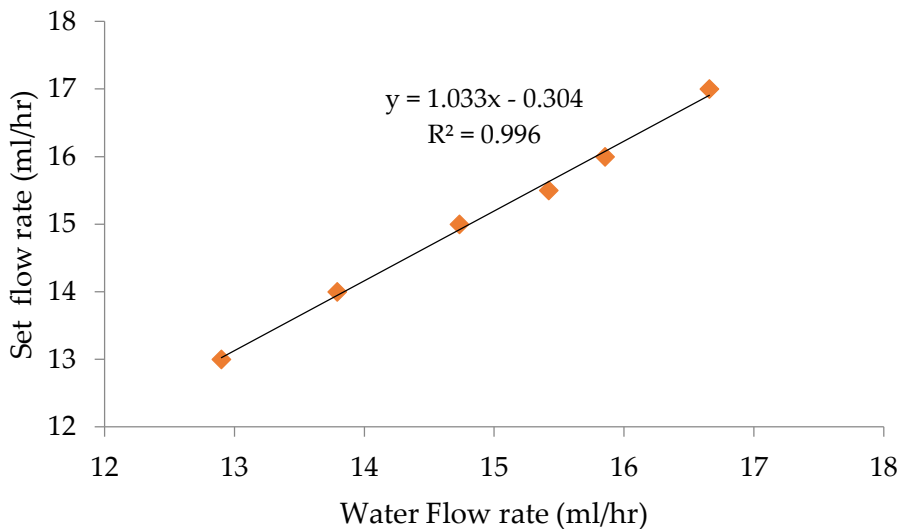


Figure A.4: Calibration data for water injection pump used for steam generation

#### Activation of biochar with CO<sub>2</sub>:

The schematic of experimental set-up for biochar activation with CO<sub>2</sub> is shown in Figure A.5. A fixed bed, Inconel reactor (25.4 mm OD, 22 mm ID, length of 660 mm) was used for activation of biochar with CO<sub>2</sub>. A vertical furnace (3210 series, max temperature of 1200 °C, Applied Test System Inc.) was used to keep the reactor at a constant temperature. Temperature of the furnace was controlled by a temperature controller (Eurotherm 2416) and temperature calibration data of bed is shown in Figure A.6. Argon and CO<sub>2</sub> flow were controlled by a mass flow controller (Brooks Instrument, 5850S A/B) and the calibration data is shown in Figures A.7 and A.8, respectively.

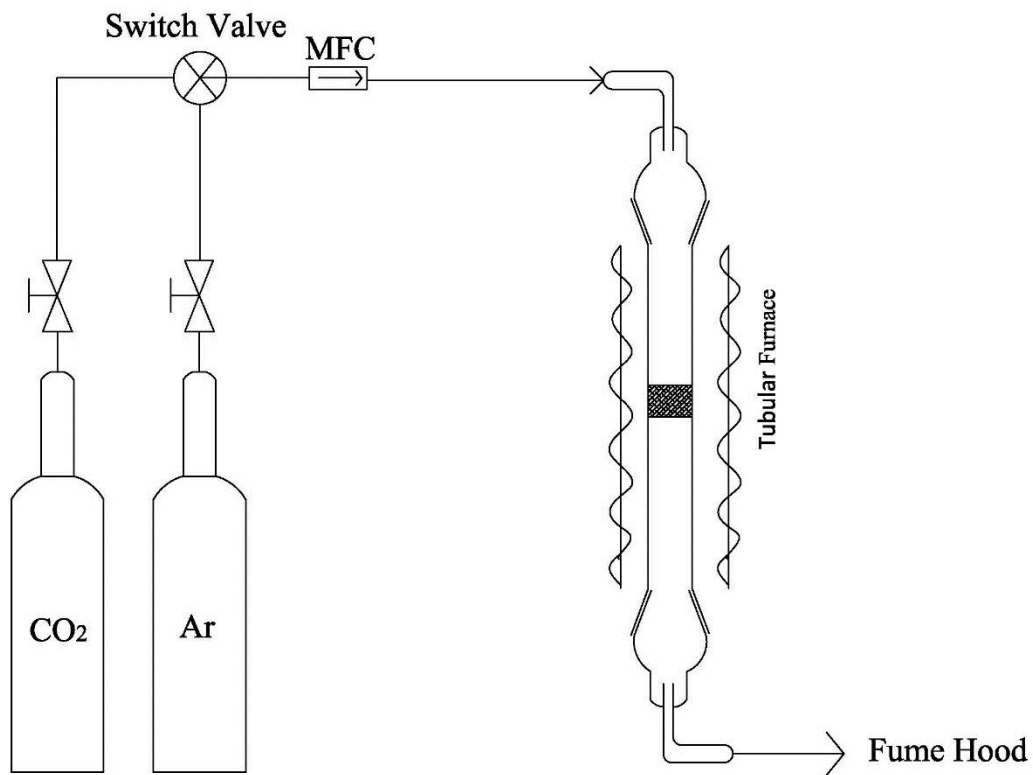


Figure A.5: Schematic of CO<sub>2</sub> activation set-up

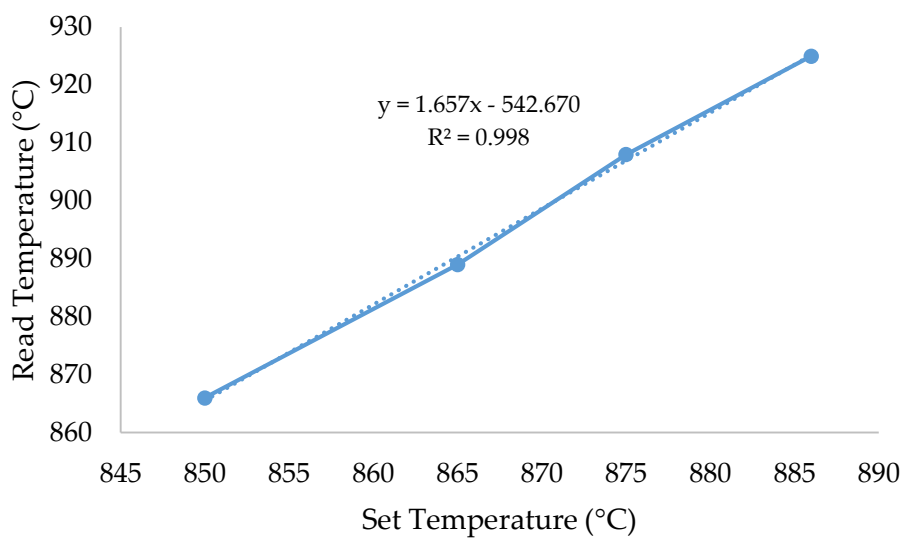


Figure A.6: Temperature calibration data for the furnace installed on the CO<sub>2</sub> activation set-up

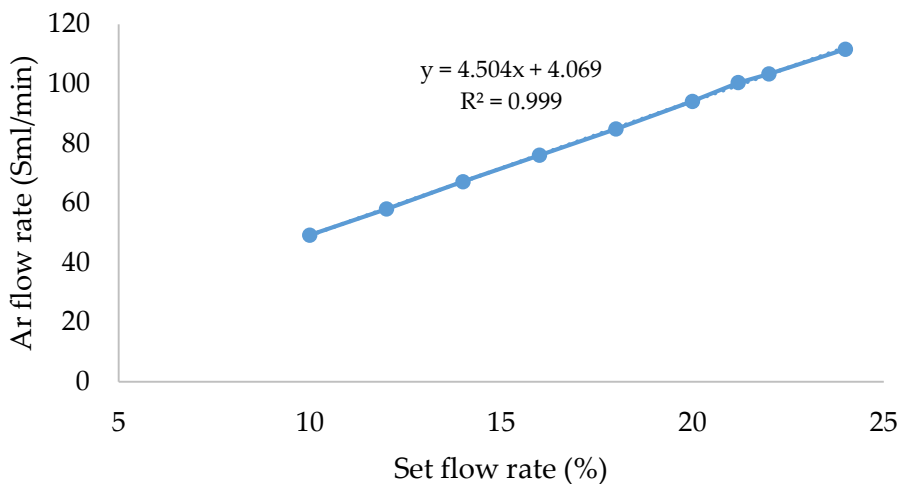


Figure A.7: Calibration data for Ar mass flow controller used in the CO<sub>2</sub> activation set-up (at 100 psi)

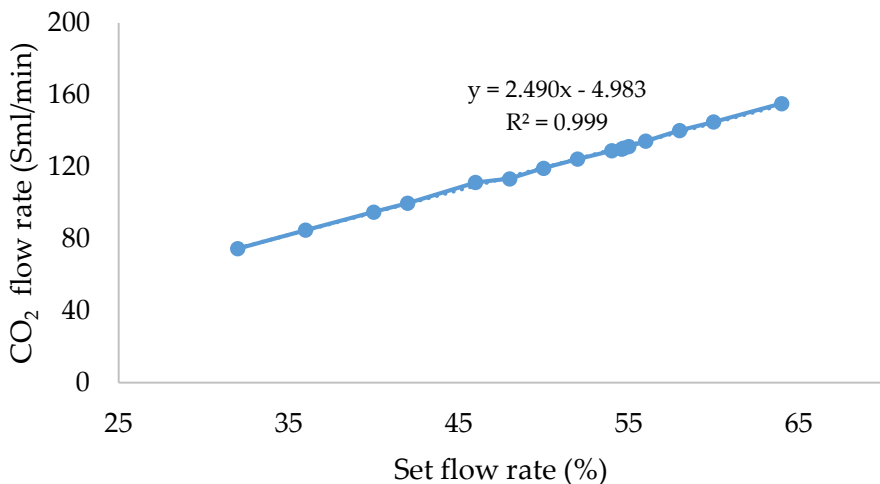


Figure A.8: Calibration data for CO<sub>2</sub> mass flow controller used in the CO<sub>2</sub> activation set-up (at 150 psi)

**Activation of biochar with KOH:**

KOH activation of biochar was carried out in the experimental set-up that was used for steam activation process (water injection line was blocked). Calibration data in Figure A.2 and A.3 are also valid for KOH activation.

## Appendix B : Fixed reactor specifications and calibration curves for CO<sub>2</sub> adsorption experiment in chapter 3

A fixed-bed reactor set-up for CO<sub>2</sub> adsorption experiments was designed and built at the Department of Chemical and Biological Engineering, University of Saskatchewan. An Inconel tubular reactor was used for CO<sub>2</sub> adsorption experiments. A heating tape (Silicone rubber insulated heating tape, Cole-Parmer) was used to supply heat to the reactor. It could be operated to a maximum temperature of 232 °C. Bed temperature was controlled by placing a K-type thermocouple in the middle of the bed coupled with a temperature controller (Eurotherm-2416). Specification of the fixed-bed reactor is shown in Table B.1. The flow rate of CO<sub>2</sub> and He were controlled by a mass flow controllers (Brooks Instrument, 5850S, max flow 200 ml/min ) and a metering valve coupled with a mass flow meter (Brooks Instrument, 5860S, max flow 500 ml/min). Calibration data for CO<sub>2</sub> and He are given in Figures B.1 and B.2.

Table B.1: Specifications of fixed-bed reactor

bed diameter	cm	2.5
bed height	cm	6
column length	cm	42

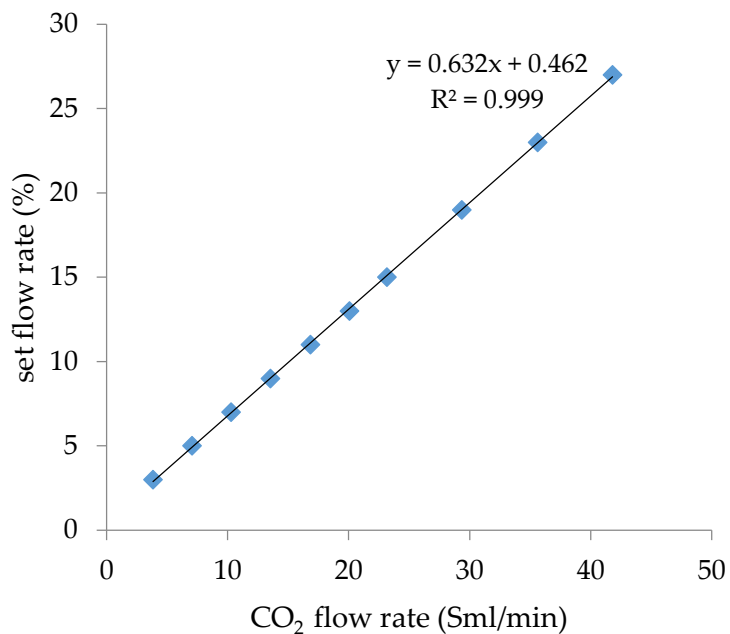


Figure B.1: Calibration data for CO<sub>2</sub> mass flow controller used in the CO<sub>2</sub>/He adsorption experiment at 100 psi

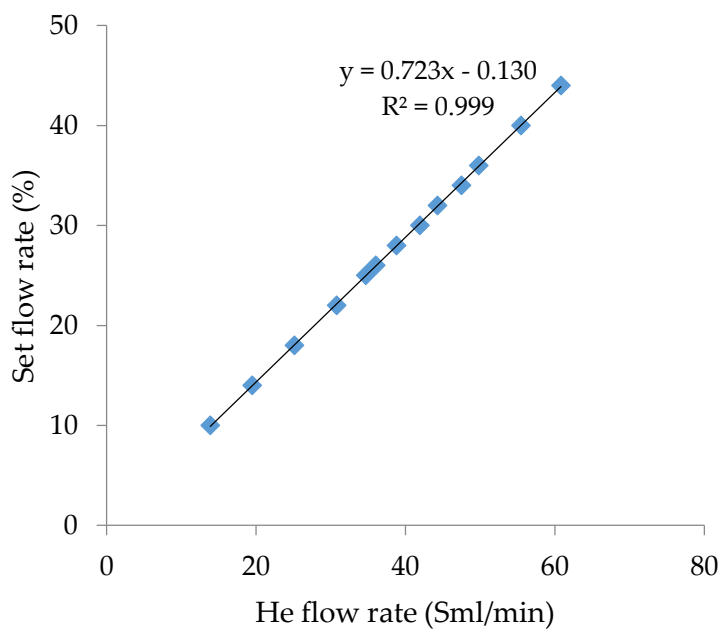


Figure B.2: Calibration data for He mass flow controller used in the CO<sub>2</sub>/He adsorption experiment at 100 psi

## GC Calibration Table

GC calibration date on Sep 5, 2013 is shown in Table B.2 and Table B.3.

Table B.2: GC Calibration data used in chapter 3

RetTime [min]	Lvl Sig	Amount [%]	Area	Amt/Area	Ref Grp Name
0.331	3 1	4.99000	72.19977	6.91138e-2	Helium
0.361	3 1	9.97000	236.94647	4.20770e-2	H2
0.405	4 1	7.01000	29.96327	2.33953e-1	CO2
0.428	4 1	3.00000	13.14342	2.28251e-1	Ethylene
0.447	4 1	4.98000e-1	2.31539	2.15082e-1	Ethane
0.477	4 1	4.98000e-1	1.60827	3.09649e-1	Acetylene
0.481	3 1	2.00000	5.55207	3.60226e-1	O2
	2	20.78000	50.79090	4.09128e-1	
0.636	3 1	62.32300	136.96855	4.55017e-1	N2
	2	74.19000	156.21611	4.74919e-1	
0.748	4 1	7.01000e-1	3.82498	1.83269e-1	Propane/Propylene
0.897	3 1	5.99000	35.67048	1.67926e-1	Methane
1.364	3 1	8.01000	17.34495	4.61806e-1	CO

Table B.3: Composition of standard gas used for GC calibration

Component	Certified Concentration	Analytical Accuracy
acetylene	0.498	±2%
Propane	0.200	±2%
Propylene	0.501	±2%
Ethane	0.498	±2%
Ethylene	3.00	±2%
Methane	5.99	±2%
Carbon monoxide	8.01	±2%
Hydrogen	9.97	±2%
Carbon dioxide	7.01	±2%
Oxygen	2.00	±2%
Nitrogen	62.32	±2%
Praxair Part Number:	NI AC5000X3C-AS	

### Appendix C : The ANOVA results of CO<sub>2</sub> activated carbon

The experimental results of CO<sub>2</sub> adsorption on CO<sub>2</sub> activated carbon are fitted with a quadratic model that proved best for lack of fit and model statistics tests. Table C.1 presents ANOVA of CO<sub>2</sub> adsorption model on CO<sub>2</sub> activated carbon. Although the Predicted R<sup>2</sup> of 0.93 is in reasonable agreement with the Adj-R<sup>2</sup> of 0.98(the difference < 0.2), there is significant lack of fit (0.0004) which indicates that the provisional model is inadequate.

Table C.1: The ANOVA results of the response surface quadratic model of CO<sub>2</sub> activated carbon

	Sum of square	Mean square	df	p-value
Model	2624.98	656.25	4	<0.0001
T	1009.91	1009.91	1	<0.0001
C <sub>CO<sub>2</sub></sub>	1498.70	1498.70	1	<0.0001
T. C <sub>CO<sub>2</sub></sub>	82.25	82.27	1	0.0041
C <sub>CO<sub>2</sub></sub> . C <sub>CO<sub>2</sub></sub>	34.11	34.11	1	0.0335
residual	41.54	5.20	8	
Lack of fit	41.05	10.26	4	0.0004
Pure error	0.49	0.12	4	0.0041
Total	2694.23		13	
Std. Dev.	2.43			
R <sup>2</sup>	0.99			
Adj-R <sup>2</sup>	0.98			
Predicted R <sup>2</sup>	0.93			

## Appendix D : Willow ring characteristic, GC calibration data, fixed-bed reactor specifications and related calibrations for CO<sub>2</sub> adsorption experiment in chapter 4

Physical characteristics of willow ring (biomass) is shown in Table D.1.

Table D.1: Approximate analysis of willow ring

Moisture Content	8.4 wt.%
Ash content	1.9 wt.%
Volatile matter	79.3 wt.%
Fixed carbon*	10.4 wt.%

\*Fixed carbon is calculated by difference

The temperature calibration data used for slow pyrolysis of biomass sample in chapter 4 is provided in Figure D.1.

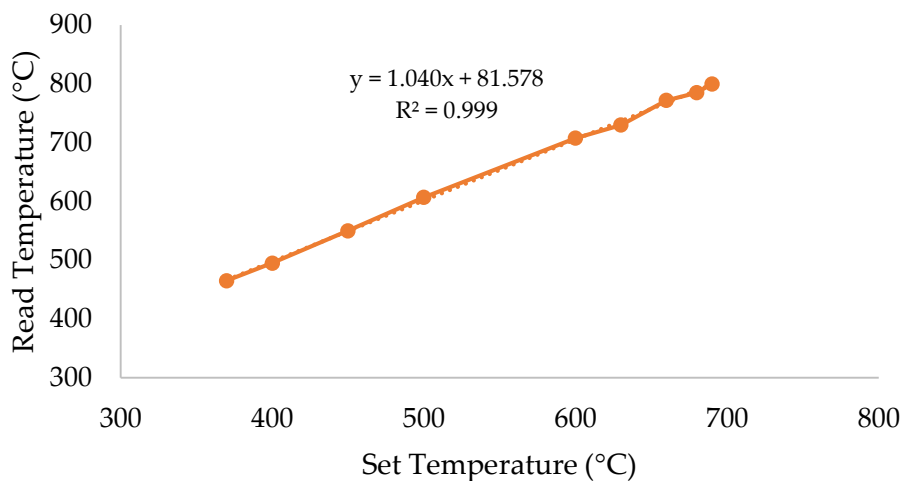


Figure D.1: Temperature calibration data for the furnace used for slow pyrolysis

### GC Calibration Table

GC calibration data used in chapter 4 is shown in Table D.2

Table D.2: GC calibration Data on 21 March, 2014

RetTime [min]	Lvl Sig	Amount [%]	Area	Amt/Area	Ref Grp Name
0.329	3 1	4.99000	72.19977	6.91138e-2	Helium
0.364	3 1	9.97000	236.94647	4.20770e-2	H2
0.402	4 1	7.01000	29.96327	2.33953e-1	CO2
	4	20.00000	90.77847	2.20317e-1	
0.429	4 1	3.00000	13.14342	2.28251e-1	Ethylene
0.446	4 1	4.98000e-1	2.31539	2.15082e-1	Ethane
0.477	4 1	4.98000e-1	1.60827	3.09649e-1	Acetylene
0.481	3 1	2.00000	5.55207	3.60226e-1	O2
	2	20.78000	50.79090	4.09128e-1	
0.650	3 1	62.32300	136.96855	4.55017e-1	N2
	2	74.19000	156.21611	4.74919e-1	
	3	100.00000	210.75797	4.74478e-1	
0.748	4 1	7.01000e-1	3.82498	1.83269e-1	Propane/Propylene
0.897	3 1	5.99000	35.67048	1.67926e-1	Methane
1.364	3 1	8.01000	17.34495	4.61806e-1	CO

Specification of the fixed-bed reactor is shown in Table D.3. The flow rate of CO<sub>2</sub>, O<sub>2</sub> and N<sub>2</sub> were controlled by three mass flow controllers of Brooks Instrument 5850E and max flow of 200ml/min, Brooks Instrument 5850TR and max flow of 12SLPH, and Brooks Instrument 5850S and max flow of 200ml/min, respectively. Calibration data for CO<sub>2</sub>, O<sub>2</sub> and N<sub>2</sub> mass flow controllers are given in Figures D.2, D.3 and D.4.

Table D.3: Specifications of the fixed-bed reactor used in chapter 4

reactor material	stainless steel	
bed diameter	cm	2.5
bed height	cm	5
column length	cm	42

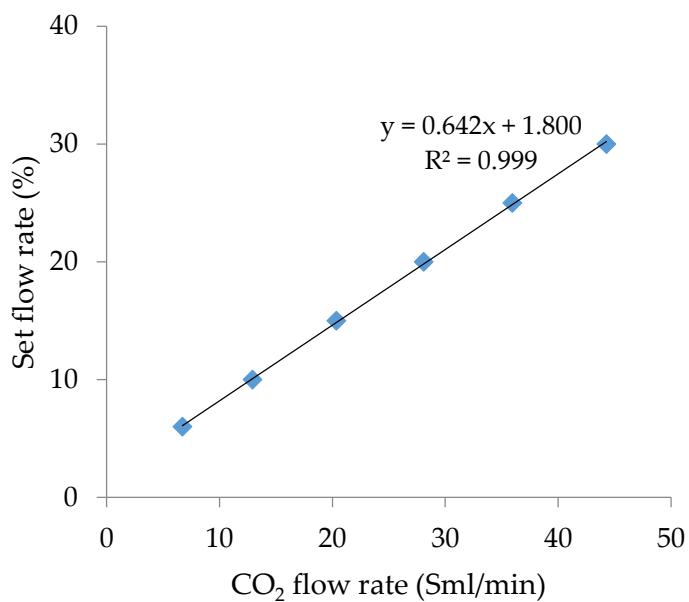


Figure D.2: Calibration data for CO<sub>2</sub> mass flow controller used in the CO<sub>2</sub>/O<sub>2</sub>/N<sub>2</sub> adsorption experiment at 100 psi

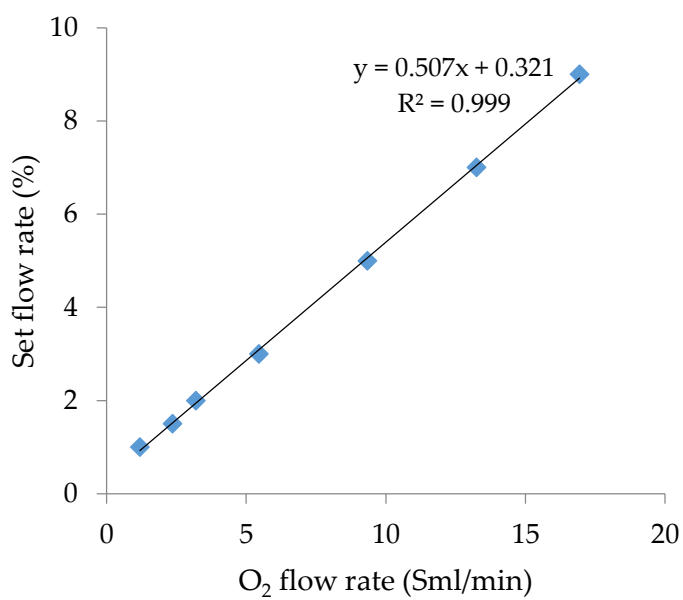


Figure D.3: Calibration data for O<sub>2</sub> mass flow controller used in the CO<sub>2</sub>/O<sub>2</sub>/N<sub>2</sub> adsorption experiment at 100 psi

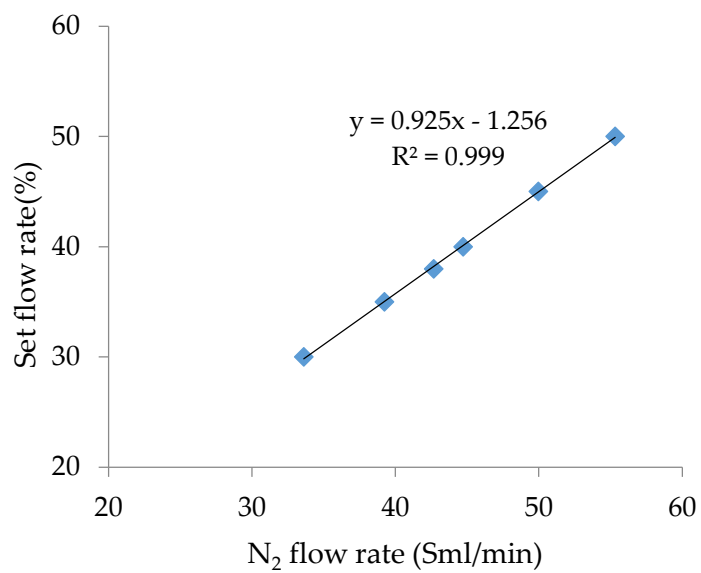


Figure D.4: Calibration data for N<sub>2</sub> mass flow controller used in the CO<sub>2</sub>/O<sub>2</sub>/N<sub>2</sub> adsorption experiment at 100 psi

## Appendix E : Calibration data and calculations used in Chapter 5

Temperature calibration data of the tubular furnace installed on the calcination set-up is shown in Figure E.1. Calibration data used for injection pump used for steam generation is shown in Figure E.2

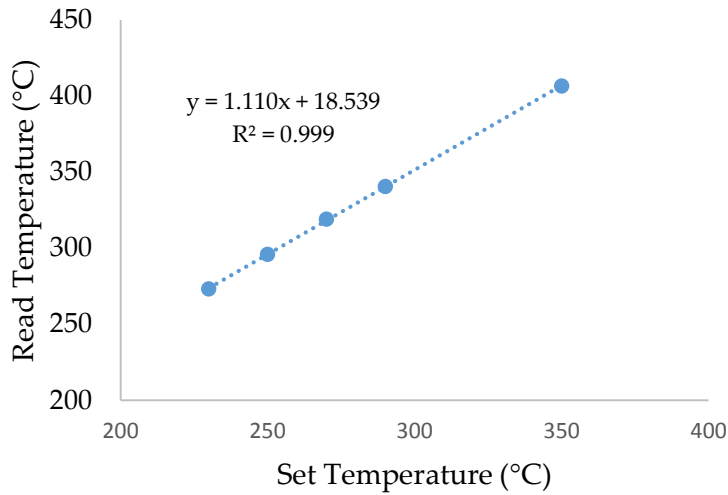


Figure E.1: Temperature calibration curve of the furnace installed on the calcination set-up

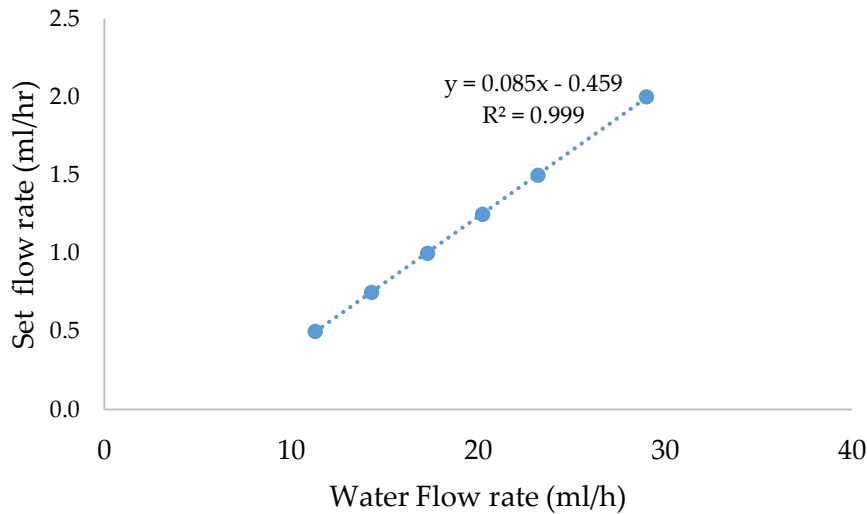


Figure E.2: Calibration data for water injection pump used for steam generation in Chapter 5

### 1- Excess Solution Impregnation of Biochar

To produce 3 and 10 wt. % MgO impregnated activated carbons, the biochar was treated with magnesium nitrate in 100 ml water for 15 h at room temperature. Then the sample was dried at 100 °C for 15 h in an oven followed by the steam activation process. The yield of activation process is ~51% and the initial salt content in the bath was selected in order to have 3 and 10 wt. % Mg in the final product. The metal content after rinsing was calculated based on the weight loss after rinsing. Details of preparation of excess solution impregnation of biochar are shown in Table E.1.

Table E.1: Preparation details of excess solution impregnation of biochar

Sampl es	Bioch ar weigh t (g)	Mg(NO <sub>3</sub> ) <sub>2</sub> .6H <sub>2</sub> O (g)	Wat er (ml)	after activati on weight (g)	Activation Temperatu re (°C)	carbo n weig ht (g)	weight differen ce (g)	metal conte nt (g)	metal conte nt (%)
3MgO -B	24.25	4.34	100. 0	13.05	700	12.37	0.68	0.41	3.2%
3MgO -B-R	24.25	4.34	100. 0	12.78	700	12.37	0.41	0.25	1.9%
10Mg O-B	22.50	15.39	100. 0	13.89	700	11.48	2.42	1.46	10.5 %
10Mg O-B-R	22.50	15.39	100. 0	13.05	700	11.48	1.58	0.95	7.3%

## 2- Excess Solution and Incipient Wetness Impregnation of Activated Carbon

For excess solution impregnation, steam activated carbons were impregnated in 100 ml water with metal nitrate of an appropriate concentration for 15 h to produce 3 and 10 wt. % of metal in

the final product. The mixtures of AC and solutions of metal nitrate were then dried in the oven for 15 h. The procedure was followed by calcination at 325 °C for 4 h. The metal content of the rinsed samples was calculated based on the weight loss after rinsing.

For incipient wetness impregnation, steam activated carbon was impregnated with Mg salt solution drop by drop. The mixture was kept at room temperature for 15 h. Then the sample was dried at 100 °C for 15 h in an oven followed by calcination at 325°C for 4h. Table E.2 shows the details of excess solution preparation and incipient wetness impregnation of activated carbon.

Table E.2: preparation details of excess solution and incipient wetness impregnation of activated carbon

Samples	after activation weight (g)	Mg(NO <sub>3</sub> ) <sub>2</sub> .6 H <sub>2</sub> O (g)	Water (ml)	Impregnated Activated Carbon (g)	Weight difference (g)	Metal content (g)	Metal content (%)	Calcination temperature (°C)
3MgO-AC	9.70	3.16	100.0	10.20	0.50	0.30	3.0%	325
3MgO-AC-R	9.70	3.16	100.0	9.94	0.24	0.14	1.5%	325
3Mgo-AC-DRY	9.70	3.16	2.6	10.23	0.53	0.32	3.1%	325
10MgO-AC	9.00	10.55	100.0	10.76	1.76	1.06	9.9%	325
10MgO-AC-R	9.00	10.55	100.0	10.32	1.32	0.80	7.7%	325
10Mgo-AC-DRY	9.00	10.55	2.4	10.78	1.78	1.07	10.0%	325

## Appendix F : Calibration data and calculations used in Chapter 6

### Skeletal Density Calculations:

The gas pycnometer (ultra-pycnometer 1000, Quantachrome Instruments) determines the skeletal density of activated carbon powders based on Eq. F-1 assuming an ideal gas:

$$V_p = V_c + V_R \left[ \frac{P_1}{P_2} - 1 \right] \quad (\text{F-1})$$

where

$V_p$ : the sample volume

$V_c$ : the volume of the empty sample chamber (known from a prior calibration step)

$V_a$ : the volume of the reference volume (again known from a prior calibration step)

$P_1$ : the first pressure (i.e. in the sample chamber only)

$P_2$ : the second (lower) pressure after expansion of the gas into the combined volumes of sample chamber and the reference chamber

Helium is used as the displacing fluid in pycnometer since it penetrates the finest pores approaching one Angstrom. Sample calculation is shown below in Table F.1.

Table F.1: Sample calculation on skeletal density

Weight of activated carbon powders	18.910	g
$P_1$	16.609	
$P_2$	6.560	
$V_a$	90.529	$\text{cm}^3$

$V_c$	147.634	$\text{cm}^3$
$V_p$	8.956	$\text{cm}^3$
Skeletal Density	2.111	$\text{g}/\text{cm}^3$

### Temperature Calibration Data of Furnace Installed on Steam Activation Setup

Figure F.1 shows the temperature calibration data of the furnace installed on activation set-up.

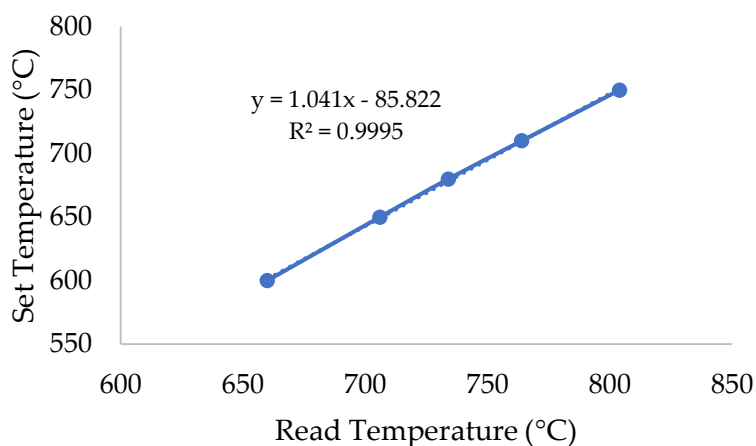


Figure F.1: Temperature calibration data for the furnace installed on the steam activation set-up used in Chapter 6

Adsorption isotherms of  $\text{CO}_2$  and  $\text{N}_2$  are fitted to dual site Langmuir isotherms using  $\text{CO}_2/\text{Ar}$  and  $\text{N}_2/\text{Ar}$  gas mixture at different temperatures. The flow rate of  $\text{CO}_2$ , Ar and  $\text{N}_2$  were controlled by three mass flow controllers of Brooks Instrument 5850E and max flow of 200 ml/min, Brooks Instrument 5850S and max flow of 200ml/min, and Brooks Instrument 5850TR and max flow of 12SLPH, respectively. Calibration data for  $\text{CO}_2$ ,  $\text{O}_2$  and  $\text{N}_2$  mass flow controllers are given in Figures F-2, F-3 and F-4.

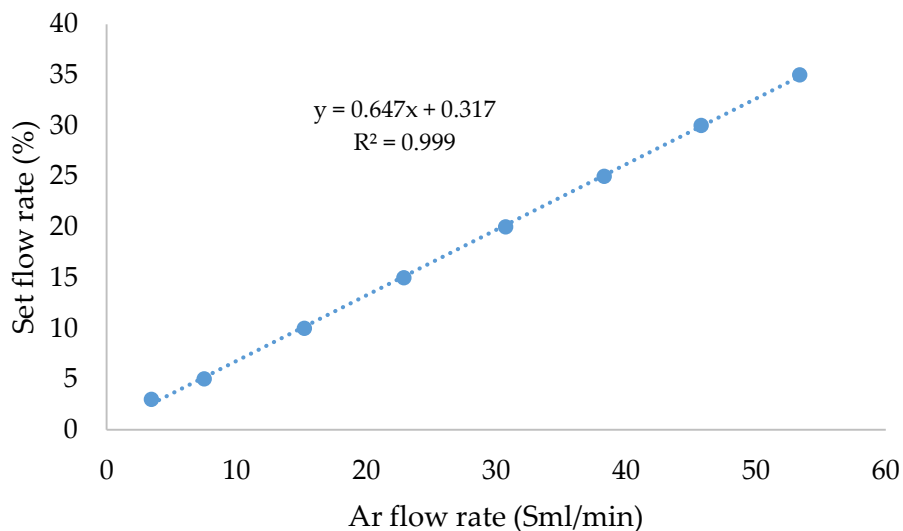


Figure F.2: Calibration data for N<sub>2</sub> mass flow controller used in the Ar/N<sub>2</sub> and Ar/CO<sub>2</sub> adsorption experiments (N<sub>2</sub> and CO<sub>2</sub> adsorption isotherms) at 100 psi

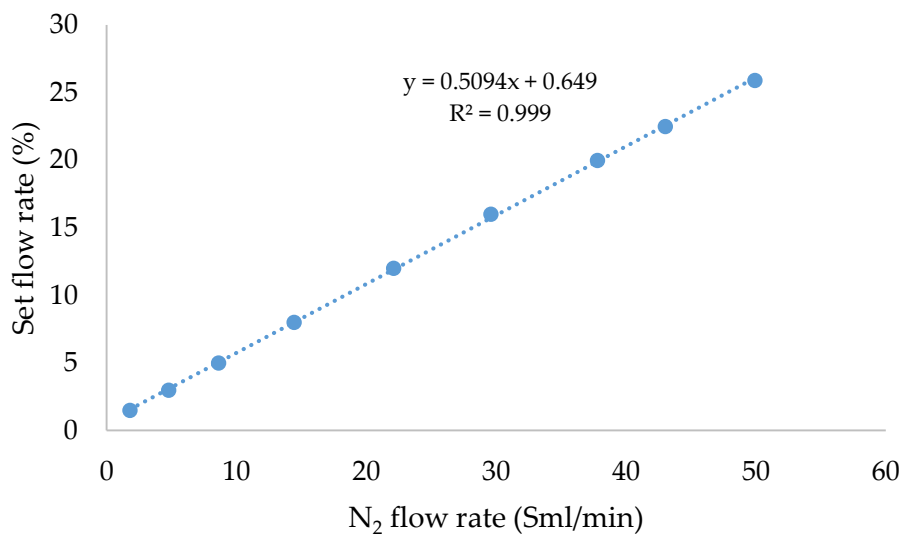


Figure F.3: Calibration data for N<sub>2</sub> mass flow controller used in the Ar/N<sub>2</sub> adsorption experiments (N<sub>2</sub> adsorption isotherms) at 100 psi

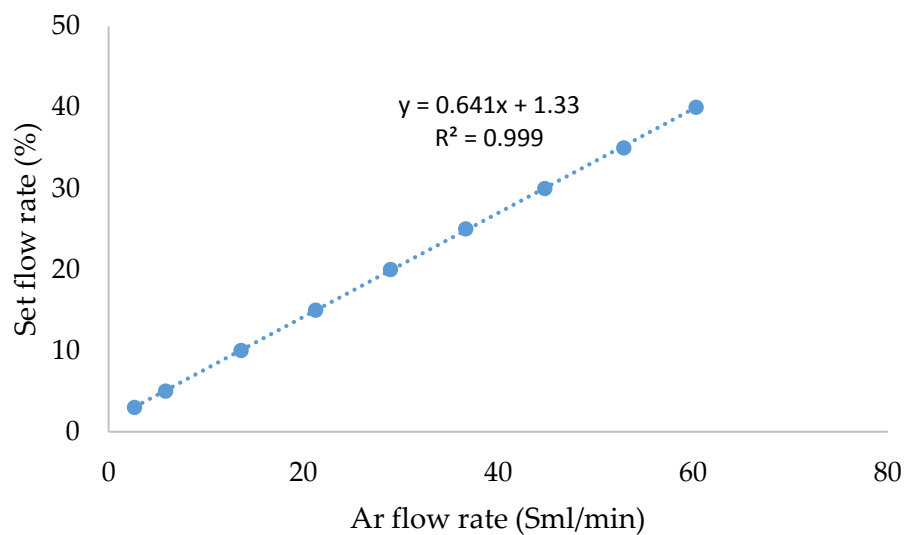


Figure F.4: Calibration data for N<sub>2</sub> mass flow controller used in the Ar/CO<sub>2</sub> adsorption experiments (CO<sub>2</sub> adsorption isotherms) at 100 psi

#### **GC Calibration Table**

GC Calibration Date on February 17, 2016 is shown in Table F.2

Table F.2: GC calibration data on February 17, 2016

RetTime [min]	Lvl Sig	Amount [%]	Area	Amt/Area	Ref Grp Name
0.348	3 1	4.99000	72.19977	6.91138e-2	Helium
0.364	3 1	9.97000	236.94647	4.20770e-2	H2
0.410	4 1	7.01000	29.96327	2.33953e-1	CO2
	4	20.00000	90.77847	2.20317e-1	
0.432	4 1	3.00000	13.14342	2.28251e-1	Ethylene
0.451	4 1	4.98000e-1	2.31539	2.15082e-1	Ethane
0.459	3 1	2.00000	5.55207	3.60226e-1	O2
	2	20.78000	50.79090	4.09128e-1	
0.483	4 1	4.98000e-1	1.60827	3.09649e-1	Acetylene
0.582	3 5	9.50000	18.59585	5.10867e-1	N2
	1	62.32300	136.96855	4.55017e-1	
	2	74.19000	156.21611	4.74919e-1	
	3	100.00000	210.75797	4.74478e-1	
0.748	4 1	7.01000e-1	3.82498	1.83269e-1	Propane/Propylene
0.897	3 1	5.99000	35.67048	1.67926e-1	Methane
1.364	3 1	8.01000	17.34495	4.61806e-1	CO

## Appendix G : Permission to reuse the published papers, submitted manuscript and Figures

Figure G.1, G.2 and G.3 show the permissions to use the published papers in this thesis.

<b>ELSEVIER LICENSE TERMS AND CONDITIONS</b>		Jul 13, 2016
<hr/> <hr/>		
This Agreement between Sepideh Shahkarami ("You") and Elsevier ("Elsevier") consists of your license details and the terms and conditions provided by Elsevier and Copyright Clearance Center.		
License Number	3907260092506	
License date	Jul 13, 2016	
Licensed Content Publisher	Elsevier	
Licensed Content Publication	Journal of Environmental Sciences	
Licensed Content Title	Breakthrough CO <sub>2</sub> adsorption in bio-based activated carbons	
Licensed Content Author	Sepideh Shahkarami,Ramin Azargohar,Ajay K. Dalai,Jafar Soltan	
Licensed Content Date	1 August 2015	
Licensed Content Volume Number	34	
Licensed Content Issue Number	n/a	
Licensed Content Pages	9	
Start Page	68	
End Page	76	
Type of Use	reuse in a thesis/dissertation	
Portion	full article	
Format	both print and electronic	
Are you the author of this Elsevier article?	Yes	
Will you be translating?	No	
Order reference number		
Title of your thesis/dissertation	CO <sub>2</sub> capture from gases using activated carbon	
Expected completion date	Dec 2016	
Estimated size (number of pages)	250	
Elsevier VAT number	GB 494 6272 12	
Requestor Location	Sepideh Shahkarami 307, 525 3rd Ave N  Saskatoon, SK S7K 2J6 Canada Attn: Sepideh Shahkarami	
Total	0.00 CAD	

Figure G.1: permission to use the published paper “Breakthrough CO<sub>2</sub> adsorption in bio-based activated carbons”.



RightsLink®

Home

Create Account

Help



ACS Publications  
Most Trusted. Most Cited. Most Read.

**Title:** Selective CO<sub>2</sub> Capture by Activated Carbons: Evaluation of the Effects of Precursors and Pyrolysis Process

**Author:** Sepideh Shahkarami, Ajay K. Dalai, Jafar Soltan, et al

**Publication:** Energy & Fuels

**Publisher:** American Chemical Society

**Date:** Nov 1, 2015

Copyright © 2015, American Chemical Society

LOGIN

If you're a [copyright.com](#) user, you can login to RightsLink using your [copyright.com](#) credentials. Already a [RightsLink user](#) or want to [learn more?](#)

#### PERMISSION/LICENSE IS GRANTED FOR YOUR ORDER AT NO CHARGE

This type of permission/license, instead of the standard Terms & Conditions, is sent to you because no fee is being charged for your order. Please note the following:

- Permission is granted for your request in both print and electronic formats, and translations.
- If figures and/or tables were requested, they may be adapted or used in part.
- Please print this page for your records and send a copy of it to your publisher/graduate school.
- Appropriate credit for the requested material should be given as follows: "Reprinted (adapted) with permission from (COMPLETE REFERENCE CITATION). Copyright (YEAR) American Chemical Society." Insert appropriate information in place of the capitalized words.
- One-time permission is granted only for the use specified in your request. No additional uses are granted (such as derivative works or other editions). For any other uses, please submit a new request.

BACK

CLOSE WINDOW

Copyright © 2016 Copyright Clearance Center, Inc. All Rights Reserved. [Privacy statement](#), [Terms and Conditions](#). Comments? We would like to hear from you. E-mail us at [customer-care@copyright.com](mailto:customer-care@copyright.com)

Figure G.2: permission to use the published paper “selective CO<sub>2</sub> capture by activated carbons: Evaluation of the effects of precursors and pyrolysis process”.

**Title:** Enhanced CO<sub>2</sub> Adsorption Using MgO-Impregnated Activated Carbon: Impact of Preparation Techniques

**Author:** Sepideh Shahkarami, Ajay K. Dalai, Jafar Soltan

**Publication:** Industrial & Engineering Chemistry Research

**Publisher:** American Chemical Society

**Date:** May 1, 2016

Copyright © 2016, American Chemical Society

LOGIN

If you're a **copyright.com** user, you can login to RightsLink using your copyright.com credentials. Already a **RightsLink user** or want to [learn more?](#)

**PERMISSION/LICENSE IS GRANTED FOR YOUR ORDER AT NO CHARGE**

This type of permission/license, instead of the standard Terms & Conditions, is sent to you because no fee is being charged for your order. Please note the following:

- Permission is granted for your request in both print and electronic formats, and translations.
- If figures and/or tables were requested, they may be adapted or used in part.
- Please print this page for your records and send a copy of it to your publisher/graduate school.
- Appropriate credit for the requested material should be given as follows: "Reprinted (adapted) with permission from (COMPLETE REFERENCE CITATION). Copyright (YEAR) American Chemical Society." Insert appropriate information in place of the capitalized words.
- One-time permission is granted only for the use specified in your request. No additional uses are granted (such as derivative works or other editions). For any other uses, please submit a new request.

[BACK](#)

[CLOSE WINDOW](#)

Figure G.3: permission to use the published paper “Enhanced CO<sub>2</sub> adsorption using MgO-impregnated activated carbon: impact of preparation techniques”.